DESIGN OF OPTIMAL POWER MANAGEMENT TECHNIQUE FOR RESILIENT OPERATION IN AN INTERCONNECTED HYBRID MICROGRID SYSTEM

By

MOSHAMMED NISHAT TASNIM

Student ID: 21MEE006F

A thesis submitted in partial fulfilment of the requirements for the degree of

MASTER of SCIENCE in Electrical and Electronic Engineering

Department of Electrical and Electronic Engineering

CHITTAGONG UNIVERSITY OF ENGINEERING AND TECHNOLOGY

March 2024

Declaration

I hereby declare that the work contained in this thesis has not been previously submitted to meet requirements for an award at this or any other higher education institution. To the best of my knowledge and belief, the thesis contains no material previously published or written by another person except where due reference is cited. Furthermore, the Thesis complies with PLAGIARISM and ACADEMIC INTEGRITY regulation of CUET.

MOSHAMMED NISHAT TASNIM

21MEE006F

Department of Electrical and Electronics Engineering

Chittagong University of Engineering & Technology (CUET)

List of Publications

Journal Article

- Moshammed Nishat Tasnim, Tofael Ahmed, Monjila Afrin Dorothi, Shameem Ahmad, G. M. Shafiullah, S. M. Ferdous, and Saad Mekhilef, "Voltage-Oriented Control-Based Three-Phase, Three-Leg Bidirectional AC–DC Converter with Improved Power Quality for Microgrids." Vol. 16(17), p. 6188, Energies, August 2023.
  DOI: https://doi.org/10.3390/en16176188
- Moshammed Nishat Tasnim, Tofael Ahmed, Shameem Ahmad, Saad Mekhilef, "Implementation of Control Strategies for Energy Storage Systems and Interlinking Converters in an Interconnected Hybrid Microgrid System for Optimal Power Management Using OPAL-RT." IEEE Transactions on Industry Applications **(Under review)**.

Conference

- Moshammed Nishat Tasnim, Tofael Ahmed, Shameem Ahmad, Saad Mekhilef, "Autonomous Power Management and Control Among Interconnected Standalone Hybrid Microgrids", 2023 10th IEEE International Conference on Power Systems (ICPS), pp.1-6, 2023.
  DOI: https://doi.org/10.1109/ICPS60393.2023.10428767
- Moshammed Nishat Tasnim, Tofael Ahmed, Shameem Ahmad, Saad Mekhilef, "Hardware in The Loop Implementation of The Control Strategies for the AC-Microgrid in OPAL-RT Simulator," in 2023 IEEE IAS Global Conference on Renewable Energy and Hydrogen Technologies (GlobConHT), 2023, pp. 1-6: IEEE.
  DOI: https://doi.org/10.1109/GlobConHT56829.2023.10087462

Approval/Declaration by the Supervisor

This is to certify that Moshammed Nishat Tasnim has carried out this research work under my supervision, and that she has fulfilled the relevant Academic Ordinance of the Chittagong University of Engineering and Technology, so that she is qualified to submit the following Thesis in the application for the degree of MASTER of SCIENCE in Electrical and Electronics Engineering. Furthermore, the Thesis complies with the PLAGIARISM and ACADEMIC INTEGRITY regulation of CUET.

DR. TOFAEL AHMED

Professor

Department of Electrical and Electronics Engineering

Chittagong University of Engineering & Technology

Acknowledgement

Above all, I would like to express my limitless thanks to Allah, the Almighty, the Most Gracious, and the Most Merciful, for providing me with the opportunity, strength, and motivation I needed to carry out and complete the thesis work.

To my supervisor, Dr. Tofael Ahmed, who chose me and provided me with the opportunity to complete the degree of Master of Science in Electrical and Electronics Engineering under his guidance, I would like to convey my gratitude and admiration. I acknowledge my supervisor's guidance, sympathy, academic advice, and assistance in every way. I am indebted to him for his careful mentorship and belief in me, which have enabled me to finish my thesis and advance my scientific understanding in the field of power systems.

The author also thanks the Chittagong University of Engineering and Technology (CUET) for providing support under the Development of the CUET Project and Project No. CUET/DRE/2021-22/EEE/016 under Directorate of Research and Extension (DRE), CUET.

Abstract

The concept of networking multiple microgrids is one of the most promising initiatives in microgrid-based power generation frameworks to address the challenges of a single microgrid's resiliency and enhance supply security. Interconnected microgrids have the potential to serve as a fundamental framework for future distribution systems due to the extensive deployment of smart grid technology. Infrastructure planning and design, control theory, and communication technologies are required to regulate microgrid clusters in a flexible and efficient manner. That is, a proper control structure with robust and reliable control strategies is required to improve the performance of the interconnected microgrids in terms of power-sharing, power quality, and stability.

The study introduces a novel control structure and a clustering method for interconnected hybrid microgrids to form an integrated framework. The proposed control structure for power flow control among hybrid microgrids places particular emphasis on the control strategies of three converters, such as the energy storage system, the interlinking converter of each hybrid microgrid, and the interconnecting converter for networking multiple microgrids. The control strategy of the hybrid microgrid’s interlinking converter is based on a voltage-frequency droop control to ensure proper operation in three operating modes, such as islanded, grid-connected, and interconnecting modes. The virtual inertia and state-of-charge-based controller of the energy storage system controls the battery bank's charging and discharging operations and provides an autonomous power flow inside each hybrid microgrid. Finally, the control strategy of a parallel interlinking converter structure is designed to interconnect and control the power flow among hybrid microgrids.

The control structure allows both islanded and grid-connected operations without swapping between two controllers. This control framework reduces the number of activation operations in response to variations in conditions. Consequently, negative consequences like an uneven transition and system failure due to an inaccurate transition can be mitigated. In summary, the suggested control framework can function seamlessly upon the occurrence of unintended situational changes, such as main grid failure or islanding (with -0.11% variation in frequency), load variation (-0.038% variation during load increment and 0.02% variation during load decrement), source failure (-0.13% and 0.18% variations in frequency during wind generator failure), and grid synchronization (with 0.04% variation in frequency), without requiring a control mode transition.

The clustering method and control structure of the interconnected microgrid system are designed in a MATLAB/Simulink environment. The OPAL-RT simulator (OP5600)-based real-time software-in-the-loop simulation technique is used to analyse the performance of the interconnected system in terms of load variations, source failure, power quality, mode transition, and energy storage system management. The results indicate that the control structure, with three control strategies, ensures reliable operation in all modes with reduced total harmonic distortion (less than 5%) and lower frequency fluctuation (less than 1%), and also maximizes power supply security.

বিমূর্ত

একাধিক মাইক্রোগ্রিডকে আন্তঃসংযোগের ধারণাটি মাইক্রোগ্রিড-ভিত্তিক বিদ্যুৎ উৎপাদন কাঠামোর ক্ষেত্রে আশাপ্রদ উদ্যোগগুলির মধ্যে একটি কারণ ধারণাটি একক মাইক্রোগ্রিডের resiliency সাথে যুক্ত চ্যালেঞ্জগুলি মোকাবেলা করতে এবং বিদ্যুৎ সরবরাহের নিশ্চয়তা বাড়াতে সবচেয়ে উপযোগী। স্মার্ট গ্রিড প্রযুক্তি ব্যাপক অন্তর্ভুক্তির কারণে আন্তঃসংযুক্ত মাইক্রোগ্রিড সিস্টেম ভবিষ্যত বিতরণ ব্যবস্থায় (distributed system) একটি মৌলিক কাঠামো হিসেবে কাজ করার সম্ভাবনা রয়েছে। একটি সর্বোত্তম এবং দক্ষ পদ্ধতিতে মাল্টি-মাইক্রোগ্রিড ক্লাস্টারগুলিকে নিয়ন্ত্রণ করার জন্য অবকাঠামো পরিকল্পনা এবং নকশা, নিয়ন্ত্রণ কাঠামো এবং যোগাযোগ প্রযুক্তি প্রয়োজন। অর্থাৎ, পাওয়ার শেয়ারিং, পাওয়ার কোয়ালিটি এবং স্থায়িত্বের ক্ষেত্রে আন্তঃসংযুক্ত মাইক্রোগ্রিডগুলির কর্মক্ষমতা উন্নত করতে শক্তিশালী এবং নির্ভরযোগ্য নিয়ন্ত্রণ কৌশল সহ একটি সঠিক নিয়ন্ত্রণ কাঠামো (control system) প্রয়োজন।

এই গবেষণায় একটি সমন্বিত আন্তঃসংযুক্ত মাইক্রোগ্রিড কাঠামো তৈরি করতে একটি অভিনব আন্তঃসংযুক্ত হাইব্রিড মাইক্রোগ্রিড নিয়ন্ত্রণ কাঠামো এবং একটি ক্লাস্টারিং পদ্ধতি প্রবর্তন করা হয়েছে। আন্তঃসংযুক্ত হাইব্রিড মাইক্রোগ্রিডগুলির মধ্যে power flow নিয়ন্ত্রণের জন্য প্রস্তাবিত নিয়ন্ত্রণ কাঠামো তিনটি কনভার্টারের নিয়ন্ত্রণ কৌশলের উপর নির্ভরশীল, যেমন শক্তি সঞ্চয় ব্যবস্থা (energy storage systems), প্রতিটি স্বতন্ত্র হাইব্রিড মাইক্রোগ্রিডের আন্তঃসংযোগকারী ব্যবস্থা এবং একাধিক মাইক্রোগ্রিড নেটওয়ার্কিং ব্যবস্থা। হাইব্রিড মাইক্রোগ্রিডের ইন্টারলিঙ্কিং কনভার্টারের নিয়ন্ত্রণ কৌশলটি একটি ভোল্টেজ-ফ্রিকোয়েন্সি (V-f) ড্রপ (droop) কন্ট্রোলের উপর ভিত্তি করে তৈরি করা হয়েছে যাতে তিনটি অপারেটিং মোড যেমন স্বাধীন (islanded), গ্রিড-সংযুক্ত(grid-connected) এবং আন্তঃসংযোগ (interconnected) মোডে যথাযথ অপারেশন নিশ্চিত করতে পারে। জড়তা এবং এনার্জি স্টোরেজ সিস্টেমের স্টেট-অফ-চার্জ (SoC)-ভিত্তিক কন্ট্রোলার ব্যাটারি ব্যাঙ্কের চার্জিং এবং ডিসচার্জিং অপারেশনগুলিকে নিয়ন্ত্রণ করে এবং প্রতিটি হাইব্রিড মাইক্রোগ্রিডের ভিতরে একটি স্বাধীন power flow নিশ্চিত করে। অবশেষে, একটি ইন্টারলিঙ্কিং

কনভার্টার কাঠামোর নিয়ন্ত্রণ কৌশল ব্যবহার করে হাইব্রিড মাইক্রোগ্রিডগুলি আন্তঃসংযোগ এবং নিয়ন্ত্রণ করা হয়েছে যাতে বিদ্যুৎ প্রবাহ নিশ্চিত করা যায়।

কন্ট্রোল স্ট্রাকচার islanded এবং grid-connected উভয় অপারেশনের অনুমতি দেয় দুটি কন্ট্রোলারের মধ্যে কোন অদলবদল করার প্রয়োজন ছাড়াই। এই ইন্টিগ্রেটেড কন্ট্রোল ফ্রেমওয়ার্ক হাইব্রিড মাইক্রোগ্রিড নেটওয়ার্কের অবস্থার পরিবর্তনের সময় অপ্রয়োজনীয় অ্যাক্টিভেশন অপারেশনের সংখ্যা হ্রাস করে। ফলস্বরূপ, মোডগুলির মধ্যে নির্ভুল স্থানান্তরের কারণে সিস্টেমের ব্যর্থতার (failure) মতো নেতিবাচক পরিণতিগুলি সহজে প্রশমিত করা যেতে পারে। সংক্ষেপে, প্রস্তাবিত কন্ট্রোল ফ্রেমওয়ার্ক অনিচ্ছাকৃত পরিস্থিতিগত পরিবর্তনে, যেমন প্রধান গ্রিড ব্যর্থতা বা আইল্যান্ডিং (ফ্রিকোয়েন্সিতে -০.১১% তারতম্য সহ), লোডের পরিবর্তন (লোড বৃদ্ধির সময় -০.০৩৮% পরিবর্তন এবং লোড হ্রাসের সময় ০.০২% পরিবর্তন), উৎস ব্যর্থতা (উইন্ড জেনারেটরের ব্যর্থতার সময় ফ্রিকোয়েন্সিতে -০.১৩% এবং ০.১৮% তারতম্য), এবং গ্রিড সিঙ্ক্রোনাইজেশন (ফ্রিকোয়েন্সিতে ০.০৪% তারতম্য সহ), কন্ট্রোলার পরিবর্তনের প্রয়োজন ছাড়াই নির্বিঘ্নে কাজ করতে পারে।

আন্তঃসংযুক্ত মাইক্রোগ্রিড সিস্টেমের ক্লাস্টারিং পদ্ধতি এবং নিয়ন্ত্রণ কাঠামো একটি MATLAB/Simulink পরিবেশে ডিজাইন করা হয়েছে। OPAL-RT সিমুলেটর (OP5600)-ভিত্তিক রিয়েল-টাইম সফ্টওয়্যার-ইন-দ্য-লুপ (RT-SiL) সিমুলেশন কৌশলটি বিভিন্ন বিষয়ের পরিপ্রেক্ষিতে আন্তঃসংযুক্ত সিস্টেমের কর্মক্ষমতা বিশ্লেষণ করতে ব্যবহৃত হয়েছে। প্রাপ্ত ফলাফলগুলি নির্দেশ করে যে নিয়ন্ত্রণ কাঠামো, তিনটি নিয়ন্ত্রণ কৌশল সহ, সমস্ত মোডে নির্ভরযোগ্য অপারেশন নিশ্চিত করে যেখানে total harmonic distortion ৫% এর কম এবং ফ্রিকোয়েন্সি variation ১% এর কম, এবং পাওয়ার সাপ্লাই নিরাপত্তাকে সর্বাধিক করে।

Table of Contents

List of Figures

List of Tables

Table No. **Table Caption** **Page No.**

Nomenclature

Acronyms and Abbreviations

AC	Alternating current
AI	Artificial intelligence
BADC	Bidirectional AC-DC converter
BDC	Bidirectional DC-DC converter
CCM	Current control method
CIL	Constant impedance load
DAB	Dual active bridge
DBC	Deadbeat controller
DC	Direct current
DER	Distributed energy resource
DFIG	Doubly-fed induction generator
DG	Distributed generator
ESS	Energy storage system
GHG	Greenhouse gas
HCM	Hybrid control method
HiL	Hardware-in-the-loop
HMG	Hybrid microgrid
HVRT	High-voltage ride-through
ICCL	Inner current control loop
IGBT	Insulated-gate bipolar transistor
LPF	Low pass filter
LVRT	Low-voltage ride-through
MG	Microgrid
MPC	Model predictive control
MPP	Maximum power point
MPPT	Maximum power point tracking
NN	Neural networks
PI	Proportional integral
PLL	Phase locked loop
PMS	Power management strategy

PV	Photovoltaic
PWM	Pulse width modulation
RC	Repetitive controllers
RES	Renewable energy source
RSC	Resonant controllers
RT-SIL	Real-time software-in-the-loop simulation
SoC	State of charge
SPWM	Sinusoidal pulse width modulation
SRF	Synchronous reference frame
STS	Static transfer switch
VCM	Voltage control method
VSC	Voltage source converter

Chapter 1

INTRODUCTION

1.1 BACKGROUND

In the field of power systems, sustainable development policies need to address various concerns, including lowering greenhouse gas (GHG) emissions while supplying increasing energy demand, developing reliable energy systems with economic optimality, and ensuring supply security in the context of upcoming shifts towards the smart grid. In an attempt to accomplish the objectives of sustainable development while reducing the adverse effects of traditional energy sources (fossil fuel-based energy sources), the current paradigm for electricity generation is shifting toward a power electronic converter-based power generation framework, like microgrids (MGs) [1]. A MG is the integration of several distributed energy resources (DERs), such as renewable energy sources (RESs) and energy storage systems (ESSs), along with loads, control schemes, and protection devices operating within a specific electrical region as a single controllable unit [2, 3]. The MG structure can be AC, DC, or hybrid AC/DC based on line technologies (as shown in Fig. 1.1) [4]. Operations in both grid-connected and islanded modes, as well as the transition between islanded and grid-connected modes, make MG-based large or small power infrastructures more adaptable than traditional electrical networks [5]. MGs are economically viable and efficient due to lower transmission and distribution losses; however, the bulk integration of DERs in a single MG is infeasible due to the nature of RESs, control, and management challenges [6].

Therefore, power generation and distribution are limited to a small geographic area, especially during the islanded mode, which constrains secure load management, uninterrupted power supply, and reliable operation [7, 8]. Moreover, the intermittent nature of RESs, limited energy exchange options, and the failure of distributed generator (DG) units cause significant swings in output power, voltage, and frequency. As a result, the load-shedding method is introduced to maintain the demand-supply balance, which is both economically and technically inconvenient [9, 10]. Therefore, promising initiatives are required in order to address the challenges associated with a single MG's resiliency and enhance the effectiveness of the MG-based power system.

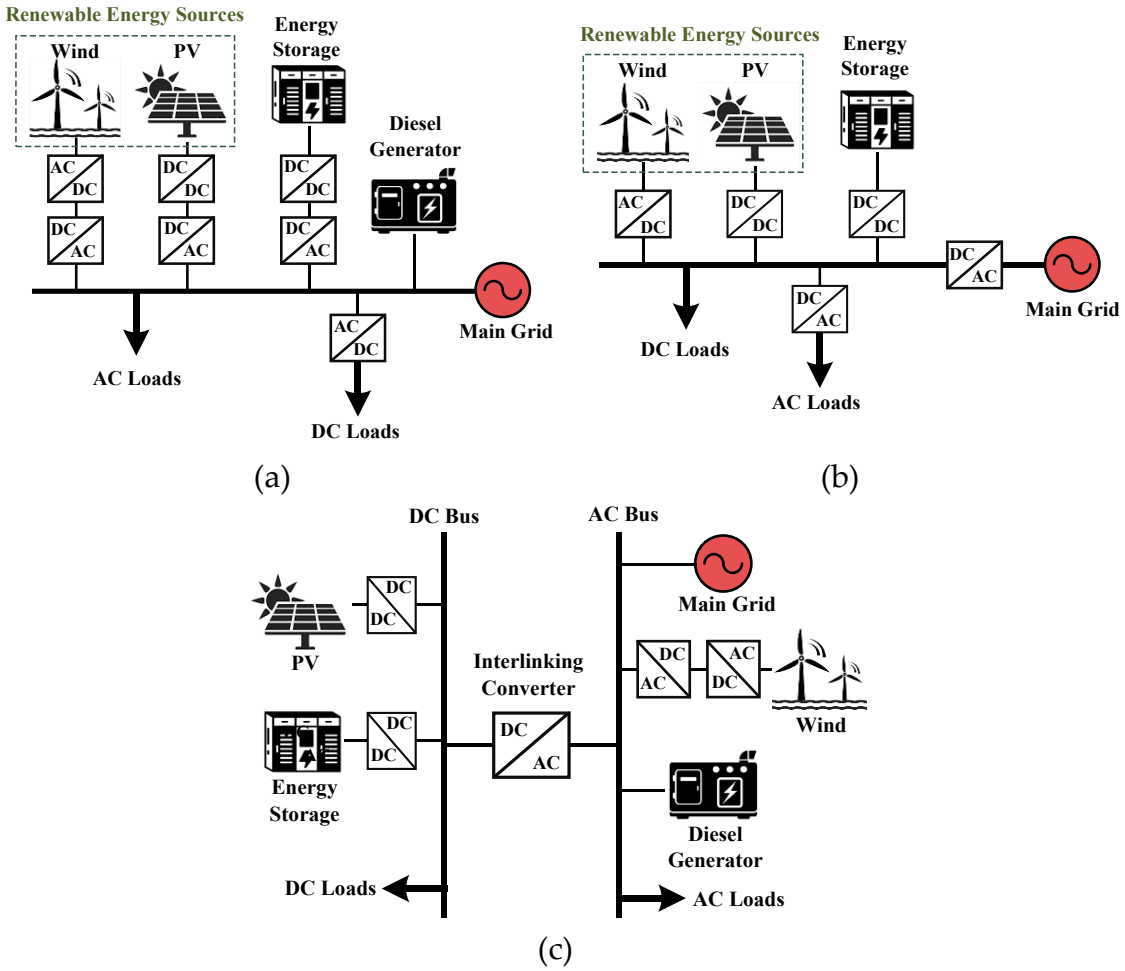

Fig. 1.1: Microgrid infrastructure [4]: a) AC microgrid, b) DC microgrid, and c) Hybrid microgrid.

1.1.1 Evolution of Interconnected Microgrids

There has been a greater emphasis on renewable energy-based power generation over the past few years because of the depletion of fossil fuel-based energy sources, such as coal, natural gas, and oils, and environmental concerns. [11]. In response to the limitations of micro-generation based on single-DER, such as insufficient generation capacity, local voltage rise, emergency conditions, and the tendency to exceed the thermal limits of specific lines and transformers, MGs consisting of several DERs have emerged [1]. However, as a single MG's power rating is limited to a few MVA, it will not be secure enough to satisfy its demand. Fig. 1.2 illustrates the three-stage development scheme for the evolution of the MG-based power system structure. According to this scheme, the limitations of a single DG and a single MG system can be addressed with the adoption of an interconnected MG system. That is, one of the most remarkable concepts is the interconnection of numerous MGs to overcome the constraints of a single DG system and a single MG system [12]. In the concept of interconnected MG, numerous distinct MGs that are in close proximity are clustered and operated simultaneously to form an integrated framework with greater flexibility, controlled power sharing, and efficient power management [13]. Because of enhanced flexibility, resilience, economic optimality, reliable operation, and better management of shortages and excess power, this novel infrastructure is evolving more and more widely [14]. The configuration of the interconnected system is determined by the nature of power transmission (AC or DC) and connections at electrical boundaries, i.e., line and interface technology [15]. Based on line technologies, it takes three forms: fully AC networked MGs [16], fully DC networked MGs [17], and AC/DC networked MGs [18]. Interfaces can be based on various devices, including tie-line connections with static switches or circuit breakers, power transformers, and interlinking converters [19-22]. However, due to the complex structure of the networked MGs compared to a single MG, further studies are required on various structures based on line and interface

technologies, coordinated control of individual MGs, and management of interconnection among MGs.

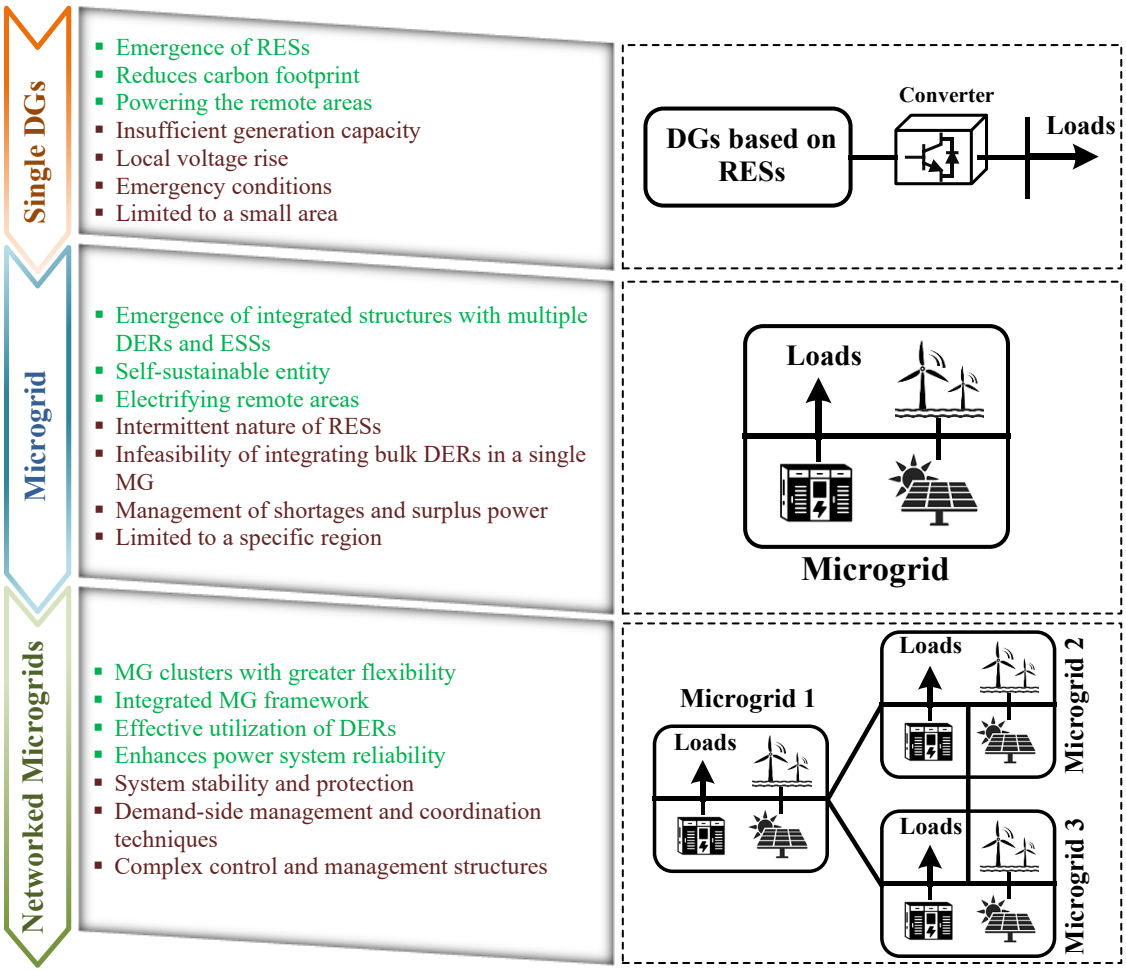

Fig. 1.2: An overview of the evolution of the MG-based power system infrastructure.

1.1.2 Control and Management System

The control and management system, a collection of software and hardware related to the power electronics converters and their controllers, is used to achieve the interconnected MG system's reliability, operational feasibility, optimal performance, and stability. Voltages and frequency regulations within specified ranges, proper power supply, sharing and balance, switching between different operating modes (islanded and grid-connected), and optimal demand-side management are the primary responsibilities of the control system [23]. Information sharing among MGs is an important aspect of the control system in

determining the best operating approach to ensure the system's reliability and effectiveness. There are several control structures for the interconnected system, such as hierarchical [24], distributed [25], decentralized [26], and centralized [26]. The distributed and hierarchical control structures facilitate the development of control systems at multiple control levels with different control responsibilities and targets by permitting controllers at various levels to communicate and exchange information or control signals.

The control system of an interconnected MG system has different control responsibilities from the component level to the system level, such as control of DERs at individual MGs, demand-supply management within each MG, and control for coordinated operation among MGs [27, 28]. To ensure seamless operation at the component level, the DERs must be equipped with suitable power electronic interfaces, controls, and management to link and separate inside a MG. Comparably, at the system level, each MG must have a reliable controller to connect with other MG in a networked system for flexible operation as a single aggregated framework [29]. All control goals must be fulfilled to accomplish precise power sharing, seamless transition and synchronization, recovery of frequency and voltage, and flexible regulation of power flow [30]. Above all, to achieve optimal performance from the interconnected system while also ensuring the stability of the system, research on the control system must be done in addition to developing reliable and effective control structures.

1.2 CONTEXT

The possible advantages of MGs can be achieved more effectively when they are interconnected to realize improved efficiency and security of supplies [10]. Therefore, it is projected that future power systems will consist of multiple interconnected MGs to form a sophisticated electric network, eliminating the limitations of individual MGs. Moreover, in smart grid concepts, this integrated electric network will serve as the main structure due to the seamless integration

of renewable energy-based generation. The interconnected MG system's main characteristics include promoting efficient management of energy consumption, ensuring favourable economic attributes, lower energy losses, optimal utilization of DGs, and effective sharing of DERs, whether in the on- or off-grid modes [31].

Several networked MG infrastructures exist based on line technologies, such as entirely AC MG clusters, entirely DC MG clusters, mixed AC-DC MG clusters, and hybrid MG-based MG clusters. Currently, AC MG clusters are the most prevalent type, in which the majority of the components are AC sources and loads and are connected by AC buses [32]. It is not essential to alter the power grid's fundamental layout to construct this infrastructure. However, integration of AC MGs is challenging due to both voltage and frequency controls, control complexity, higher conversion stages, active and reactive power controls, and the requirements of frequency synchronization [4]. Therefore, interest in DC technologies is growing due to the predominant benefits, such as higher efficiency, lower losses, elimination of the skin effect and bulky transformers, no reactive power and synchronization requirements, improved reliability, and lower conversion stages [33]. The development of AC/DC MG clusters that combine the benefits of both AC and DC technologies for interconnections is becoming a possible scenario [34]. Although various studies [20, 35-37] have proposed different structures to realize distinct objectives, the MG cluster composed of fully AC or DC MGs is the primary focus of the study. Multiple separate hybrid microgrids (HMGs), each with its AC and DC MGs, compose the networked HMGs [38]. This configuration of networked MGs leads to a more sophisticated infrastructure for power coordination, which needs to be analysed.

MGs in an interconnected MG system can be connected using various interface technologies, such as direct tie lines, power transformers, and interlinking converters [15]. Static switches and circuit breakers can be used as interlinking devices to interconnect MGs with the same standard frequencies and

AC or DC voltages in the simplest way [19]. Power transformers can be used for interconnecting only AC technologies of different voltages and not different phases and frequencies [39]. Moreover, tie-line and power transformer-based interfaces for MG interconnection cannot provide a controlled environment for power coordination among multiple MGs. In contrast, interfaces with interlinking converters can be utilized in both AC and DC technologies with high levels of controllability in terms of frequency and voltage, effective power management, improved power quality, and flexibility [35]. Therefore, it is preferable to connect MGs using converter interfaces for controlled power-sharing and more flexible operations under various conditions.

Networked MGs offer a MG cluster with more flexibility for resilient and cooperative operations by sharing necessary DERs to compensate for possible electrical deficits. Power coordination among networked MGs must, however, be governed by a reliable and robust control structure that gathers and combines the data supplied by individual MGs, directs their contribution and interaction in the cluster, and evaluates the optimum power flow to coordinate their operations in an organized manner [31]. Otherwise, interconnecting multiple MGs can lead to undesirable behaviours such as voltage distortions, power fluctuations, and frequency oscillations [40]. Thus, for the coordinated performance of interconnected MGs, a lot of emphasis has recently been given to developing flexible structures, robust control techniques for associated power electronics converters, an effective and feasible multi-functionality-based power management system, and optimal power system planning in various operating modes. Moreover, the interconnected HMG structure leads to a more complex control structure since it simultaneously balances two control goals: coordinated operation between DC and AC MGs in a single HMG using an interlinking converter and power coordination among neighbouring HMGs using interconnecting converters [38]. It is vital to examine power management and the

control structure of HMG clusters, considering the two control targets under various operating modes for flexible operations, as there are no studies that specifically focus on this aspect.

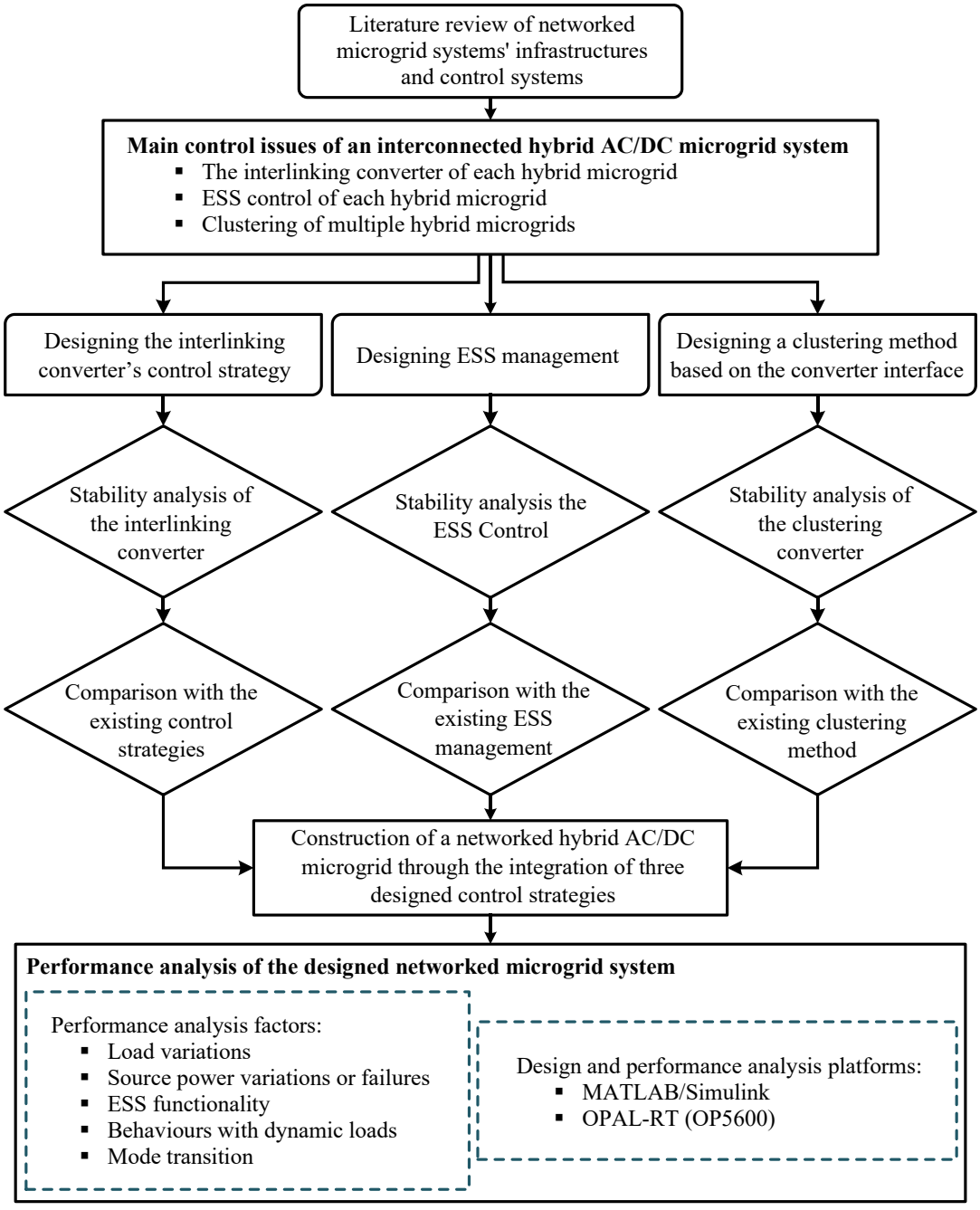

Fig. 1.3: An overview of the context of this thesis.

The significant real-time energy management challenges, such as output power variation and voltage instability caused by the intermittent nature of DERs and inelastic loads in the system, can be mitigated by a reliable power supply or

appropriate-size ESSs [41]. The fundamental task of the ESS and its control strategy is to achieve a balance between generation and demand, depending on the dispatchable power of each storage unit, while preserving voltage and frequency within reasonable limits in all operating modes [42]. As a result, optimal ESS management and control are essential for efficient operation, proper power management, smooth transit between the different modes, and regulating the variations of system voltage and frequency in a tolerable range. An overview of the context (statement of the problem) of this thesis is presented in Fig. 1.3.

1.3 AIMS AND OBJECTIVES

The key purposes of this thesis are to design a clustering method and a distributed control structure for flexible power flow control among interconnected hybrid microgrids, with particular emphasis on the control strategies of three converters: the controller of energy storage system, the interlinking converter of individual hybrid microgrids, and the networking converter of interconnected hybrid microgrids. Designing this efficient control structure will be accomplished by implementing the following four objectives:

1. To develop a reliable control strategy for an interlinking converter to interconnect the AC and DC microgrids in an individual hybrid microgrid.
2. To design a virtual inertia-based controller for energy storage system (ESS) in each hybrid microgrid.
3. To develop a clustering method to form an integrated framework by interconnecting hybrid microgrids.
4. To analyse the performance and effectiveness of the clustering method and control structure of the interconnected system based on various factors such as load variations, source power variations or failures, ESS

functionality, behaviours with dynamic loads, and mode transition using MATLAB/Simulink and the OPAL-RT (OP5600) simulator.

1.4 SIGNIFICANCE OF THE OBJECTIVES

In electric power systems, resilience and flexibility improvement serve as a line of protection to prepare and defend the system against several types of occurrences. MG clusters will serve as the foundation of forthcoming power systems, providing a complete, resilient, and flexible integrated network. The key to this approach is a well-designed management and control system. Therefore, in this study, a control structure is proposed considering three control objectives to ensure the reliable performance of an interconnected MG system.

1.4.1 Objective 1: Related to Hybrid Microgrid's Interlinking Converter

The interlinking converter with a proper control strategy plays a crucial role in interconnecting the AC and DC MGs in a single HMG and HMG with the main grid while providing cooperation between AC and DC MGs and ensuring stable operation of the HMG under various operational modes [43]. A HMG can function in both islanded and grid-connected modes using this converter control approach. In grid-connected mode, the converter is employed to regulate DC voltage; DG outputs, ESS charging and discharging powers, and HMG demand all determine the interlinking power. The main responsibilities in islanded mode are controlling the AC voltage and frequency as well as the DC bus voltage through coordinated control between the ESSs, DGs, and interlinking converter [44]. A scalable and effective control technique is needed to achieve autonomous power transfer and flexible AC/DC connections between MGs in individual HMGs while taking renewable energy constraints into account and facilitating a smooth mode transition between grid-connected and islanded modes. Therefore, an advanced and flexible control strategy of the bidirectional AC/DC interlinking converters for autonomous operation of individual HMGs in grid-connected, islanded, and interconnected modes is proposed.

1.4.2 Objective 2: Related to the Energy Storage System Control Strategy

With benefits including quick response times, continuous power supply, and regional independence, ESSs are widely regarded as one of the prospective solutions to the unpredictable and intermittent nature of renewable energy [45]. To provide more steady and sustainable operation, ESSs are an essential element of the MG framework. In islanded mode, the ESS charges and discharges according to the demand. If the ESS is completely charged in grid-connected mode, the DG surplus electricity must feed into the main grid because the ESS is unable to absorb it. Conversely, when the lower SoC level is attained, the main grid begins to sustain the load requirements in conjunction with the DG, and the ESS is not required to inject any more power. To maintain these operations in both grid-connected and islanded modes while preventing high-rate power peaks and extending the ESS life cycle, the charging and discharging operations of ESS must be regulated using suitable control strategies [42]. A virtual inertia and SoC-based power management approach is proposed to control the battery bank-based ESS's charging and discharging operations depending on the power flow of interconnected MGs. In grid-connected mode, the controller aids in achieving independent power flow, whereas the AC main grid only concentrates on establishing the DC bus and handling power surpluses or shortages.

1.4.3 Objective 3: Related to the Hybrid Microgrids Clustering Technique

The flexibility of interconnected MG control and operational modes increases due to the flexible control capabilities of converter interfaces. When generation in each MG is sufficient to satisfy demand, the interconnection converter control supports autonomous power management in individual HMGs and enables bidirectional power sharing when MGs experience power shortages or surpluses. Moreover, due to the increasing sharing power and the possibility of multiple connection ports., the parallel operation of several interconnecting

converter frameworks is needed to improve power capacity, avoid overstressing any individual entity, and enhance power supply reliability.

1.4.4 Objective 4: Related to the Networked System's Performance Analysis

Performance analysis, from the component level to the network level, is a crucial objective to ensure the reliable operation of any designed system under various conditions. Power quality and stability are significant characteristics of the MG-based power system, as the increasing penetration of nonlinear loads, renewable energy-based DGs, and power electronic converter interfaces can result in distorted waveforms, system instability, and increased energy costs. Therefore, it is essential to analyse the system's capability to ensure standard power quality and sustain system reliability under different circumstances, including load variations, ESS management, various load penetrations, source failures, and mode transition.

The behaviour of electrical loads is a vital aspect of a realistic approach to power systems due to their significant impact on system generation, characteristics, and the stability of the network. Various types of statics (constant power, constant current, and constant impedance loads) and dynamics loads (induction motors) exist in power systems. It is important to investigate how a network reacts to various load characteristics since the outcomes from one type of load are not representative of the actual load demographics in a network.

The MG clusters can be operated both in grid-connected and islanded modes, while power transfer and operation are controlled by the converters and related control structures. When a fault arises in the grid or any connecting line, the MG interfacing converter and the main grid coupling converter must trip automatically to isolate the faulty parts. To transit in islanded mode, followed by a failure in the grid or interconnecting lines, the power converters must operate in grid-forming mode and contribute to sustaining system voltage and frequency. Therefore, MGs in a cluster need to operate in both modes to ensure

continuous power supply to critical loads and increase infrastructure flexibility during grid faults and any other crises. To achieve this goal, control techniques must allow the MG to switch smoothly between the grid-connected and islanded modes and to prevent variations and oscillations in voltage, frequency, and current caused by phase and frequency mismatches during the transition.

1.5 SUMMARY OF RELEVANT CONCEPTS

MGs differ greatly from conventional grids in terms of their structure and operational features. The following is a summary of various topics related to the MG-based power system that are associated with the concept of this thesis.

Hybrid AC/DC microgrid: The concept of MGs has evolved as a way to develop and integrate RESs like photovoltaic (PV) and wind energy into power systems to combat climate change and the world's rising energy demand. Among the three MG structures, the AC and DC MGs have been extensively examined in the literature [46, 47]. The third type of MG, i.e., the HMG, is the most feasible because it combines the benefits of both AC and DC technologies into a single MG infrastructure [48]. The AC MG is composed of several AC loads as well as AC sources such as wind turbines, diesel generators, and microturbines. The DC MG, on the other hand, is comprised of various DC loads as well as DC sources like PV and ESSs. This MG structure uses an interface of bidirectional interlinking converters between AC and DC MGs to allow bidirectional power flow by minimizing conversion stages [49]. Active power is transferred from an AC MG to a DC MG and vice versa according to the MG's capacities to improve the coordination and utilization factors of AC and DC RESs [50].

Microgrid Cluster: A group of nearby MGs that are physically connected by AC (or DC) buses using tie-lines or converter interfaces is referred to as an MG cluster. By permitting MGs to support one another during power unbalance, the network of MGs aims to address the difficulties experienced by the individual MG. Because there is no support from an outside source, this structure is crucial

and necessary for the islanded condition [38]. With this idea, energy sources may be utilized to their maximum potential in both islanded and grid-connected modes; reliability is increased; economic optimality is increased by flexible energy exchange in clusters; and stress and ageing of the MGs' components, such as power electronic converters, are reduced [27]. In addition, it could minimize costs related to maintenance and increase the network's operational period.

Role of Interlinking Converter: Linking several MGs using passive devices like power transformers or tie lines presents several challenges in terms of controllability and flexibility and also restricts the MGs' ability to interlink. With such conditions, interlinking converters have become a standard method for connecting multiple MGs, irrespective of their features [51]. By offering many ancillary services, these power converters can interconnect MGs with different characteristics in addition to controlling power flow. Moreover, in order to achieve several control functions, including coordinated power supply among MGs, power quality enhancement, and smooth mode transit, interlinking converters are essential interconnecting devices [52]. Thus, it is anticipated that interlinking converters, which effectively connect and regulate interactions among MGs, will serve as the energy routers of the future.

Importance of Control Structure in Networked Microgrid: Enabling flexible structures, grid networking, and integrated operation among numerous MGs are important for the MG cluster. Therefore, the MG cluster needs to implement advanced control systems to maximize the use of its DERs while providing an improved level of service, such as power flow control and voltage regulation [53]. There are several control structures based on communication systems, such as distributed, decentralized, and centralized, for coordinating MGs in the MG cluster [15]. Under the concept of active consumer involvement and distributed generation, controlling networked MGs with distributed control structures is becoming increasingly prevalent since it is very challenging to manage and

regulate individual MGs with a large number of DG units employing either a decentralized or centralized control structure [54]. Utilizing local communication systems, distributed control minimizes the negative aspects of both centralized and decentralized management while integrating their positive aspects. The implementation of hierarchical control, comprising primary, secondary, and tertiary levels, is anticipated to enhance the system's intelligence by facilitating continuously integrated coordination among generation, storage, and consumption [27].

Energy Storage System (ESS): The ability to preserve energy during low-demand periods and supply energy during times of high demand has made the MG concept, i.e., renewable energy technologies linked with ESSs, more and more appealing. Because ESS facilitates the integration of renewable energy in various ways and maintains a stable supply of power during power outages, system stability has a big impact on the entire electric network by storing energy at lower costs during low-demand periods [55]. Because of its extremely low inertia, a power system comprised of power electronic interfaces may become unstable. By including ESSs, the system's inertia can be introduced, increasing its resilience and resistance to external perturbations such as load variations or source power variations because of atmospheric instability [56]. An ESS can be implemented using a wide range of technologies, including flywheels, batteries, supercapacitors, and superconducting magnetic storage.

1.6 THESIS OUTLINE

This thesis is mainly focused on designing an interconnected MG system with a robust distributed control structure and flexible clustering method. The modelling, implementation, and performance evaluation of the proposed control system are discussed in detail in the remaining chapters of this thesis. A brief overview of the contents of each chapter in designing the reliable MG cluster is presented as follows:

Chapter 2 presents a comprehensive review of the MG cluster's infrastructure based on layout, line, and interface technologies, control systems for power management and coordination among interconnected MGs, characteristics of the MG cluster, and various control strategies for interlinking converters and ESS management.

Chapter 3 introduces the structure of the designed interconnected HMGs with the proposed distributed control structure and clustering method. This chapter also provides the details of the structure and configuration of the three proposed control strategies associated with the interlinking converters of HMGs, ESSs, and interconnecting converters.

Chapter 4 addresses the performance of the proposed control structure and clustering method in an interconnected HMG system under various conditions, such as load variations, source failures, ESS management, power quality, and mode transitions.

Chapter 5 provides a detailed analysis of the three control strategies under different operating modes and parameter variations for stability assessment.

Chapter 6 presents a comparative study of the three control strategies with previously existing control strategies in the respective field based on various factors.

Chapter 7 finally concludes this study with a summary of this thesis, significant findings, limitations, and a discussion of future research direction.

Chapter 2

INFRASTRUCTURES, CONTROLS, AND CHARACTERISTICS OF NETWORKED MICROGRIDS

2.1 INTRODUCTION

Recent advancements in RESs-based distributed electrical generation systems, along with technological developments in power electronics, gave rise to the prospect of self-governing future electrical infrastructure, such as MGs. These tiny, self-sufficient electrical system zones have the potential to improve effectiveness and reliability while facilitating the integration of renewable energy. However, the bulk integration of DERs in a single MG is infeasible due to the nature of RESs, control, and management challenges. Therefore, the power generation and distribution capabilities of a single MG system are limited to a small geographic area, which constrains secure load management, uninterrupted power supply, and reliable operation. Therefore, the networking of multiple MGs concept is one of the most promising initiatives in the field of MG-based power systems to address the challenges associated with a single MG's resiliency. In the MG cluster concept, numerous distinct MGs that are physically in close proximity are clustered and operated simultaneously to form an integrated framework with greater flexibility, controlled power sharing, and efficient power management. Because of the diversity of DERs, enhanced flexibility, resilience, economic optimality, reliable operation, regulation of systems' voltage and frequency during emergencies, provision of backup power for particularly critical loads,

and better management of shortages and excess power among MGs, this novel infrastructure is evolving more and more widely.

2.2 INFRASTRUCTURE OF NETWORKED MICROGRIDS

To develop a networked MG-based electrical system that operates effectively according to current and future power grid requirements, it is essential to consider all possibilities of the networked MG architecture. The development of different MG structures, interlinking lines, devices, various interlinking converter topologies, control techniques, and communication approaches results in diverse MG cluster infrastructures. Nonetheless, the three key ideas that distinguish the various interconnection architectures are discussed in this subsection: layout, line, and interlinking technologies.

2.2.1 Layout

In an MG cluster system, the layout specifies how MGs are connected. Various layouts such as series, parallel, and mixed connections exist, as depicted in Fig. 2.1, depending on the connection with the main grid and the connection with each MG.

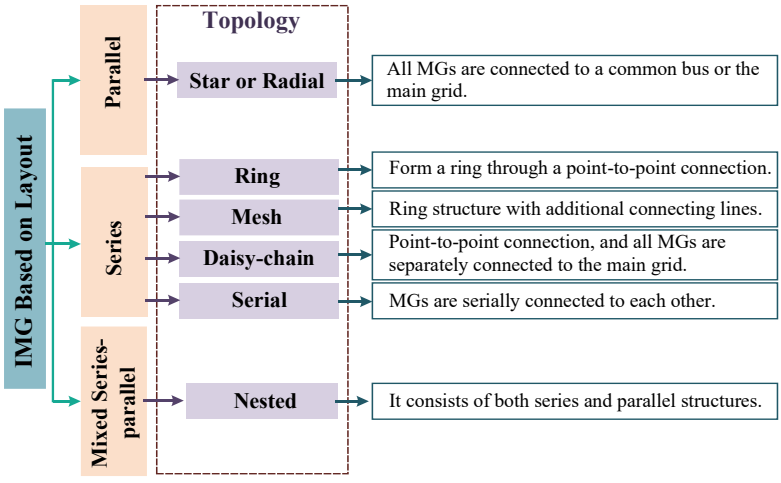

Fig. 2.1: Microgrid cluster infrastructure based on layout.

Parallel-connected MGs refer to a framework in which all MGs are connected to a common node or the main grid. In [57], a parallel-connected MG

cluster with an autonomous control technique is presented where both AC and DC MGs are connected to a common point through suitable interfaces. In a series-connected structure, MGs are connected according to the point-to-point connection to develop a cluster of MGs and share power with adjacent MGs. A series-connected MG cluster based on tie-line connections with various types of DERs and ESSs is used in [58] to explore the load frequency regulation of MGs in islanded mode. A mixed series-parallel structure is more feasible because it consists of both series and parallel structures and combines the benefits of both structures into a single structure [59]. In [60], a grid architecture model based on mixed series-parallel clusters is proposed to assist the system architect for the smart distribution network.

2.2.2 Line and Interface Technologies

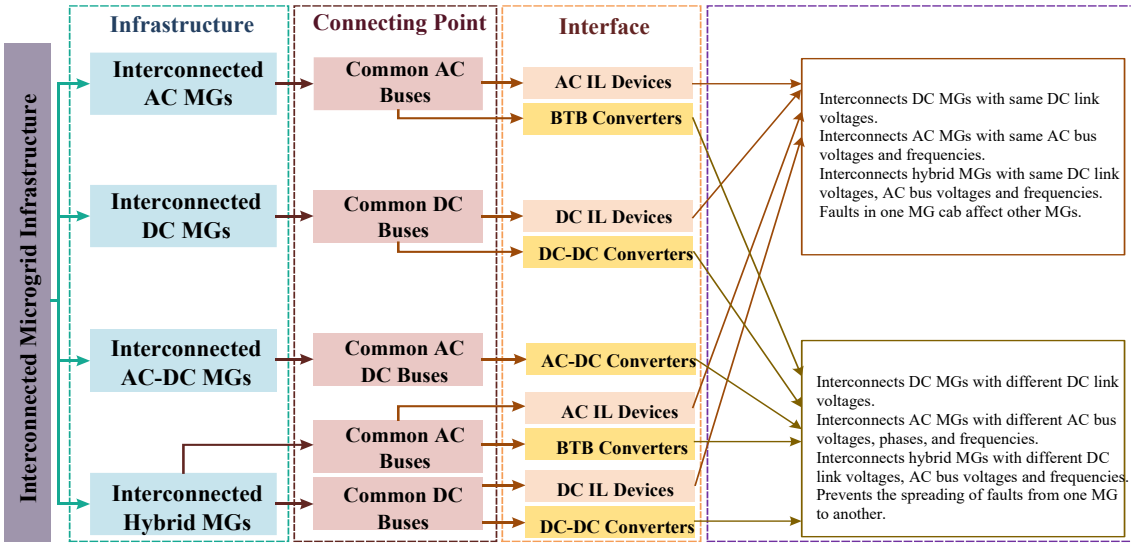

Fig. 2.2: An overview of the microgrid cluster infrastructure based on line and interface technologies.

The nature of power transmission (AC or DC) and connections at electrical boundaries are determined by line and interface technology. Interfaces can be based on various devices, including tie-lines, power transformers, and converters. In the tie-line-based architecture, MGs involved in the network have the same voltages and frequencies. Power transformers can be used for

interconnecting only AC technologies of different voltages and not different phases and frequencies. In contrast, a combination of transformers and converters can be utilized in both AC and DC technologies with high levels of controllability in terms of frequency and voltage, effective power management, improved power quality, and flexibility [43, 44]. As demonstrated in Fig. 2.2, there are several IMG infrastructures based on line and interface technologies.

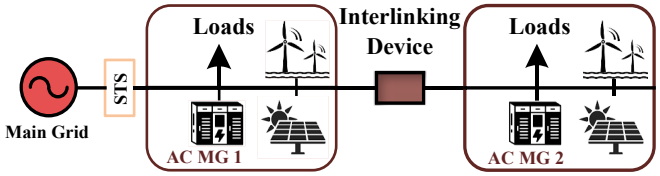

Fig. 2.3: Interconnection of AC MGs using AC interlinking device (circuit breaker or switch) and tie-line [16].

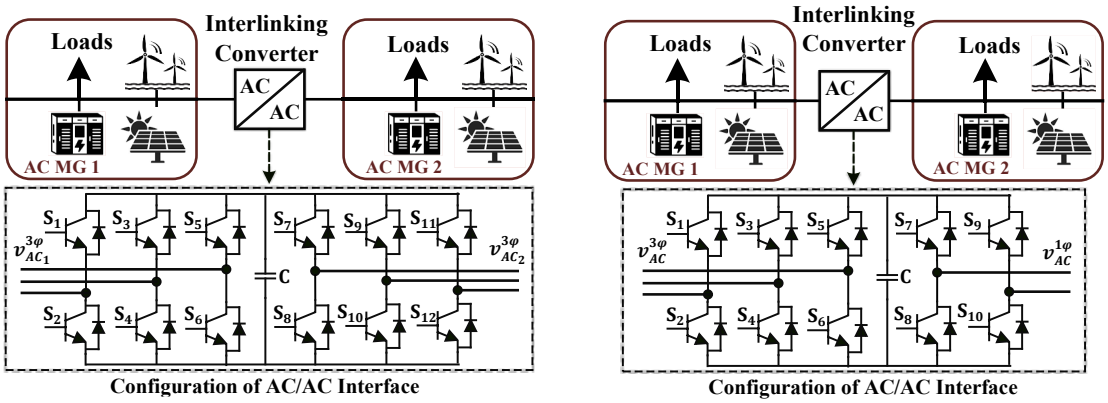

Fig. 2.4: a) Interconnection of AC MGs using back-to-back converter topology [32], and b) Interconnection of three-phase and single-phase AC MGs using AC-AC converter [61].

Tie-line-based interfaces, as shown in Fig. 2.3, are commonly used to interlink multiple AC MGs. A distributed multi-agent control strategy for AC MG cluster (tie-line-based) impacted by time-delay disturbances and additive noise is proposed to obtain the best active power-sharing feature and synchronize the voltage and frequency of inverter-based DERs with standard values [16]. Voltage source converters (VSCs)-based back-to-back converters are frequently utilized to connect AC power systems with different voltages and frequencies due to the converter's small size, independent operation of MGs, and faster

operation [32], as shown in Fig. 2.4a. A decentralized technique is proposed in [61] for a converter structure that interconnects a traditional three-phase AC system to a single-phase AC system, as shown in Fig. 2.4b to provide a power-sharing link and regulate the power transfer among them.

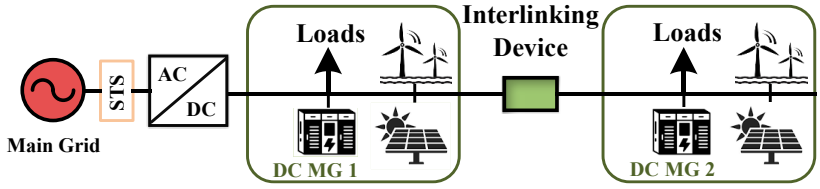

Fig. 2.5: Interconnection of DC MGs using DC interlinking device (circuit breaker or switch) and tie-line [62].

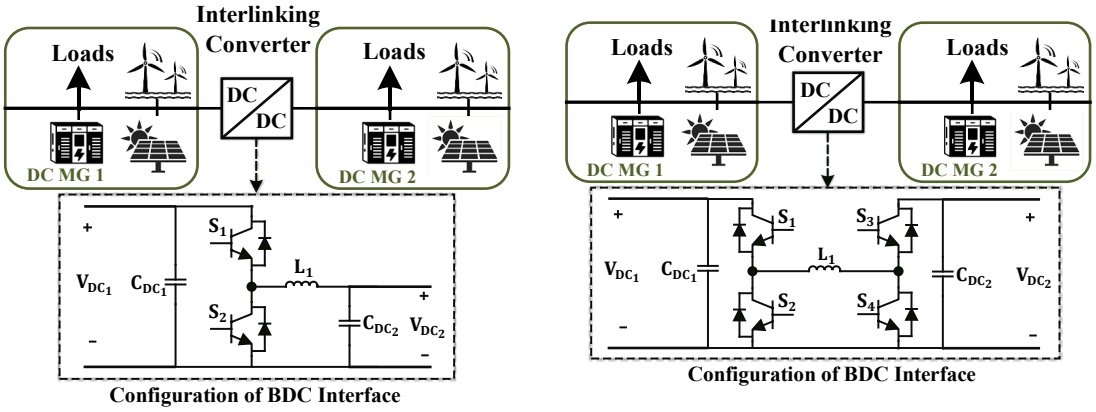

Fig. 2.6: a) Interconnection of DC MGs using DC converters based on buck-boost converter topology [63], and b) Interconnection of DC MGs using DC converters based on bidirectional cascaded buck-boost converter topology [64].

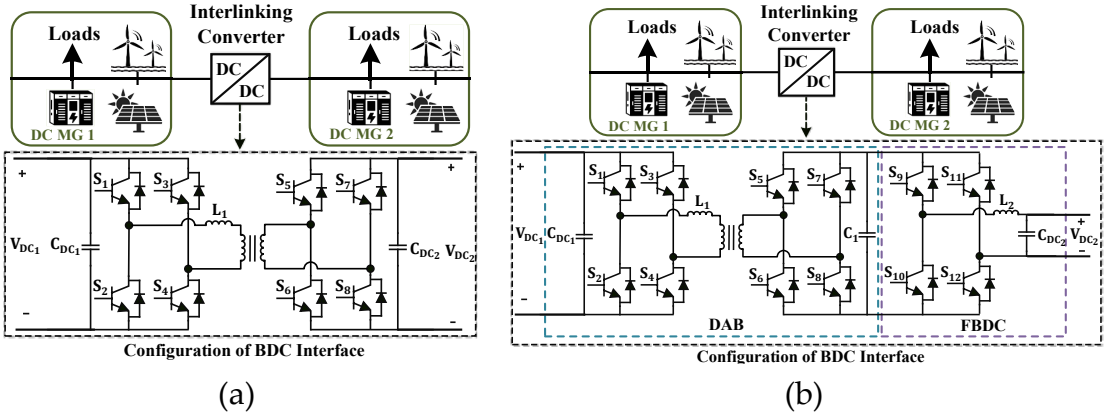

Fig. 2.7: a) Interconnection of DC MGs using DC converters based on DAB converter topology [65], and b) Interconnection of DC MGs using DC converters based on DAB converter and full-bridge DC topologies [66].

In [62], two DC MGs with constant power load (CPL) are interconnected using a tie-line, as shown in Fig. 2.5, to regulate the power flow. A decentralized control structure based on primary and secondary controllers to locally adjust the common DC bus voltage, minimize average voltage variation, and guarantee dependable operation is presented in [63]. A DC MG cluster structure, as illustrated in Fig. 2.6a, for integrating two DC MGs functioning at distinct DC voltages in off-grid mode is proposed in [67] to control the bidirectional flow of power between the interconnected DC MGs under different operating and fault conditions. A DC MG cluster, as shown in Fig. 2.6b, is developed in [64] using a DC-DC interconnecting converter to mitigate the impact of parasitic resistance on voltage regulation and enable controlled power transfer. An active dual active bridge (DAB) converter topology-based interface, as illustrated in Fig. 2.7a, is used in [65] to connect low and high-voltage buses on multiple DC MGs for reliable and efficient power sharing. Another interface topology that consists of a DAB and a full-bridge DC-DC converter, as shown in Fig. 2.7b, is proposed in [66] to interconnect DC MGs.

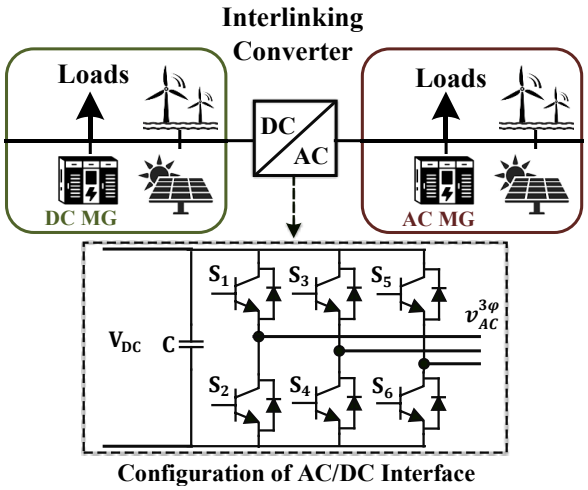

Fig. 2.8: Interconnection of AC and DC MGs using BADC interface [68].

The development of AC-DC MG clusters that consider both AC and DC line technologies for interconnections is growing as a possible scenario in MG cluster infrastructure. Its structure may vary, but in all cases, the connections and control

of the power exchange are established by only the bidirectional AC-DC converters (BADCs), as shown in Fig. 2.8. An integrated power management strategy (PMS) along with an adaptive droop control strategy is proposed in [68] for intra- and inter-MG power sharing in an MG cluster system to guarantee optimal utilization of available RESs in each MG under various operating modes. In [69], an improved multi-port interlinking converter with greater versatility and an efficient structure for the AC-DC MG cluster is proposed.

Table 2.1: Comparison of line and interface technology-based microgrid cluster configurations

Attributes		AC	DC	AC/DC	Comments
Conversion stages	**TL with ILDs**	H	L	N/A	IMG sequences in terms of conversion stages (ILC-based AC IMG > TL-based AC MG > AC/DC IMGs> ILC-based DC IMG> TL-based DC IMG)
	ILCs	VH	M	M	
Power loss	**TL with ILDs**	H	L	N/A	IMG sequences in terms of power losses (ILC-based AC IMG > TL-based AC MG > AC/DC IMGs> ILC-based DC IMG> TL-based DC IMG)
	ILCs	VH	M	M	
Cost	**TL with ILDs**	H	L	N/A	MG sequences in terms of cost (ILC-based AC IMG > TL-based AC MG > AC/DC IMGs> ILC-based DC IMG> TL-based DC IMG)
	ILCs	VH	M	M	
Efficiency	**TL with ILDs**	M	VH	N/A	MG sequences in terms of efficiency (TL-based DC IMG > AC/DC IMGs> ILC-based DC IMG > TL-based AC MG > ILC-based AC IMG)
	ILCs	L	H	H	
Expansion Capacity	**TL with ILDs**	L	H	N/A	MG sequences in terms of expansion capacity (TL-based DC IMG > ILC-based DC IMG > AC/DC IMGs > TL-based AC MG > ILC-based AC IMG)
	ILCs	VL	M	M	
Integration capacity	**TL with ILDs**	M	H	N/A	IMG sequences in terms of integration capacity (TL-based DC IMG > TL-based AC MG > ILC-based DC IMG > AC/DC IMGs > ILC-based AC IMG)
	ILCs	L	M	M	
Technological accessibility	**TL with ILDs**	H	L	N/A	IMG sequences in terms of technological accessibility (TL-based AC IMG > ILC-based AC MG > AC/DC IMGs > TL-based DC IMG> ILC-based DC IMG)
	ILCs	M	L	M	
Protection requirement	**TL with ILDs**	H	L	N/A	IMG sequences in terms of protection requirement (ILC-based AC IMG > TL-based AC MG > AC/DC IMGs > ILC-based DC IMG> TL-based DC IMG)
	ILCs	VH	M	M	
Complexity	**TL with ILDs**	H	L	N/A	IMG sequences in terms of complexity (ILC-based AC IMG > AC/DC IMGs > TL-based AC MG > ILC -based DC IMG> TL-based DC IMG)
	ILCs	VH	M	H	

VL Very Low **L** Low **M** Moderate **H** High **VH** Very High

N/A Not Applicable **TL** Tie-line **ILD** Interlinking Device **ILC** Interlinking Converter

IMG Interconnected microgrid

The interconnection of DC and AC MGs using bidirectional interlinking converters forms a HMG, which is more feasible than AC and DC MGs and combines the benefits of both AC and DC technologies into a single MG infrastructure. The interconnection of multiple HMGs can provide more flexibility and reliable operations. In [70], a communication-free control scheme for a hybrid MG cluster system with a ring layout is presented. To provide flexible connections between MGs with less power conversion components, a flexible and adaptable hybrid MG cluster is proposed in [38], along with a unique interlinking converter and an associated decentralized control structure. illustrates a comparison of AC and DC technologies in the presence of tie-line and interlinking converter for interconnection. Table 2.1 illustrates a comparison of AC and DC technologies in the presence of interlinking devices and interlinking converters.

2.3 CONTROL STRUCTURE OF NETWORKED MICROGRIDS

The networked MG control system, a collection of software and hardware related to the power electronics converters and their controllers, is used to achieve the system's reliability, operational feasibility, optimal performance, and stability. Voltages and frequency regulations within specified ranges, proper power supply, sharing and balance, switching between different operating modes (on- and off-grid), and optimal demand-side management are the primary responsibilities of the MG cluster control system. Thus, to achieve optimal performance from the MG cluster system, research on the control system must be done in addition to developing reliable and effective control structures.

2.3.1 Control Structures

In an IMG system, information sharing amongst MGs assists the control system in determining the best operating approach to ensure the system's reliable and effective performance. The networked MGs' assigned communication system is employed for information sharing amongst MGs. There are several

control structures illustrated in Fig. 2.9 based on communication systems, such as hierarchical, distributed, decentralized, and centralized, for coordinating MGs in the MG cluster system.

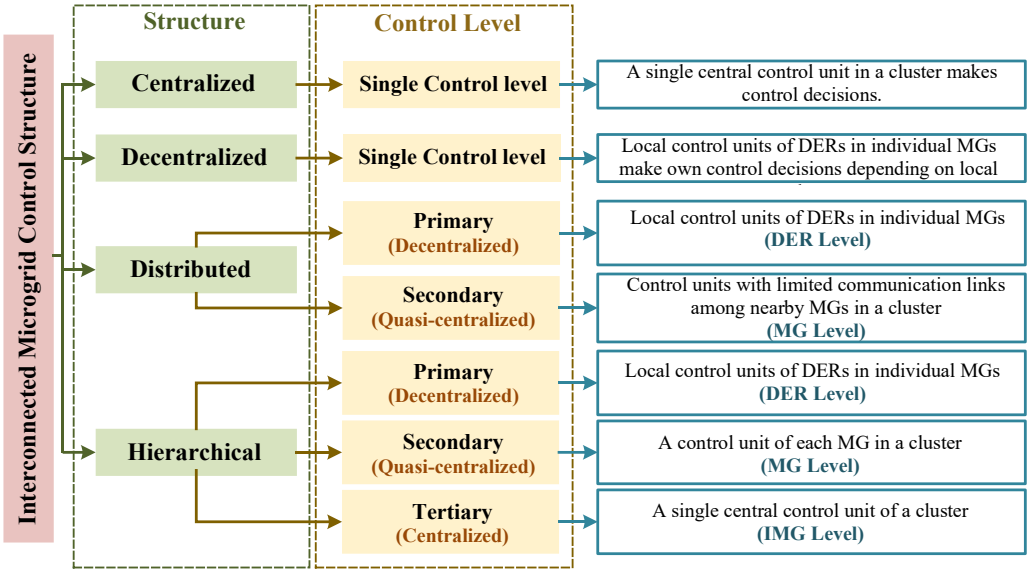

Fig. 2.9: Various control structures for MG cluster system.

Table 2.2 presents an overview of various literature based on four control structures along with their merits and demerits.

2.3.1.1 Centralized Control

In a centralized control structure (as shown in Fig. 2.10a), a single central entity is responsible for collecting data from all of the MG's measurement units using a communication channel along with determining, verifying, and analysing the control operations of all MGs in the system to provide the necessary instructions for optimum management of DERs and loads [71]. Based on information collected from each MG's local unit, the central control unit manages and coordinates the operations of every MG that is a part of the MG cluster [72]. However, the entire cluster's operation, cost, and reliability are compromised by a single point of failure caused by the huge amounts of data handled and concentrated in a single area, higher bandwidth specifications, a lower expansion rate due to the centralized structure, reliance on a wide-band communication system, and restrictions on plug-and-play capabilities [73]. Furthermore, a two-

way information exchange is necessary between the central control unit and each MG's local unit, as the central controller must receive data and provide signals to control all local units. In [74], a unique centralized/decentralized technique is proposed in which the reactive power in the AC MG cluster system is accurately shared before the communication link fault by using a centralized control technique that relies on the adaptive virtual impedance. In [75], a centralized control framework for managing and regulating power sharing in networked MGs is suggested.

2.3.1.2 Decentralized Control

In a decentralized control structure (as shown in Fig. 2.10b), instead of a central controller, the local control units of each MG in a cluster are responsible for collecting local information, determining its control activities, coordinating optimum operation without depending on information sharing with adjacent MGs, and making decisions based on information obtained from local specifications [73]. In decentralized control, a droop control approach is frequently employed so that each DER unit can independently regulate the voltage or frequency signal without assistance from the central controller. This approach provides independence, stability, and resilience against failures in communication for each MG unit, along with higher expansion capability for the networked system with reduced complexity. Because of the lack of communication links, this method is unable to ensure the cluster's suitable performance, and the increasing competition between individual MG units may compromise the cluster's overall effectiveness [71]. A decentralized self-optimizing power management strategy for interlinking converters in a hybrid MG-based MG cluster is proposed in [70] to reduce the overall voltage variation, expense, and geographical constraints. To improve the resilience and flexibility of clustered MGs with mobile ESSs, a three-stage dynamic distributed control strategy based on rolling optimization is considered in [76]. Another

decentralized control structure based on a voltage droop technique for interconnected DC MGs is considered in [77].

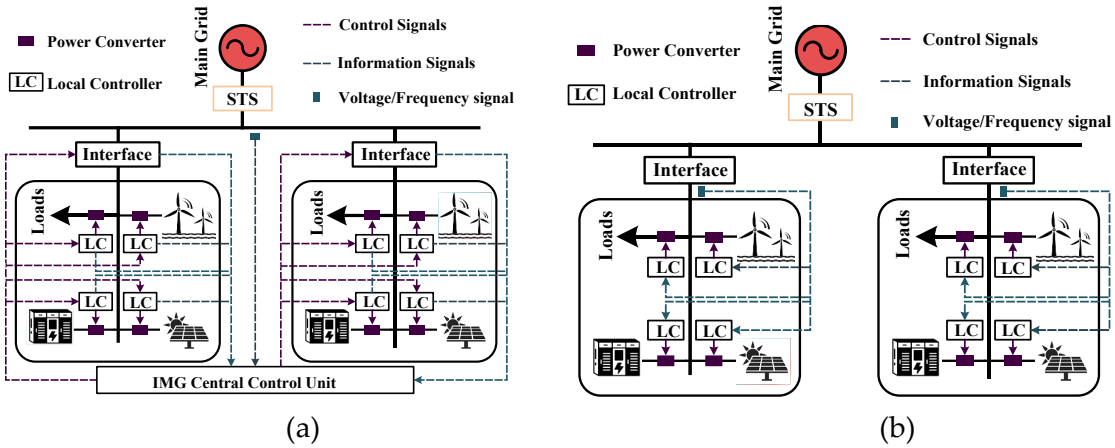

Fig. 2.10: a) Centralized control structure [71], and b) Decentralized Control Structure [73].

2.3.1.3 Distributed Control

The distributed control structure, a two-level control structure, as shown in Fig. 2.11a, is used in order to balance the advantages of centralized and decentralized controllers while coordinating the performance of local MG units. Each central unit or agent in the control structure is responsible for collecting data from adjacent agents and from the local MG units to achieve optimum performance and power-sharing across linked MGs [71]. Hence, the operation of each MG taking part in the MG network is managed and coordinated by several distributed central units, where each central unit consists of multiple local control units. For an AC MG cluster system operating in off-grid mode, a distributed control structure constructed with artificial neural networks is presented in [25] to achieve voltage harmonic suppression and frequency synchronization during load changes, controller startup and shutdown, and delays in communication. A distributed secondary control technique based on quantization inputs for DC MG cluster is developed in [78] to achieve voltage restoration, current sharing, and a reduction in communication burden.

2.3.1.4 Hierarchical Control

The hierarchical control structure, as illustrated in Fig. 2.11b, facilitates the development of MG cluster control at multiple control levels with different control responsibilities and targets by permitting controllers at various levels to communicate and exchange information or control signals [71]. Therefore, in the hierarchical control of an MG cluster, the operations of every MG in the cluster are managed and synchronized through three separate control levels, as shown in Fig. 2.12. These layers are multiple local units from individual MGs in the first control level (primary), the central control unit of each MG in the second control level (secondary), and the central unit of the overall MG cluster system in the third control level (tertiary) [71]. In order to reduce the overall cost of operation and the transmission loss, a hierarchical control method for DC MG cluster under real-time uncertainties of RESs, real-time fluctuation in power, and loads deviating from the prediction data is proposed in [24]. A hierarchical control structure is proposed in [79] in order to accomplish control goals such as precise power sharing, seamless transition and synchronization, recovery of frequency and voltage, and flexible regulation of power flow.

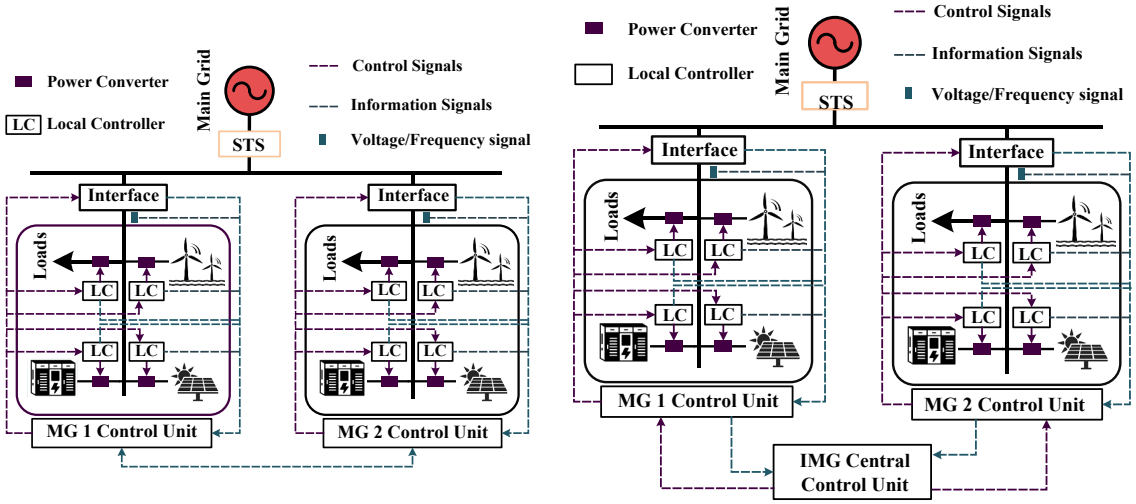

Fig. 2.11: a) Distributed control structure [71], and b) Hierarchical Control Structure [71].

2.3.1.4.1 Primary Control Level

Voltage/frequency control, operating mode identification, and initial power-sharing management are the fundamental responsibilities of the decentralized primary control [80]. It is comprised of voltage and frequency synchronization control, local protection devices, an outer control loop, and an inner control loop. It generates suitable switching in the converter in order to properly track the intended reference in the DER converter output [81]. The appropriate references for the inner control loop are generated by the outer control loop and voltage/current measurements [49, 82]. In comparison to secondary and tertiary control methods, primary control should operate more quickly (within a 10-second time frame) [81]. Fig. 2.12 presents the primary control in both AC and DC MG clusters.

2.3.1.4.2 Secondary Control Level

The MG's central controller, or secondary control, is responsible for monitoring the MG's voltage and frequency and sending reference signals in the form of voltage magnitude and angle to the DER converters [80]. Secondary control addresses issues such as grid synchronization, generation control, optimum DER operation within an MG, voltage and frequency stabilization resulting from primary-level deviation, power quality control, and real-time control of energy to preserve the power balance of each MG within the network [83]. Fig. 2.12 presents the function of the secondary control in both AC and DC MG clusters.

2.3.1.4.3 Tertiary Control Level

The network system's central control, or tertiary control (as shown in Fig. 2.12), is in communication with the network's circuit breakers and protection devices, as well as the central controllers in each MG and distribution network operator, for optimal power flow in the networked MGs. The level connects individual MGs to form the network, provides a connection with the main grid, and manages the power flow in the network. Additionally, this controller

observes the system data, determines whether two connected MGs are supposed to be separated, and instructs the appropriate circuit breakers to activate [80].

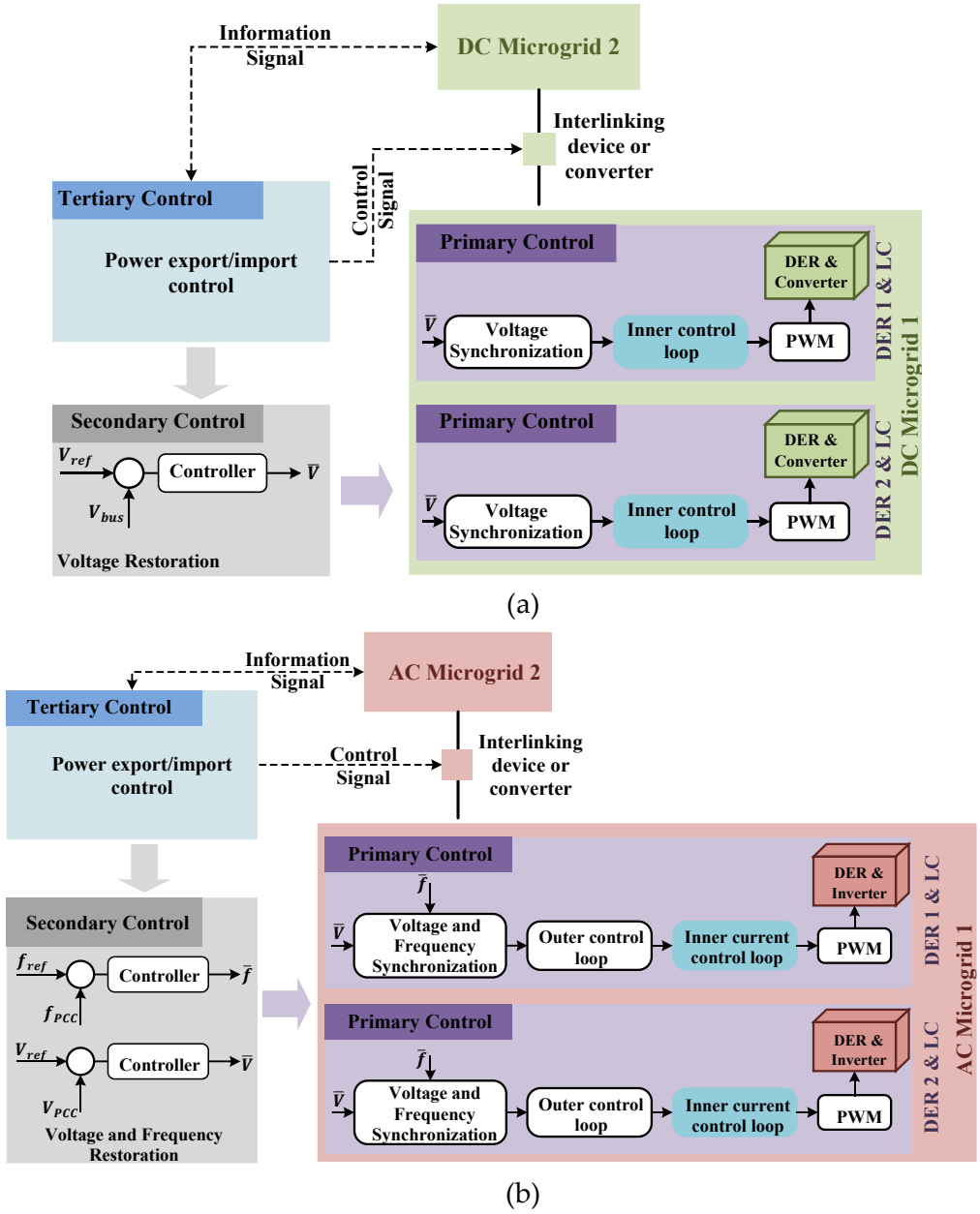

Fig. 2.12: a) Hierarchical control of DC MG cluster [81], and b) Hierarchical control of AC MG cluster [83].

2.4 CONTROL STRATEGIES

Under various operating scenarios and system configurations, managing the MG cluster is a challenge due to network voltage and frequency regulation. Thus, robust and accurate control strategies for managing the network voltage or frequency and the output powers of the electronically coupled DER unit are

required for the MG network to operate reliably. A wide range of strategies are used to regulate networked systems in various operating conditions. Table 2.4 presents an overview of various control techniques. The most common control strategies used in recent research are covered in the following subsections:

Table 2.2: An overview of the four control structures with advantages and disadvantages.

Control	Ref.	IMG type	Mode	Merits	Demerits
Centralized	[26]	DC IMG	IS	High precision; Flexibility in application; Reduced operation charge; High reliability in IS mode	Vulnerable to single-point failure; Lower Scalability, Higher bandwidth; Two-way communication; Computation burden
	[74]	AC IMG	GC/IS		
	[75]	DC IMG AC IMG	GC/IS		
Decentralized	[76]	AC IMG	GC/IS	Communication-free; Higher expandability; Resiliency against failures in communication; Appropriate coordination of several autonomous units; Strong against single-point failures; High computation efficacy	Inadequate system efficiency due to the absence of communication; High operational cost; Low resiliency in IS mode; Costly point-to-point communication
	[70]	Hybrid AC/DC IMG	IS		
	[77]	DC IMG	IS		
Distributed	[25]	AC IMG	IS	Restricted communication requirement; High scalability and flexibility; Offers cooperation among separate structures; Better reliability	Security concerns; Implementation complexity; Lower stability and speed; Communication lines among each nearby MGs
	[78]	DC IMG	IS		
	[34]	AC-DC IMG	IS		
Hierarchical	[24]	DC IMG	GC/IS	Offers flexible control with a multiple-system network; Cost effective; Easier to implement	Vulnerability to failure as a result of a strong connection between lower and higher control layers
	[84]	AC-DC IMG	GC/IS		
	[79]	AC IMG	GC/IS		

MG Microgrid **IMG** Interconnected Microgrid **GC** Grid-connected **IS** Islanded

2.4.1 Droop-based Control Techniques

The primary control level's main goal is to emulate the operation of a synchronous generator by altering frequency in response to variations in active

power generation [85]. This concept can be utilized in converters for AC and DC MGs by employing droop techniques. The droop control strategy is a well-known approach for load sharing with several advantages, such as plug-and-play functionality, communication-free energy distribution, and improved flexibility [73].

2.4.1.1 Droop Characteristics of Different IMG Systems

A DG with the droop characteristic has grid-forming abilities to regulate the system's frequency and voltage, similar to a synchronous generator's governor [73]. Moreover, droop characteristics provide quick and decentralized power sharing based solely on local measurements. Different droop characteristics are employed, as presented in Table 2.3, to achieve optimum load sharing amongst DERs within each MG and amongst all MGs in clustered MGs.

Table 2.3: Various droop characteristics [86].

Control Unit	Droop characteristic	Variable		Droop gain
AC IMG	Active power – Frequency	P_{AC}	f	m_p
AC IMG	Reactive power – Voltage	Q	V_{AC}	m_q
DC IMG	DC power – Voltage	P_{DC}	V_{DC}	n_p
AC-DC IMG	Interlinking converter transferred power – Performance difference between frequency and DC voltage	P_{ilc}	E	n_{ilc}

IMG Interconnected Microgrid

The droop characteristic of a networked MG is a combination of the droop characteristics of all MGs in the cluster. The droop characteristics of a single AC MG are expressed in equations 2.1 and 2.2, which indicate that an abrupt power supply imbalance will result in variations to the AC MG's voltage and frequency.

$$f = f^n - m_p(P_{AC} - P_{AC}^n) \quad 2.1$$

$$V_{AC} = V_{AC}^n - m_q(Q - Q^n) \quad 2.2$$

Here V_{AC} and f are the measured values of the voltage and frequency, V_{AC}^n and f^n are the reference values of the voltage and frequency, P_{AC} and Q are the

measured active and reactive power, P_{AC}^{n} and Q^{n} are the reference active and reactive power, and m_p and m_q are the frequency and voltage droop coefficients. The individual responses of the two AC MGs can be equivalently described as an integrated droop characteristic of the MG cluster level, as shown in Fig. 2.13. At the nominal frequency f^{n}, the generated powers in both MGs are P_1^{n} and P_2^{n}, respectively. Any MG experiencing a quick rise or decrease in power consumption causes the networked system frequency to fluctuate immediately, which is followed by an increase or decrease in generation in both MGs. It is evident that the droop features cause two MGs in the cluster to distribute the load change proportionately.

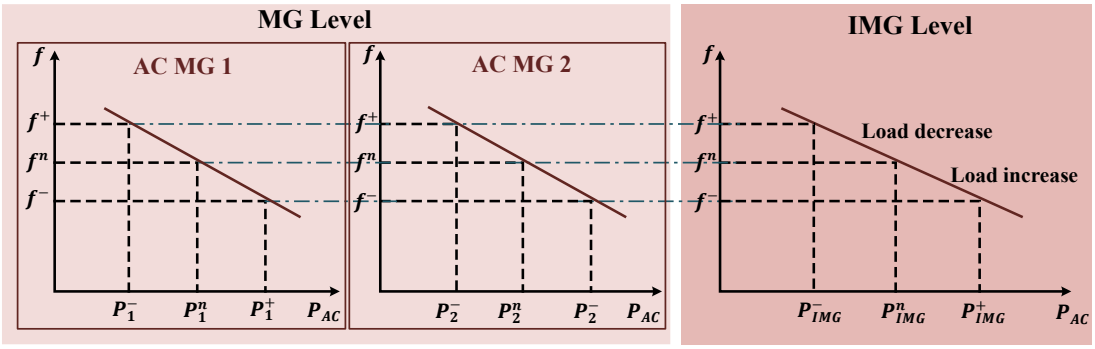

Fig. 2.13: Droop characteristic of AC microgrid cluster.

In a single DC MG, the droop characteristic between power and voltage is expressed in equation 2.3.

$$V_{DC} = V_{DC}^{n} - n_p(P_{DC} - P_{DC}^{n}) \qquad 2.3$$

Here V_{DC} and V_{DC}^{n} are the measured and reference values of the DC voltage, V_{AC}^{n} and f^{n} are the reference values of the voltage and frequency, P_{DC} and P_{DC}^{n} are the measured and reference DC power, and n_p is the DC voltage droop coefficients. Fig. 2.14 shows the integrated droop characteristic of a DC MG cluster system after the superposition of two separate droop characteristics of two MGs.

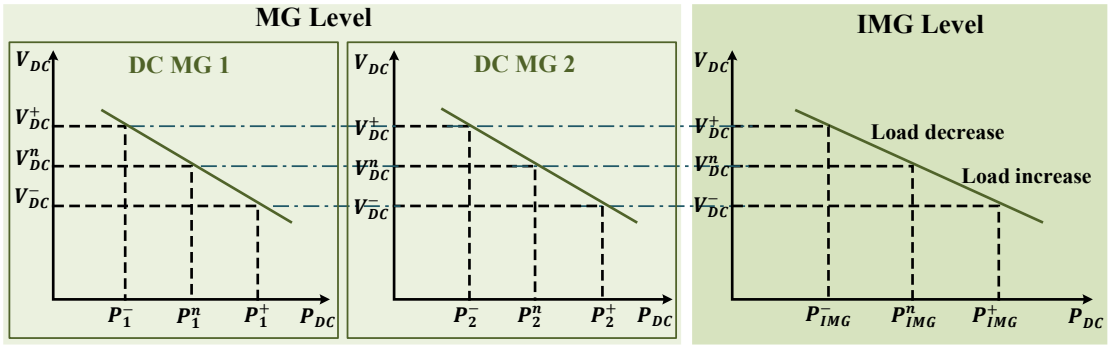

Fig. 2.14: Droop characteristic of DC IMG.

Due to the regulation of both frequency and DC voltage, the load-sharing droop characteristics in interconnected AC and DC MGs are more complex than in DC and AC MG clusters. In the AC-DC MG cluster, the bidirectional power flow is primarily controlled by the interlinking converter, which mainly connects the AC and DC MGs. When a MG experiences a deficit in power, the interlinking converter allows the other MG to restore the power balance through power transfer. That is, in order to request power assistance, each MG just needs to communicate with the interlinking converter so that the other MG in operation can trade power with the converter. Therefore, the interlinking converter in the AC-DC network maintains the power transfer among MGs. The converter maintains the following droop characteristics to control power transfers in both directions (as shown in Fig. 2.15) [86]:

$$P_{DC-AC} = P_{DC-AC}^{n} - n_{DC-AC}(f - f^{n}) \quad 2.4$$

$$P_{AC-DC} = P_{AC-DC}^{n} - n_{AC-DC}(V_{DC} - V_{DC}^{n}) \quad 2.5$$

Here P_{DC-AC} and P_{AC-DC} are the transferred power from DC to AC MG and from AC to DC MG, P_{DC-AC}^{n} and P_{AC-DC}^{n} are the nominal transferred powers, n_{DC-AC} and n_{AC-DC} are the droop coefficients. As illustrated in Fig. 2.15, the AC MG experiencing a power outage will approach the interlinking converter for extra power. Ultimately, the partial droop characteristic controlling the power delivered into the AC MG and the frequency droop curve of the AC MG will interact to stabilize the frequency at a lower value. Similar to this, when there is

a power outage in the DC MG, the equivalent voltage droop curve and the partial droop characteristic interact together to maintain the voltage magnitude at a lower value for additional power transfer. In the above situations, the interlinking converter communicates with each MG independently, which isn't feasible. As a result, prior to identifying the power transfer, the interlinking converter must determine the direction of power flow. However, the two partial droop characteristics are combined into an integrated droop characteristic (in equation 2.6), considering DC to AC as the reference power direction to coordinate the operations between AC and DC MGs.

$$E = E^n - n_{ilc}(P_{ilc} - P_{ilc}^n) \qquad 2.6$$

Here E and E^n are the measured and reference values of the performance difference between DC and AC MGs based on frequency and DC voltage, P_{ilc} and P_{ilc}^n are the measured and nominal transferred powers, n_{ilc} is the droop coefficients.

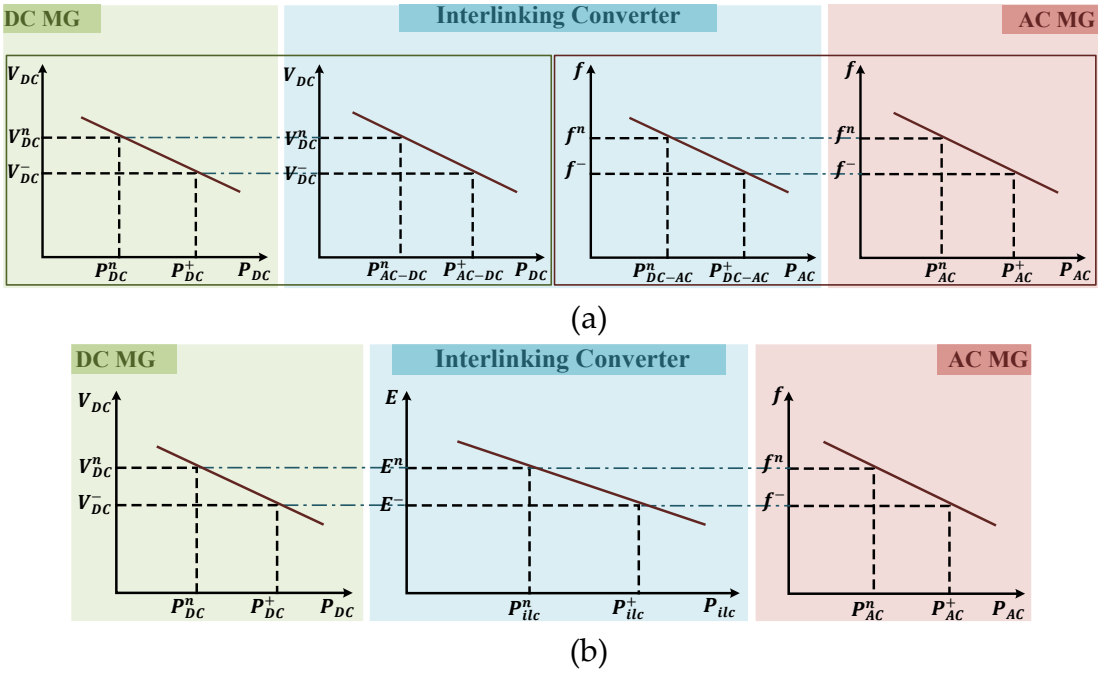

Fig. 2.15: a) Partial droop characteristics of AC-DC IMG [86], and b) Integrated droop characteristics of AC-DC IMG [86].

The integrated droop characteristic of the AC-DC MG cluster is shown in Fig. 2.15b. When there is a power outage in the AC MG, the frequency deviation

causes the DC MG to transmit additional power faster to satisfy the increased demand, which lowers the DC voltage in the interlinking converter. The MG cluster's operating state finds a new equilibrium once the power transfer has been stabilized.

2.4.1.2 Droop Control Methods

The droop method is useful in preserving voltage and frequency within allowable limits in parallel-connected inverters by eliminating communication lines. However, the conventional scheme has some drawbacks, such as deviations in voltage and frequency, inaccurate reactive and active power sharing, slow transient response, unregulated power injection in on-grid mode, and poor harmonic sharing of load among inverters under non-linear load and line impedance disparity conditions. Various strategies have been established to solve the problems caused by the conventional droop technique.

A good way to achieve droop control in a system with a low (<1) X/R ratio is to employ virtual impedance in the voltage control loop. Designing the system control output impedance via virtual impedance modelling is a useful technique for eliminating the requirement of real impedances and finding an appropriate application to implement droop techniques. By improving reactive power sharing across parallel inverters, virtual impedance-based droop approaches eliminate the line impedance disparity challenge. However, voltage regulation deterioration is the main negative aspect of this control. To address the reactive power sharing issue brought on by the variation in line impedance, a virtual impedance control based on a compromise between voltage drop and precision of reactive power sharing without communications is suggested in [87].

In [88], a modified droop controller is suggested to increase the voltage regulation and precision of current sharing in DC MGs while maintaining the system's modularity under various line parameters and loading scenarios. The adaptive droop technique is another improved version of droop control that is

used to address delayed transient responses and facilitates precise power sharing among inverters by preserving system voltage and frequency within a reasonable range. In [89], a novel approach is developed for stabilizing the VSC-based AC MG cluster (mesh layout) by the use of an adaptive droop control with a significant degree of fluctuation in the transmission line's X/R ratio. In [68], a unique adaptive droop control method is introduced that continuously adjusts the droop coefficients of the VSCs to guarantee the optimum utilization of the resources available in each MG under various operating modes.

2.4.2 Predictive Control Method

Predictive control is a collection of control strategies that maximize the use of the entire system model under certain constraints to optimize predetermined cost functions or objective goals and obtain control signals or commands. A precise system model is the primary requirement for deploying this strategy to carry out an impending control action and enhance a system's transient responses. To coordinate the operations of the separate MGs and sustain the system's supply and demand balance in a cost-effective way during generation and demand uncertainties, a novel distributed model predictive control (MPC) for the clustered MGs is proposed in [90]. In [91], another distributed MPC-based controller is presented to control the frequency while preserving the voltage restrictions of all buses in the IMG system with various system topologies and operating scenarios. In [92], a novel structure for energy management is presented for off-grid MG clusters using tube-based MPC, which allows for robustness against systemic uncertainties in the energy management approach while sacrificing less computational effectiveness and economic performance.

2.4.3 Active Power Sharing Control

Active power sharing-based control is classified as master-slave and instantaneous average current sharing control strategies. Within a networked system, several MGs function as slaves and one MG as master (the highest

capacity MG) in master-slave control. The master MG serves as the voltage-controlled unit and is responsible for generating voltage and frequency references. Slave MGs keep track of references specified by the master MG for reducing frequency and voltage deviation. In this control method, the MG cluster is regulated by a centralized control structure, and the master MG is responsible for preserving the stability of the entire system [73]. To achieve resilience management of power in the networked system, a multilayer dynamic master-slave control technique using two-layer configurations is proposed in [93]. To control DER output and accomplish power management within individual MGs, the first layer with the DERs feature is employed. After that, to accomplish power management among MGs, the secondary layer with the MG feature communicates with bidirectional converters to share control signals. In [94], a novel coordinated control scheme using a master-slave control is proposed for interconnected AC-DC MGs to achieve voltage and frequency control and active and reactive power sharing. To accomplish precise current sharing and economical allocation, rapid consumption along with faster convergence, and resilience against variable communication scenarios, a master-slave coordination structure for the DC MG cluster is presented in [95].

2.4.4 Artificial Intelligence Control

The networked system's dynamic requirements cannot be supported by classical control methods due to their lower accuracy, speed, and reliability. Using artificial intelligence (AI)-based control approaches appears to be a viable way to improve MG cluster control and functionality [96]. AI-based techniques have been used in different studies to regulate the power, frequency, and voltage. Distributed cooperative control and adaptive neural networks (NN) are used to introduce an adaptive voltage and frequency control scheme for inverter-based DGs in a clustered MG topology. To accomplish PQ power sharing between DERs and lessen the controllers' reliance on system dynamics, AI-based

strategies were used in the controllers' architecture [97]. In [98], a control method based on a genetic algorithm is proposed to successfully reduce power fluctuation and offer reliable control performance in a PV-based MG network under varying operational conditions. Three deep NNs, such as a deep critic NN for performance evaluation, a deep prediction NN for next state prediction, and a deep action NN for command or control signals, are combined to minimize a system's frequency deviation by replacing load frequency control [99]. To achieve resilient performance by rejecting load disturbances and damping frequency variations, an effective fuzzy cascade control is proposed in [100] that supports a frequency perturbation-based demand management program.

Table 2.4: Merit and demerits of various control strategies.

Control Strategies		Merits	Demerits
Droop Control	Conventional	Simple structure; Communication free.	Line impedance disparity; Inaccurate reactive power sharing; Reduced power quality; Poor harmonic sharing under non-linear load.
	Virtual Impedance	Eliminates line impedance disparity; Improves reactive power sharing.	Voltage regulation issues; Additional current sensor requirement; Increases system cost.
	Adaptive	Accurate power sharing; Eliminates slow transient response	Incapable of handling non-linear loads; Requirement for parameter specification
Predictive control		Reduce data losses; Fast dynamic response; High robustness	Reduced delay handling capacity; Complex algorithm; Large computation burden; High demand for the mathematical model.
Active Power Sharing Control	Master-slave	No PLL requirement; Better dynamic response; Simple to control; No circulating current among DERs.	Entire system failure due to master unit failure; Single point of communication infrastructure failure; Communication requirement; Privacy concerns.
	Instantaneous Average Current Sharing	Precise steady-state and transient current sharing; Better voltage regulation	No circulating current reduced reliability and redundancy; Additional current sensors requirement; Communication requirement.
Artificial Intelligence Control		Better dynamic performance; Higher accuracy and speed; Fast convergence	Long processing time; Excessive memory requirement; Higher cost.

PLL Phase Locked Loop **DER** Distributed Energy Resource

2.5 INTERLINKING CONVERTER CONTROL

Interlinking converters have become the standard process of connecting MGs, irrespective of their properties like voltage and frequency [51]. The control of interlinking converters is more challenging than controlling on-grid devices and other DER controllers because their primary and secondary sides are not fixed by a power supply and because they must engage in primary regulation and perform other ancillary functions without any primary reserve.

2.5.1 Interlinking Converter in AC-DC Microgrid Cluster

Interconnection of AC and DC MGs is only possible using converter interfaces. This converter interface plays a crucial role in sustaining system performance by ensuring the stability of the AC and DC bus voltages and power equilibrium between AC and DC MGs. In on-grid mode, the primary responsibility of the interlinking converter is to control the DC bus voltage and ensure the power balance between the AC and DC MGs, while the AC voltage and frequency are stabilized by the main grid. Because the main grid does not support off-grid mode, the converter must supply a steady voltage and frequency to the system in addition to ensuring appropriate power balance. Therefore, the controller, as shown in Fig. 2.16, must be designed to provide proper operation and ensure system stability in all modes.

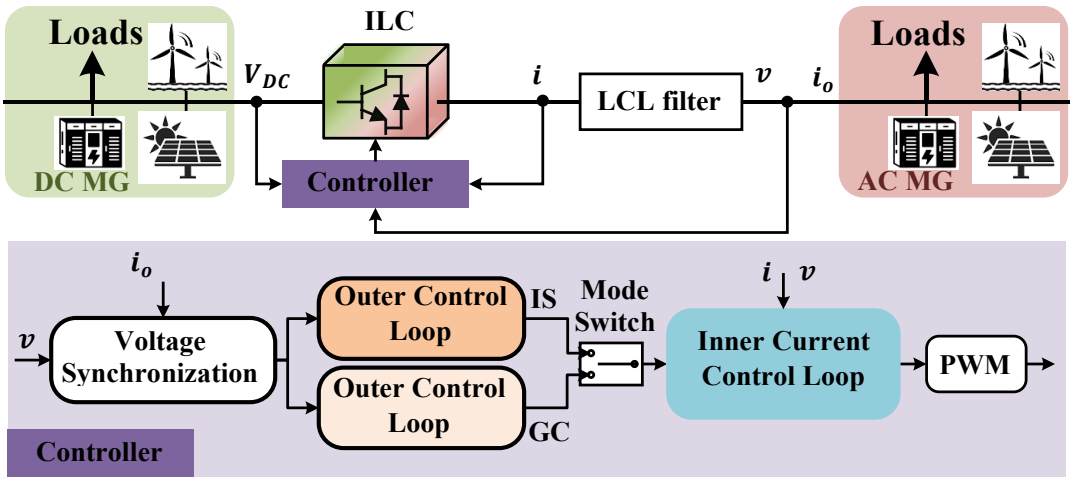

Fig. 2.16: Controller for interlinking Converter in AC-DC Microgrid Cluster.

A control strategy, as shown in Fig. 2.17, is proposed for the interlinking converter in [101] to operate in both on- and off-grid modes. Depending on how much power is exchanged between the AC and DC systems, the converter switches between a PQ and a V_{DC}-Q control method in on-grid mode. When the PQ control mode is activated, the DC MG keeps supplying the AC MG with constant power, and the ESS is essential in absorbing and releasing power to keep the DC bus constant. The converter changes from V_{DC}-Q (M_2) control mode to PQ (M_1) control mode when the transferred power supplied to the AC side from the DC side exceeds the converter's maximum rating (M_1). The V_{DC}-Q (M_2) or PQ (M_1) control approach can be used to ensure continuous power flow between the DC and AC MGs when the transferred power from the DC side is less than the nominal capacity of the converter. The V/F control scheme in off-grid mode is employed to operate properly.

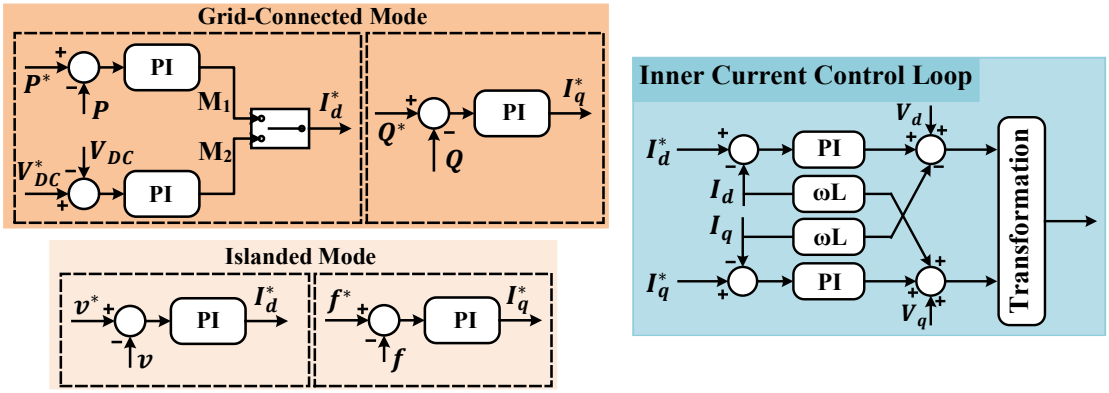

(a) (b)

Fig. 2.17: Control strategy of interlinking converter [101]: b) Outer control Loop, and b) Inner control Loop.

To enable power exchange and control in off-grid mode between AC and DC MGs, a DC voltage droop and an AC frequency droop are employed in the outer control loop of the converter [102], as shown in Fig. 2.18a. The power flow through the converter will adjust in accordance with the frequency droop caused by any change in load in the AC MG. Similarly to this, any difference in the load on the DC MG will cause a change in the DC voltage, which will alter the

converter power in accordance with the DC voltage droop. The suggested approach permits independent power transfer in either direction without any communication links. In [103], it is suggested to use an interlinking converter controller to incorporate ESS and enhance the power quality of an IMG system. The interlinking converter is driven by two control loops, where the external loop regulates the voltage on the DC-link capacitors while the internal loop regulates the current. The interlinking converter and main grid are synchronized through the use of a PLL. To do this, the Park transform—which requires the synchronous angle produced by the SRF-PLL—uses the three-phase voltages and currents obtained at the common point as inputs. The voltage control, as shown in Fig. 2.18, generates an error for the PI controller's input by taking the squared deviation between the measured DC voltage and the voltage reference. In order to retain the control output within the operational region, saturation is employed along with a negative gain for non-minimum phase change.

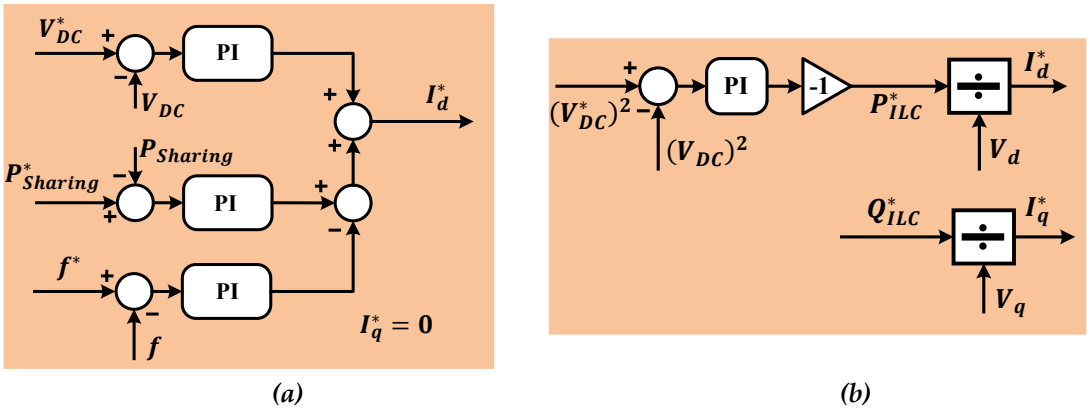

Fig. 2.18: a) Outer control loop of interlinking converter [102], and b) Outer control loop of interlinking converter [103].

2.5.2 Interlinking Converter in DC Microgrid Cluster

Distribution sectors are becoming more and more involved in interconnections of DC MGs because of the benefits of improved reliability, reduced ESS sizes, resilient operations, and efficient resource utilization.

A buck-boost converter controller (Fig. 2.19) is developed in [37] to connect DC MGs via a secondary control scheme based on charging/discharging power

and SoC, allowing the MGs to share power while keeping the standard DC bus voltages. The power transfer controller in the interlinking converter is properly designed and tuned in order to accomplish the power-sharing function. To combine the droop characteristics of both MGs, the DC bus voltage droop characteristics of each MG are normalized. Therefore, the voltage droop characteristics of the DC bus voltages are related to the load difference between the two MGs. The suggested controller functions in two modes for optimal efficiency. The controller runs in peak charging control mode in mode 1. The controller uses a power-sharing mechanism based on SoC balance when it is in mode 2.

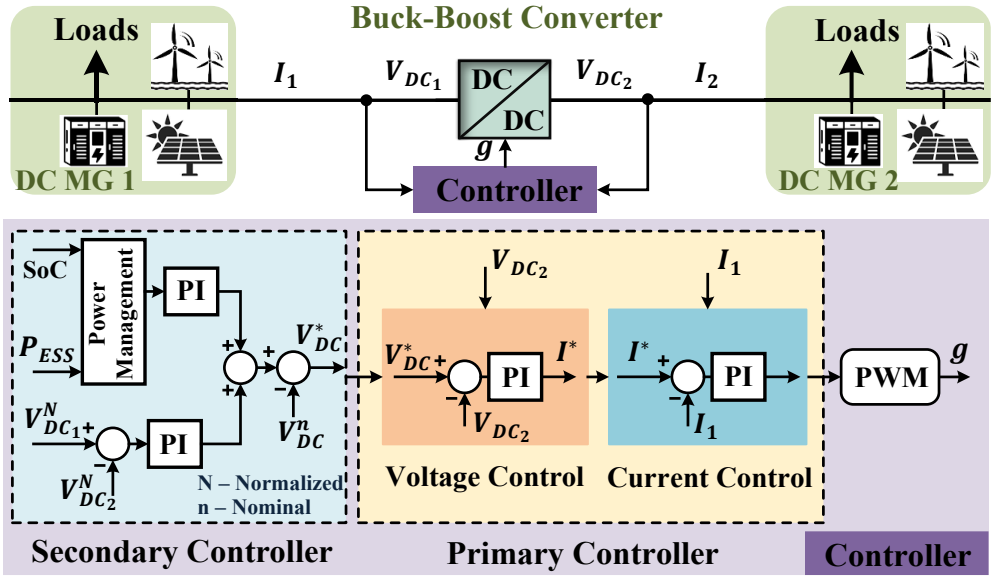

Fig. 2.19: Buck-boost interlinking converter Controller [37].

A DAB-based interlinking converter controller is employed to ensure power sharing between interconnected DC MGs, as illustrated in Fig. 2.20. The controller consists of two loops: an outer voltage loop and an inner current loop. When one of two DC MGs has excess power and the other MG can absorb it, the interlinking converter enters an active mode. The transfer of power from DC MG 2 to DC MG 1 is regarded as positive, whereas the opposite is regarded as negative. When DC MG 1 has surplus energy available and another MG is prepared to absorb it, it begins exporting the power by controlling the bus voltage

via the outer voltage controller and supplying the negative reference current. An inner current controller is then used to track the reference current by interlinking the converter current, producing the necessary negative phase shift. Similar to this, during the power transfer from DC MG 2 to DC MG 1, the voltage is controlled through the outer loop to release a positive reference current. The inner loop then produces the positive phase shift.

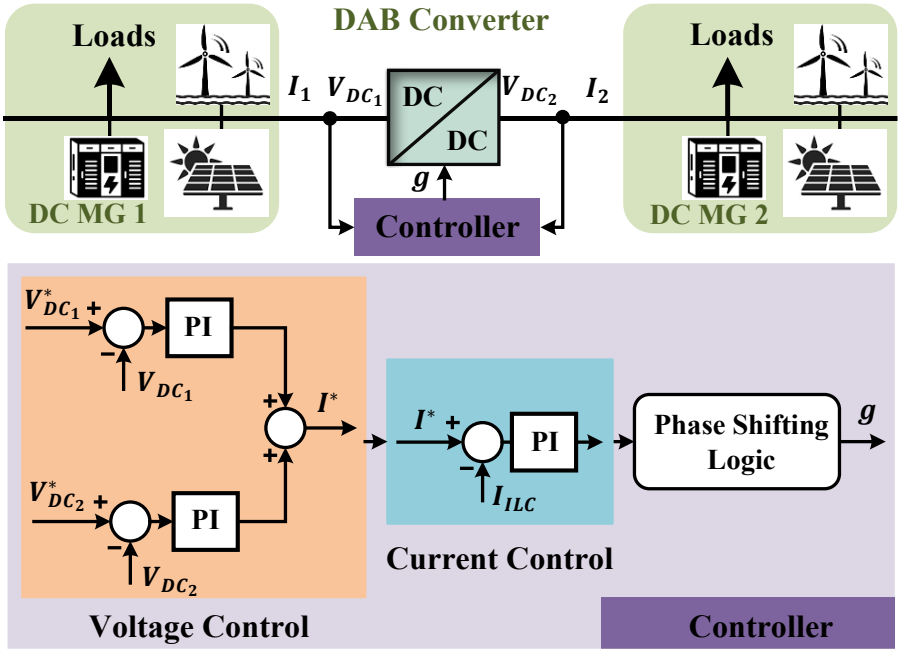

Fig. 2.20: Dual active bridge interlinking converter controller [35].

A two-stage converter interface, as shown in Fig. 2.21, to interconnect two adjacent DC MGs and control bidirectional power exchange between them is proposed. The first stage of the converter interface (DAB converter) operates in power regulation mode, ensuring that even when the input voltage (V_{DC_1}) and output current (I_o) fluctuate, the output voltage (V_{DC_o}) is consistently maintained at its reference value. The full bridge converter, or second stage of the converter interface, receives its input from the DAB output. For the purpose of producing an adjustable DC voltage (V_{DC_2}), the full bridge converter is run in voltage control mode with pulse width modulation (PWM). Thus, the necessary voltage can be produced across the full bridge converter's output with the appropriate polarity depending on the power reference. The suggested controller regulates voltage

with the proper polarity to manage power flow between DC MGs in both steady-state and transient scenarios.

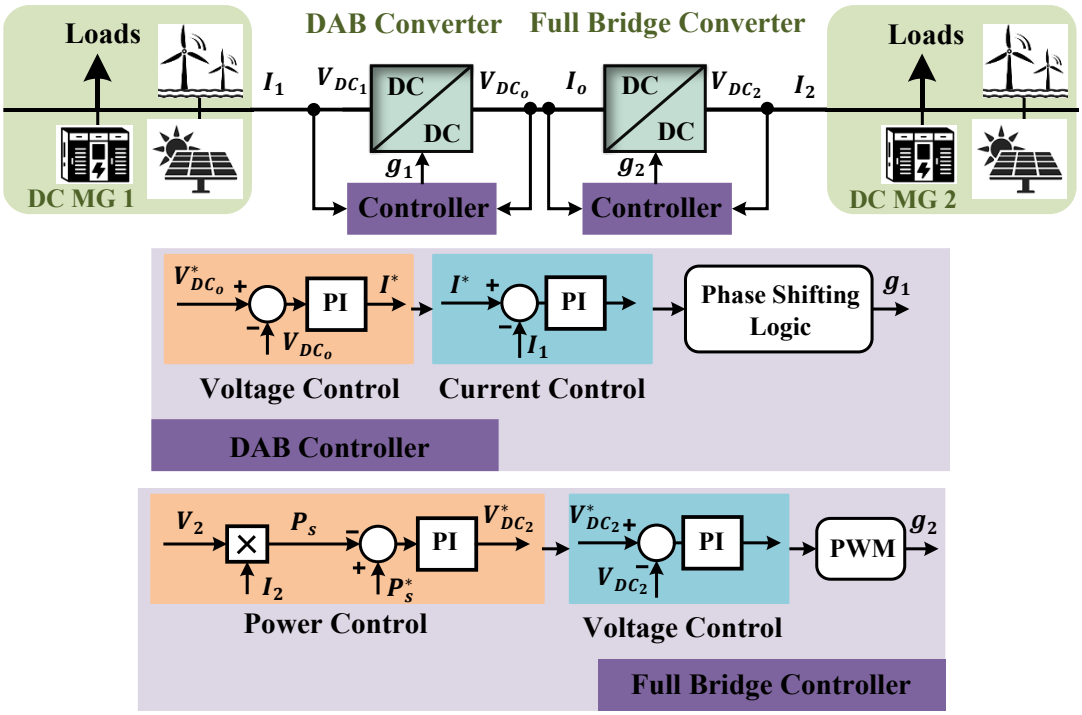

Fig. 2.21: Two-stage interlinking converter controller [66].

2.5.3 Interlinking Converter in AC Microgrid Cluster

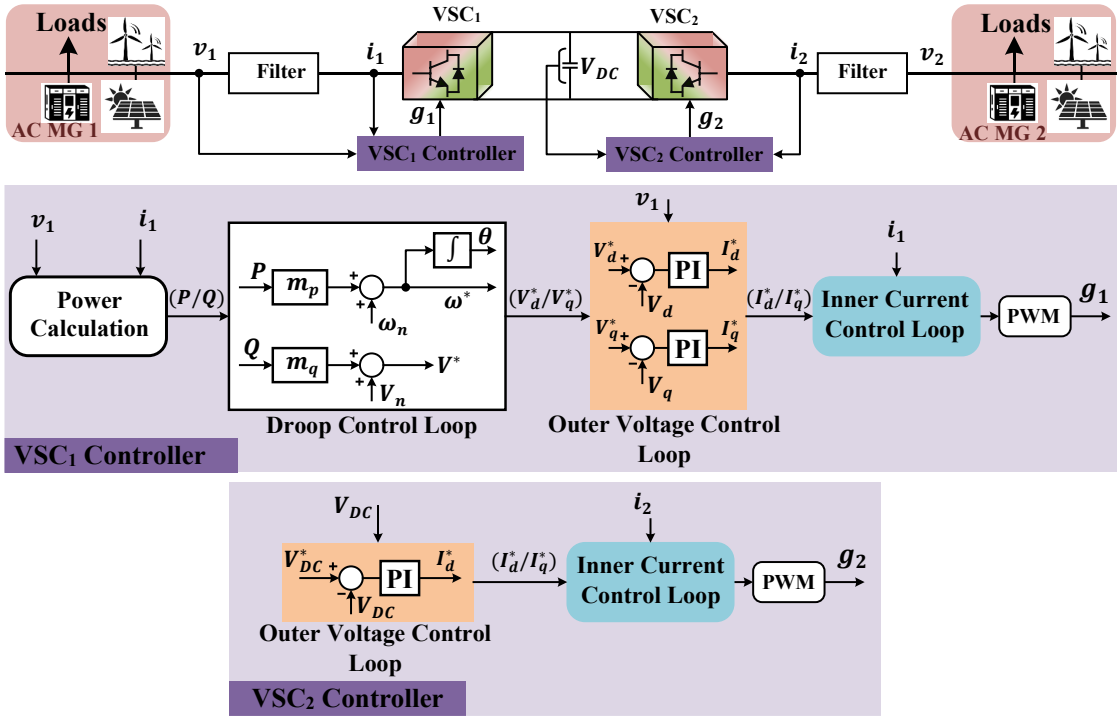

Fig. 2.22: Back-to-back converter controller in AC microgrid cluster [38].

Due to its versatility in performing a number of functions, including power transfer between MGs, power quality enhancement, and smooth mode transit, interconnection via the interlinking converter is preferred over tie-line connections. In [38], the control strategy of the back-to-back converter, as shown in Fig. 2.22, is presented to ensure proper power supply between two AC MGs. The P-ω and Q-V droop control [104] and AC voltage-based outer voltage control loop are used to control the VSC_1 converter on the AC MG-1-side. The VSC_2 on the AC MG-2-side is controlled using the DC-link voltage between the two VSCs.

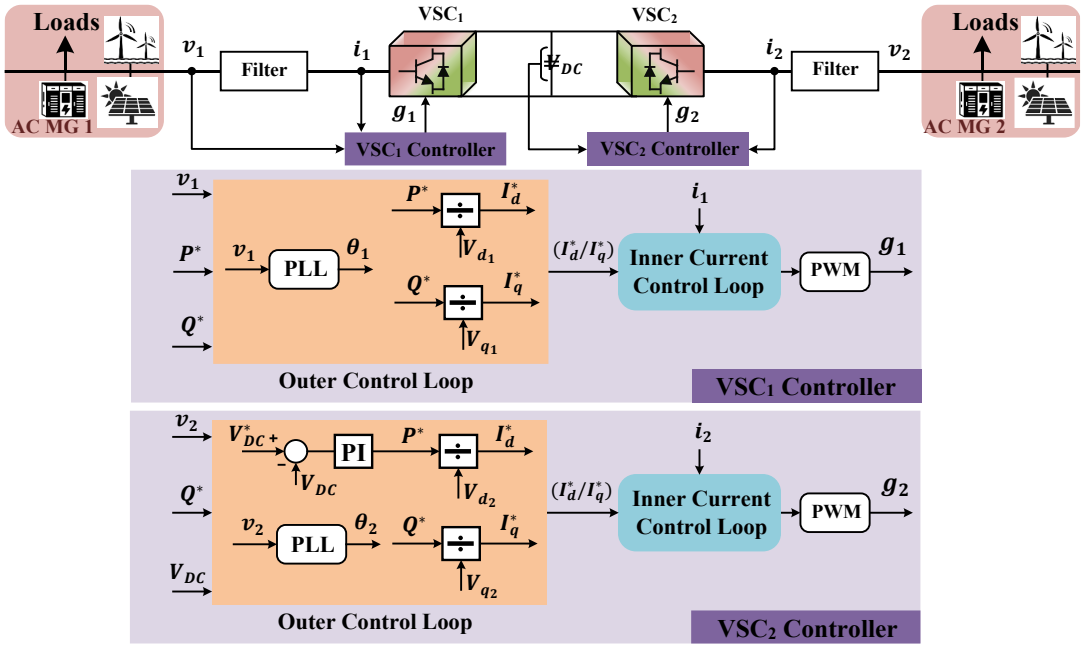

Fig. 2.23: Back-to-back converter controller in AC microgrid cluster [32].

In [32], two controllers are designed to control the back-to-back converter's VSCs to exchange power between two AC MGs (in Fig. 2.23). One common DC link and two AC sides constitute the back-to-back converter interface. The power interface comprises two AC sides and one common DC link. A higher-level controller, or the global control level of the MG system, provides the power controller of VSC_1 with active and reactive power references. The power controller of VSC_1 then attempts to exchange planned powers by regulating the VSC_1 current. Conversely, the DC voltage controller regulates the VSC_2 current in order to stabilize the DC voltage (V_{DC}). For the VSCs to synchronize with the

MGs, two PLLs are needed. The AC and DC sides, a power controller, a DC voltage controller, and PLLs are the main components of an accurate dynamic model of a back-to-back converter

2.6 CHARACTERISTICS OF NETWORKED MICROGRIDS

The characteristics of a networked MG system depend entirely on the configuration and performance of the individual MGs within the cluster, i.e., the characteristics of individual MGs affect the ultimate performance, such as power quality, stability, and dynamics of the cluster.

2.6.1 Stability

A stable operation of the MG cluster is difficult to achieve and maintain at all relevant operating points because of the extensive integration of MGs with various DERs, loads, interface technologies, control strategies, and both inter- and intra-system analysis. Although stability analysis of MG cluster follows a similar pattern to that of traditional power systems, the high penetration of RESs, higher unpredictability, higher feeder resistance to reactance (R/X) ratio, low system inertia, unbalanced three-phase loading, and constrained short-circuit capacity make stability analysis more challenging. Moreover, inter- and intra-MG oscillations and both AC and DC voltage stability have a great influence on the entire system's stability [105]. Thus, it is necessary to analyse various issues that lead to power system instability in order to mitigate those challenges. The stability analysis of a system involves five major steps, such as determining the physical reason for the instability, the disturbance's relative size, the physical elements engaged in the process, the duration of the instability, and the methodology used to evaluate or forecast the instability. The networked microgrid system's stability classification [106] is presented in Fig. 2.24. There are two primary categories of instability in the networked microgrid system: phenomena related to the components and control systems and phenomena related to the sharing and balancing of active and reactive power. Both types of

instability can be short- or long-term phenomena; short-term stability problems last for a few seconds or less, but longer-term problems affect the system's long-term stability.

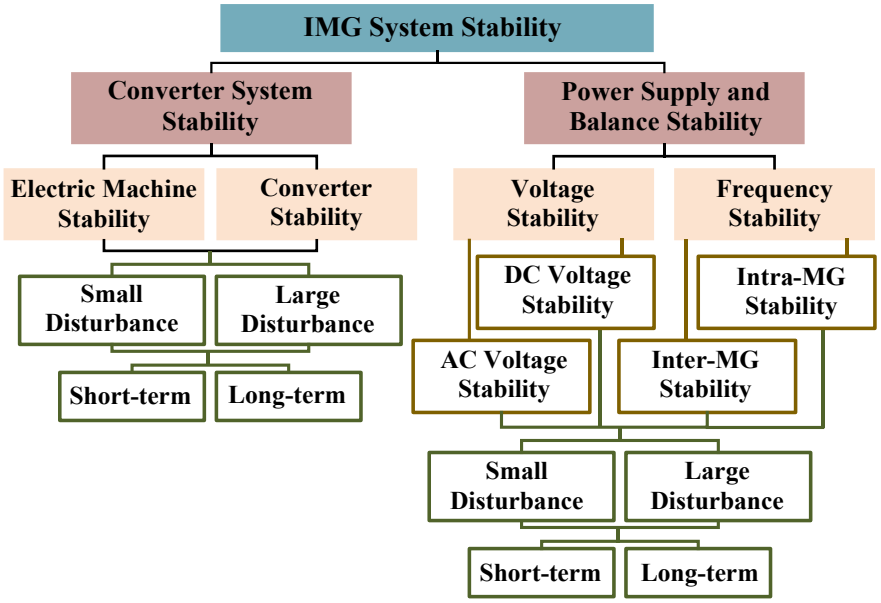

Fig. 2.24: Stability classification in the networked microgrid system.

2.6.1.1 Power System and Balance Stability

Inaccurate power sharing and balancing, loss of a generating unit, and the effects of different loads were the major causes of power system instability.

Frequency stability is a prime concern in a MG-based power system due to the high intermittent nature of RESs, low X/R ratios of MG cables, insufficient system response, and low system inertia. To improve an interconnected hybrid MG's frequency stability, an optimally resilient controller-based virtual inertia control is suggested in [107]. In [108], a specific structure-based controller is suggested to maintain the networked microgrid system's frequency stability. To maintain the frequency variation at a manageable level in the context of high load perturbations system uncertainties, and strong wind energy accessibility, an effective control approach is designed for a three-area power system [109].

The voltage stability of the networked microgrid system is ensured by using distributed local control units to keep the AC and DC-link voltages within

acceptable limits. Reactive power limitation, dynamic load interactions, and reactive power balancing issues are strongly associated with voltage instability in MGs. To address issues with DC bus voltage stability in the DC MG cluster, a hierarchical control approach is implemented in [110], with the sub-MG integration control located at the top, voltage compensation and droop coefficient adjustment control at the second layer, and droop control and voltage closed-loop regulation at the bottom. To reduce real power losses, voltage variations, and power generation expenses, an energy management system for on-grid MGs is developed in [111] that considers generation restrictions and voltage stability.

2.6.1.2 Control System Stability

The main causes of control system stability are insufficient management schemes and improper tuning of one or more device controllers. This particular type of stability is relevant to phase-locked loop (PLL), LCL filters, converter control loops, and electric equipment. Stability problems in MGs are intrinsically linked to the requirement for power conversion via power electronics interfaces to attain various voltage levels, which is essential for connecting ESSs, sources, and loads. The unique characteristics of the power-converter-dominated MG, such as its time-varying nature, nonlinearity, poor suppression of interference, low inertia, and multi-time scale, make it more difficult to maintain system stability. Due to difficulties with tuning, failure of inverter-based DERs, high harmonic-frequency fluctuations, and PLL synchronization, converters are vulnerable to small- and large-perturbation instabilities. To track the MG voltage reference for active load synchronization, a new technique is employed in place of the conventional PLL. This new approach avoids design complexity, poor accuracy, nonlinearity, tuning challenges, slow response, and detrimental effects on the PLL [112]. To improve system stability and respond to power changes, disturbances, and parameter modifications, a novel fuzzy logic-based online tuning technique for proportional-integral (PI) controllers is suggested in [113] for large MG systems. A novel harmonic droop controller is suggested to

distribute the harmonic power across parallel inverters that are regulated by the frequency droop approach and to lessen the voltage harmonic distortion [114].

2.6.2 Power Quality

Power quality is one of the significant characteristics of the MG-based power system, as the increasing penetration of nonlinear loads, renewable energy-based DGs with PQ challenges, and power electronic converter interfaces can result in distorted waveforms and increased energy costs. Therefore, novel power quality improvement strategies and analysis of power quality issues become essential in MG cluster systems due to the load sensitivity, higher utilization of RESs, and converter interfaces. Different power quality improvement devices, such as the dynamic voltage restorer, static transfer switch, automatic voltage regulator, Static VAR compensator, distributed static compensator (D-STATCOM), and unified power quality controller have been developed to enhance the power quality indices such as voltage fluctuations, frequency deviations, and harmonic distortion of MGs [115]. Smart impedance, electrical springs, and novel control methods are multi-functional power quality enhancement devices or systems that can perform multiple tasks simultaneously using the same hardware, which not only increases reliability and efficiency but also lowers costs [116]. Table 2.5 presents the allowed voltage characteristics, frequency variation range, and total harmonic distortion (THD) according to different countries and IEC and IEEE standards. adaptive control technique based on artificial neural networks and fuzzy logic is used in the inverter of each MG in a parallel DC IMG structure, and coupling VSC is proposed in [117] in order to improve the various power quality issues such as voltage unbalance, voltage sag/swell, frequency deviations, neutral current compensation, and THD.

2.6.2.1 THD and Voltage Quality

Waveforms of voltage or current that are integer multiples of the nominal frequency (50 Hz or 60 Hz) are known as harmonics. Harmonic distortion can be

caused by nonlinear loads, switching modes of power electronics converters, and other devices in the network that have nonlinear voltage and current characteristics [118]. These nonlinear loads and elements introduce harmonic current within the system, and voltage distortion will occur when the harmonic current flows through the system's or the main grid's high impedance. The harmonic problem is especially concerning because significant harmonic distortion might result in power quality issues, which leads to system damage. Moreover, various problems, such as voltage distortion, extra losses, overloading of the neutral in a three-phase power system, resonances, and overheating transformers and cables, can result from extensive harmonics [116].

Table 2.5: Standards for various power system characteristics [119].

Voltage							
Voltage sag			**Voltage swell**			**Voltage Unbalance**	
Country	**Limit**	**Time**	**Country**	**Limit**	**Time**	**Standard**	**Limit**
China, Denmark	20 %	0.625s, 0.5s	China, Japan, UK, Canada, and Romania	Not mandatory		IEEE	3%
Japan	20 %	1.0s	USA	120%	1.0s		
USA, Romania	15 %	0.6s	Denmark, Germany	120%	0.1s	IEC	2%
UK	15 %	0.14s	Spain	130%	0.25s		

Frequency							
Country	**Nominal frequency**	**Frequency variation**		**Country**	**Nominal frequency**	**Frequency variation**	
		Min.	**Max.**			**Min.**	**Max.**
China	50 Hz	49.5 Hz	50.2 Hz	Canada	60 Hz	59.4 Hz	60.6 Hz
UK	50 Hz	49.5 Hz	50.0 Hz	USA	60 Hz	58.5 Hz	61 Hz
Bangladesh	50 Hz	49.5 Hz	50.5Hz	West of Japan	60 Hz	58 Hz	61.8 Hz

THD						
	Voltage level	**Standards**	**Limit**		**Standards**	**Limit**
Voltage	(V >161) kV	IEC and IEEE 519	1.5%	Current	IEC 61000-3-2	5%
	(69 ≤ V ≤ 161) kV	IEC and IEEE 519	2.5%			
	(2.3 ≤ V ≤ 69) kV	IEC	5%			
	(1 ≤ V ≤ 69) kV	IEEE 519	5%		IEEE 1547	5%
	(V ≤ 1) kV	IEEE 519	8%			

Both passive filters (L, LC, and LCL) [120] and active filters (series and shunt) [121] can be utilized to create low-impedance routes for harmonics in order to minimize harmonics and enhance the MG system's power quality.

However, because the sources of the harmonics are dispersed, installing specialized filters is more expensive and does not yield very good results. Therefore, in order to reduce the harmonics in MGs without incurring additional costs, harmonic mitigation has been included in the interface converters' control strategies. In order to mitigate voltage distortion, the controller gain is increased to lower the output impedance at the harmonic orders. Deadbeat controllers (DBC) [122], resonant controllers (RSC) [123], and repetitive controllers (RC) [124] in the feedback loops are the most popular controllers to improve system power quality by mitigating harmonics. These controllers can be implemented based on operating modes, such as grid-connected and islanded, and control methods, such as current control method (CCM), voltage control method (VCM), and hybrid control method (HCM) [125]. The converter with CCM functions as a current source due to the high impedances at the fundamental frequency, and it is mostly convenient in on-grid mode. An advanced CCM with PI and a repetitive controller for the on-grid operation of DG to flow sinusoidal current into the main grid regardless of voltage distortion and nonlinear loads is proposed in [126]. The harmonic compensation in VCM is based on voltage and frequency references from the virtual synchronous generator controller and droop controller, and this method is functional in both off-grid and on-grid modes. A coordinated control strategy is proposed in [127] for harmonics compensation in off-grid MGs using VCM. With the parallel control framework, the HCM can regulate the converter's output voltage and current simultaneously [128]. The harmonic performance of the converter is also affected by the control delay, lower sampling rate, parameters of the controllers, and droop coefficient. In droop-based control techniques, the process of tuning the droop coefficient for proper power sharing can cause the system to experience harmonic problems prior to the instability. The impacts of droop coefficient variation on the MG's stability and power quality (THD and voltage flicker) are analysed in [129] using a bifurcation analysis approach.

Voltage sag (dip) is a short reduction in voltage magnitude due to the fast injection of load currents and faults. Swell is the opposite of sag and occurs due to the fast removal of load currents. In [117], it is observed that the sag result is 12.5% and the swell result is 2.9% with a proposed adaptive control technique. High-voltage ride-through (HVRT) and low-voltage ride-through (LVRT) are becoming prevalent in cases of voltage swell and sag with the MG integration. According to the German standard, if there is a sag event, the MGs must continue to supply reactive power to the system and remain connected, even if the voltage drops to 0% from the specified value of 0.15 s. If not, removal is mandatory [130]. The German standard uses HVRT during a swell occurrence, implying that the MG must remain connected for 0.1 seconds even if the voltage rises to 120% of its normal value; separation is required otherwise [131].

2.6.2.2 Voltage Unbalance

The voltage imbalance condition arises when there is a minimal phase shift of 120° or a difference in the three-phase voltage's magnitude. In a MG system, voltage imbalance due to the irregularity of line impedances, uneven distribution of single-phase sources, single-phase loads, and grid faults reduces power quality and can lead to equipment failure, especially power electronics device failure [132]. In addition, imbalanced situations lead to power line insulation failure, increased losses, overheating of electrical machines, overloading of transformers, capacity restrictions of power electronics devices, decreased stability, and adverse effects on converter interfaces and induction motors [133]. Therefore, it is crucial to have a balanced system. The voltage imbalance factor is a ratio of the positive to the negative sequence of voltage components to calculate the level of unbalance.

$$\text{Voltage imbalance factor} = \frac{V_+}{V_-} \times 100\% \qquad 2.7$$

$\boldsymbol{V}_-$ and $\boldsymbol{V}_+$ are the negative and positive sequence of voltage components.

Several techniques can be used to achieve imbalanced voltage compensation: passive devices, series-parallel compensators for injecting negative sequence current with a parallel converter and negative sequence voltage with a series converter, shunt active filter for injecting negative sequence current, STATCOM for injecting positive and negative sequence reactive power, and series active filter for injecting negative sequence voltage [134]. However, the interfacing converters' control strategies within the MG system can offer more effective and economical unbalanced voltage improvement. In [134], various strategies for the unbalanced elimination techniques for the IS and GC modes of operation for three-phase MGs are presented. A novel control approach for interfacing converters in networked MGs to take part in voltage imbalance compensation based on their possible capacities without exchanges of information is proposed, where all MG-coupling converters are designed separately with positive- and negative-sequence control loops [135]. A control strategy is proposed in [136] that concurrently addresses the issues of negative-sequence current sharing and negative-sequence voltage compensation in grid-operated MGs using grid-feeding inverters.

2.6.3 Operating Modes

In a networked system, each MG is made up of loads and RESs. There could be a large mismatch between the single MG's local supply and demand because of the RESs' unpredictable power generation. As a result, this phenomenon or power mismatch in individual MGs will result in a power imbalance or blackout in the networked MGs. In this case, to maintain a power balance within the networked system, any MG in the MG cluster needs to develop a connection with the main grid for exchanging electrical power [137]. The networked system should continue to function even after being disconnected from the main grid to guarantee load supply security. A MG may begin operating autonomously for one of two purposes, such as planned islanding for financial and maintenance

purposes or unplanned islanding resulting from a network breakdown that causes the main grid to collapse [138]. The DERs supplying the networked system are in charge of sharing power and preserving voltage and frequency immediately after the system has been separated. It's crucial to keep inverters from being overloaded during island operation and to make sure they handle load variations in a properly managed way [139]. As a whole, the MG must have the capability to function in both on- and off-grid modes to meet the high standards of consumers and maintain a highly consistent and flexible electrical system for the better quality of the distributed power. Static transfer switches (STS) that are based on semiconductor devices are typically used to physically link or separate the MG from the main grid.

An MG system's operational modes are presented in Fig. 2.25. The MG operates in on-grid mode with STS = ON (1) during normal operations. Nevertheless, the MG system will go to off-grid mode with STS = OFF (0) if any problems arise and the main grid's power quality falls short of the required levels for operation. Following a seamless transition from grid-connected to standalone modes, the system operates in islanded mode, offering promising availability and flexibility. To re-establish the connection between the MG system and the main grid, active synchronization is going to be initiated following the main grid's restoration. The control objectives under different modes are flexible injection and adjustment of power; smooth shift from on-grid to off-grid modes; reliable power sharing, voltage, and frequency control in autonomous mode; and shift from off-grid to on-grid modes through active synchronization for main grid connection restoration. To ensure continuous power supplies and minimize surge currents, a smooth transition between the two modes is crucial [140].

To achieve proper operation in all modes, control techniques must be implemented to allow the MG system to switch smoothly between the on- and off-grid modes and to prevent variations and oscillations in voltage, frequency,

and current caused by phase and frequency mismatches during the transition. A modified dq-based PLL is suggested in [141] for three-phase inverters to achieve a smooth mode transition. In grid-connected mode, the PLL synchronizes the phase of the load voltage with the grid voltage, and in islanded mode, it creates the desired frequency phase. A control strategy that consists of a voltage controller with a capacitor current feedback input and a current controller with a current feed-forward input, along with modified droop control, is proposed in [142]. A distributed control structure that provides flexible operation in four modes, such as on-grid, off-grid, islanding transition, and active synchronization, to achieve all the control targets related to the four modes is proposed in [79].

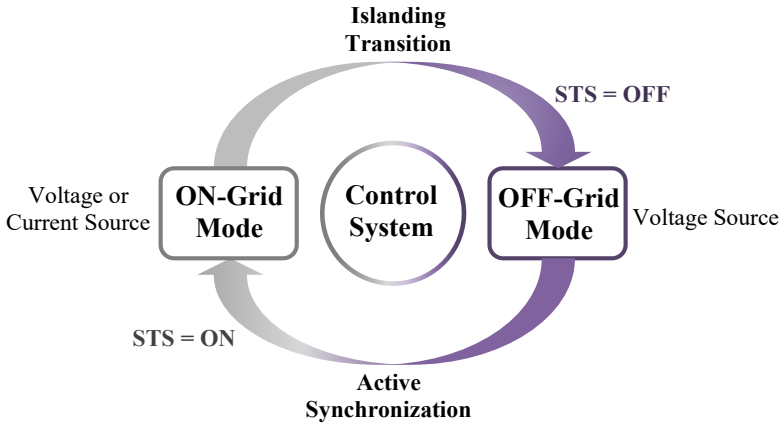

Fig. 2.25: Operating modes of a MG system.

2.7 SUMMARY

MGs need to be connected, exchange power and support the voltage and frequency of overloaded MGs to reap the full benefits, such as enhanced reliability and the incorporation of renewable energy. The analysis presented on MG cluster system infrastructure points out that architecture with various lines and interface technologies can be highly beneficial in enhancing power system resilience, reliability, and efficiency. Even though MG clusters maximize MGs' advantages and minimize their shortcomings, networked MGs still need suitable infrastructure, control techniques, and management systems to ensure desirable operation in different operating modes.

This chapter presents various interconnected MG systems based on line (AC or DC) and interface (tie-line, transformer, and converter) technologies. Considering the wide range of the AC distribution network, implementing AC interconnection in an on-grid condition is feasible. However, integration of AC MGs is challenging due to both voltage and frequency controls, control complexity, active and reactive power controls, and the requirements of frequency synchronization. Therefore, interest in DC technologies is growing due to the predominant benefits of this system, such as higher efficiency, lower losses, elimination of bulky transformers, no reactive power and synchronization requirements, improved reliability, and lower conversion stages.

More sophisticated control structures with enhanced control strategies are crucial to facilitate the control capabilities of some specific converters of DERs in each MG and the interface converters between MGs since the majority of generating sources are based on power electronic converters. Thus, robust and accurate control strategies for managing the network voltage or frequency and the output powers of the DER units are required for the MG network to operate reliably. This chapter highlights different control aspects of an interconnected MG system to address the importance of the various control objectives, such as interlinking converter control and ESS management. However, the control objectives of multiple interconnected HMGs and ESS management require significant attention to achieve reliable operation. Therefore, this thesis mainly focuses on achieving control objectives related to interconnected HMGs, such as interlinking converter control, ESS control, and clustering methods.

Several characteristics of the MG cluster system, such as stability, power quality, and mode transition, need to be addressed to improve its performance and identify possible operational constraints of the developed system.

Chapter 3

METHODOLOGY AND DESIGNING OF A DISTRIBUTED CONTROL STRUCTURE FOR NETWORKED MICROGRIDS

3.1 INTRODUCTION

Active power distribution systems are substituting passive distribution networks due to the increasing adoption of RESs and DGs, as well as the deployment of power electronic interfaces, distributed control, and bidirectional flow of power. Optimally linking AC and DC DERs and loads to corresponding MGs enhances system efficiency as a whole by lowering the overall number of power conversion steps. MGs are linked together to establish MG clusters with the purpose of utilizing cooperation to address the problems faced by individual MGs. Chapter 2 has covered a number of research pertaining to the control system and infrastructure of the MG cluster in order to guarantee dependable operation. Nevertheless, the HMG cluster is made up of numerous separate HMGs, each of which has its own AC and DC MG, making coordinated control more difficult. This is due to the fact that, in order to achieve connection and mutual support, power management between AC and DC MGs must be given preference for a single HMG. Then, it will be expected that coordinated action among nearby HMGs will be achieved in the form of clusters.

This thesis target is primarily concentrated on the MG cluster, which is made up of hybrid AC/DC MGs, regardless of different infrastructure and control methods to efficiently fulfil varying operational purposes, as suggested

in the numerous research studies described in Chapter 2. In order to configure a networked HMG system, this chapter (Chapter 3) provides modelling and analysis of the control techniques for three primary converters in the designed interconnected system. The model of each converter control strategy describes the details of the control loops.

3.2 CONFIGURATION OF NETWORKED MICROGRID

Fig. 3.1 illustrates the HMG clustering structure, which consists of two individual HMGs interconnected by parallel BDCs. Each HMG has its own RESs-based DERs, loads, converter interfaces, and control system. The power coordination between AC and DC MGs in HMG is maintained by the local controller in conjunction with the interlinking converter controller of each individual HMG. The HMG cluster's power balance is then maintained with the support of a distributed control system.

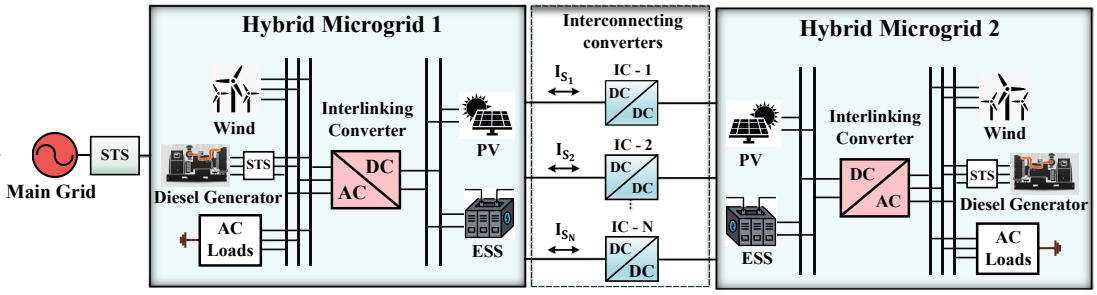

Fig. 3.1: Configuration of the networked microgrid system.

3.2.1 Configuration of Hybrid Microgrid

Each HMG comprises DGs, such as PV generators and wind generators, ESS, diesel generators, the main grid, and 3-phase AC loads. The structures of HMG-1 and HMG-2 and the associated control strategies of interlinking converters are presented in Fig. 3.2. HMG-1 operates in both islanded and grid-connected modes, and HMG-2 only operates in islanded mode. A static transfer switch (STS) is used to link HMG-1 to the main grid. Power converters, their associated controllers, and management strategies ensure suitable voltage and

frequency regulation and desired power flow in the system [143]. Each element considered in designing HMG is described in the following subsections:

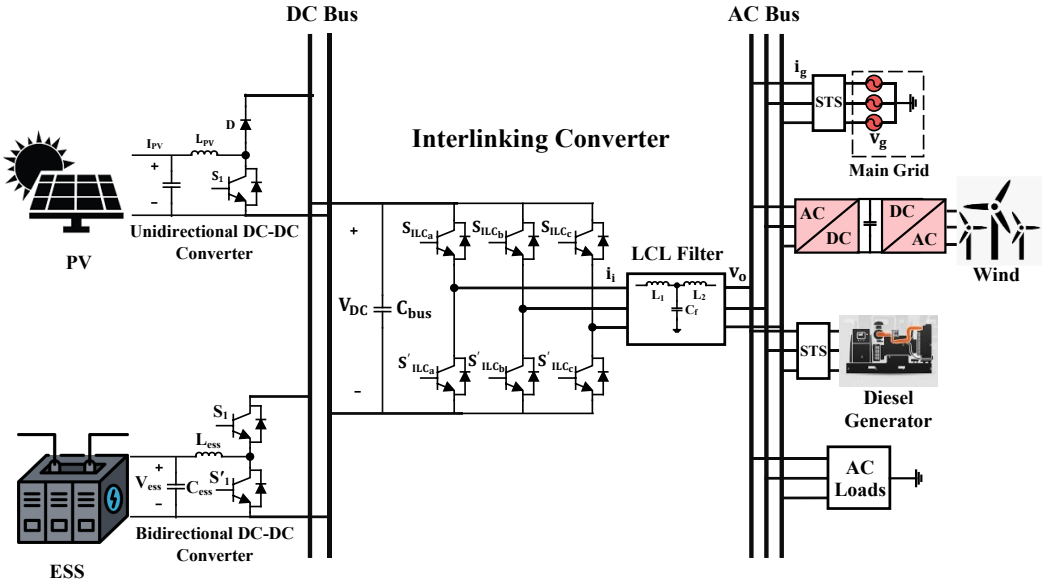

Fig. 3.2: Configuration of hybrid AC/DC microgrid.

3.2.2 Distributed Generations and Loads

DGs are designed as a current source using power converter interfaces that can inject active power into the system as required. The HMG under analysis is rated at the power specified by the DGs. Since RESs are typically preferred as the DGs, PV and wind generators are considered as the DGs. The behavior of these DGs is dependent on wind speed and solar radiation patterns.

3.2.2.1 Photovoltaic (PV) System

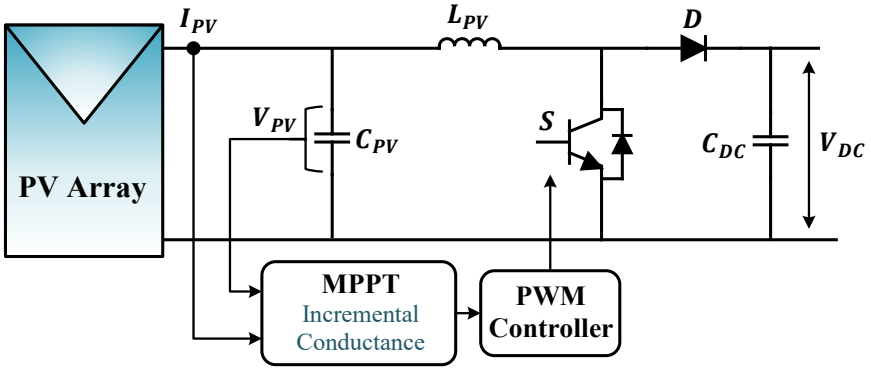

Fig. 3.3: Configuration of PV system.

The PV system is modelled as a DC source, operating with the incremental conductance-based maximum power point tracking (MPPT) algorithm [144], and connected to the DC bus using a boost converter. The PV system model is shown in Fig. 3.3. To achieve the proper DC bus voltage level and maximum power point, the boost converter is controlled according to the signal output from the MPPT.

A PV system's performance is contingent upon its operational environment. Then, three factors—irradiance, cell temperature (ambient temperature), and load profile (load impedance)—have a significant impact on the maximum power collected from the PV generator. Temperature and irradiance both affect a PV module's output I − V characteristic. The current and voltage at which a solar module generates the maximum power are known as the maximum power point (MPP). The location of the maximum power point is not known in advance due to changes in irradiance and temperature. An MPP tracking technique adjusts the output voltage of the PV to extract the maximum available power at any given change (irradiance and temperature). MPPT causes the MPP to move depending on the temperature and irradiation conditions. It is feasible to place a unidirectional DC/DC converter between the PV panel and the batteries to mitigate the adverse impacts on the output PV power and extract its maximum power. The MPPT computation system computes the power to regulate the converter input impedance by varying the duty cycle of the control signal after measuring the input and/or output voltage, current, and climatological fluctuations. The incremental conductance method consists of differentiating the PV power with respect to voltage. MPP is located when the differentiation result is zero.

$$\frac{dP_{pv}}{dV_{pv}} = \frac{d(V_{pv}I_{pv})}{dV_{pv}} = I_{pv} + V_{pv}\frac{dI_{pv}}{dV_{pv}} \tag{3.1}$$

$$\frac{I_{pv}}{V_{pv}} = -\frac{dI_{pv}}{dV_{pv}} \tag{3.2}$$

Where V_{pv} and I_{pv} PV system voltage and current. P_{pv} is the PV-generated power. Based on the circumstances given in equation 3.3, the first derivative can determine if the PV generator is running at its MPP or far from it by examining equation 3.2. The flowchart used for the incremental conductance approach is displayed in Fig. 3.4.

$$\begin{aligned} \frac{I_{pv}}{V_{pv}} &= -\frac{dI_{pv}}{dV_{pv}} \text{ at MPP} \\ \frac{I_{pv}}{V_{pv}} &< -\frac{dI_{pv}}{dV_{pv}} \text{ left to MPP} \\ \frac{I_{pv}}{V_{pv}} &> -\frac{dI_{pv}}{dV_{pv}} \text{ right to MPP} \end{aligned} \qquad 3.3$$

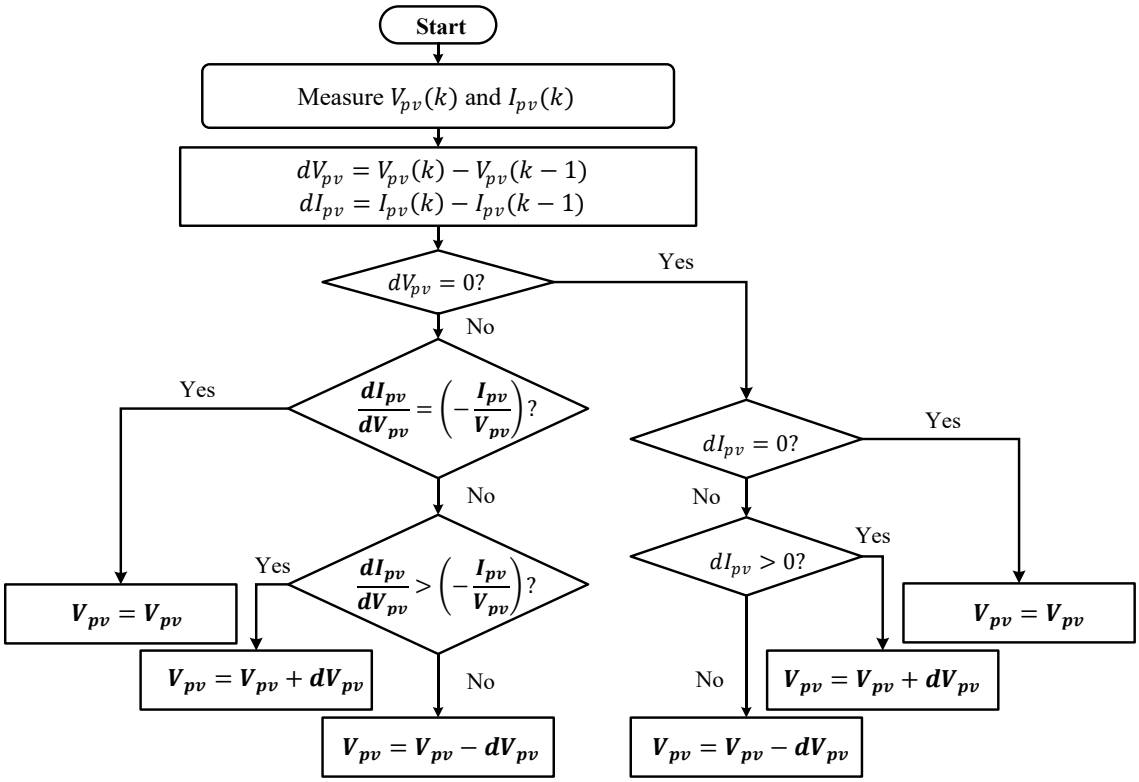

Fig. 3.4: Flowchart of incremental conductance method [145].

Table 3.1 illustrates the control and DC/DC converter parameters of the PV system.

3.2.2.2 Wind Generator

The wind generator is modelled as an AC source and connected to the AC bus using a BTB converter, as shown in Fig. 3.5. The wind generator consists of a

variable-speed doubly-fed induction generator (DFIG) with two VSCs connected to the rotor and stator [146]. The rotor-side converter helps in achieving the MPPT of the wind turbine using flux-oriented vector control. The d-coordinate is based on the stator flux estimator, and both reactive power and terminal voltage are controlled in the q-coordinate. The grid-side converter regulates DG power generation by controlling the DC-link voltage of the BTB converter. In the grid-side converter control loops, the d-coordinate regulates the DC-link voltage, and the q-coordinate maintains the unity power factor by keeping the reactive current reference zero.

Table 3.1: Control and management parameters of photovoltaic system.

Parameters		**Symbols**	**Values**
DC bus Voltage		V_{DC}	800V
Sampling Time		T_s	50μs
Inductance		L_{PV}	0.5mH
Capacitance		C_{PV}	3.5mF
Switching Frequency		f_{sw}^{pv}	2.5kHz
PV Array	Parallel strings		10
	Series-connected modules per string		22
	Temperature	T	25°C
Voltage PI Controller	Proportional Gain	k_{pv}^{pv}	0.5
	Integral Gain	k_{iv}^{pv}	0.1

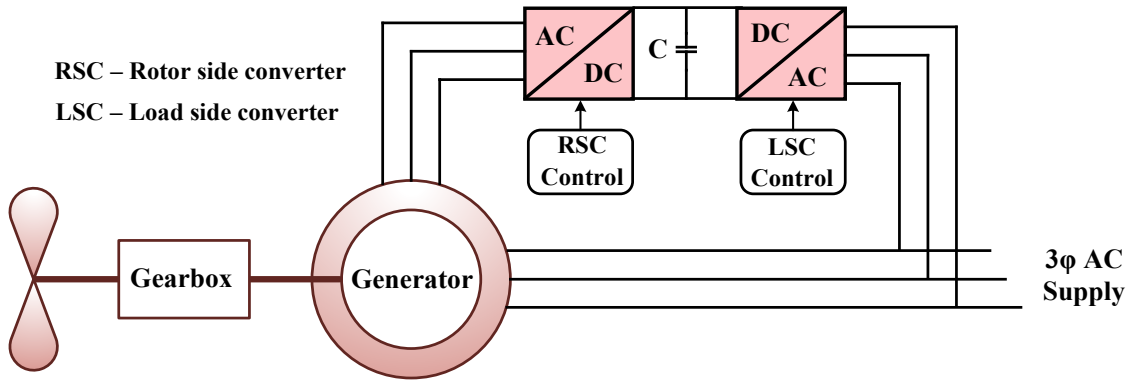

Fig. 3.5: Configuration of doubly-fed induction generator.

Table 3.2 illustrates the control and back-to-back converter parameters of the DFIG system.

Table 3.2: Control and management parameters of wind generator system.

Parameters			Symbols	Values
DC bus Voltage			V_{DC}^{WG}	700V
DC bus Capacitance			C_{DC}^{WG}	5mF
Sampling Time			T_s	50µs
Inductance			L_{WG}	6mH
Switching Frequency		Rotor-side converter	$f_{sw_R}^{WG}$	1620Hz
		Grid-side converter	$f_{sw_G}^{WG}$	2700Hz
Rotor-side converter	Speed regulator	Proportional Gain		200
		Integral Gain		0.1
	Current PI Controller	Proportional Gain		5
		Integral Gain		900
	Reactive power and voltage regulator	Proportional Gain		0.05
		Integral Gain		5
Grid-side Converter	DC bus voltage controller	Proportional Gain		1
		Integral Gain		5
	Current PI Controller	Proportional Gain		20
		Integral Gain		500

3.2.2.3 Diesel Generator

Diesel generators are typically used as backup sources in islanded mode and connected to the AC bus as an AC source. In this study, it should only be activated when the power shortage cannot be compensated by other DGs and ESSs in islanded mode and it is unable to respond to an overall power surplus. It does not operate in grid-connected mode.

3.2.2.4 Energy Storage System (ESS)

A 360V battery bank-based ESS is connected to the DC bus using a BDC that enables both charging and discharging. The battery bank capacity, SoC, and proposed PMS control the ESS's behavior, and their rated power is 30kW. In islanded mode, the ESS charges and discharges according to the load requirements. In grid-connected mode, when the ESSs are fully charged (SoC ≥ 90%), the DGs surplus power from both HMGs has to run into the main grid, as the ESSs are unable to absorb this energy. In contrast, if the lower SoC level (SoC ≤ 20%) is reached, the ESS must stop injecting power, and the main grid begins to serve the load demands beside the DGs.

3.2.2.5 AC Main Grid

A balanced 3-phase, 50Hz, 220V_{rms} line-to-line utility grid coupled with an AC bus is employed in this study to perform the GC mode. In an AC grid, each voltage source signifies a phase, with 120◦ of phase-shift between each phase, in the positive sequence. The PMS used in this study forces the AC grid to act only as a backup system, while the ESS must guarantee the power flow for the DG and load variations.

3.2.2.6 Loads

Devices that consume active and reactive power are referred to as loads. Load demand is met by the power generation available in the interconnected MG system at any instant. Both constant impedance loads (CILs) and dynamic loads, such as induction motors, are used to perform the analysis. Sets of impedance made up of balanced 3-phase resistors and inductors (RL) connected in series or parallel indicate CILs.

3.3 INTERLINKING CONVERTER OF HYBRID MICROGRID

The interlinking converter combines the AC and DC MGs in the HMG structure. In order to provide several control features, including power supply between MGs, power quality enhancement, and smooth mode change, the interlinking converter is an essential connecting technology [147]. An approach to decentralized control for both HMGs is presented in this work. The converter and control parameters of the interlinking converter are listed in Table 3.3.

The droop control approach permits the MG to transit between grid-connected and islanded modes flexibly and conveniently while facilitating the "plug and play" feature of DG and loads. For the interlink converter, the suggested technique employs $V - f$ droop characteristics (in Fig. 3.6) to achieve universal power sharing between the DC and AC MGs. The adjustment of each HMG's frequency is specifically done as an individual linear function of the output voltage of each HMG. The interlinking controller allows the controller to

function in on-grid mode as well by adjusting the difference in the AC bus voltage based on the variations in the DC bus voltage.

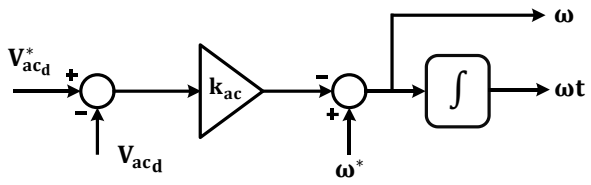

Fig. 3.6: Configuration of the proposed $\boldsymbol{V-f}$ droop.

Table 3.3: Control parameters of interlinking converter of both hybrid microgrids.

Parameters		**Symbols**	**Values**
Nominal RMS Phase Voltage		v_{rms}	220V
Nominal Frequency		f	50Hz
Sampling Time		T_s	50μs
LCL Filter	Load-side Inductance	L_1	0.5mH
	VSC-side Inductance	L_2	6mH
	Filter Capacitor	C_f	8μF
	Active Damping	k	20
Droop Coefficient		k_{ac}	0.0001
Switching Frequency		f_{sw}^{ilc}	5.1kHz
Proportional Gain		k_{ilc}	0.001
Current PI Controller	Proportional Gain	$k_{p_{I_{dq}}}$	60
	Integral Gain	$k_{i_{I_{dq}}}$	200
AC Voltage PI Controller	Proportional Gain	$k_{p_{v_{ac}}}$	0.45
	Integral Gain	$k_{i_{v_{ac}}}$	5
DC Voltage PI Controller	Proportional Gain	$k_{p_{V_{dc}}}$	350
	Integral Gain	$k_{i_{V_{dc}}}$	45

The proposed control strategy of HMG's interlinking converter, as shown in Fig. 3.7, consists of an inner current loop and a unique voltage loop with dual voltage controllers (DC and AC voltage controllers) in the synchronous reference frame (SRF). The converter is controlled as a voltage source by the outer voltage and inner current loops in both grid-connected and islanding operations. However, the voltage loop of the HMG-2's interlinking converter control only consists of the AC voltage controller shown in Fig. 3.8. As a result, this HMG can only operate in islanded mode.

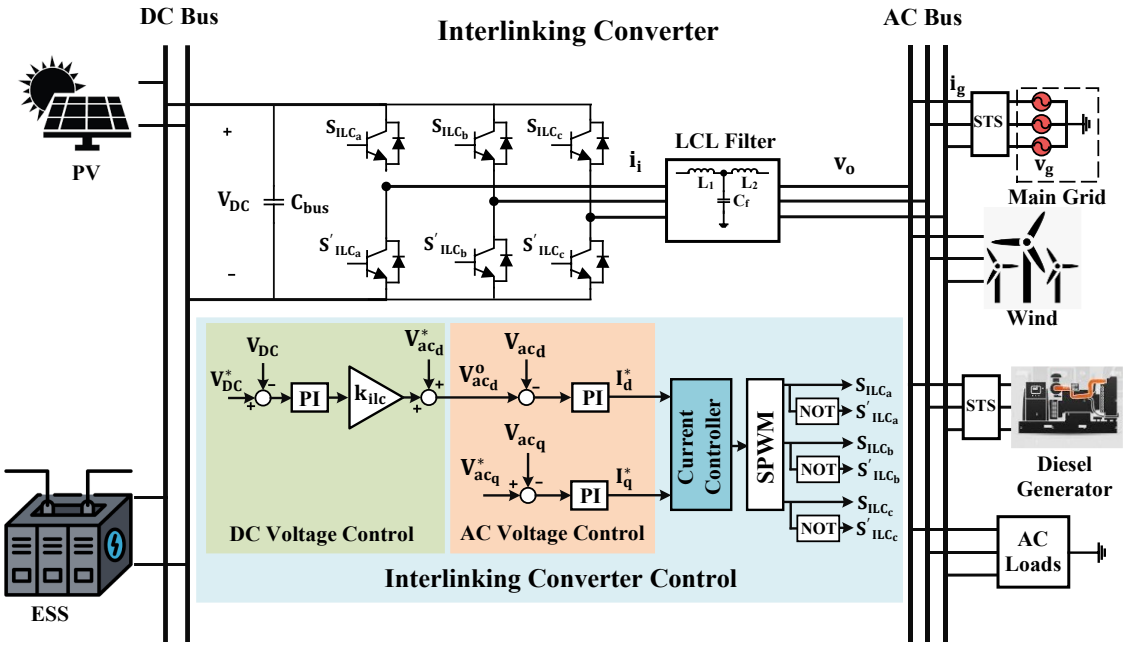

Fig. 3.7: Configuration of HMG-1's interlinking converter control.

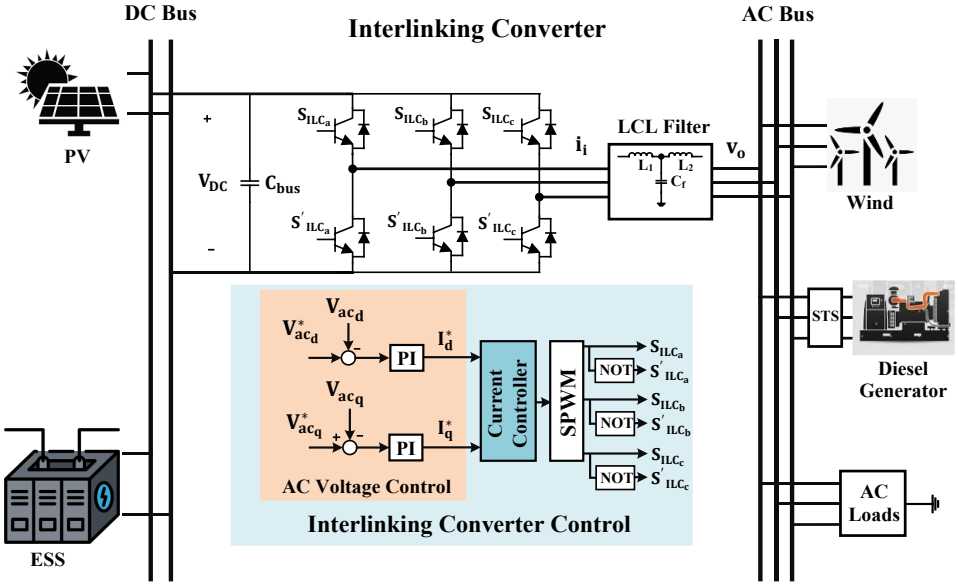

Fig. 3.8: Configuration of HMG-2's interlinking converter control.

The HMG-1 can function in both on-grid and off-grid modes in a steady state. In grid-tied mode, an STS connects the HMG-1's AC bus to the main grid so that power can be exchanged as needed. The switch can be employed to separate the HMG-1 from the utility grid in the event of any faults in the main grid or MG. Since the main grid is not accessible to absorb excess power and provide power deficiencies, the HMG-1, along with the whole networked system,

is operating in independent mode, maintaining an extremely tight balance between supply and demand.

3.3.1 LCL Filter with Active Damping

The challenges associated with the harmonic content have made the development of a stable and effective converter extremely challenging. The power quality and stability of the MG system are negatively impacted by this harmonic content [148]. As a result, the power generated and converted in the MG systems must adhere to grid rules and fulfill all relevant national and international standards for efficiency and dependability. Various types of filters, such as L, LC, and LCL filters, are used to eliminate the harmonic content. When compared to LCL-filtered VSC, L-filtered VSC has substantial weight and volume as well as higher costs, loss, and inductor value [149, 150]. Therefore, the LCL filter is used in high-power, low-frequency systems to smooth the converter's output current by lowering current ripple with lower inductor values [151, 152]. Nevertheless, the LCL filter's complex conjugate resonance poles lessen the system's effectiveness. The LCL filter's inherent resonance effect causes the exceptionally low impedance at resonance frequencies to allow even low voltages to produce currents of very large magnitudes [153]. This can make it challenging for the converter system to achieve closed-loop stability due to the possible fluctuation in resonance frequency.

Passive damping and active damping techniques are used to reduce the high-order filters' resonance problem [154]. Because of the significant power loss, resistor-based passive dampening is not suitable for high-power applications [155]. Therefore, in order to prevent further power losses and boost system reliability, an active damping strategy (in Fig. 3.9) is employed in this study. Usually, active damping can be achieved by replacing the physical damping resistor with a virtual gain in the current controller using the voltage or current of the filter capacitor feedback [156-158]. In practice, using a current sensor

instead of a voltage sensor for high-power commercial applications can cost more. Furthermore, because of the filter capacitor's extreme low magnitude and noise sensitivity, measuring its current can be difficult. In reality, it is challenging for any current sensor to precisely detect such low-magnitude current components since a lower filter capacitor value produces low-magnitude current. To address these issues with the direct capacitor current feedback method, an observer-based active damping strategy is used.

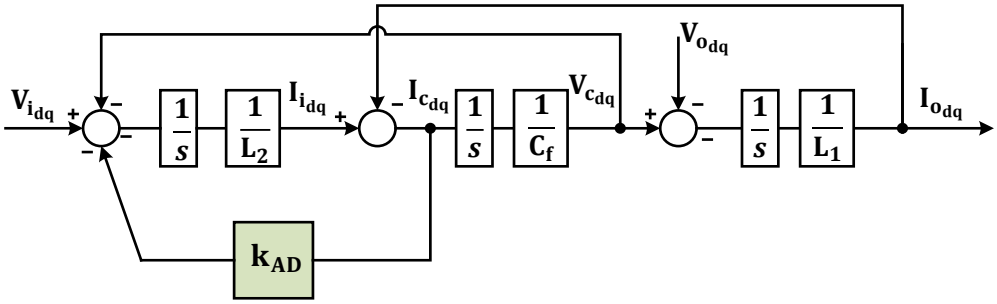

Fig. 3.9: Block diagram of the LCL filter with active damping.

Using a state observer (Luenberger observer), the suggested technique used in this study estimates the capacitor current from the capacitor voltage. To accomplish active damping, the predicted capacitor current is then connected to the current controller. In order to reduce the resonance effects of the LCL filter and enhance system stability, observer-based active damping is taken into consideration in this study rather than direct capacitor current feedback active damping. Using a Luenberger observer, one can measure the capacitor voltage and use that information to estimate the capacitor current in order to execute active damping. Equation 3.4 represents the state-space model of the LCL filter in the interlinking converter.

$$\dot{x} = Ax + Bu$$
$$y = Cx \qquad 3.4$$

Here,

$$A = \begin{bmatrix} -\frac{1}{L_2} & -\frac{1}{L_2} & 0 \\ \frac{1}{C_f} & 0 & -\frac{1}{C_f} \\ 0 & \frac{1}{L_1} & -\frac{1}{L_1} \end{bmatrix} \qquad B = \begin{bmatrix} \frac{1}{L_2} & 0 & 0 \\ 0 & -\frac{1}{L_1} & 0 \\ 0 & 0 & 0 \end{bmatrix} = [B_{v_i} \quad B_{v_o} \quad 0]$$

$$x = \begin{bmatrix} I_i \\ V_c \\ I_o \end{bmatrix} \qquad u = \begin{bmatrix} V_i \\ V_o \\ 0 \end{bmatrix}$$

x is the state vector with three state variables (I_i, V_c, I_o), where I_o and I_i are the output-side and converter-side currents, and V_c is the voltage across the filter capacitor. u is the system's input vector with two variables (V_i, V_o). A is the system or state matrix, B the input matrix, and C the output matrix of the system. As capacitor voltage is considered to estimate the filter capacitor current, the output matrix for the capacitor voltage is $C = [0 \quad 1 \quad 0]$. In particular, the output of the observer is multiplied by a matrix L after being subtracted from the output of the primary plant model in order to build the Luenberger observer.

$$\begin{gathered} \dot{\hat{x}} = A\hat{x} + Bu + L\{y - \hat{y}\} \\ \Rightarrow \dot{\hat{x}} = A\hat{x} + Bu + LC\{x - \hat{x}\} \\ \hat{y} = C\hat{x} \end{gathered} \tag{3.5}$$

Here, $L = [l_1 \quad l_2 \quad l_3]^T = \left[0 \quad \frac{C_f}{nT_s} \quad 0\right]^T$. L denotes observer feedback gain matrix, while $C = [0 \quad 1 \quad 0]$ signifies measured states vector (in this study, grid voltage and capacitor voltage). In matrix L, only the value of element l_2 is considered; as the significance of the other elements can be neglected. With equation 3.6, the dynamic of the estimation error ($e = (x - \hat{x})$) is,

$$\begin{gathered} \dot{e} = (\dot{x} - \dot{\hat{x}}) \\ \Rightarrow \dot{e} = (A - LC)(x - \hat{x}) \\ \Rightarrow \dot{e} = \hat{A}(x - \hat{x}) \end{gathered} \tag{3.6}$$

The Luenberger observer is asymptotically stable when the matrix ($\hat{A}$ in continuous-time) has all the eigenvalues on the left-side of the s plane. Moreover, the eigenvalues (poles) of the matrix ($\hat{A}$) can be selected randomly by proper

selection of the observer gain L as the system is observable. Fig. 3.10 shows the active damping using capacitor current feedback, in which capacitor current is measured using an observer, and it provides great damping capability. In this method, a closed-loop Luenberger observer is used to estimate states in advance, and then the anticipated filter capacitor current is employed to attain damping.

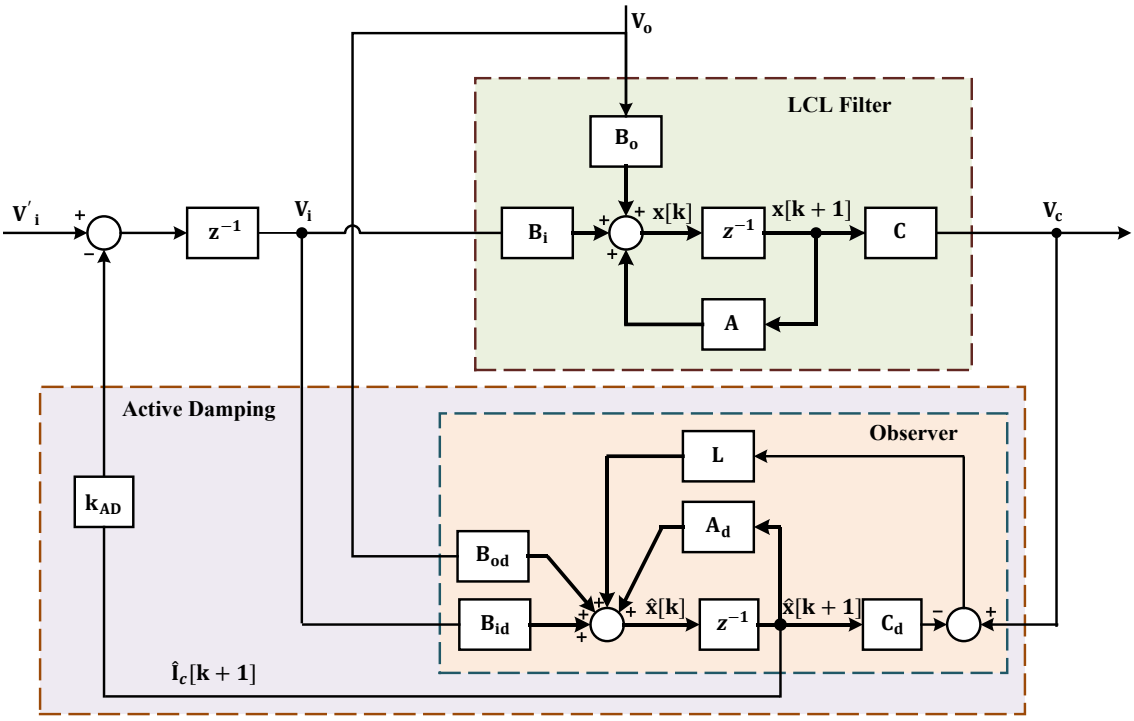

Fig. 3.10: An observer-based active damping utilizing estimated state as feedback.

3.4 ENERGY STORAGE SYSTEM CONTROL AND MANAGEMENT

The crucial function of ESS, which is dependent on DC-bus controls and frequency tracking in the MG, is a difficult task that necessitates appropriate control and management techniques to guarantee reliable performance. Power electronic converters with extremely low inertia make the entire MG vulnerable during transient conditions because low inertia causes a quick response [159]. In this instance, some inertia is introduced to the ESS controller to handle fluctuations in power flow and avoid abrupt charging or discharging, allowing the ESS in each HMG to run independently in grid-connected mode. The ESS power management includes a virtual inertia model with grid current

feedforward to enhance the ESS's dynamic response in on-grid mode. The transfer function of the considered virtual inertia model is given by:

$$G_{JD}(s) = \frac{1}{Js + D} \quad 3.7$$

The inertia coefficient (J) improves the ESS's response time during transitions or transients. This parameter delays the ESS response time and prevents the ESS from undergoing undesirable charging or discharging processes. The ESS's ability to supply or absorb power is limited or increased by the damping coefficient (D), which functions as a droop factor. The control and management parameters of ESS are given in Table 3.4.

Table 3.4: Control and management parameters of energy storage system.

Parameters		**Symbols**	**Values**
DC bus Voltage		V_{DC}	800V
Sampling Time		T_s	50µs
Inductance		L_{ess}	10mH
Capacitance		C_{ess}	500µF
Energy Storage System	Capacity		84Ah
	Nominal Voltage		12V
	No of Batteries in Series		30
	State-of-Charge		10%≤SoC≤90%
	Active Power limit		30kW
Gain related to the Grid power		k_1	4.5
Gain related to the Sharing power		k_2	1.5
Low Pass Filter of Grid Power		ω_1	4
Low Pass Filter of Sharing Power		ω_2	5
Switching Frequency		f_{sw}^{ess}	3kHz
Inertia Parameters	Inertia Coefficient	J	4.5
	Damping Factor	D	1
Current PI Controller	Proportional Gain	$k_{p_I}^{ess}$	1
	Integral Gain	$k_{i_I}^{ess}$	2
DC Voltage PI Controller	Proportional Gain	$k_{p_V}^{ess}$	40
	Integral Gain	$k_{i_V}^{ess}$	15

Fig. 3.11 illustrates the ESS control strategy. The ESS power management block generates the necessary ESS current reference for the inner current controller. This management block mainly generates the power difference from DC bus voltage error, grid current, and sharing current to generate the required

ESS power. The block associated with grid current feedforward is only operated in on-grid mode and balances ESS power. k_1 and k_2 are the coefficients associated with grid power and sharing power that convert total power error into equivalent ESS power to ensure proper power management of ESS.

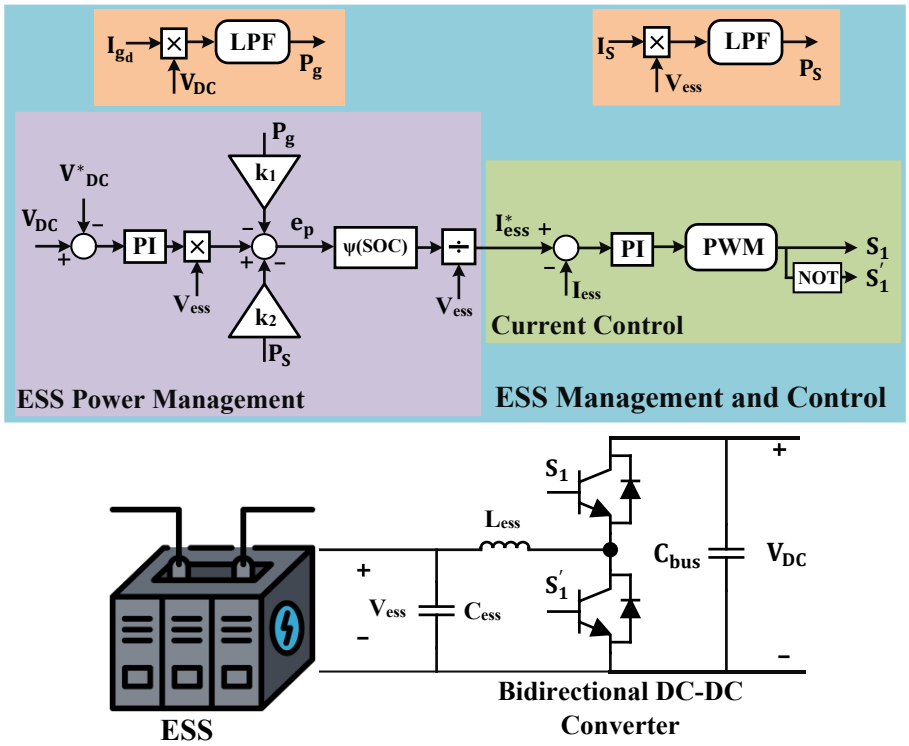

Fig. 3.11: Configuration of storage system control.

The proposed ESS system makes extensive use of the battery bank; hence, prolonging the battery bank's life requires effective management and control of the ESS power. The SoC represents the battery-based ESS's available capacity.

The ESS initiates discharging mode if the power difference (e_p) is negative. The ESS must be able to supply the power imbalance between the DG's generated power and the power consumed by the load in the discharging mode. Until a certain SoC ($SoC_d = 20\%$) is reached, the ESS must supply the MG with the maximum amount of power available. The ESS power then starts to decrease until the lowest SoC ($SoC_{min} = 10\%$)) is attained. After the minimal SoC level (SoC_{min}) is reached, the battery bank is prohibited from providing any more power in order to prevent an undesired depth of charge.

The ESS starts to charge if there is a positive power difference. The ESS is required to absorb the excess power in the MG system while it is in charging mode. Until a predetermined SOC ($SoC_c = 80\%$) is reached, the ESS absorbs all available power. Up until the maximum permitted SoC ($SoC_{max} = 90\%$) is reached, the power passing through the ESS is then reduced. After the maximum SOC level (SoC_{min}) is reached, the ESS is not permitted to hold any extra power in order to prevent overcharging; as a result, any excess power within the MG system should be transferred into the main grid. Therefore, there are three requirements that need to be identified to maintain the SoC level of ESS.

- The ESS has the capability to handle the power imbalance in a network system while the SoC level stays in condition I, that is, 20% < SoC < 80%. In this scenario, the ESS is supposed to charge or discharge without constraint.
- The case where the SoC hits 80% and stays below 90% is referred to as Condition II. Under these conditions, the ESS charging rate starts to decrease from the SoC level of 80% and becomes zero when the SOC level reaches 90%.
- The third condition states that the SoC decreases to 20% and stays above 10%. The ESS discharging rate in this scenario begins to drop at the 20% SoC level and stops when the SOC level approaches 10%.

Batteries are prone to exhibit overcharging or over-discharging behaviour when the SoC value reaches conditions II or III if no measure is initiated. Therefore, the main grid or other adjacent MGs in the cluster must compensate for any excess or deficiency of power that is required for charging or discharging.

To ensure the safety of the ESS life span, the following SoC management function, $\psi(SOC)$ is developed based on the three SoC conditions and charging or discharging modes [38, 42].

In charging mode,

$$\psi(SOC) = \begin{cases} 1 & SoC \leq SoC_c \\ \dfrac{(SoC - SoC_{max}}{SoC_{max} - SoC_c} & SoC_c < SoC < SoC_{max} \\ 0 & SoC \geq SoC_{max} \end{cases} \quad 3.8$$

In discharging mode,

$$\psi(SOC) = \begin{cases} 0 & SoC \leq SoC_{min} \\ \dfrac{SoC - SoC_{min}}{SoC_d - SoC_{min}} & SoC_{min} < SoC < SoC_d \\ 1 & SoC \geq SoC_d \end{cases} \quad 3.9$$

3.5 CLUSTERING METHOD

The configuration of the clustering converter with its associated control strategy is shown in Fig. 3.12. A bidirectional cascaded buck-boost converter is used as a converter topology to connect two HMGs using their DC buses. The power-sharing is almost absent when both HMGs have enough reserve power to satisfy demand. If any HMG has a net surplus (or deficit) of power, the clustering method guarantees that power is exported to (or imported from) the nearby HMGs. The control parameters of the clustering converter are given in Table 3.5.

A voltage control unit consists of the voltage parameters of HMG-2 (DC and AC voltages), and a current control unit constitutes the control system. The voltage control unit controls the power-sharing between HMGs using a double-loop controller.

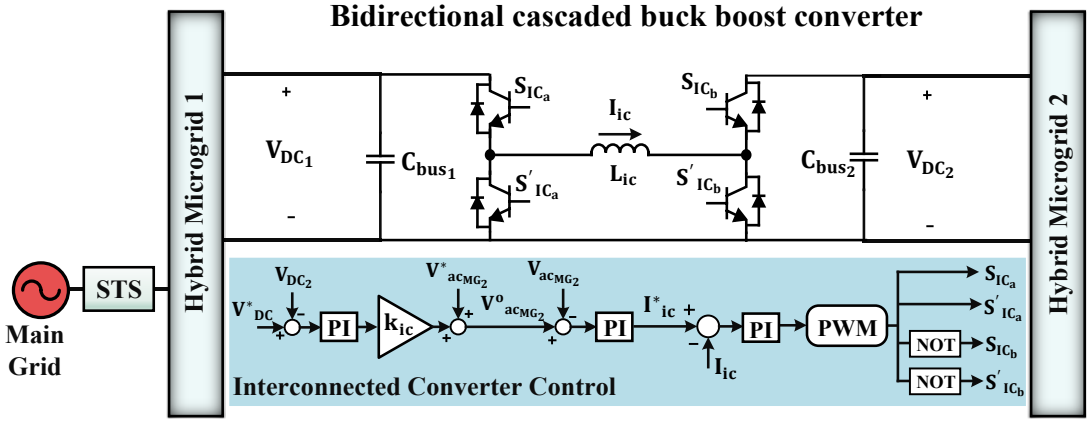

Fig. 3.12: Configuration of clustering converter control.

A power sharing-based, $\psi(P_S)$, function is used to limit the power-sharing in proportion to the converters power ratings to avoid overstressing any individual IC. In this study, three parallel ICs with a 20kW power rating are used, where IC-1 is always in function, while IC-2 and IC-3 are functional when the power exceeds the limits.

$$\psi(P_S) = \begin{cases} IC-1=1, IC-2,3=0 & |P_S| \leq 20kW \\ IC-1,2=1, IC-3=0 & |P_S| \leq 40kW \\ IC-1,2,3=1 & |P_S| \leq 60kW \end{cases} \quad 3.10$$

Table 3.5: Control parameters of clustering converter.

Parameters		**Symbols**	**Values**
DC Bus Voltage of Hybrid Microgrid-1		V_{DC_1}	800V
DC Bus Voltage of Hybrid Microgrid-2		V_{DC_2}	800V
Sampling Time		T_s	50μs
Inductance		L_{ic}	10mH
Capacitance		C_{ic}	500μF
Switching Frequency		f_{sw}^{ic}	3kHz
Proportional Gain		k_{ic}	0.01
Current PI Controller	Proportional Gain	$k_{p_I}^{ic}$	0.5
	Integral Gain	$k_{i_I}^{ic}$	1
AC Voltage PI Controller	Proportional Gain	$k_{p_{v_{ac}}}^{ic}$	0.5
	Integral Gain	$k_{i_{v_{ac}}}^{ic}$	3
DC Voltage PI Controller	Proportional Gain	$k_{p_{V_{dc}}}^{ic}$	30
	Integral Gain	$k_{i_{V_{dc}}}^{ic}$	1

3.6 SUMMARY

A promising MG cluster consisting of HMG architectures with converter interfaces, an integrated control structure, and diverse control features is configured to overcome the shortcomings of a single MG and MG cluster. The networked MG structure and control characteristics permit the development of standard MG clusters while implementing an energy network over a broader region.

The suggested control structure is based on three design concepts. The first concept concerns the two control goals of a single HMG, such as improving local

consumption and RES utilization and achieving a stable power balance between AC and DC MGs. The second premise seeks to achieve a balanced and limited ESS charging or discharging process with an ensured power supply in individual HMGs for ESS-safe operation. In order to achieve the third concept, HMGs must actively participate in the cluster's coordinated operations.

The initial control goal of the control structure is accomplished by means of an enhanced interlinking converter control method. The control technique uses a V-f-based droop control to ensure maximum utilization of RESs and proper power coordination between AC and DC MGs. Moreover, this improved droop control reduces the power calculation delay and additional sensor requirements, along with mode switch difficulties. The dual voltage control loop based on DC and AC voltage controllers ensures reliable performance in both on- and off-grid modes.

A virtual-inertia-based ESS control along with a SoC-based management function is used to realize the second concept of the proposed control system. The virtual-inertia-based concept helps to maintain the ESS charging and discharging phases in grid-connected mode, preventing abrupt or unnecessary charging or discharging. The SoC management function is implemented to avoid ESS overcharging or over-discharging by maintaining the SoC levels within certain limits.

Finally, the third control goal is achieved with the help of the converter-based clustering method. In addition to managing the excess or deficit in any HMG, this converter interface balances the power-sharing between two HMGs. Furthermore, the cluster method provides a controlled environment for power management among MGs in a networked system.

Chapter 4

PERFORMANCE ANALYSIS OF THE NETWORKED MICROGRID STRUCTURE WITH PROPOSED CONTROL SYSTEM

4.1 INTRODUCTION

The performance of the proposed distributed control structure is validated based on various factors such as load variations, source power variations or failures, ESS functionality, behaviours with dynamic loads, and mode transition using the OPAL-RT simulator-based real-time software-in-the-loop simulation technique. This chapter analyses the performance of the proposed system in both island and grid-connected modes. The power surplus and power shortage conditions are effectively analysed using both load variations and power source failures in both operating modes. The behaviour of the ESS in both HMGs in islanded, interconnected, and grid-connected modes is analysed. The behaviour of system parameters such as AC voltage, DC voltage, and frequency and power quality scenarios in terms of THD is also one of the factors in performance analysis.

4.2 PERFORMANCE ANALYSIS TOOLS

By including all required components and subsystems, the entire interconnected MG system is designed and simulated using the MATLAB/Simulink environment. Afterwards, the OPAL-RT digital platform is used to verify the feasibility of the Simulink model that was developed.

4.2.1 MATLAB/Simulink Platform

The MATLAB/Simulink environment is a suitable platform for developing simulation models of MG systems, control strategies for power electronic converters, and other physical aspects of MG-based systems utilizing the "Simscape Electrical" system. In order to verify the developed model using a real-time simulator (OPAL-RT digital platform), it is necessary to develop the model as a discrete model with an appropriate step time. For this reason, the interconnected MG model is designed with a sampling frequency of 20kHz (50μs step time).

4.2.2 Real-Time Simulation

Real-time simulation employing the OPAL-RT platform is utilized as a first step towards experimental verification. This platform, also known as real-time software-in-the-loop simulation (RT-SIL), serves to demonstrate the validity of Simulink models in real-time for both small- and large-scale systems. This means that Simulink models can be quickly transformed into real-time workshops using this technique. RT-LAB facilitates real-time validation by allowing Simulink models to communicate with the OPAL-RT platform. The experimental set-up comprises the host PC and the OPAL-RT simulator as the target, as illustrated in Fig. 4.1a, which is based at the Advance Power System Research Laboratory, Chittagong University of Engineering and Technology. The OPAL-RT platform, based on OP5600, a fully functional simulation system that can operate on Vir-Tex-6 or Spartan-3 FPGA systems, is designed to be utilized as a standard rack mount or shelf top. It operates under the Linux operating system and features four operational Intel Xeon E5 processor cores clocked at 3.2 GHz.

Fig. 4.1b illustrates the procedures of the RT-SIL simulation. The RT-LAB software (version 2019.2.3.176), which is completely integrated with MATLAB/Simulink and enables Simulink models to interface with the real environment, is the means by which the OPAL-RT platform and

MATLAB/Simulink interact with one another. As a multi-domain medium, it provides flexible and scalable alternatives for power systems and power electronics. Using the RT-LAB software, the Simulink model is loaded onto the OPAL-RT simulator, and real-time information is then transferred back to the MATLAB/Simulink environment.

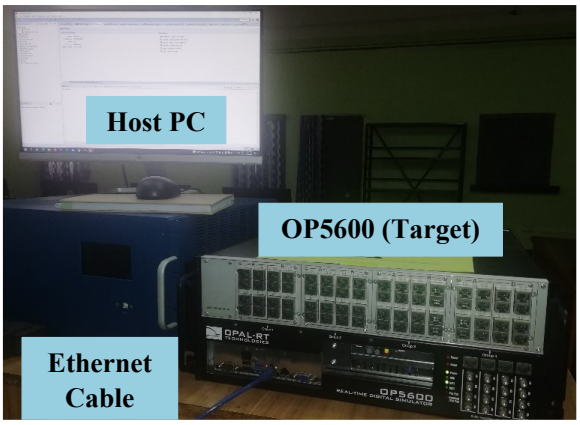

(a)

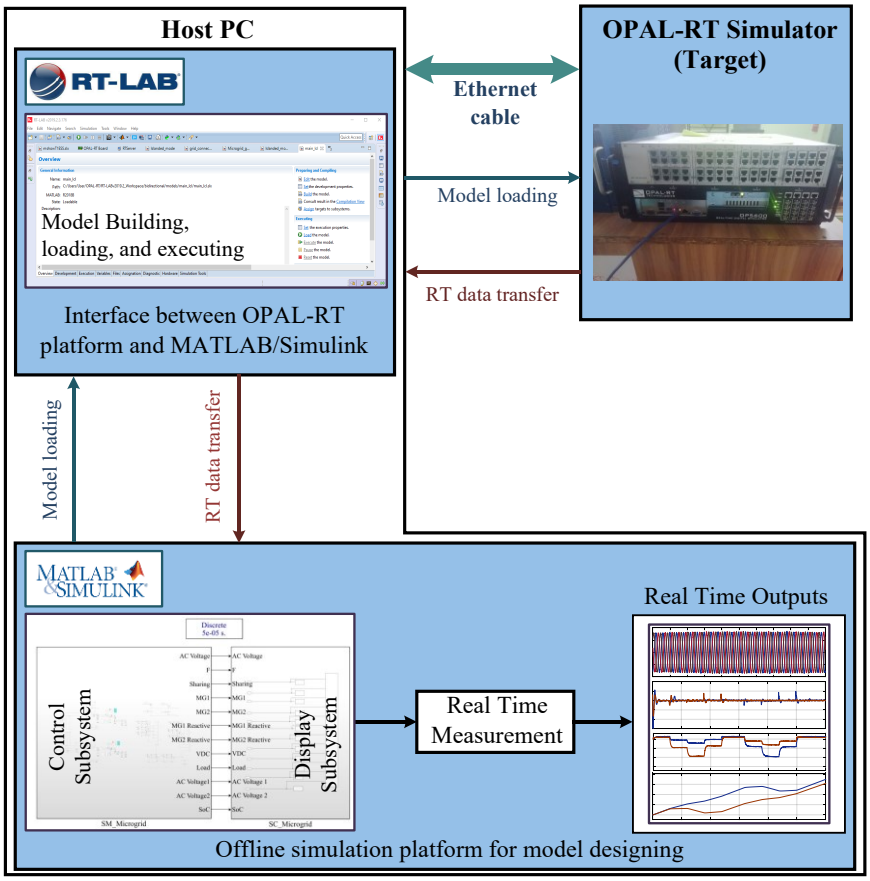

(b)

Fig. 4.1: Real-time software-in-the-loop setup: a) RT SIL setup with Ethernet cable, host PC, and OP5600 target, and b) procedure of RT SIL with the OPAL-RT digital platform.

Two subsystems are included in the Simulink model: one comprises all of the power and control parts, while the other contains display blocks. The display subsystem allows the user to see the system's behaviours while it is in operation, and the controller subsystem contains the entire model together with the suggested control structure. In order to facilitate communication between the subsystems, the OpComm blocks from the Simulink library of RT-LAB are presented. The created model is then built and compiled using RT-LAB software into executable programs, which are then loaded and executed in OP5600 on many potent processors. After loading the model and getting the real-time data, real-time waveforms can be obtained using the MATLAB/Simulink environment.

4.3 ASSUMED SOURCE GENERATION

The generation sources used in this study include PV and ESS as DC sources and wind and diesel generators as AC sources. Certain generation capacities are considered to analyse the performance of the interconnected MG system under designed control strategies. Table 4.1 lists the capacity assumption of the HMG-1 sources considered in this study:

Table 4.1: Considered generation capacity of each source in hybrid microgrid-1

Source Types	Parameters	Values
Photovoltaic generation	Maximum Power at 1000 W/m^2 and temperature 25°C	45kW
Wind Generation	Maximum Power at 15 m/s	45kW
Diesel Generator	Capacity	10kVA
Energy Storage System	Battery Type	Li-ion battery
	Nominal voltage	12V
	No. of batteries in series	30
	SoC	10%≤SoC≤90%
	Rated Capacity	30kW

Table 4.2 lists the capacity assumption of the HMG-2 sources considered in this study.

Table 4.2: Considered generation capacity of each source in hybrid microgrid-2

Source Types	Parameters	Values
Photovoltaic generation	Maximum Power at 1000 W/m² and temperature 25°C	45kW
Wind Generation	Maximum Power at 15 m/s	35kW
Diesel Generator	Capacity	5kVA
Energy Storage System	Battery Type	Li-ion battery
	Nominal voltage	12V
	No. of batteries in series	30
	SoC	10%≤SoC≤90%
	Rated Capacity	30kW

4.4 ISLANDED MODE

In islanded mode, the performance of the networked microgrid system with the proposed control system is evaluated under various load conditions and source power variations. The considered maximum generation capacity of each source is presented in Table 4.1 for HMG-1 and Table 4.2 for HMG-2.

4.4.1 Analysis Under Load Variations

For three scenarios (positive power sharing (HMG-1 to HMG-2), negative power sharing (HMG-2 to HMG-1), and almost zero or very low power sharing) with different load scenarios and no source power changes, the power flow and system performance analysis are examined in this subsection. Table 4.3 provides an overall summary of power generation, consumption, and sharing under load variations in both HMGs.

According to Fig. 4.2, all the RESs-based generation sources (PV and wind) are operating at their maximum capacity in both HMGs (45kW at 1000W/m² for PV in both HMGs; 45kW at 15m/s for wind in HMG-1; 35kW at 15m/s for wind in HMG-2). The diesel generator's output power is very low in both HMGs due to the available power supply from the RESs-based sources. Variations in load cause the wind generation to fluctuate every few intervals.

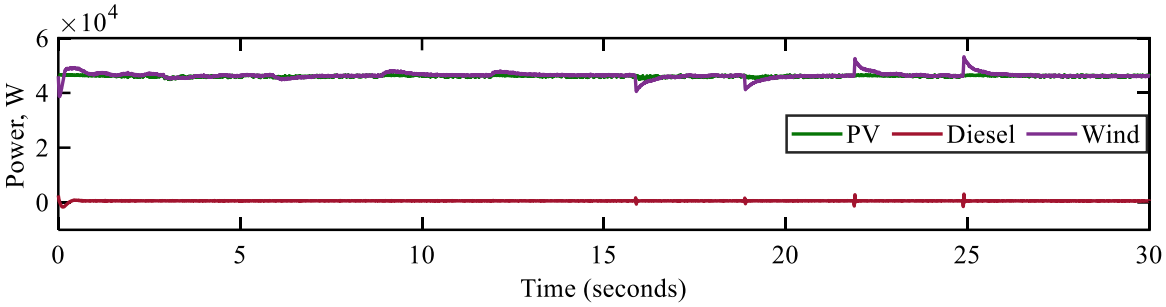

(a)

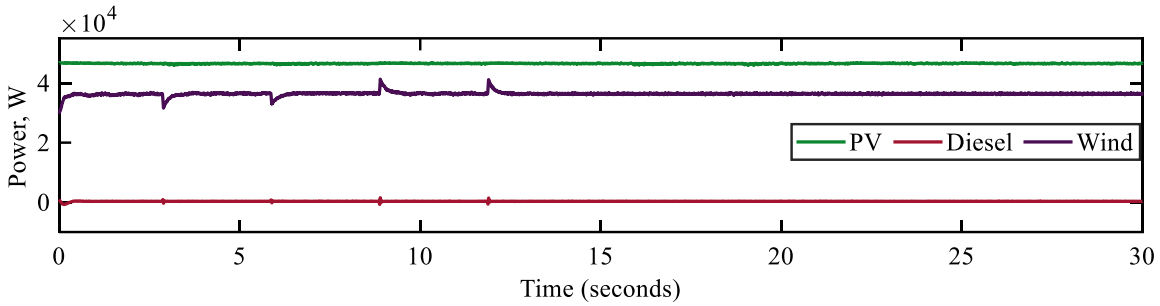

(b)

Fig. 4.2: Generation in both hybrid microgrids: a) In hybrid microgrid-1, and b) In hybrid microgrid-2.

Fig. 4.3 illustrates the reactive power management in both HMGs in islanded mode. In Fig. 4.3a, the wind generator reactive power is approximately -2.23kVAR and the reactive power support from the interlinking converter is 2.38kVAR. In Fig. 4.3b, the wind generator reactive power is approximately -2.12kVAR, and the reactive power support from the interlinking converter is 2.83kVAR. With the loads in both HMGs, the reactive power from both the wind generator and interlinking converter varies.

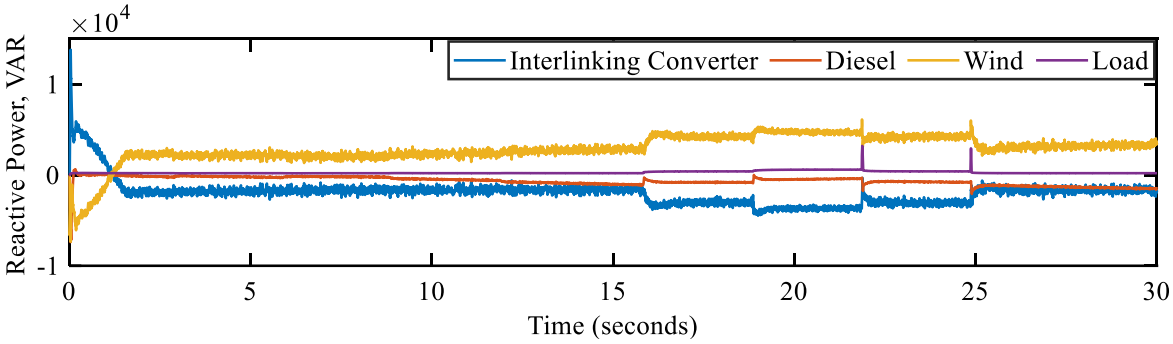

(a)

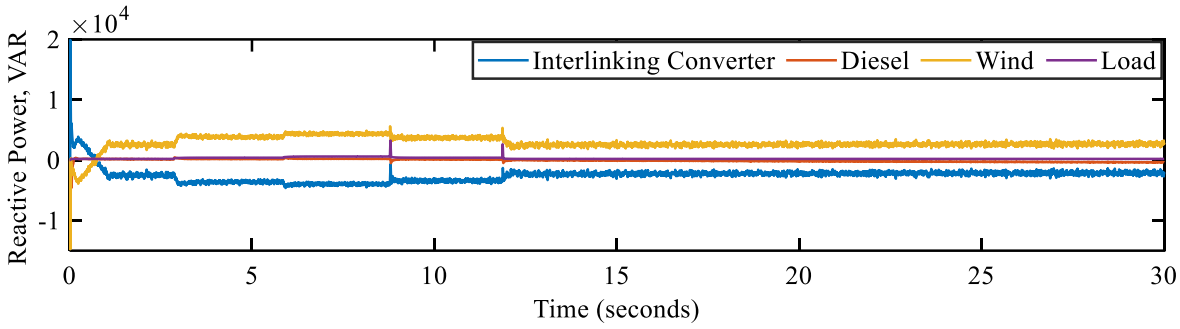

(b)

Fig. 4.3: Reactive Power in both hybrid microgrids: a) In hybrid microgrid-1, and b) In hybrid microgrid-2.

Fig. 4.4 illustrate the load scenarios in both HMGs. Initially, the loads in HMG-1 and HMG-2 are fixed at 60kW and 60kW, respectively. At t = 2.8s, a 30kW load is added to HMG-2; therefore, the demand in HMG-2 is shifted to 90kW. Again, at t = 5.8s, another 25kW load is added, and the demand becomes 115kW in HMG-2. The additional 25kW load is now reduced at t = 8.8s, and the further 30kW load is removed at t = 11.8s, bringing the total demand down to 60kW after 11.8s. From t = 0 to 15.8s, the load in HMG-1 is fixed at 65kW. However, at t = 15.8s, a 30kW load is added in HMG-1, while demand in HMG-2 is fixed at 60kW. At t = 18.8s, HMG-1 receives an additional 30kW load, increasing its total demand to 125kW. The additional loads in HMG-1 are removed at t = 21.8s and t = 24.8s, respectively, returning both HMGs to their initial demand levels.

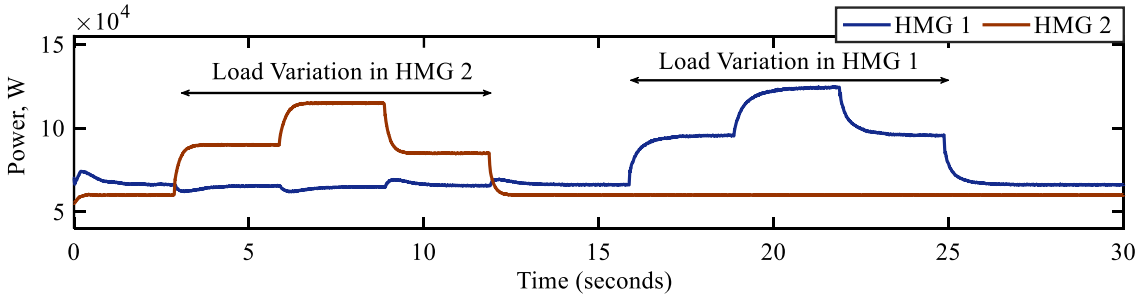

Fig. 4.4: Demand in both hybrid microgrids.

ESS power management under load variations is presented in Fig. 4.5 Initially, both ESSs are charging with 25kW and 20.9kW of power, respectively, from the available power generation from the respective HMGs. Due to the load

increment in HMG-2, the charging rate of ESS-2 decreased to 2.3kW. Another 25kW load addition at t = 5.8s leads the ESS-2 to discharge at -17.5kW (SoC level is decreasing). However, at t = 8.8s and t = 11.8s, ESS-2 starts to charge at 2.5kW and 20.9kW power due to a decrease in loads in HMG-2. The charging status of the ESS in HMG-1 is impacted by load variations in HMG-2, resulting in a drop in charging power to 13.6kW and 8.4kW at t = 2.8s and 5.8s, respectively. The ESS-1's charging power has now dropped to 2.6kW as a result of the load increase in HMG-1 at t = 15.8s, and an additional 30kW load increment at t = 21.8s leads the ESS-1 to discharge at -17.4kW (the SoC level is lowering). The charging power of ESS-2 is also reduced by load variation in HMG-1 at t = 15.8s (13.3kW) and t = 18.8s (3.3kW). When the load in each of the two HMGs is lowered to 65kW and 60 kW, respectively, both ESSs resume charging at their original rates.

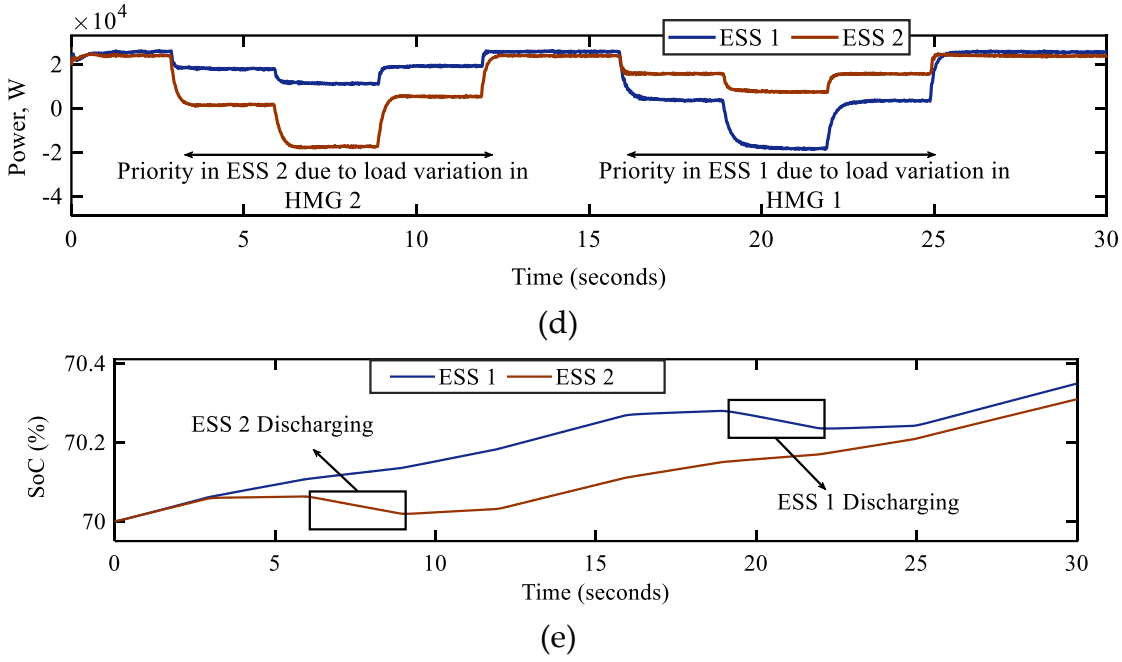

Fig. 4.5: ESS power in both hybrid microgrids: a) ESS Powers, and b) SoC levels.

The power sharing scenarios for load variations are presented in Fig. 4.6. From t = 0 to 2.8s, the sharing power is very low, which is 0.6kW due to the available power in each HMG to satisfy demand. ach HMG uses its excess power generation to charge the ESS. Due to the increase in load in HMG-2 at t = 2.8 s, a certain amount of power (12kW) is being shared from HMG-1 to HMG-2. The

sharing is taking place despite the available power in HMG-2, which reduces the burden of ESS in HMG-2 due to load increments. Because of the continued increase in load in HMG-2, more power is being shared (17.2kW) at t = 5.8s. Once more, this power sharing keeps the ESS-2 from being discharged at maximum capacity, minimizing the impact on the ESS-2's life cycle. The removal of the loads causes the sharing power to drop to 12.2kW and 0.6kW at t = 8.8s and t = 11.8s, respectively. Now, due to the load increment in HMG-1, reverse sharing takes place, which is from HMG-2 to HMG-1. These conditions similarly reduce the burden on ESS-1 and improve its life cycle. The power sharing from HMG-2 to HMG-1 is -7kW, -17kW at t = 15.8s and t = 18.8s. Due to the reduction in load, the power sharing is reduced to -7.2kW and 0.6kW at t = 21.8s and t = 24.8s.

Table 4.3: A summary of the power generation and consumption of under load variations

Time	Hybrid microgrid 1					Hybrid microgrid 2				
	DERs			ESS (kW)	Load (kW)	DERs			ESS (kW)	Load (kW)
	PV (kW)	Wind (kW)	Diesel (kW)			PV (kW)	Wind (kW)	Diesel (kW)		
0 – 2.8s	45	45	0.6	25	65	45	35	0.3	20.9	60
	Sharing Power		HMG-1 to HMG-2 – 0.6kW							
2.8 – 5.8s	45	45	0.6	13.6	65	45	35	0.3	2.3	90
	Sharing Power		HMG-1 to HMG-2 – 12kW							
5.8 – 8.8s	45	45	0.6	8.4	65	45	35	0.3	-17.5	115
	Sharing Power		HMG-1 to HMG-2 – 17.2kW							
8.8 – 11.8s	45	45	0.6	13.4	65	45	35	0.3	2.5	90
	Sharing Power		HMG-1 to HMG-2 – 12.2kW							
11.8 – 15.8s	45	45	0.6	25	65	45	35	0.3	20.9	60
	Sharing Power		HMG-1 to HMG-2 – 0.6kW							
15.8 – 18.8s	45	45	0.6	2.6	95	45	35	0.3	13.3	60
	Sharing Power		HMG-2 to HMG-1 – -7kW							
18.8 – 21.8s	45	45	0.6	-17.4	125	45	35	0.3	3.3	60
	Sharing Power		HMG-2 to HMG-1 – -17kW							
21.8 – 24.8s	45	45	0.6	2.8	95	45	35	0.3	13.1	60
	Sharing Power		HMG-2 to HMG-1 – -7.2kW							
24.8 – 30s	45	45	0.6	25	65	45	35	0.3	20.9	60
	Sharing Power		HMG-1 to HMG-2 – 0.6kW							

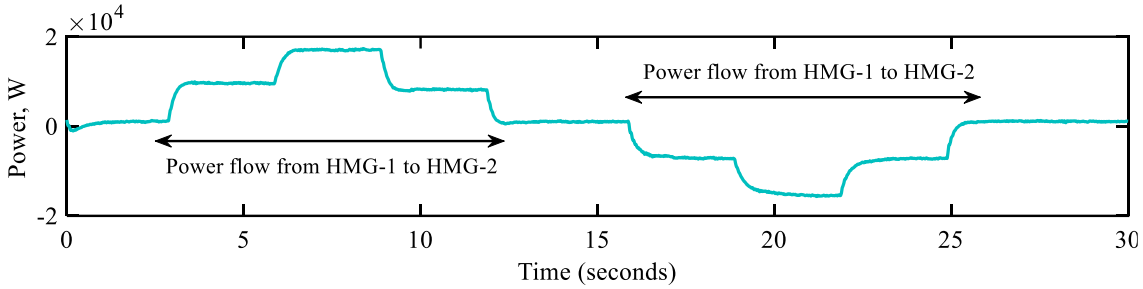

Fig. 4.6: Power sharing curve.

The performance of the networked system under load variations in terms of system voltage and frequency is illustrated in Fig. 4.7. System voltage and frequency change as a result of sudden load changes, such as for AC voltage, the change is from 220V rms to higher or lower, for DC voltage, it is from 800V to higher or lower, and for frequency, it is from 50Hz to higher or lower. Large changes in individual HMG's AC voltage and frequency occur during load changes in individual HMG, and changes in one HMG do not greatly affect another HMG's AC voltage and frequency, as shown in Fig. 4.7c and Fig. 4.7d. The frequency variation ranges due to load variations are -0.038% variation in load increment and 0.02% variation in load decrement, which is in line with IEEE Standard 1547 [160]. But the DC voltages of both HMGs change equally due to load variations.

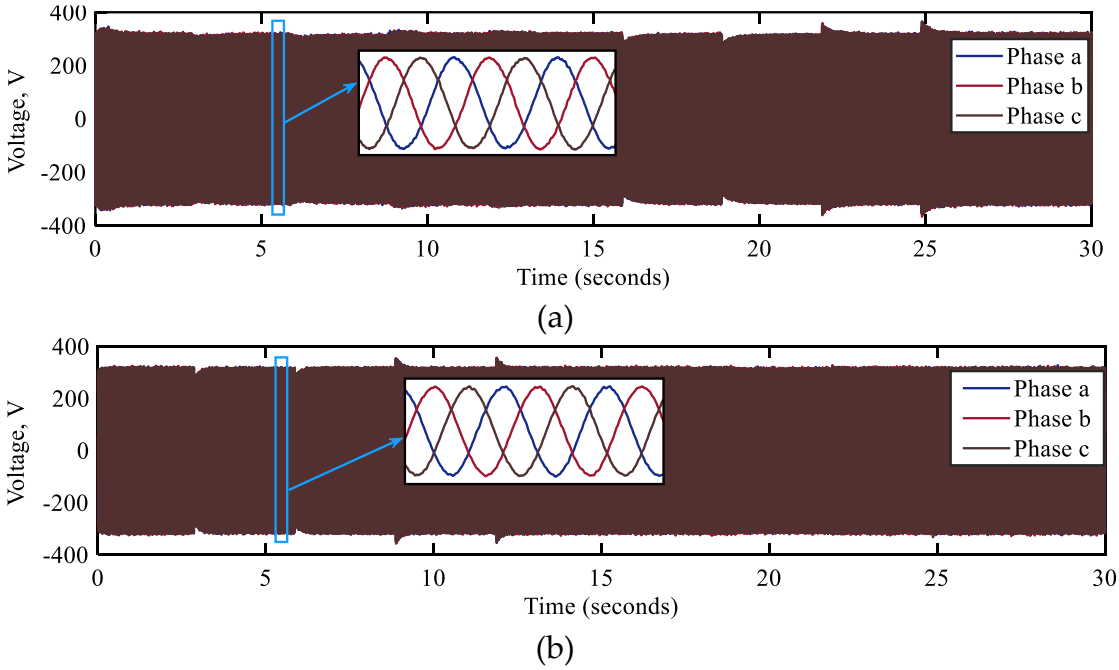

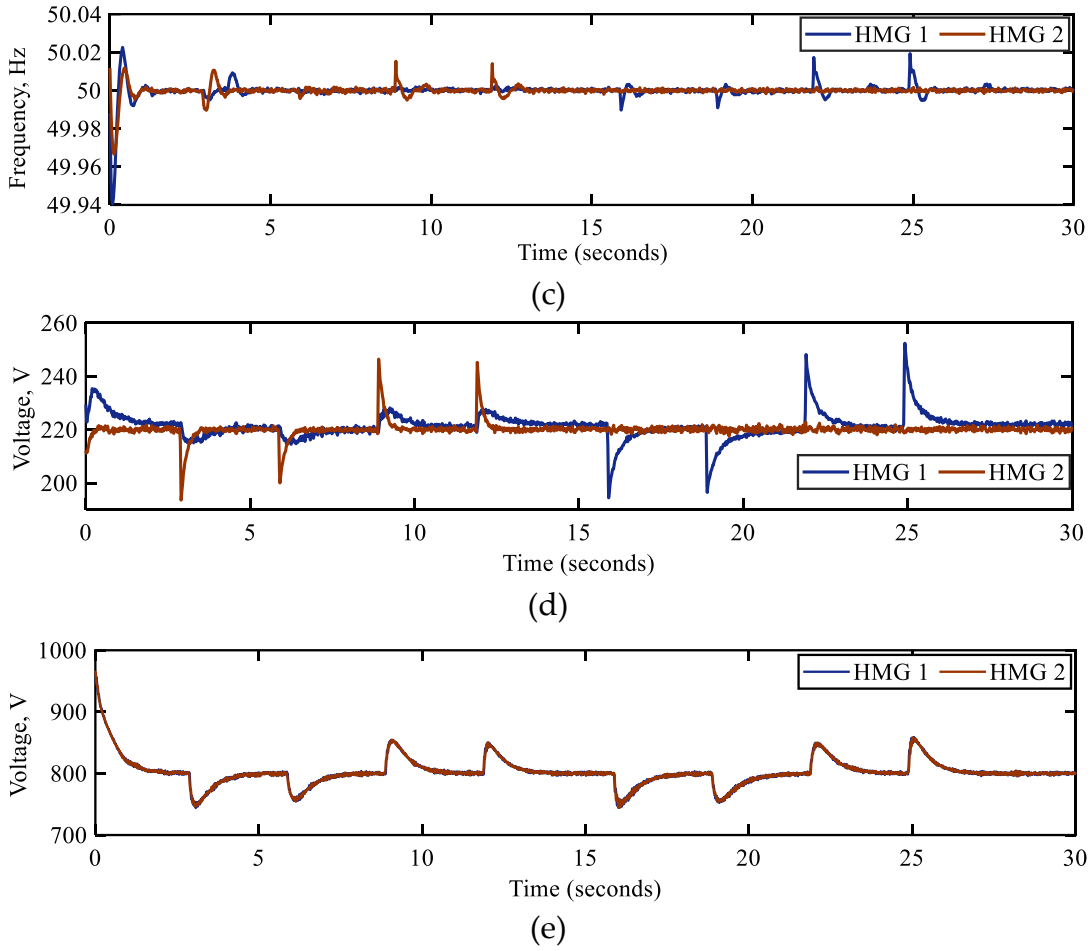

Fig. 4.7: Networked microgrid system parameters under load variations: a) AC sinusoidal voltage of hybrid microgrid-1, b) AC sinusoidal voltage of hybrid microgrid-2, c) Frequency, d) AC RMS voltage, and e) DC-bus voltage.

4.4.2 Analysis Under Source Power Variations or Failures

For various source (RES) conditions, such as solar irradiance variation of PV, PV failure, wind speed variation of wind generators, and wind generator failure, the power flow and system performance analysis are examined in this subsection. Table 4.4 provides an overall summary of power generation, consumption, and sharing under source power variations in both HMGs.

Fig. 4.8 illustrates the source power variation scenarios in both HMGs. At first (from t = 0 to 1.8s), both PV and wind are generating power at their maximum capacity, i.e., in HMG-1, both PV's and wind's power outputs are 45kW at 1000W/m^2 irradiance and 15m/s wind speed, and in HMG-2, generation from PV is 45kW at 100W/m^2 and generation from wind is 35kW at 15m/s. PV

generation drops to 25kW at t = 1.8s as a result of the solar irradiation in both HMGs decreasing to 500W/m^2, while wind generations remain at their initial capacity levels. When the solar irradiation approaches zero (0W/m^2) at t = 3.8 s, the PV generation in both HMGs also reaches zero (0kW). However, at t = 5.8, the PV generation in both HMGs increased to 32kW due to an increase in solar irradiances to 650 W/m^2. This generation scenario for PV is maintained for the remaining time frame. Now, the variation in wind generation starts at t = 9s. At t = 9s, the wind generation drops to 32kW in HMG-1 and 25kW in HMG-2 due to the drop in wind speed to 11m/s. However, at t = 12.5s, the wind generation in both HMGs again returns to their maximum generation capacity. The wind turbines in both HMGs abruptly stopped producing any power (0kW) at t = 15.8s. Due to a generation shortage in HMG-1 and insufficient supply from HMG-2, the diesel generator in HMG-1 starts to supply power after wind generation failure in both HMGs. However, the diesel generator in HMG-2 is operating in its initial generation condition, as the generation in HMG-2 is sufficient to supply the available load.

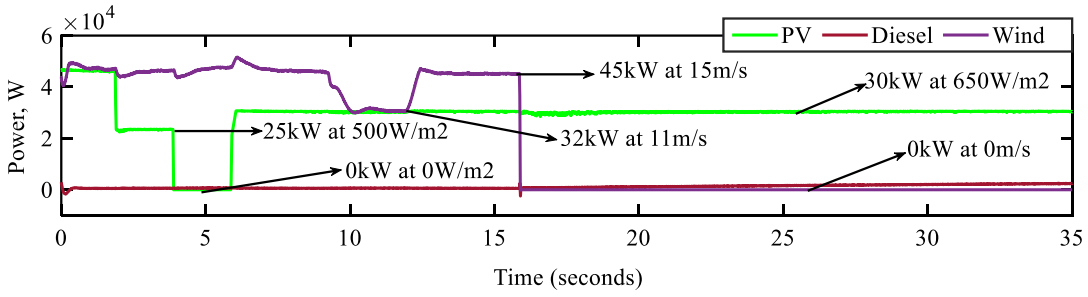

(b)

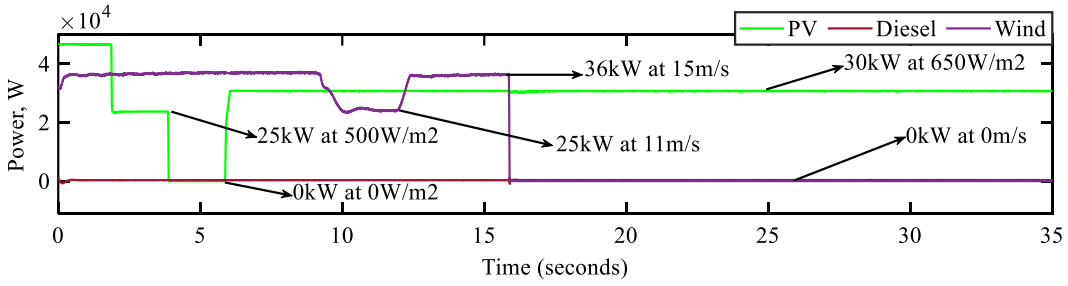

(c)

Fig. 4.8: Generation in both hybrid microgrids: a) In hybrid microgrid-1, and b) In hybrid microgrid 2.

The load curve for each of the HMGs is displayed in Fig. 4.9. For the sole purpose of analysing the effects of source power variation, the demand in both HMGs is kept at 65 kW and 60 kW, respectively. From t = 0 to 17s, there are fluctuations in the load curve due to variation in wind and PV generations. The failure of the wind generator in both HMGs causes an excessive amount of fluctuation in the load curve at t = 15.8s, and this disturbance remains until t = 17s.

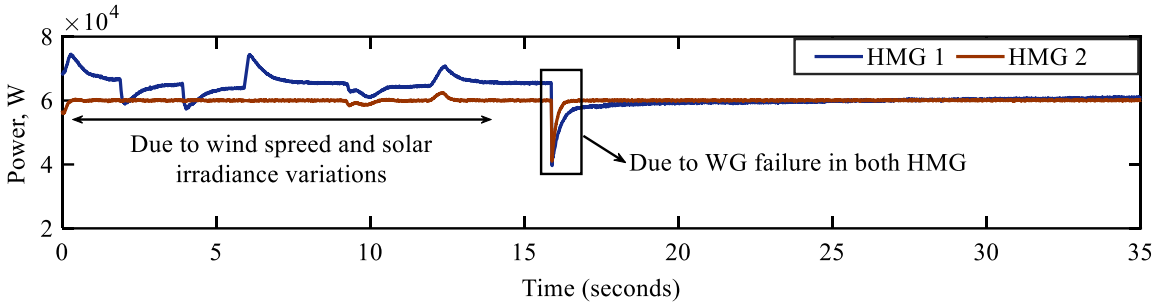

Fig. 4.9: Demand in both hybrid microgrids.

ESS power management and SoC level under source power variations is presented in Fig. 4.10. Initially, both ESSs are charging with 25kW and 20.9kW of power, respectively, from the available power generation from the respective HMGs. Due to the decrease in PV generation in both HMGs at t = 1.8s, the charging rates of both ESS decreased to 4.1kW and 1.8kW, respectively. Then the failure in PV generation in both HMGs at t = 3.8s leads both the ESSs to discharge at -21.1kW and -23kW (SoC level is decreasing). However, because of a rise in PV generation, at t = 5.8s, both ESSs begin to charge with 9.6kW and 6.3kW of power. Now, at t = 9s, ESSs begin to discharge with -4.2kW and -5 kW of power, respectively, as a result of the wind power drop in both HMGs. However, both ESSs begin to charge at t = 12.5s with 9.9kW and 6kW of power due to an increase in wind generation. Due to wind generator failure in both HMGs, both ESSs are almost discharging at their full rate (-30kW) at t = 15.8s. When both ESSs are discharging at their maximum rate and PVs are producing their maximum power

with their respective solar irradiation, HMG-1's diesel production begins to support at t = 15.8s in order to make up for the power shortage.

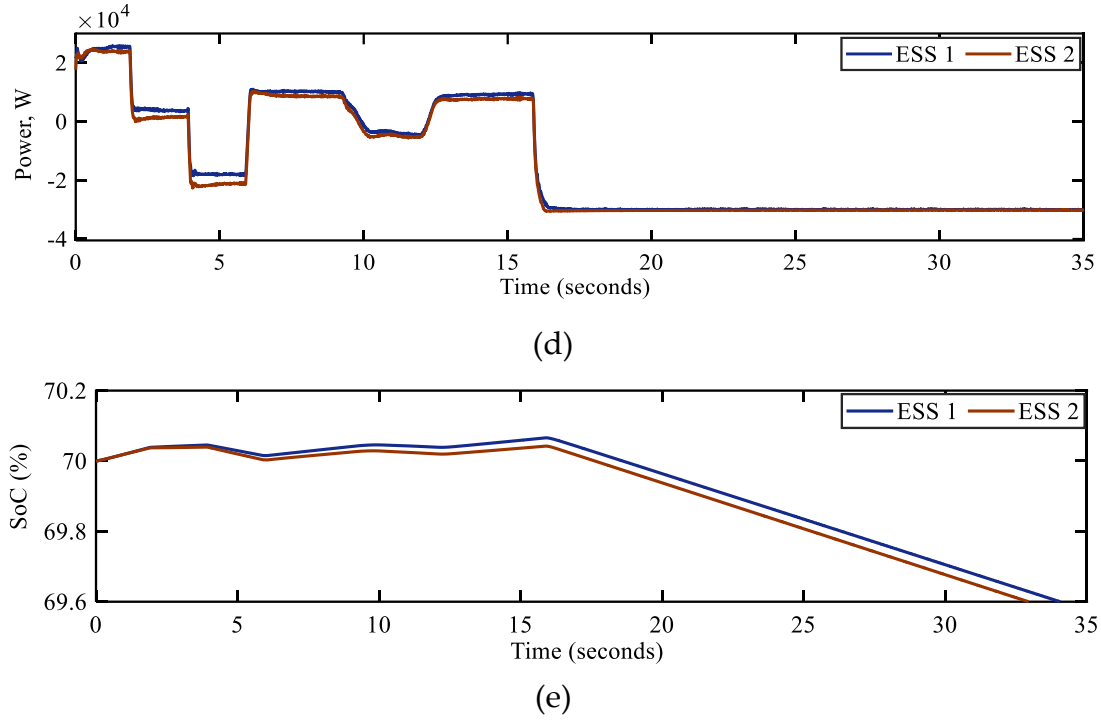

Fig. 4.10: ESS power in both hybrid microgrids: a) ESS Powers, and b) SoC levels.

The power sharing scenarios for source power variations are presented in Fig. 4.11. Because there is enough power in each HMG to meet demand, the sharing power (0.6kW) is quite low from t = 0 to 1.8s. Every HMG charges the ESS with the extra power it generates. Due to the PV power decrement in both HMGs at t = 1.8 s, a small amount of power (1.5kW) is being shared from HMG-1 to HMG-2. The sharing is taking place despite the available power in HMG-2, which reduces the burden of ESS in HMG-2. The 1.7kW power sharing is shared from t = 3.8 to 5.8s when the PV generation becomes zero in both HMGs. The sharing power is again back to 1kW due to an increment in PV generation. Due to wind generation decrease the sharing power is almost 0.7kW from HMG-1 to HMG-2. However, as wind turbines in both shut down at t = 15.8s, the sharing power became -0.3 kW (from HMG-2 to HMG-1). The sharing power is very low from t = 15.8 to 35s due to the generation and load balance constraints, i.e., the power generated in each HMG is almost equal to the total demand. Therefore,

after supplying demand, there is very little power left in each HMG to share. Moreover, the diesel generator in HMG-1 starts to supply to meet the demand.

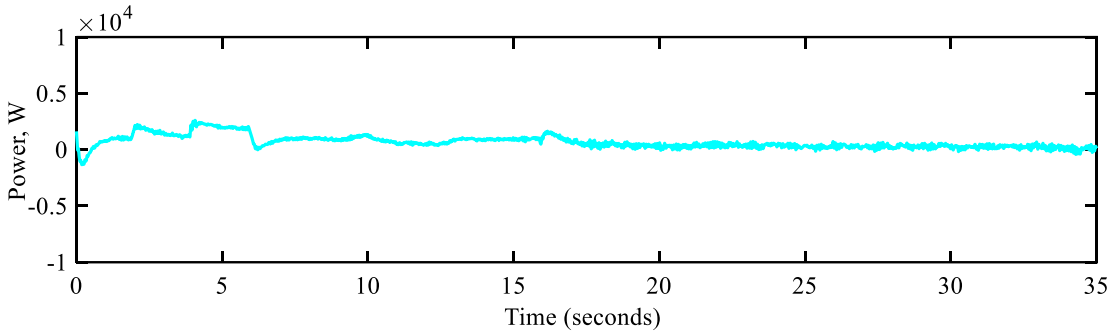

Fig. 4.11: Power sharing curve.

Table 4.4: A summary of the power generation and consumption of under source power variations

Time	Hybrid microgrid 1					Hybrid microgrid 2				
	DERs			ESS (kW)	Load (kW)	DERs			ESS (kW)	Load (kW)
	PV (kW)	Wind (kW)	Diesel (kW)			PV (kW)	Wind (kW)	Diesel (kW)		
0 – 1.8s	45	45	0.6	25	65	45	35	0.3	20.9	60
	Sharing Power		HMG-1 to HMG-2 – 0.6kW							
1.8 – 3.8s	25	45	0.6	4.1	65	25	35	0.3	1.8	60
	Sharing Power		HMG-1 to HMG-2 – 1.5kW							
3.8 – 5.8s	0	45	0.6	-21.1	65	0	35	0.3	-23	60
	Sharing Power		HMG-1 to HMG-2 – 1.7kW							
5.8 – 9s	30	45	0.6	9.6	65	30	35	0.3	6.3	60
	Sharing Power		HMG-1 to HMG-2 – 1kW							
9 – 12.5s	30	32	0.6	-4.2	65	30	25	0.3	-5	60
	Sharing Power		HMG-1 to HMG-2 – 0.6kW							
12.5 – 15.8s	30	45	0.6	9.9	65	30	35	0.3	6	60
	Sharing Power		HMG-2 to HMG-1 – 0.7kW							
15.8 – 35s	30	0	4.7	-30	65	30	0	0.3	-30	60
	Sharing Power		HMG-2 to HMG-1 – -0.3kW							

The network MGs characteristics, including voltages and frequencies, are shown in Fig. 4.12 under variations in source power. For both PV and wind power changes, the AC voltage and frequency in both HMGs are adjusted or vary. In both HMGs with power variation, the DC bus voltage variation is the same. Due to the wind generator failure in both HMGs, there is a significant

variation in both AC and DC voltage as well as a significant fluctuation in frequency. The voltage and frequency fluctuations, however, are within acceptable bounds.

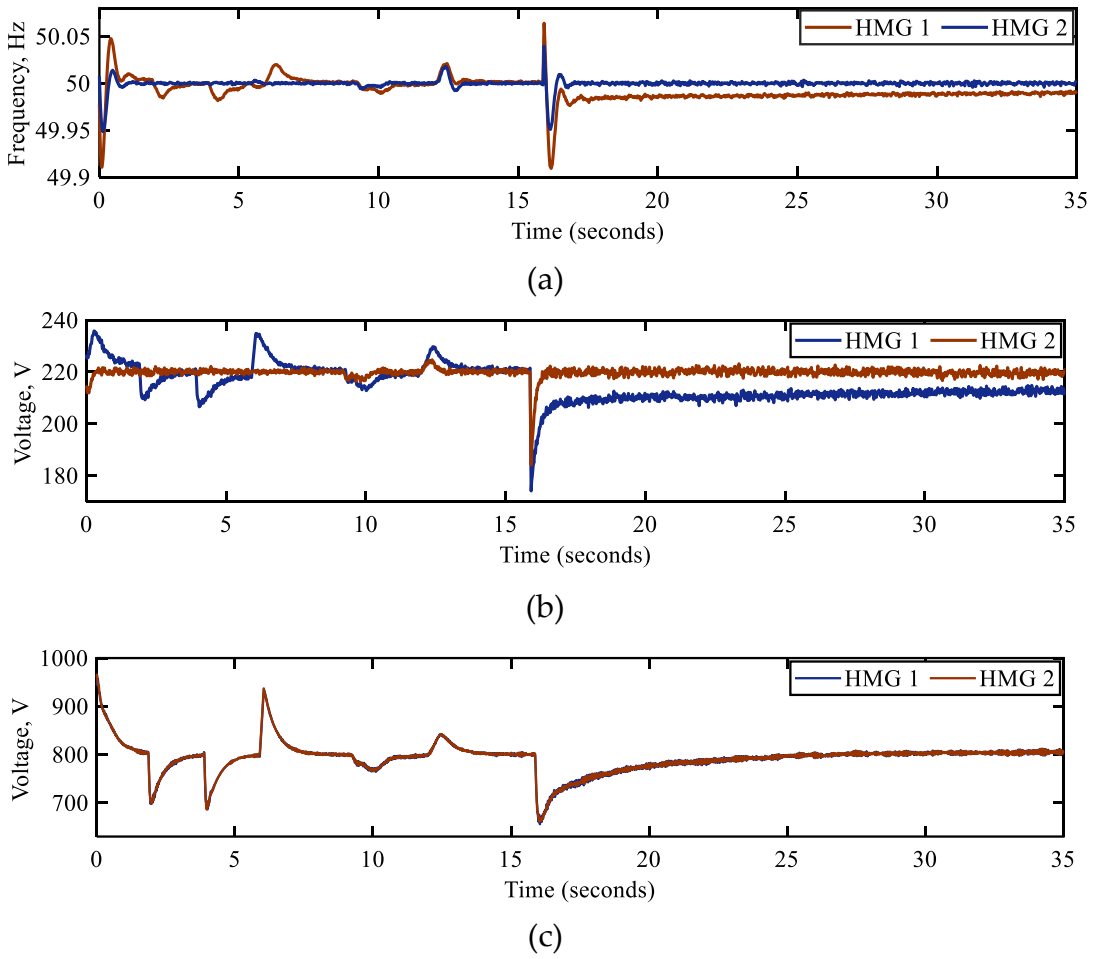

Fig. 4.12: Networked microgrid system parameters under source power variation: a) AC RMS voltage, b) Frequency, and c) DC-bus voltage.

4.4.3 Harmonic Analysis

The networked system performance in terms of THD is analysed in this section. The THDs of the system voltages or respective currents in islanded mode are in accordance with IEEE standards, i.e., lower than 5%.

Fig. 4.13 illustrates the THD performance of HMG-1 with the proposed control system. The waveform of the load current of HMG-1 shows that the peak magnitude is 140.5 A for a total load of 65 kW. The THD is 1.53% for both load current and system voltage. Fig. 4.13 also illustrates the THD performance of the

wind generator in HMG-1. As the wind generator generates 45kW of power at a 15m/s wind speed, the respective current magnitude is 98.73A. The THD of the wind generator's current waveform is 2.53%.

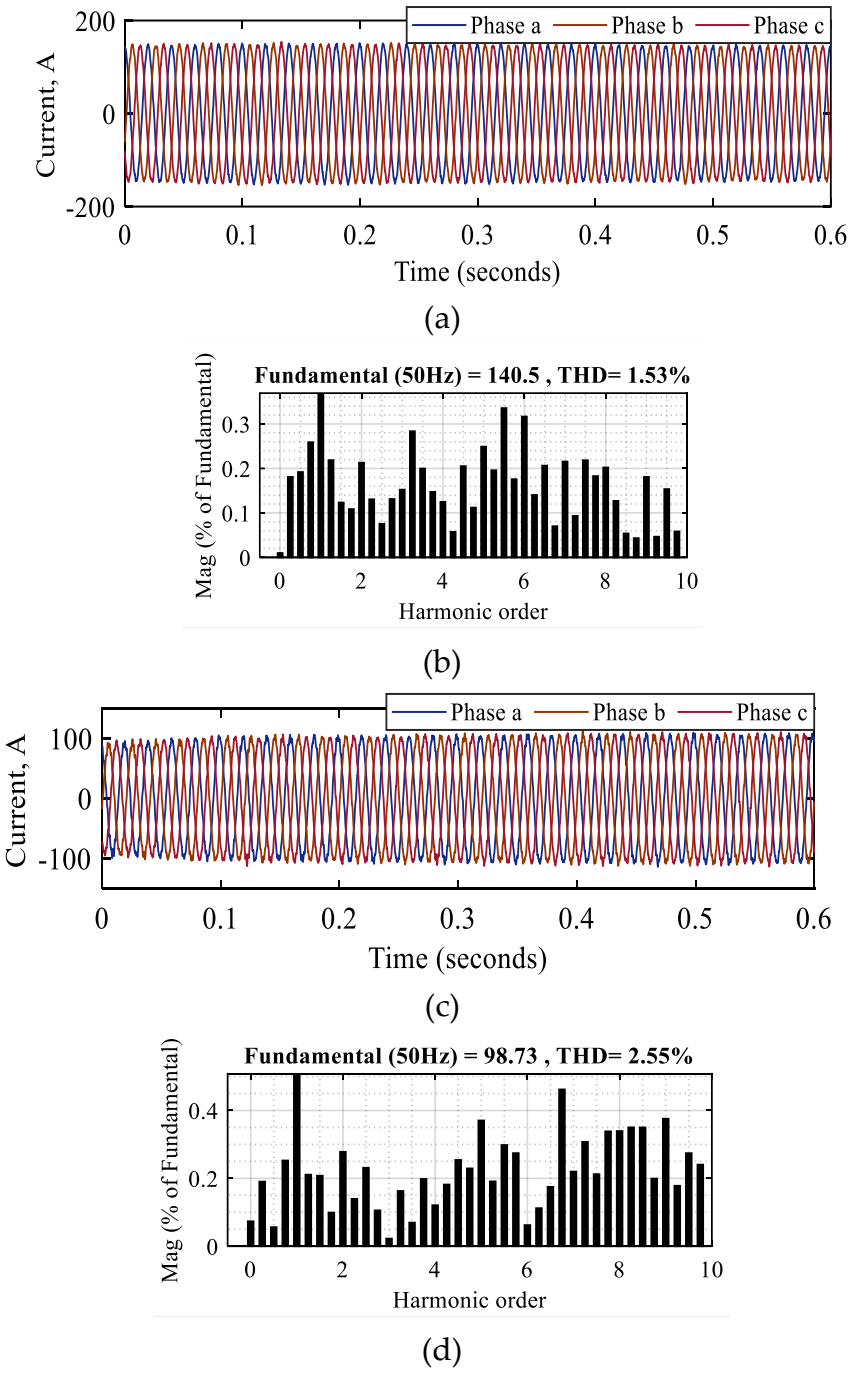

Fig. 4.13: THD Analysis: a) Load current of HMG-1, b) THD of load current of HMG-1, c) Wind generator current of HMG-1, and d) THD of wind generator current of HMG-1.

The THD performance of HMG-2 using the suggested control mechanism is shown in Fig. 4.14. The load current waveform of HMG-2 indicates that, for a

total load of 65 kW, the peak magnitude is 140.5 A. For both system voltage and load current, the THD is 1.59%. The wind generator's THD performance in HMG-2 is also shown in Fig. 4.14. The corresponding current magnitude is 98.73A, given that the wind generator produces 45kW of power at a wind speed of 15 m/s. The current waveform of the wind generator has a THD of 3.26%.

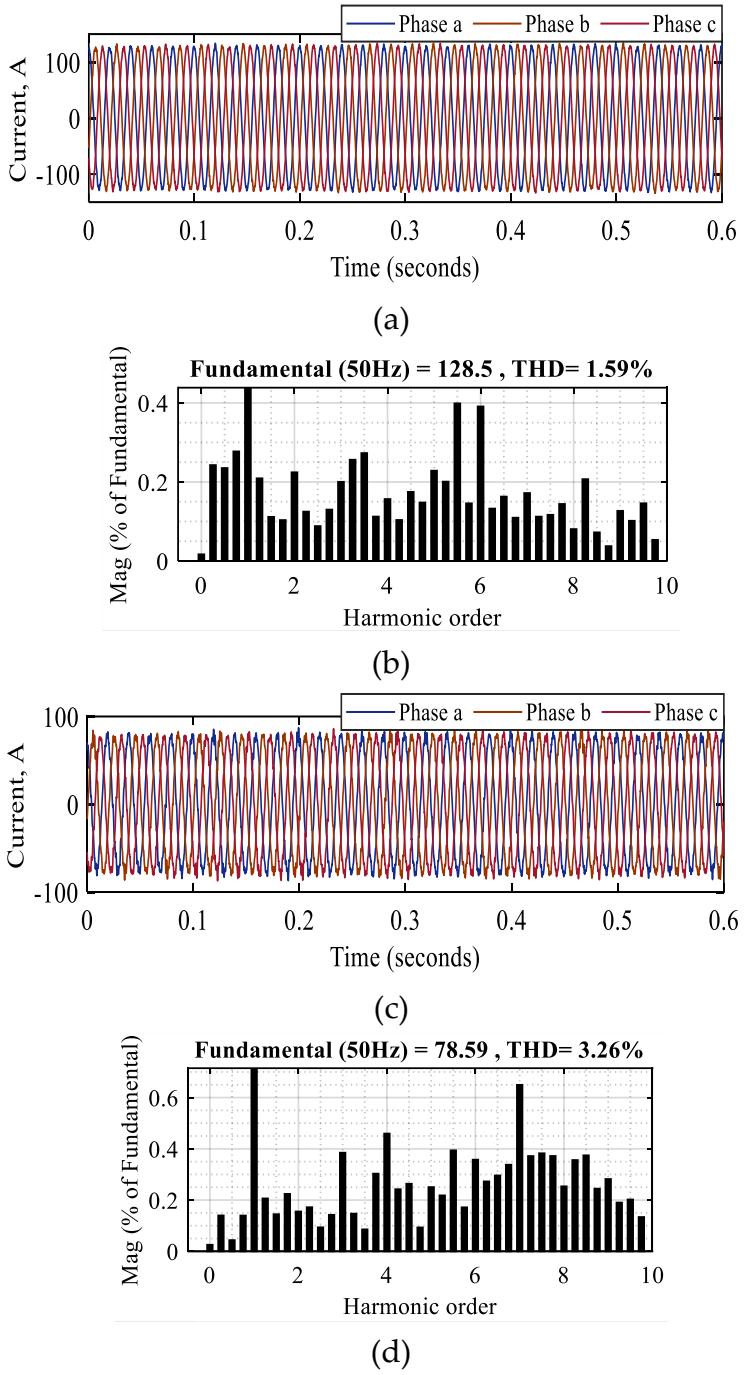

Fig. 4.14: THD Analysis: a) Load current of HMG-2, b) THD of load current of HMG-2, c) Wind generator of HMG-2, and d) THD of wind generator current of HMG-2.

4.4.4 Analysis with Dynamic Load

The dynamic loads (induction motors) would dramatically affect the overall networked system characteristics at low power demand than at rated power conditions. The extremely non-linear induction motor loads with electro-mechanical oscillations, which interact with the system's supply frequency, voltage, active power, and reactive power, challenge the system's stability by introducing low-frequency oscillations. In this subsection, the system performance with certain dynamic load penetration in both HMGs is analysed.

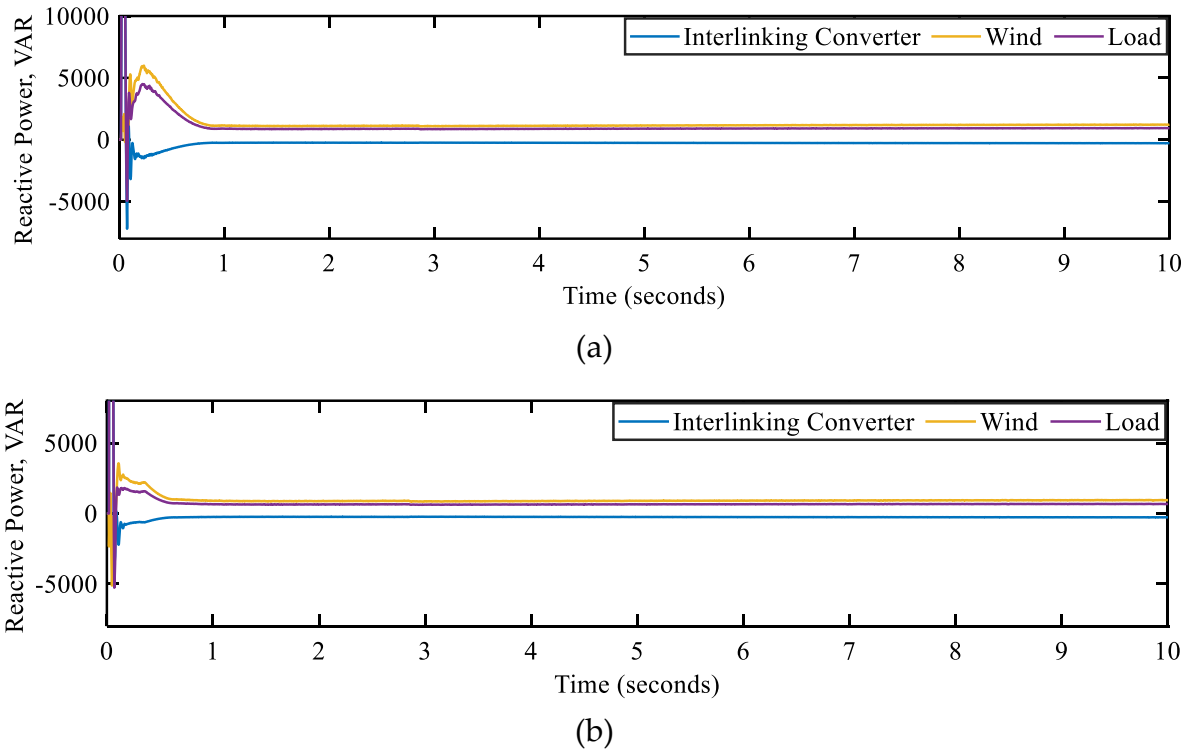

Fig. 4.15: Reactive Power in both hybrid microgrids: a) In hybrid microgrid-1, and b) In hybrid microgrid-2.

Fig. 4.15 illustrates the reactive power management in both HMGs in islanded mode with dynamic loads. In Fig. 4.15a, the wind generator reactive power is approximately 1.195kVAR and the reactive power support from the interlinking converter is -0.268kVAR. In Fig. 4.15b, the wind generator reactive power is approximately 0.928kVAR, and the reactive power support from the interlinking converter is -0.25kVAR. With the loads in both HMGs, the reactive power from both the wind generator and interlinking converter varies.

Fig. 4.16 illustrate the load scenarios in both HMGs with dynamic loads. Initially, the loads in HMG-1 and HMG-2 are fixed at 85kW (65kW CIL and 20kW induction motor load) and 75kW (60kW CIL and 15kW induction motor load), respectively. At t = 2.8s, a 20kW CIL load is added in both HMGs; therefore, the demand in HMG-1 and HMG-2 is shifted to 105kW and 95kW. However, at t = 5.8s, the added 20 kW load is removed from both HMGs, therefore returning both HMGs to their initial demand levels. The load curve illustrates that, due to the presence of certain dynamic loads, there are oscillations in transient conditions.

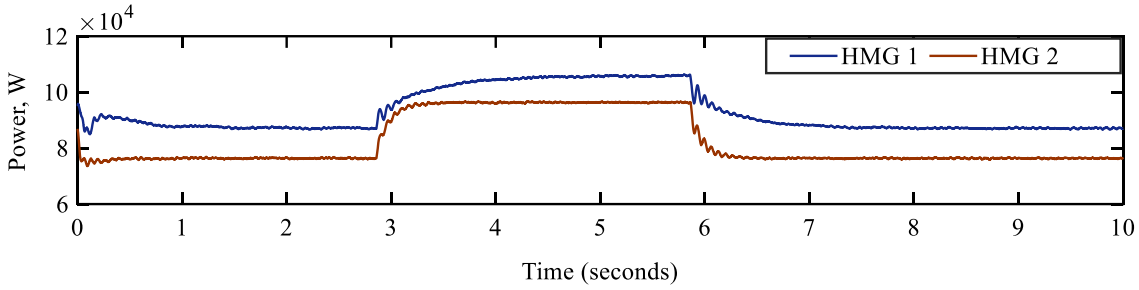

Fig. 4.16: Demand in both hybrid microgrids.

The ESS power curve in the presence of dynamic induction motor loads is presented in Fig. 4.17. Initially, both ESSs are charging with 6 kW of power, respectively, from the available power generation from the respective HMGs. Due to the load increment in both HMGs at t = 2.8s, both ESSs start to discharge at approximately -15 kW (SoC level is decreasing). However, at t = 5.8 s, ESS-1 and ESS-2 start to charge at the initial charging rate of 6 kW due to a decrease in loads in both HMGs. There is a slight fluctuation in the ESS power curve at the moment of load variations due to the presence of dynamic loads.

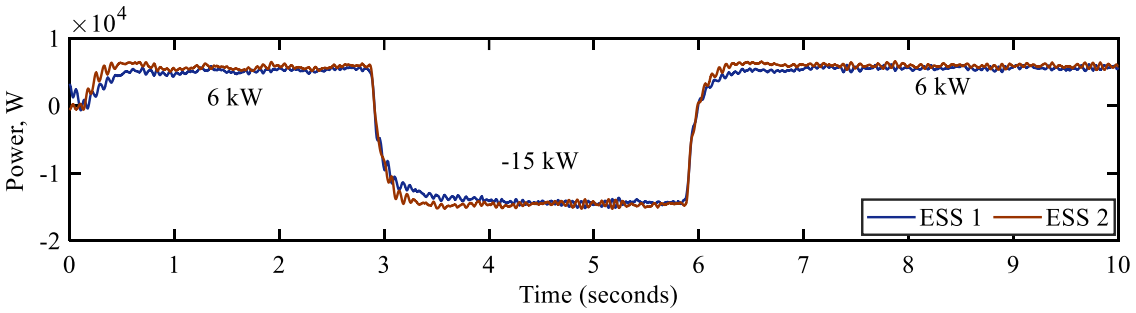

Fig. 4.17: ESS power in both hybrid microgrids.

The power-sharing scenarios in this condition are presented in Fig. 4.18. From t = 0 to 2.8s, the sharing power is very low, which is -0.25kW (HMG-2 to HMG-1) due to the available power in each HMG to satisfy demand. Each HMG uses its excess power generation to charge the ESS. Due to the same amount of load increment in both HMGs at t = 2.8s, the power flow is also very low, which is approximately 0.3kW from HMG-1 to HMG-2. The removal of the added loads brings the sharing power back to its previous value (-0.25kW).

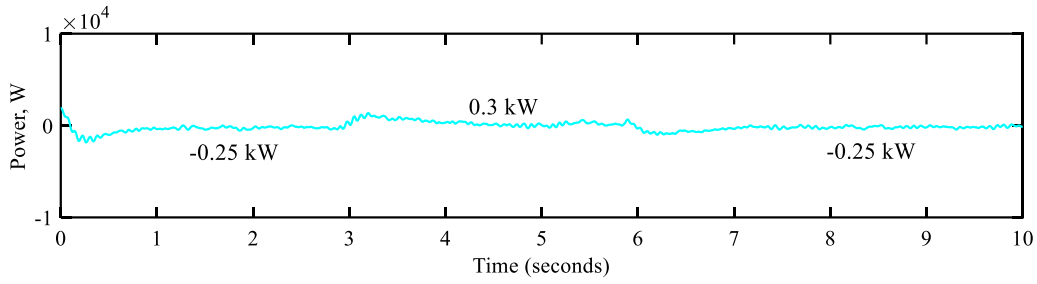

Fig. 4.18: Power sharing curve.

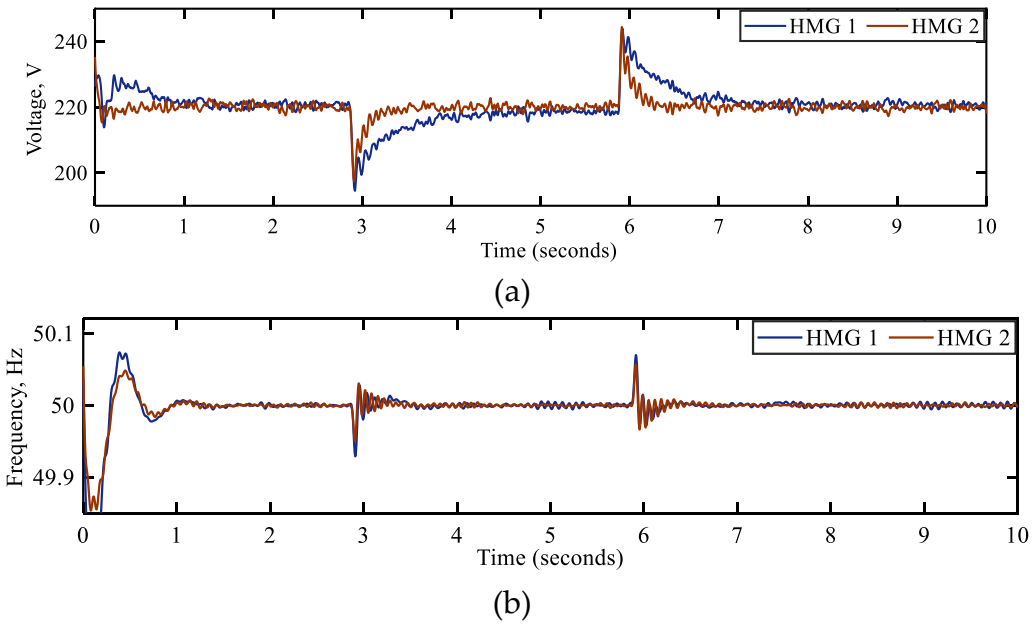

Fig. 4.19: Networked microgrid system parameters under source power variation: a) AC RMS voltage, and b) Frequency.

The performance of the networked system with dynamic loads under load variations in terms of system voltage and frequency is illustrated in Fig. 4.19. System voltage and frequency change as a result of sudden load changes. However, during the changes, there are oscillations in voltages and frequencies

due to the presence of dynamic loads. The frequency variation for load increment is -0.14% and load decrement is 0.135%.

4.5 MODE TRANSITION

In an interconnected MG system, the suggested control structure allows both islanded and grid-tied operation without requiring the critical detection of islanding or swapping between two associated controllers. An STS is closed or opened during the mode transition process and maintain the connection to the main grid. Fig. 4.20 illustrates the results associated with the transitions among various modes. At first, by using a droop-based controller to keep their voltage and frequency within acceptable bounds, both HMGs are running in islanded mode. At t = 2.8 s, grid synchronization is achieved by closing the STS of HMG-1. With this mode change, the MG cluster starts to operate in grid-connected mode instead of islanded mode. The controller of the HMG-1's interlinking converter alters its functionality to enable the mode transition. Fig. 4.20a illustrates that the voltage of HMG-1 closely traces the main grid voltage, which results in a smooth grid synchronization at t = 2.8s. The frequency and voltage of HMG become stable at 50 Hz and 220 volts, as shown in Fig. 4.20b and Fig. 4.20c. Now, at t = 6.8s, HMG-1 becomes disconnected from the main grid; therefore, transition to islanded mode is required. It is evident from Fig. 4.20 that the controller helps to transit between islanded and grid-connected modes and vice versa without any significant fluctuation or distortion, i.e., the designed controller provides a smooth transition. There is no change in HMG-2's parameters because the clustering converter interface helps the HMG-2 operate in islanded mode when HMG-1 is operating in on-grid mode. The frequency variation due to main grid failure or islanding is -0.11%, and due to grid synchronization, it is 0.04%.

Fig. 4.21 illustrates the power generation curve, load curve, and function of ESS management during mode transition. The generation from PV and wind is

almost the same in both modes, and there is no change due to mode changes. The DERs of each HMG are distributing power according to the load requirements. Most importantly, ESS is functioning properly with the proposed virtual inertia-based controller. There is no overcharge or over discharge scenario for ESSs in both HMGs due to the mode transition. ESS charges with the available power from the corresponding HMG in both on-grid and off-grid modes. Furthermore, there aren't any notable variations when switching between modes.

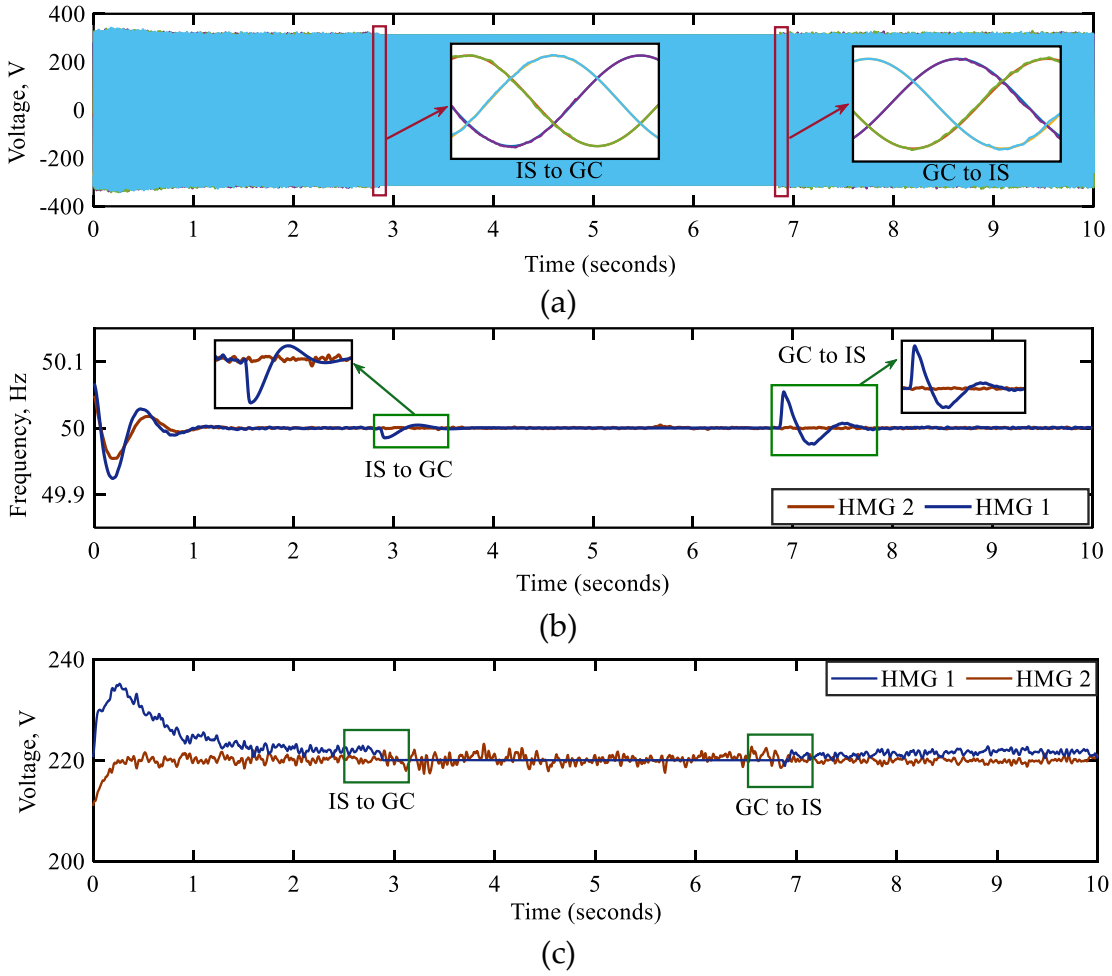

Fig. 4.20: Mode transition result: a) AC sinusoidal voltage, b) Frequency, and c) AC RMS voltage.

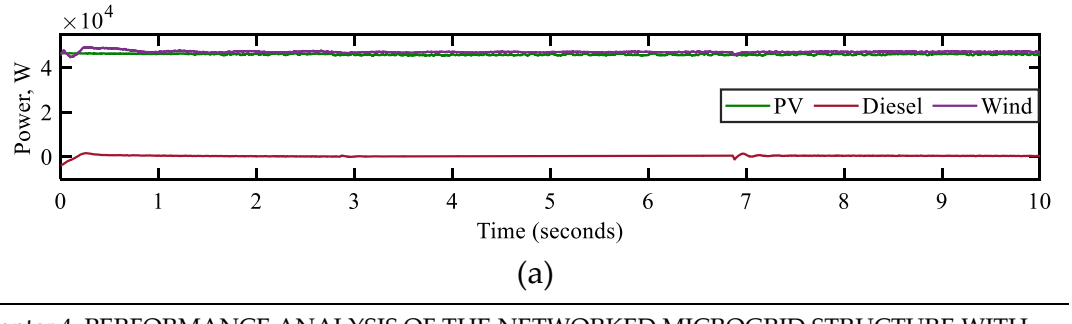

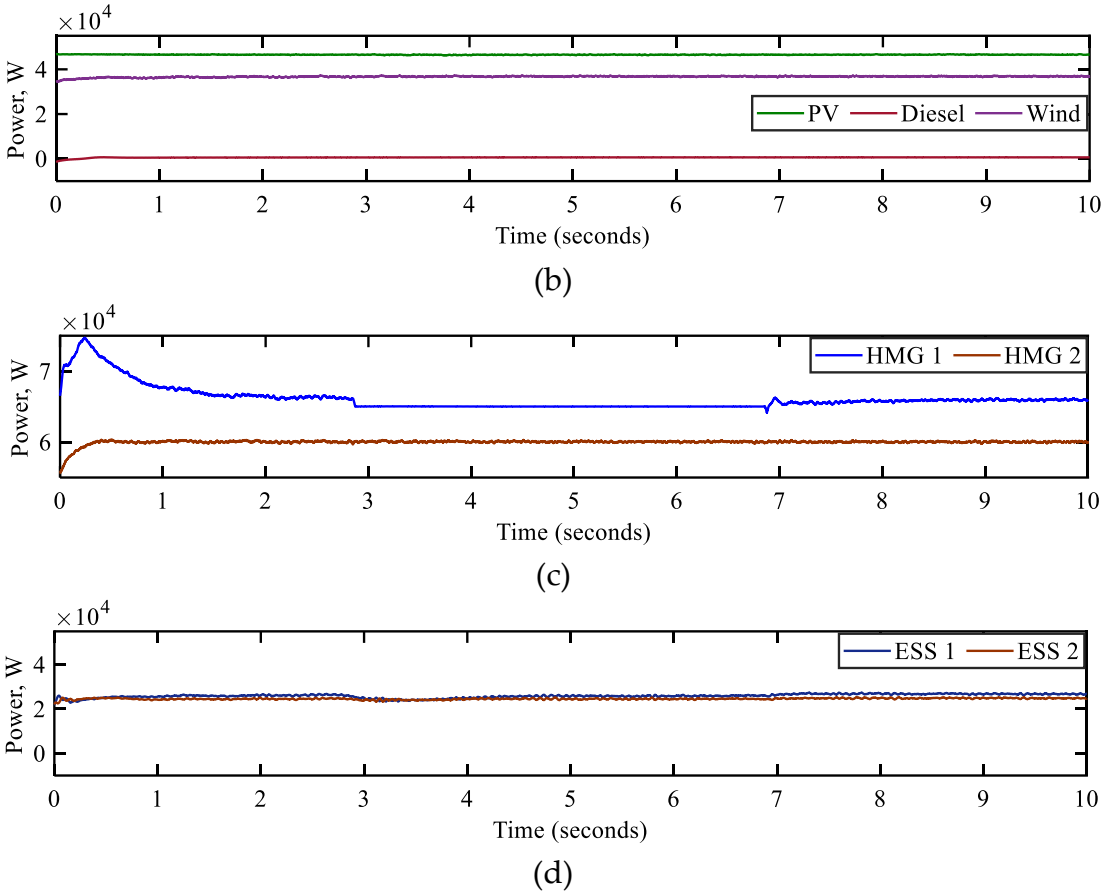

Fig. 4.21: a) Generation in HMG-1, b) Generation in HMG-2, c) Load curve, and d) ESS power curve.

4.6 GRID CONNECTED MODE

In grid-tied mode, the performance of the proposed control system in networked MGs is evaluated in this subsection under various load conditions. Only HMG-1 is connected to the main grid, and HMG-2 always operates in islanded mode in order to analyse the effectiveness of the proposed control structure operation.

According to Fig. 4.22, all the RESs-based generation sources (PV and wind) are operating at their maximum capacity in both HMGs (45kW at 1000W/m^2 for PV in both HMGs; 45kW at 15m/s for wind in HMG-1; 35kW at 15m/s for wind in HMG-2). The diesel generator's output power does not operate in on-grid mode, as it is used as a backup source in off-grid mode.

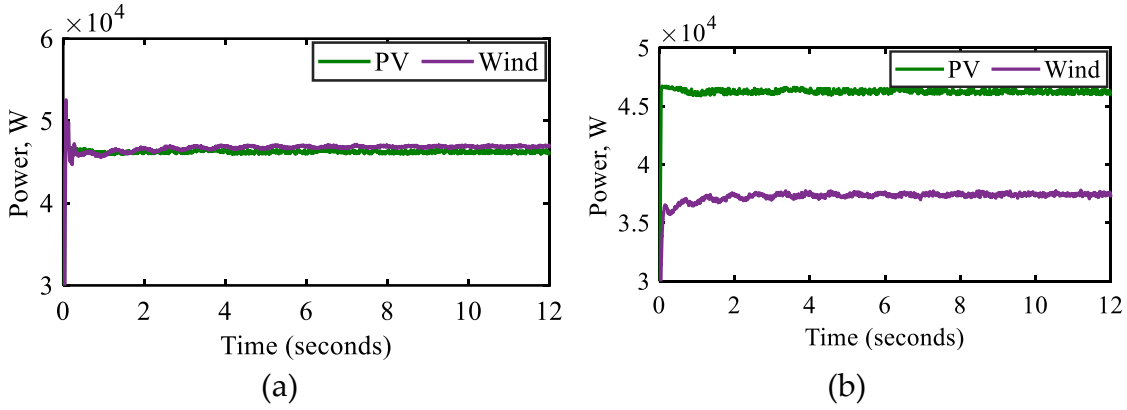

Fig. 4.22: Generation in both hybrid microgrids: a) In hybrid microgrid-1, and b) In hybrid microgrid 2.

Fig. 4.23 illustrates the reactive power management in HMG-1 in grid-connected mode. In Fig. 4.23, the wind generator reactive power is approximately 100kVAR, and the reactive power support from the interlinking converter is -106kVAR. With the load increment in HMG, the reactive power remains the same.

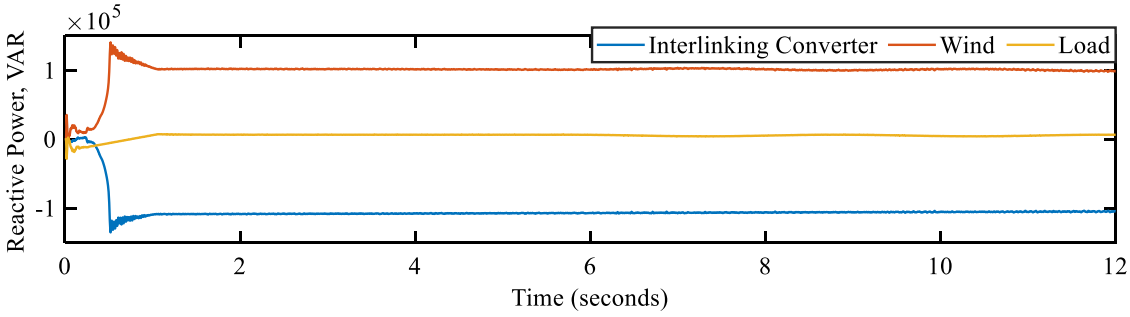

Fig. 4.23: Reactive Power in both hybrid microgrids: a) In hybrid microgrid-1, and b) In hybrid microgrid-2.

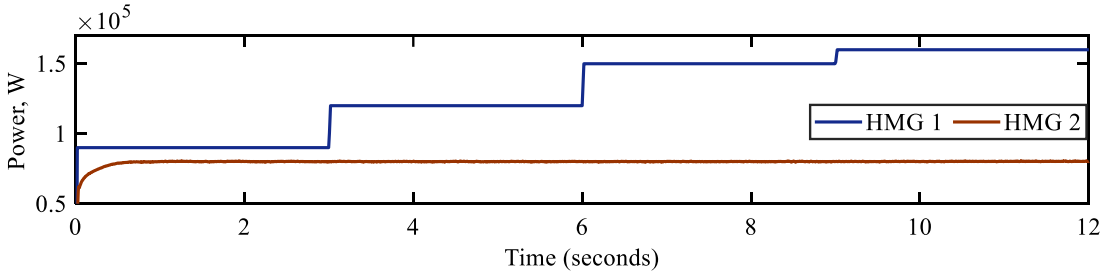

Fig. 4.24: Demand in both hybrid microgrids.

Fig. 4.24 illustrate the load scenarios in both HMGs. Initially, the loads in HMG-1 and HMG-2 are fixed at 90kW and 80kW, respectively. At t = 3s, a 30kW

load is added to HMG-1; therefore, the demand in HMG-1 is shifted to 120kW. Again, at t = 6s, another 30kW load is added, and the demand becomes 150kW in HMG-2. The addition of a 10kW load at t = 9s makes the total demand equal to 160kW in HMG-1. However, the load in HMG-2 is fixed at 80kW from t = 0 to 12s.

ESS power management under load variations is presented in Fig. 4.25. Initially, both ESSs are charging with 1.5kW of power from the available power generation in both HMGs. Due to the load increment in HMG-1 at t = 3s, both ESSs start to discharge at -19.5kW and -6kW, respectively. The charging rate of the ESS-2 decreased to 2.3kW. Another 30kW load addition at t = 6s leads the ESS-1 to discharge at full rate (-30kW) and the ESS-2 at -21kW. Finally, a 10kW load addition in HMG-1 causes both ESSs to discharge at full rate (-30kW).

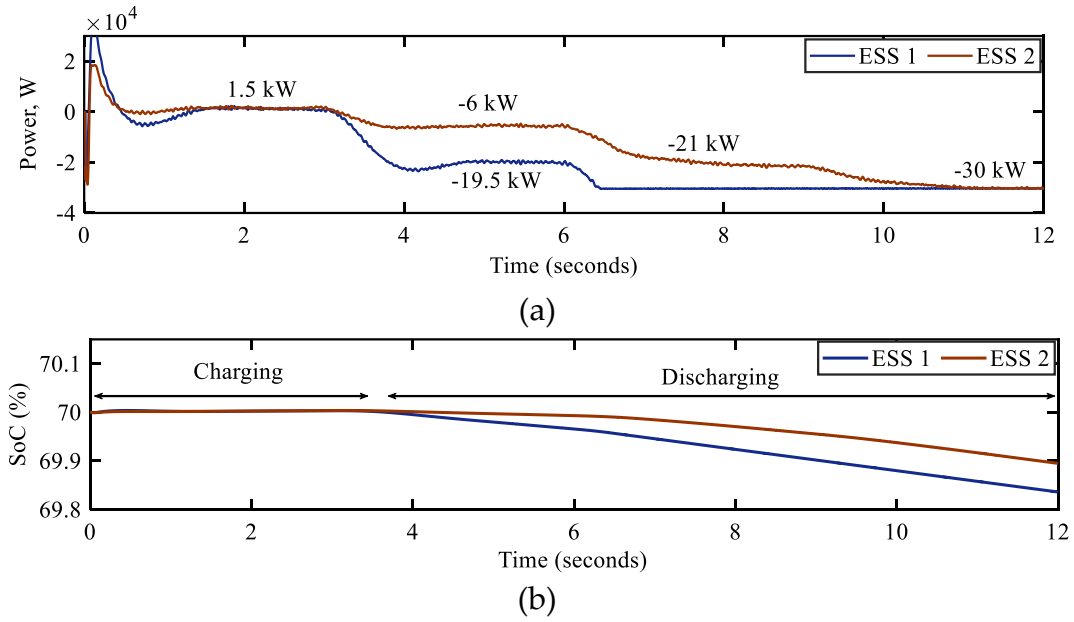

Fig. 4.25: ESS power in both hybrid microgrids: a) ESS Powers, and b) SoC levels.

The power sharing scenarios for load variations in grid-connected mode are presented in Fig. 4.26. From t = 0 to 3s, the sharing power is very low, which is 0.2kW (HMG-2 to HMG-1) due to the available power in each HMG to satisfy demand. Each HMG uses its excess power generation to charge the ESS. Due to the increase in load in HMG-1 at t = 3 s, a certain amount of power (-7kW) is being shared from HMG-2 to HMG-1. Because of the continued increase in load in

HMG-1, more power is being shared (-23kW) at t = 6s. Finally, a 10kW load increment in HMG-1 causes HMG-2 to share more power, which is -32kW.

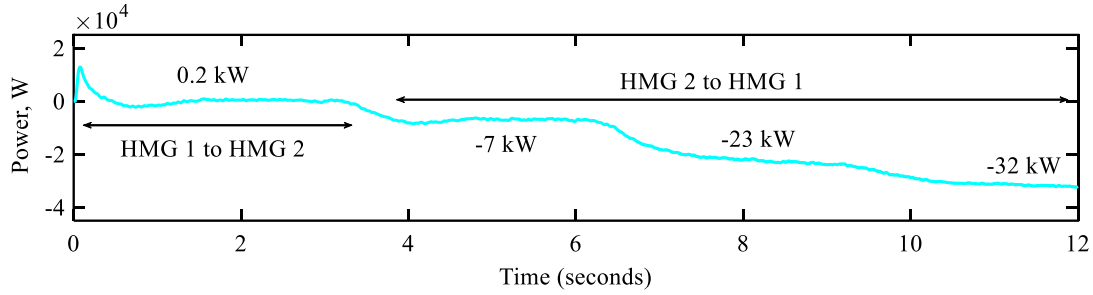

Fig. 4.26: Power sharing curve.

Fig. 4.27 illustrates the power output from the main grid due to the main grid connection. From t = 0 to 3s, the main grid supplies less power (0.35 kW), as the generation from each HMG is sufficient to meet demand. At t = 3s, load increment in HMG-1, 3kW power is delivered from the main grid. The power transfer from the main grid increases with the increase in loads in any HMG.

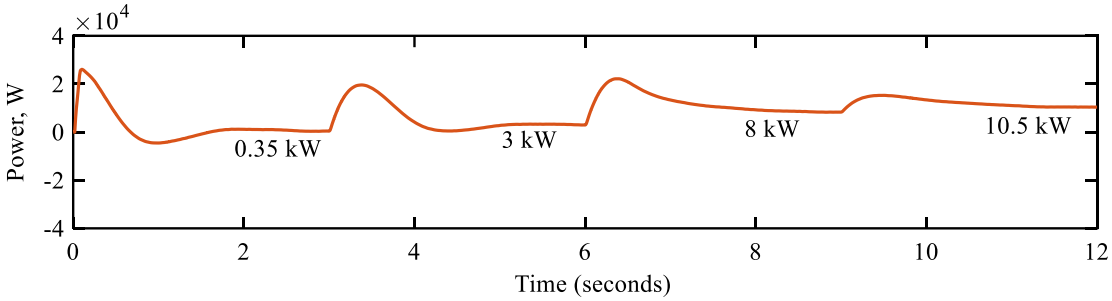

Fig. 4.27: Grid Power Curve.

Fig. 4.28 illustrates the THD performance of HMG-1 with the proposed control system in grid-connected mode. Fig. 4.28 illustrates the THD performance of the load current and wind generator in HMG-1. As the wind generator generates 45kW of power at a 15m/s wind speed, the respective current magnitude is 100.9A. The THD of the load current is 1.30%, and the wind generator's current waveform is 2.30%.

Fig. 4.29 illustrates the THD performance of HMG-2 with the proposed control system in grid-connected mode. Fig. 4.29 illustrates the THD performance of the wind generator in HMG-2. As the wind generator generates 45kW of power

at a 15m/s wind speed, the respective current magnitude is 80.22A. The THD of the load current is 1.31%, and the wind generator's current waveform is 2.60%.

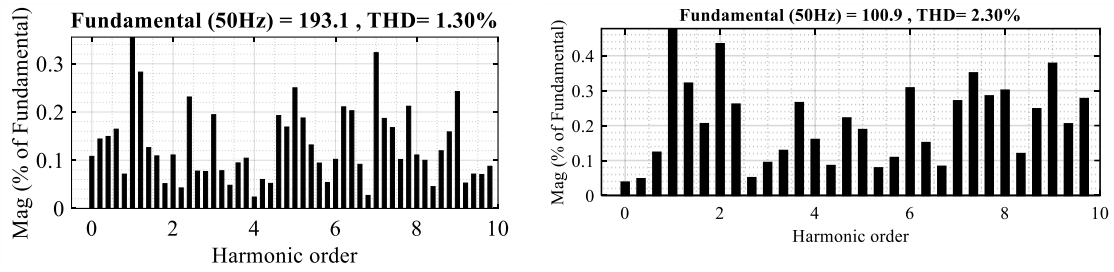

(a) (b)

Fig. 4.28: THD Analysis of HMG-1: a) THD of load current, and b) THD of wind generator current.

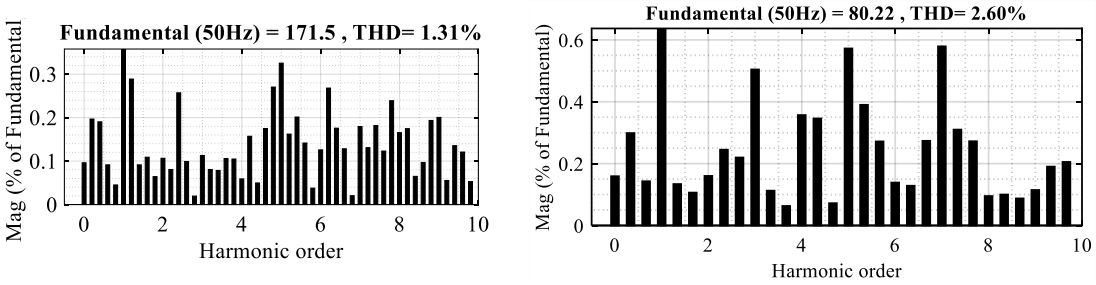

(a) (b)

Fig. 4.29: THD Analysis of HMG-2: a) THD of load current, and b) THD of wind generator current.

4.7 SUMMARY

The performance of the networked MG system with three proposed control strategies is analysed under various conditions, such as load power variations, source power variations, power quality, and dynamic loads.

In islanded mode, the networked configuration enables the management of power surges and shortages in any MGs due to load and source power variations. The THD performance under the proposed interlinking converter control provides satisfactory results, i.e., THD less than 5%. The system also powers a certain amount of dynamic load without affecting system stability in islanded mode. For load variation, the frequency variations are respectively -0.038% during load increment and 0.02% during load decrement. The addition of

dynamic load causes a frequency variation of -0.14% during load increment and 0.135% during load decrement.

The suggested control system provides a smooth mode transition between grid-connected and islanded modes without switching between two controllers. There is very little fluctuation in voltage and frequency due to mode changes. Therefore, system function reliability in both modes. The frequency variation due to main grid failure or islanding is -0.11%, and due to grid synchronization, it is 0.04%.

In grid-connected mode, the system is able to sustain autonomous operation due to the proposed control system. The ESS's overcharging and discharging can easily be avoided with the proposed ESS control, thus improving the ESS life cycle.

Chapter 5

STABILITY ANALYSIS OF THE PROPOSED CONTROL STRATEGIES

5.1 INTRODUCTION

Stability analysis is one of the key issues with the stable operation of a MG-based system. Traditional power networks' stability assessment is well-developed due to the generally accepted standard models of synchronous machines, excitation systems, and governors of various orders. However, for converter-based MG systems, no such standard models exist, and it might be challenging to develop any standard models because of the variety of power technologies available. Therefore, it is necessary to determine how certain oscillatory modes and instability conditions are caused by circuit configurations and control aspects in MG system.

The interconnected system can be operated in two modes: off-grid or on-grid mode. In on-grid mode, the DGs function as constant sources that are regulated to deliver the required power into the network, while the main grid controls the system-level dynamics. In off-grid mode, the micro sources managed to meet all the required demand while retaining the voltage and frequency within the permitted ranges. The micro sources in distinct MGs, power management control, and the network itself control the system dynamics in off-grid mode.

This chapter presents the stability analysis of the three converter systems with the proposed control strategies under various parameter conditions. To

verify the stability of the proposed control strategies, stability analyses are presented based on bode plots and pole zero maps in the MATLAB/Simulink.

5.2 STABILITY ANALYSIS OF THE HYBRID MICROGRID'S INTERLINKING CONVERTER

The interlining converter functions as a VSC to interface the DC MG with the AC MG in an HMG. The model of interlinking converter incorporates power sharing control dynamics (droop control dynamics), output LCL filter dynamics, voltage and current controller dynamics, and coupling inductor dynamics. The VSC controller comprises three distinct components as shown in Fig. 5.1: a separate droop control loop that regulates the output voltage droop characteristics to determine the frequency of the output voltage's fundamental component; a voltage control loop; and a current control loop that rejects high-frequency disturbances and offers adequate damping for the output filter.

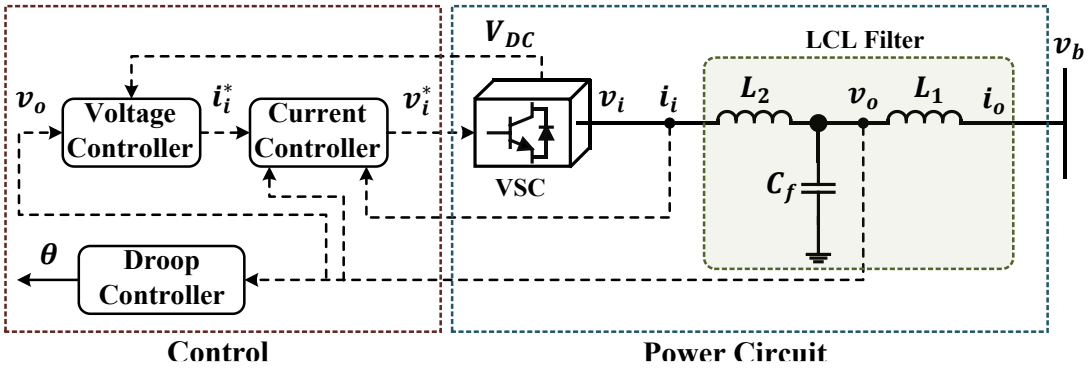

Fig. 5.1: Block diagram of VSC-based interlinking converter.

5.2.1 State space Model of interlinking converter

A particular inverter's small-signal state-space model is established by putting the controllers, output filter, and coupling inductor on a synchronous reference frame, the rotation frequency of which is controlled by the inverter's power controller.

5.2.1.1 Droop Controller

The fundamental notion of the power balancing concept is to reduce the system's frequency and voltage amplitude with the droop characteristics to

balance any rise in load. Instead of using active and reactive power droop, the output voltage droop characteristics are used in this study to characterize the system's frequency. From (1), it is evident that the angle of the VSC voltage can be changed according to the system's output voltage magnitude.

$$\omega = \omega^* - k_{ac}V_{od} \qquad V_{oq} = 0 \tag{5.1}$$

$$k_{ac} = \frac{\omega_{max} - \omega_{min}}{V_{max}} \tag{5.2}$$

Where, ω^* is reference angular frequency, k_{ac} is the droop gain, V_{od} and V_{oq} are the output voltage in the dq-frame, the terms with the max and min subscripts are the maximum and minimum values of the variables.

The small-signal model of the angular frequency in two axes (d and q) are:

$$\Delta\omega = -k_{ac}\Delta V_{od} \qquad \Delta V_{oq} = 0 \tag{5.3}$$

To standardize all the variables, the angle difference between each VSC's dq-frame and the common DQ-frame can be expressed as follows:

$$\delta = \int (\omega - \omega_{com})\, dt \tag{5.4}$$

δ is the angle between an individual VSC reference frame and the common reference frame and ω_{com} is the angular frequency of the common DQ-frame. The small-signal model is:

$$\Delta\dot{\delta} = \Delta\omega - \Delta\omega_{com} \qquad \Delta\dot{\delta} = -k_{ac}\Delta V_{od} - \Delta\omega_{com} \tag{5.5}$$

5.2.1.2 Voltage Controller

The voltage controller in Fig. 5.2 makes use of PI controllers, which contrast the measured output voltage with the reference value. This controller is based on a dual voltage control loop, which includes both DC and AC voltage controllers.

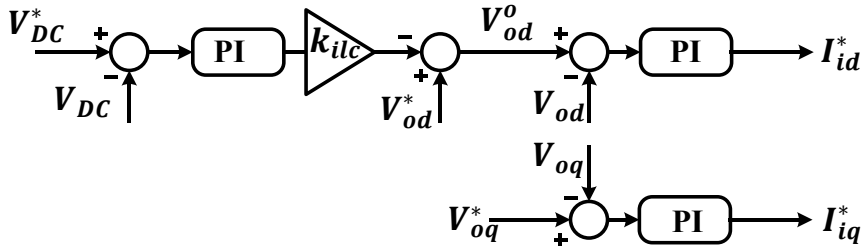

Fig. 5.2: Block diagram of voltage controller.

The relevant state equations are given as follows:

$$\frac{d\varphi_{DC}}{dt} = V_{DC}^{*} - V_{DC} \tag{5.6}$$

$$\frac{d\varphi_{d}}{dt} = V_{od}^{o} - V_{od} \qquad \frac{d\varphi_{q}}{dt} = V_{oq}^{*} - V_{oq} \tag{5.7}$$

$$I_{id}^{*} = k_{p_{v_{ac}}} V_{od}^{*} - k_{p_{v_{ac}}} k_{ilc} k_{p_{V_{dc}}} V_{DC}^{*} + k_{p_{v_{ac}}} k_{ilc} k_{p_{V_{dc}}} V_{DC} - k_{p_{v_{ac}}} k_{ilc} k_{i_{V_{dc}}} \varphi_{DC} - k_{p_{v_{ac}}} V_{od} + k_{i_{v_{ac}}} \varphi_{d} \tag{5.8}$$

$$I_{iq}^{*} = k_{p_{v_{ac}}} \left(V_{oq}^{*} - V_{oq}\right) + k_{i_{v_{ac}}} \varphi_{q}$$

$k_{p_{v_{ac}}}$ and $k_{i_{v_{ac}}}$ are the proportional and integral gains of the AC voltage controller. $k_{p_{V_{dc}}}$ and $k_{i_{V_{dc}}}$ are the proportional and integral gains of the DC voltage controller. k_{ilc} is the gain to balance the AC reference voltage with the DC bus voltage deviation. V_{DC}^{*} and V_{DC} are the reference and measured DC bus voltage. The voltage controller's small-signal model can be obtained by:

$$\Delta\dot{\varphi}_{DC} = \Delta V_{DC}^{*} - \Delta V_{DC} \tag{5.9}$$

$$\Delta\dot{\varphi}_{d} = \Delta V_{od}^{o} - \Delta V_{od} \qquad \Delta\dot{\varphi}_{q} = \Delta V_{oq}^{*} - \Delta V_{oq} \tag{5.10}$$

$$\Delta I_{id}^{*} = k_{p_{v_{ac}}} \Delta V_{od}^{*} - k_{p_{v_{ac}}} k_{ilc} k_{p_{V_{dc}}} \Delta V_{DC}^{*} + k_{p_{v_{ac}}} k_{ilc} k_{p_{V_{dc}}} \Delta V_{DC} - k_{p_{v_{ac}}} k_{ilc} k_{i_{V_{dc}}} \Delta\varphi_{DC} - k_{p_{v_{ac}}} \Delta V_{od} + k_{i_{v_{ac}}} \Delta\varphi_{d} \tag{5.11}$$

$$\Delta I_{iq}^{*} = k_{p_{v_{ac}}} \left(\Delta V_{oq}^{*} - \Delta V_{oq}\right) + k_{i_{v_{ac}}} \Delta\varphi_{q}$$

5.2.1.3 Current Controller

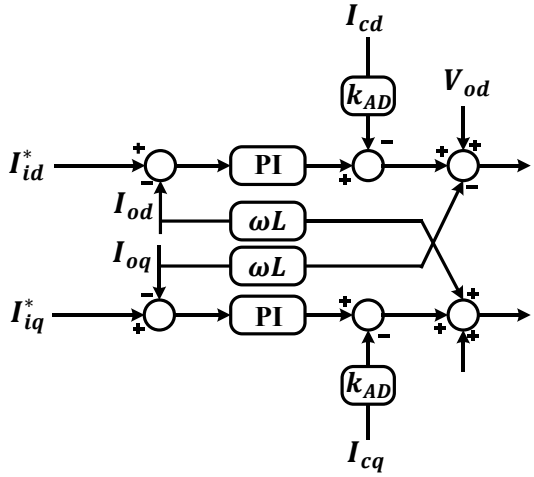

Fig. 5.3: Block diagram of current controller with active damping.

As illustrated in Fig. 5.3, the inner current controller, like the voltage controller, generates the sinusoidal pulse width modulation (SPWM) signal after

comparing the measured current with the reference value provided by the voltage controller via a PI controller. This controller also includes a feed-forward voltage gain and observer-based feed-forward capacitor current gain to damp the LCL filter resonance issue.

The relevant state equations for current controller are given as follows:

$$\frac{d\gamma_d}{dt} = I_{id}^* - I_{id} \qquad \frac{d\gamma_q}{dt} = I_{iq}^* - I_{iq} \tag{5.12}$$

$$V_{id}^* = k_{p_{I_i}}(I_{id}^* - I_{id}) + k_{i_{I_i}}\gamma_d - \omega^* L I_{iq} - k_{AD} I_{cd} + V_{od}$$
$$V_{iq}^* = k_{p_{I_i}}\left(I_{iq}^* - I_{iq}\right) + k_{i_{I_i}}\gamma_q + \omega^* L I_{id} - k_{AD} I_{cq} + V_{oq} \tag{5.13}$$

$k_{p_{I_{dq}}}$ and $k_{i_{I_{dq}}}$ are the proportional and integral gain of the current controller. k_{AD} is the virtual gain of the LCL filter. The current controller's small-signal model can be obtained by:

$$\Delta\dot{\gamma}_d = \Delta I_{id}^* - \Delta I_{id} \qquad \Delta\gamma_q = \Delta I_{iq}^* - \Delta I_{iq} \tag{5.14}$$

$$\Delta V_{id}^* = k_{p_{I_i}}\Delta I_{id}^* - k_{p_{I_i}}\Delta I_{id} - k_{i_{I_i}}\Delta\gamma_d - \omega^* L\Delta I_{iq} - k_{ad}\Delta I_{cd} + \Delta V_{od}$$
$$\Delta V_{iq}^* = k_{p_{I_i}}\Delta I_{iq}^* - k_{p_{I_i}}\Delta I_{iq} - k_{i_{I_i}}\Delta\gamma_q + \omega^* L\Delta I_{id} - k_{ad}\Delta I_{cq} + \Delta V_{oq} \tag{5.15}$$

5.2.1.4 LCL Filter Model

To eliminate the harmonic signal close to the switching frequency, an LCL filter connects the interlinking converter to the AC bus. However, in order to reduce the resonance effect of the LCL filter and improve the system's stability, active damping is used in the current controller.

The relevant equations are given as follows:

$$\frac{dI_{id}}{dt} = \frac{1}{L_2}V_{id} - \frac{1}{L_2}V_{od} - \frac{R_2}{L_2}I_{id} + \omega I_{iq}$$
$$\frac{dI_{iq}}{dt} = \frac{1}{L_2}V_{iq} - \frac{1}{L_2}V_{oq} - \frac{R_2}{L_2}I_{iq} - \omega I_{id} \tag{5.16}$$

$$\frac{dV_{od}}{dt} = \frac{1}{C_f}I_{id} - \frac{1}{C_f}I_{od} + \omega V_{oq}$$
$$\frac{dV_{oq}}{dt} = \frac{1}{C_f}I_{iq} - \frac{1}{C_f}I_{oq} - \omega V_{oq} \tag{5.17}$$

$$\frac{dI_{od}}{dt} = \frac{1}{L_1}V_{od} - \frac{1}{L_1}V_{bd} - \frac{R_1}{L_1}I_{od} + \omega I_{oq}$$
$$\frac{dI_{oq}}{dt} = \frac{1}{L_1}V_{oq} - \frac{1}{L_1}V_{bq} - \frac{R_1}{L_1}I_{oq} - \omega I_{od} \quad (5.18)$$

L_2 is the VSC-side inductor, C_f is the filter capacitor, and L_1 is the AC bus-side inductor. R_2 and R_1 are, respectively, the equivalent series resistances of the VSC-side inductor and grid-side inductor. I_{id} and I_{iq} are the VSC-side current in the dq-frame. I_{od} and I_{oq} are the output current in the dq-frame. V_{bd} and V_{bq} are the AC bus voltage in the dq-frame.

The small-signal model of the LCL filter is given as follows:

$$\Delta\dot{I}_{id} = \frac{1}{L_2}\Delta V_{id} - \frac{1}{L_2}\Delta V_{od} - \frac{R_2}{L_2}\Delta I_{id} + I_{iq}\Delta\omega + \omega_o\Delta I_{iq}$$
$$\Delta\dot{I}_{iq} = \frac{1}{L_2}\Delta V_{iq} - \frac{1}{L_2}\Delta V_{oq} - \frac{R_2}{L_2}\Delta I_{iq} - I_{id}\Delta\omega - \omega_o\Delta I_{id} \quad (5.19)$$

$$\Delta\dot{V}_{od} = \frac{1}{C_f}\Delta I_{id} - \frac{1}{C_f}\Delta I_{od} + V_{oq}\Delta\omega + \omega_o\Delta V_{oq}$$
$$\Delta\dot{V}_{oq} = \frac{1}{C_f}\Delta I_{iq} - \frac{1}{C_f}\Delta I_{oq} - V_{od}\Delta\omega - \omega_o\Delta V_{od} \quad (5.20)$$

$$\Delta\dot{I}_{od} = \frac{1}{L_1}\Delta V_{od} - \frac{1}{L_1}\Delta V_{bd} - \frac{R_1}{L_1}\Delta I_{od} + I_{oq}\Delta\omega + \omega_o\Delta I_{oq}$$
$$\Delta\dot{I}_{oq} = \frac{1}{L_1}\Delta V_{oq} - \frac{1}{L_1}\Delta V_{bq} - \frac{R_1}{L_1}\Delta I_{oq} - I_{od}\Delta\omega - \omega_o\Delta I_{od} \quad (5.21)$$

I_{id}, I_{iq}, I_{od}, I_{oq}, V_{od}, V_{oq}, and ω_o are steady state values at the initial operating point. These values are presented in Appendix A.

5.2.1.5 Complete Model of Interlinking Converter

The output variables must be changed to the common reference frame in order to couple a converter to the common bus. With the transformation matrix shown below, output variables (I_{odq}) and input variables (V_{bdq}) can be converted to the common DQ-frame:

$$[\Delta i_{oDQ}] = [T][\Delta i_{odq}] + [T_c^{-1}][\Delta\delta]$$
$$[\Delta i_{oDQ}] = \begin{bmatrix} cos\delta_o & -sin\delta_o \\ sin\delta_o & cos\delta_o \end{bmatrix}[\Delta i_{odq}] + \begin{bmatrix} -I_{od}sin\delta_o - I_{oq}cos\delta_o \\ I_{od}cos\delta_o - I_{oq}sin\delta_o \end{bmatrix}[\Delta\delta] \quad (5.22)$$

$$[\Delta v_{bdq}] = [T^{-1}][\Delta v_{bDQ}] + [T_v{}^{-1}][\Delta\delta]$$

$$[\Delta v_{bdq}] = \begin{bmatrix} cos\delta_o & sin\delta_o \\ -sin\delta_o & cos\delta_o \end{bmatrix}[\Delta v_{bDQ}] + \begin{bmatrix} -V_{bD}sin\delta_o + V_{bQ}cos\delta_o \\ -V_{bD}cos\delta_o - V_{bQ}sin\delta_o \end{bmatrix}[\Delta\delta] \quad 5.23$$

Incorporating the state-space representations of the output LCL filter, voltage controller, current controller, and droop controller depicted in equations 4.1–4.23 yields the full state-space small-signal representation of the interlinking converter. A standard interlinking converter model can be achieved by selecting thirteen state variables, resulting in a complete 13-order small-signal state space equation and output equation of the interlinking converter unit in common frame:

$$[\Delta\dot{x}_{ILC}] = [A_{ILC}][\Delta x_{ILC}] + [B_{ILC}][\Delta V_{bDQ}] + B_{com}[\Delta\omega_{com}] \quad 5.24$$

$$\begin{bmatrix} \Delta\omega \\ \Delta i_{oDQ} \end{bmatrix} = \begin{bmatrix} C_{ILC_\omega} \\ C_{ILC_i} \end{bmatrix}[\Delta x_{ILC}] \quad 5.25$$

Where, $[\Delta x_{INV,i}] = [\Delta\delta_i \quad \Delta\varphi_{dqi} \quad \Delta\gamma_{dqi} \quad \Delta i_{ldqi} \quad \Delta v_{odqi} \quad \Delta i_{odqi}]^T$ is the state variables matrix. A_{ILC}, B_{ILC}, B_{com}, C_{ILC_ω}, and C_{ILC_i} are matrix related to the state variables, which are presented in Appendix B.

5.2.2 Eigenvalue Analysis

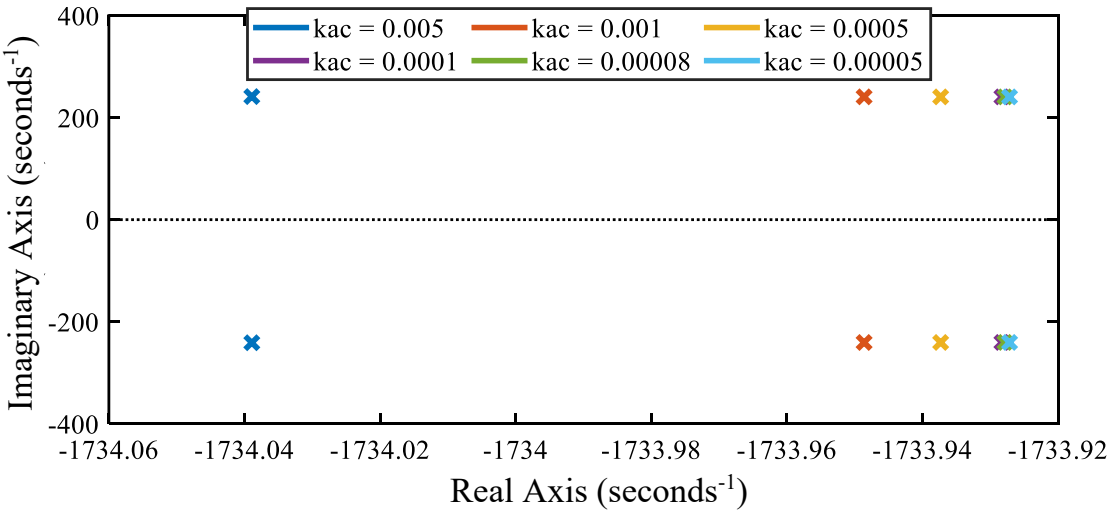

Fig. 5.4: Pole zero map due to the droop coefficient variation.

The interlinking converter system's stability and performance as a result of droop coefficient fluctuations are shown in Fig. 5.4. To achieve appropriate

power sharing, maintain system frequency, and preserve system stability, the control strategy's droop coefficient must be adjusted appropriately. Fig. 5.4 shows that the system poles are moved toward the right side of the plane as the droop coefficient increases, therefore affecting system stability. While a large droop coefficient shifts the pole position to the left, it also has negative effects on power sharing and system power quality.

Moreover, all values of the PI controller have a great impact on system performance, which needs to be analysed properly. The following summary can be made from the eigenvalue analysis of the state-space model:

- The droop coefficient needs to be selected properly in order to maintain system stability and performance.
- All PI controller values also need to be tuned properly.

5.3 ENERGY STORAGE SYSTEM CONTROL STABILITY

The block diagram of the ESS's control strategy contains an ESS PMS and a current control unit, as shown in Fig. 5.5. The PMS unit controls the charging and discharging of ESS in both islanded and grid-connected modes and generates the reference ESS current for the current controller. The proposed ESS control is able to operate in both modes without a mode switch. The controller consists of an ESS power management and a current control loop.

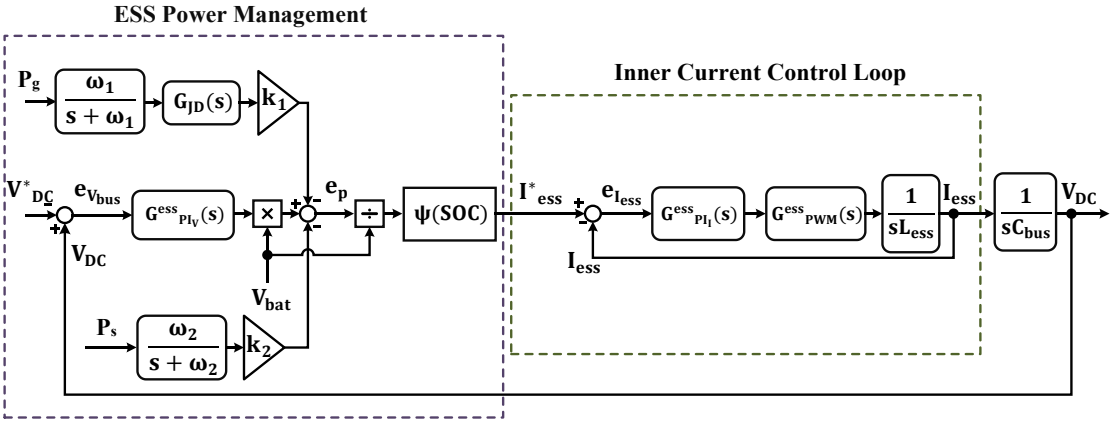

Fig. 5.5: Block diagram of the energy storage system control and management.

5.3.1 Stability Analysis

The transfer function of the whole ESS controller consists of the transfer function of the ESS PMS and the closed loop transfer function of the current controller. $G_{PWM}^{ess}(s)$ is the transfer function relating controller delay. $G_{PI_I}^{ess}(s)$ is the PI current controller.

$$G_{PWM}^{ess}(s) = \frac{1}{1 + 10T_s s} \tag{5.26}$$

$$G_{PI_I}^{ess}(s) = \frac{k_{p_I}^{ess} s + k_{i_I}^{ess}}{s} \tag{5.27}$$

L_{ess} is the ESS inductor. $k_{p_I}^{ess}$ and $k_{i_I}^{ess}$ are the proportional and integral gains of the ESS current controller. T_s is the sampling frequency. The closed loop transfer function of the current controller, $G_{cl_{ICCL}}^{ess}(s)$ is:

$$G_{cl_{ICCL}}^{ess}(s) = \frac{I_{ess}}{I_{ess}^*} = \frac{G_{PWM}^{ess}(s) * G_{PI_I}^{ess}(s) * \frac{1}{sL_{ess}}}{1 + G_{PWM}^{ess}(s) * G_{PI_I}^{ess}(s) * \frac{1}{sL_{ess}}} \tag{5.28}$$

e_p is the power related to the ESS charging and discharging power.

$$e_p(s) = P_{DC}(s) - G_{P_g}(s)P_g(s) - G_{P_s}(s)P_s(s) \tag{5.29}$$

$$P_{DC}(s) = V_{ess} * G_{PI_V}^{ess}(s) * e_{V_{bus}}(s) \tag{5.30}$$

$$G_{PI_V}^{ess}(s) = \frac{k_{p_V}^{ess} s + k_{i_V}^{ess}}{s} \tag{5.31}$$

$P_{DC}(s)$ is the power value obtained from the DC voltage controller output, $P_g(s)$ is the grid power, $G_{P_g}(s)$ is the transfer function related to the grid power, $P_s(s)$ is the sharing power, and $G_{P_s}(s)$ is the transfer function related to the sharing power. $G_{PI_V}^{ess}(s)$ is the transfer function of the DC voltage controller, $k_{p_V}^{ess}$ and $k_{i_V}^{ess}$ are the proportional and integral gains of the DC voltage PI controller, and $e_{V_{bus}}(s)$ is the DC voltage error.

$$G_{P_g}(s) = \frac{\omega_1}{s + \omega_1} * G_{JD}(s) * k_1 \tag{5.32}$$

$$G_{JD}(s) = \frac{1}{Js + D} \tag{5.33}$$

$$G_{P_s}(s) = \frac{\omega_2}{s+\omega_2} * k_2 \tag{5.34}$$

$G_{JD}(s)$ is the transfer function of the virtual-inertia, J is the inertia coefficient, and D is the damping factor. ω_1 and ω_2 are the coefficients related to the grid and sharing power low-pass filter. k_1 and k_2 are the coefficients associated with grid power and sharing power that convert total power error into equivalent ESS power to ensure proper power management of ESS. The transfer function between e_p and I_{ess} is given as follow:

$$\frac{I_{ess}}{e_p} = G^{ess}_{cl_{ICCL}}(s) * \psi(SoC) * \frac{1}{V_{ess}} \tag{5.35}$$

From the ESS control block,

$$I_{ess}(s) = G^{ess}_{cl_{ICCL}}(s) * \psi(SoC) * \frac{1}{V_{ess}} * e_p(s) \tag{5.36}$$

$$\begin{aligned} I_{ess}(s) = {} & G^{ess}_{cl_{ICCL}}(s) * \psi(SoC) * G^{ess}_{PI_V}(s) e_{V_{bus}}(s) - G^{ess}_{cl_{ICCL}}(s) * \psi(SoC) \\ & * \frac{1}{V_{ess}} * \frac{\omega_1}{s+\omega_1} * \frac{1}{Js+D} * k_1 * P_g(s) - G^{ess}_{cl_{ICCL}}(s) * \psi(SoC) \\ & * \frac{1}{V_{ess}} * \frac{\omega_2}{s+\omega_2} * k_2 P_s(s) \end{aligned} \tag{5.37}$$

There are three transfer functions in the ESS control system. The transfer function between $I_{ess}(s)$ and $e_{V_{bus}}(s)$; between $I_{ess}(s)$ and $P_g(s)$; and between $I_{ess}(s)$ and $P_s(s)$ can be obtained as

$$\left.\frac{I_{ess}(s)}{e_{V_{bus}}(s)}\right|_{P_g(s),\ P_s(s)=0} = G^{ess}_{cl_{ICCL}}(s) * \psi(SoC) * G^{ess}{}_{PI_V}(s) \tag{5.38}$$

Now the transfer function between DC voltage error and DC bus voltage can be obtained as follows:

$$G^{ess}_{VL}(s) = \frac{V_{DC}(s)}{e_{V_{bus}}(s)} = \frac{I_{ess}(s)}{e_{V_{bus}}(s)} * \frac{1}{sC_{bus}} \tag{5.39}$$

The closed loop transfer function,

$$G^{ess}_{cl_{VL}}(s) = \frac{V_{DC}(s)}{V^*_{DC}(s)} = \frac{G^{ess}_{cl}(s)}{1 + G^{ess}_{cl}(s)} \tag{5.40}$$

The characteristic equation of the $G^{ess}_{cl_{VL}}(s)$ transfer function is provided by:

$$10L_{ess}C_{bus}T_s s^5 + L_{ess}C_{bus}s^4 + k_{p_I}^{ess}C_{bus}s^3 + \left(k_{i_I}^{ess}C_{bus} + k_{pV}^{ess}k_{p_I}^{ess} * \psi(SoC)\right)s^2 + \left(k_{p_I}^{ess}k_{i_V}^{ess} + k_{pV}^{ess}k_{i_I}^{ess}\right) * \psi(SoC) * s + k_{i_I}^{ess}k_{i_V}^{ess} * \psi(SoC) = 0 \quad 5.41$$

The transfer function related to grid power is:

$$\left.\frac{I_{ess}(s)}{P_g(s)}\right|_{e_{V_{bus}}(s),\ P_s(s)=0} = -G_{cl_{ICCL}}^{ess}(s) * \psi(SoC) * \frac{1}{V_{ess}} * \frac{\omega_1}{s+\omega_1} * \frac{1}{Js+D} * k_1 \quad 5.42$$

$$G_{P_g}^{ess}(s) = \frac{I_{ess}}{P_g} = -\frac{\left(k_{p_I}^{ess}s + k_{i_I}^{ess}\right) * \psi(SoC) * \omega_1 * k_1}{(s+\omega_1) * V_{ess} * \left(10L_{ess}T_s s^3 + s^2 L_{ess} + k_{p_I}^{ess}s + k_{i_I}^{ess}\right) * (Js+D)} \quad 5.43$$

The characteristic equation of the $G_{P_g}^{ess}(s)$ transfer function is provided by:

$$(s+\omega_1) * \left(10L_{ess}T_s s^3 + s^2 L_{ess} + k_{p_I}^{ess}s + k_{i_I}^{ess}\right) * (Js+D) = 0 \quad 5.44$$

The poles related to the characteristic equation 4.44 can be obtained as follows:

$$\begin{gathered} s_1 = -\omega_1 \\ s_1 = -\frac{D}{J} \\ \left(10L_{ess}T_s s^3 + s^2 L_{ess} + k_{p_I}^{ess}s + k_{i_I}^{ess}\right) = 0 \end{gathered} \quad 5.45$$

The values of L_{ess}, T_s, $k_{p_I}^{ess}$, and $k_{i_I}^{ess}$ determine the poles s_3, s_4, and s_5. L_{ess} and T_s cannot cause the system to become unstable because they are positive values. To preserve stability, it's crucial to tune the PI current control precisely.

Pole s_1 corresponds to the low pass filter (LPF)'s cutoff frequency, which has an impact on how the system behaves. Nonetheless, the system is kept from becoming unstable by a positive cutoff frequency value. Ultimately, the s_2 analysis makes it evident that stability cannot be achieved until the virtual-inertia parameters take on positive values rather than null ones.

The transfer function related to sharing power is:

$$\begin{gathered} \frac{I_{ess}(s)}{P_s(s)} = -G_{cl_{ICCL}}^{ess}(s) * \psi(SoC) * \frac{1}{V_{ess}} * \frac{\omega_2}{s+\omega_2} * k_2 \\ G_{P_s}^{ess}(s) = \frac{I_{ess}(s)}{P_s(s)} = -\frac{\left(k^{ess}{}_{p_I}s + k^{ess}{}_{i_I}\right) * \psi(SoC) * \omega_2 * k_2}{(s+\omega_2) * V_{ess} * \left(10L_{ess}T_s s^3 + s^2 L_{ess} + k_{p_I}^{ess}s + k_{i_I}^{ess}\right)} \end{gathered} \quad 5.46$$

The characteristic equation of the $G_{P_s}^{ess}(s)$ transfer function is provided by:

$$(s + \omega_2) * \left(10L_{ess}T_s s^3 + s^2 L_{ess} + k_{p_I}^{ess} s + k_{i_I}^{ess}\right) = 0 \qquad 5.47$$

The poles s_2, s_3, and s_4 are related to the values of inductor, sampling frequency, and PI current controller values. Pole s_1 corresponds to the cutoff frequency of the sharing power's LPF.

5.3.2 Parameter Analysis

This subsection examines how system stability and performance are affected by parameter selections pertaining to the three transfer functions of the ESS control method.

5.3.2.1 Closed-loop Transfer Function of DC Bus Voltage

When the two inputs relating to grid power and sharing power are absent, the system response in both grid-connected and islanded modes is represented by the closed-loop transfer function of the DC bus voltage (see equation 4.40). Parameters related to this transfer function are the inductor (L_{ess}), DC bus capacitor (C_{bus}), sampling time (T_s), both the current and voltage controller's PI values, and the SoC management function ($\psi(SoC)$). The stability of the system is unaffected by the constant and positive values of the inductor, capacitor, and sampling period. The SoC-based management function has no effect on system stability because it merely determines how the controller functions and what extent the ESS performs under various SoC conditions. Finally, the proportional and integral values of both the current and voltage PI controllers have a significant impact on system performance. Therefore, these values need to be tuned carefully to maintain system stability and performance.

Different methods are employed to adjust the PI controller's values. The Ziegler-Nichols method, which exclusively uses parameters derived from the system step response, is the most widely used design technique [161]. Fig. 5.6 shows the impact of voltage PI controller on system performance. The system's step response shows that a proportional value larger than 9 ($k_{pV}^{ess} > 9$) can lead to

instability in the system. At $k_{pV}^{ess} = 9$, the system maintains the step response, but the response is full of transient oscillations. With the decrease in proportional gain, the oscillation decreases. At $k_{pV}^{ess} = 9$, the oscillation greatly decreases. When the k_{pV}^{ess} is set to 1, the oscillation disappears totally, but the system's response becomes slow. A higher value of integral gain causes overshoot in the system step response. Overshoot decreases when the value of integral gain decreases to a certain value. At $k_{pV}^{ess} = 1$ and $k_{iV}^{ess} = 2$, the system's step response becomes smooth.

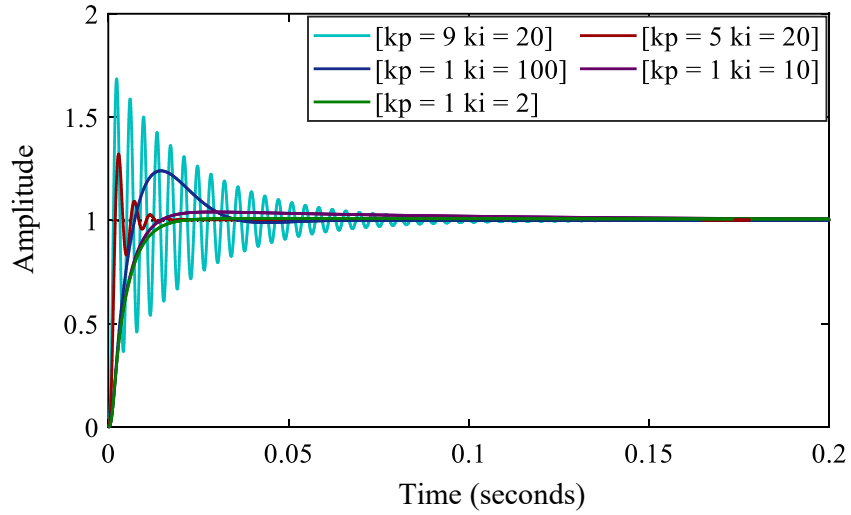

Fig. 5.6: Step response of the closed-loop DC voltage transfer function due to changes in the voltage PI controller.

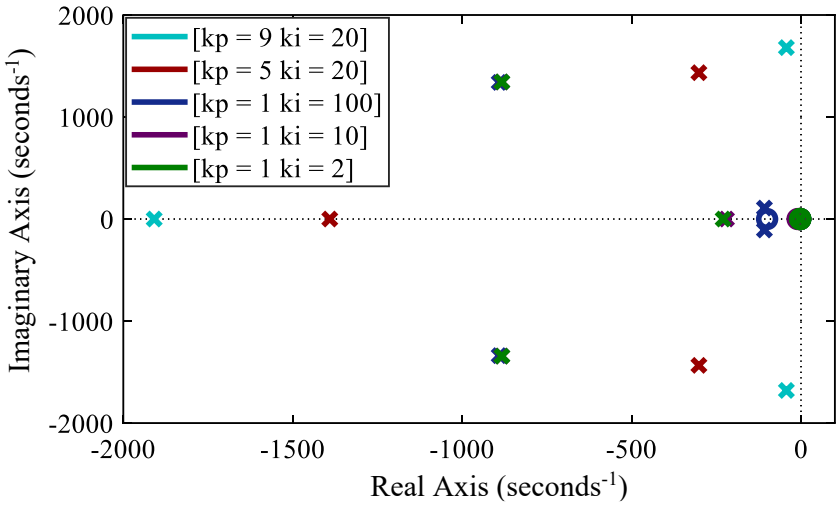

Fig. 5.7: Pole-zero map of the closed-loop DC voltage transfer function due to changes in the voltage PI controller.

The pole-zero map with different proportional and integral values of the voltage PI controller is displayed in Fig. 5.7. The map illustrates how system instability can result from a proportional value larger than 9 that moves the system pole to the right side of the plane. As the k_{pv}^{ess} decreases, the roots move further on the left side of the plane and restore system stability. The value of k_{iv}^{ess}, however, only has an impact on the system's transient performance; it has no effect on the poles shifting to the right.

Fig. 5.8 shows the impact of current PI controller on system performance. The system's step response shows that proportional values have a great impact on system performance and stability. A proportional value less than 0.5 ($k_{iv}^{ess} < 0.5$) causes system instability. At $k_{iv}^{ess} = 0.5$, the system maintains the step response, but the response is full of transient oscillations. With the increase in proportional gain, the oscillation decreases. At $k_{iv}^{ess} > 6$, the oscillation greatly decreases. When the k_{iv}^{ess} is set to 15, the oscillation disappears totally, but the system's response gets slow. However, the integral gain (k_{ii}^{ess}) doesn't have any impact on the system's stability.

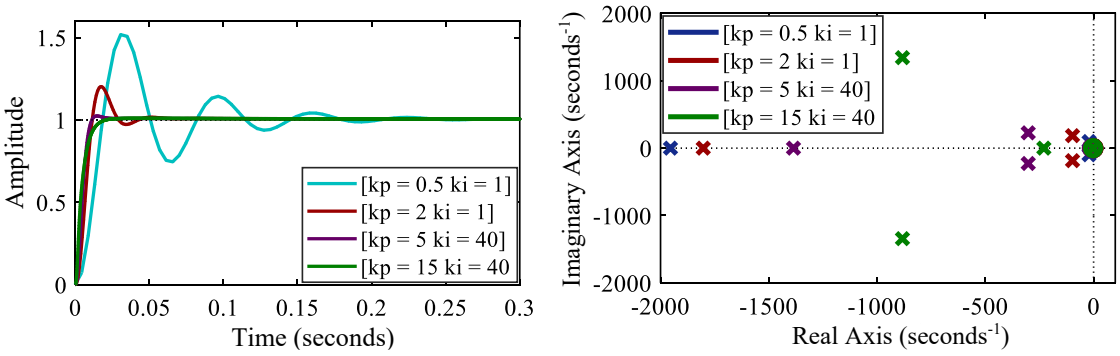

Fig. 5.8: Closed-loop DC voltage transfer function due to changes in the current PI controller: a) Step response, and b) Pole-zero map.

Fig. 5.9 displays the system response of the ESS controller for the DC bus voltage part. This response is obtained for certain and well-tuned values of both voltage and current in the PI controller ($k_{pv}^{ess} = 1$, $k_{pI}^{ess} = 2$, $k_{iv}^{ess} = 15$, and $k_{iI}^{ess} = 40$). For certain values of the PI controller, the gain margin is 21.2 dB and the

phase margin is 171.95 degrees. Moreover, the system and controller parameters under consideration result in a bandwidth of 29.1 Hz.

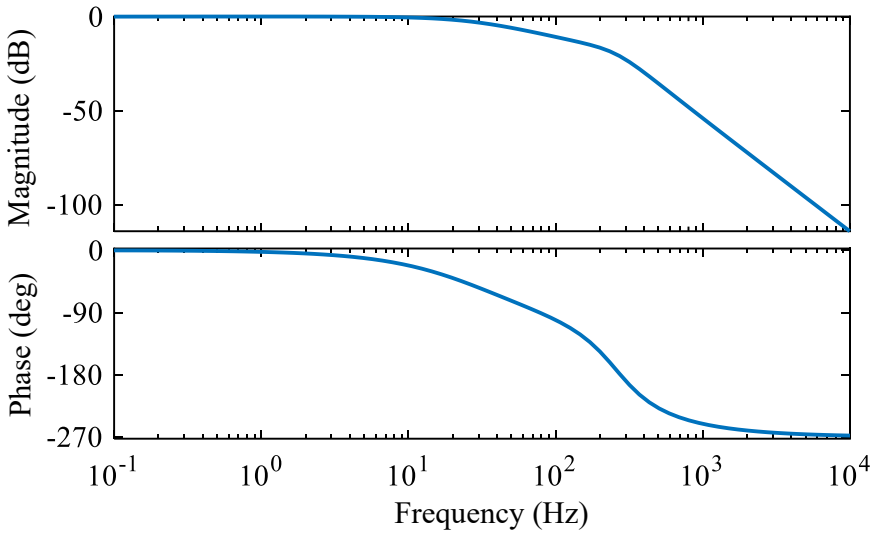

Fig. 5.9: Bode plot of the closed loop transfer function of DC bus voltage.

5.3.2.2 Transfer Function Related to Grid Power

In grid-connected systems, the transfer function of the grid power and ESS current (in equation 4.42) represents the system response when the two inputs associated with DC voltage error and sharing power are not present. Parameters related to this transfer function are the ESS voltage (V_{ess}), inductor (L_{ess}), LPF cutoff frequency (ω_1), sampling time (T_s), inertia coefficient (J), damping factor (D), the current controller's PI values, and the SoC management function ($\psi(SoC)$). The stability of the system is unaffected by the constant and positive values of the inductor, ESS voltage, and sampling period. Since the SoC-based management function only defines the controller's operation and the extent to which the ESS executes under different SoC situations, it has no impact on system stability. The proportional and integral values of the current PI controller have a significant impact on system performance and stability, which have already been analysed for DC bus voltage. Due to the overpowering effects of damping and inertia coefficients in this transfer function, the values of the current PI controller have little effect on the stability of the system. However, a very low value of

proportional gain needs to be avoided to maintain system stability. Therefore, the values of the current PI controller need to be tuned according to the DC bus voltage transfer function response, as accurate parameter tuning of these values can be impeded by the inertia transfer function.

It is evident from Fig. 5.10a that the parameter J modifies the ESS's inertia via influencing the system's time response. Larger values of J decrease response times, whereas smaller values make responses happen rapidly. In Fig. 5.10b, the mapping of the transfer function's poles, $G_{P_g}^{ess}(s)$, when J rises is illustrated. An undesirable stability margin results from forcing the dominant poles of $G_{P_g}^{ess}(s)$ toward the origin as J values increase. That is, with the increase in J, the pole's position is shifting in the direction of the origin.

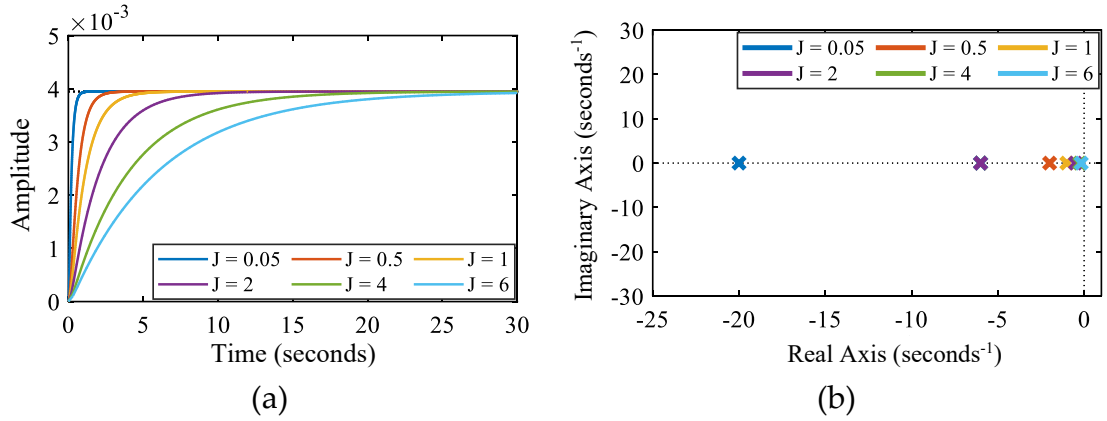

Fig. 5.10: Inertia coefficient variations: a) Step response, and b) Pole zero map.

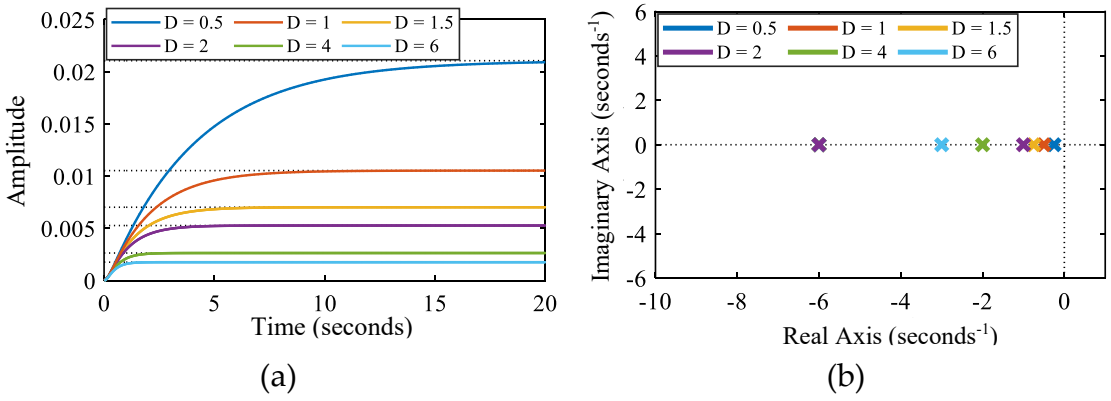

Fig. 5.11: Damping factor variations: a) Step response, and b) Pole zero map.

From Fig. 5.11a, it's clearly evident that for a certain value of J, modifying the parameter D leads to a steady-state value. D less than 1 results in a steady-state value bigger than anticipated, while a smaller steady-state response results from a value of D that is higher than 1. The dominant poles shift further from the origin as a result of increasing D values, as demonstrated in Fig. 5.11b.

In a nutshell, parameters J and D need to be non-null and positive. To prevent a little stability range in the system, values that are almost equal to zero are prohibited. The stability margin gets reduced by larger J values, but it is strengthened by greater D values. Therefore, a compromise between D and J must be explored to obtain the required behaviour of the system. Lastly, while D influences the steady-state response, parameter J influences the ESS time response. A decreased steady-state value is the result of higher D levels. In this study, $D = 1$ is utilized in order to obtain the anticipated steady-state value.

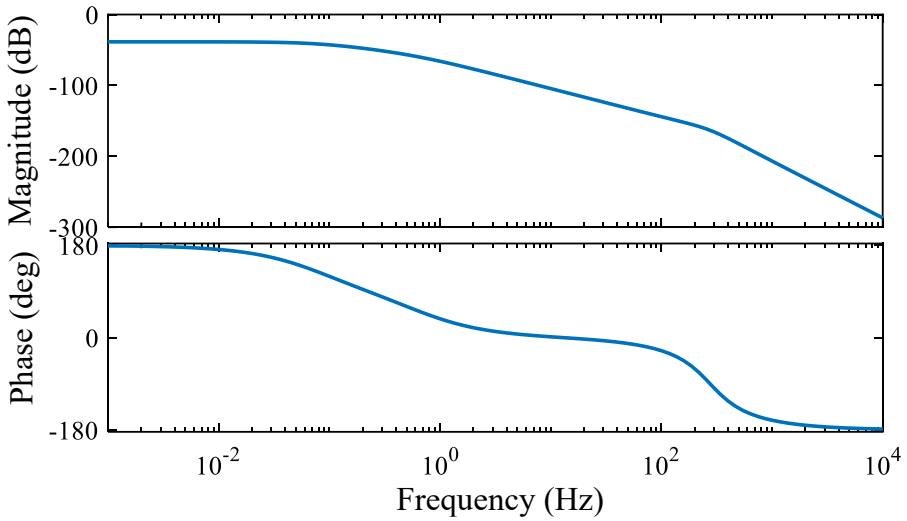

Fig. 5.12: Bode plot of the grid power-based transfer function.

Fig. 5.12 shows the system response of the ESS controller for the grid power part. This response is obtained for well-tuned values of current PI controller ($k_{i_V}^{ess} = 15$, and $k_{i_I}^{ess} = 40$), cutoff frequency ($\omega_1 = 4$), inertia coefficients ($j = 3, D = 1$), and gain ($k_1 = 4.5$). This open-loop transfer function provides stable operation with a gain margin of 38.5dB.

5.3.2.3 *Transfer Function Related to Sharing Power*

Parameters related to this transfer function (equation are the ESS voltage (V_{ess}), inductor (L_{ess}), LPF cutoff frequency (ω_2), sampling time (T_s), the current controller's PI values, constant gain (k_2), and the SoC management function ($\psi(SoC)$). The stability of the system is unaffected by the constant and positive values of the inductor, ESS voltage, gain, and sampling period. The SoC-based management function has no effect on system stability because it merely specifies how the controller operates and how much the ESS runs in various SoC scenarios. The system enters marginal stability at low values of the LPF cutoff frequency, ω_2. Consequently, while developing the filter, these values need to be considered. The effect of the proportional and integral values of the current PI controller has already been analysed in the DC bus voltage-based transfer function. To keep the system stable, a very low proportional gain value must be avoided; an integral value has no significance on stability. The values of the current PI controller require adjustment according to the DC bus voltage transfer function, since accurate tuning of these values is based on other transfer functions in the system.

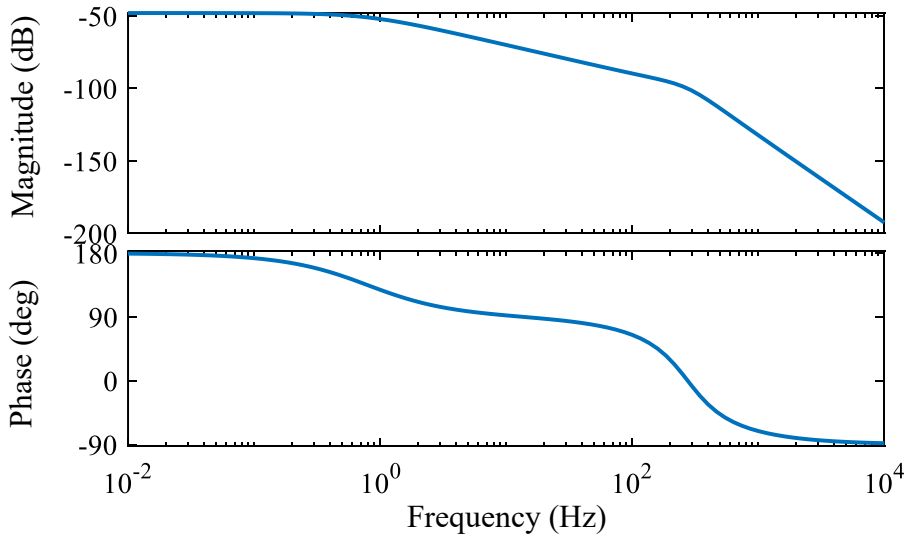

Fig. 5.13: Bode plot of the sharing power-based transfer function.

Fig. 5.13 shows the system response of the ESS controller for the sharing power part. This response is obtained for well-tuned values of current PI

controller ($k_{i_V}^{ess} = 15$, and $k_{i_I}^{ess} = 40$), cutoff frequency ($\omega_2 = 5$), and gain ($k_2 = 1.5$). This open-loop transfer function provides stable operation with a gain margin of 48.1dB.

The ESS controller's parameter analysis yields the following overview:

- Because of the increased proportional value of the DC bus voltage PI controller, the system's stability and response deteriorate. Overshoot is caused by a greater integral value of the DC voltage PI controller, although system stability is unaffected.
- With the decrease in the current PI controller's proportional gain, the system's response and stability degrade; however, the integral gain doesn't have any impact on the system's stability.
- The ESS time response is influenced by parameter J, while the steady-state response is influenced by D. The greater value of the inertia coefficient (J) and the smaller value of the damping factor (D) must not be permitted to prevent a narrow stability range in the system. As a result, to get the desired system behaviour, a compromise between J and D needs to be investigated.
- Since precise parameter tuning of these values can be based on other transfer functions in the system, the current PI controller values need to be adjusted in accordance with the DC bus voltage transfer function response.

5.4 STABILITY ANALYSIS OF THE INTERCONNECTING CONVERTER OF THE NETWORKED MICROGRIDS

The configuration and block diagram of the interconnecting converter control is shown in Fig. 5.14. A voltage control unit consists of the voltage parameters of HMG-2 (DC and AC voltages), and a current control unit constitutes the control system. The voltage control unit controls the power sharing between HMGs using a double-loop controller.

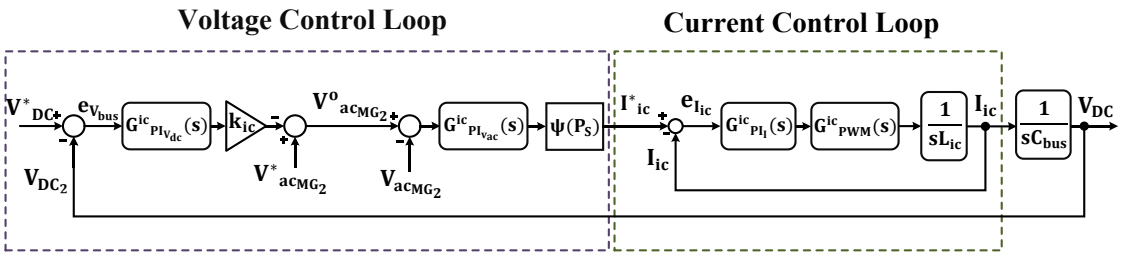

Fig. 5.14: Block diagram of the clustering converter control.

5.4.1 Stability Analysis

The transfer function of the whole controller consists of the transfer function of the voltage control loop and the current control loop. $G^{ic}_{PWM}(s)$ is the transfer function related to the converter controller delay. $G^{ic}_{PI_I}(s)$ is the PI current controller.

$$G^{ic}_{PWM}(s) = \frac{1}{1 + 10T_s s} \quad 5.48$$

$$G^{ic}_{PI_I}(s) = \frac{k^{ic}_{p_I} s + k^{ic}_{i_I}}{s} \quad 5.49$$

L_{ic} is the inductor. $k^{ic}_{p_I}$ and $k^{ic}_{i_I}$ are the proportional and integral gains of the current controller. T_s is the sampling time. The closed loop transfer function of the current controller, $G^{ic}_{cl_{ICCL}}(s)$ is:

$$G^{ic}_{cl_{ICCL}}(s) = \frac{I_{ic}}{I^*_{ic}} = \frac{G^{ic}_{PWM}(s) * G^{ic}_{PI_I}(s) * \frac{1}{sL_{ic}}}{1 + G^{ic}_{PWM}(s) * G^{ic}_{PI_I}(s) * \frac{1}{sL_{ic}}} \quad 5.50$$

The outer voltage control loop consists of the PI voltage controller of AC voltage, $G^{ic}_{PI_{v_{ac}}}(s)$, the PI voltage controller of DC voltage, $G^{ic}_{PI_{V_{dc}}}(s)$, and a proportional gain, k_{ic}.

$$G^{ic}_{PI_{v_{ac}}}(s) = \frac{k^{ic}_{p_{v_{ac}}} s + k^{ic}_{i_{v_{ac}}}}{s} \quad 5.51$$

$$G^{ic}_{PI_{V_{dc}}}(s) = \frac{k^{ic}_{p_{V_{dc}}} s + k^{ic}_{i_{V_{dc}}}}{s} \quad 5.52$$

Where $k^{ic}_{p_{v_{ac}}}$ and $k^{ic}_{i_{v_{ac}}}$ are the proportional and integral gain of the AC voltage PI controller. $k^{ic}_{p_{V_{dc}}}$ and $k^{ic}_{i_{V_{dc}}}$ are the proportional and integral gain of the

DC voltage PI controller. The transfer function of the whole IC controller, $G_{IC}(s)$, consists of the transfer function of the voltage controller, $G^{ic}_{outer}(s)$, and closed loop transfer function of the current control loop, $G^{ic}_{cl_{ICCL}}(s)$.

$$\begin{gathered} V^{o}_{ac_{MG_2}} = V^{*}_{ac_{MG_2}} - k_{ic} * G^{ic}_{PI_{V_{dc}}}(s) * e_{V_{bus}} \\ I^{*}_{ic} = \psi(P_S) * G^{ic}_{PI_{v_{ac}}}(s) * (V^{o}_{ac_{MG_2}} - V_{ac_{MG_2}}) \\ I^{*}_{ic} = \psi(P_S) * G^{ic}_{PI_{v_{ac}}}(s) * V^{*}_{ac_{MG_2}} - \psi(P_S) * G^{ic}_{PI_{v_{ac}}}(s) * k_{ic} * G^{ic}_{PI_{V_{dc}}}(s) \\ * e_{V_{bus}} - \psi(P_S) * G^{ic}_{PI_{v_{ac}}}(s) * V_{ac_{MG_2}} \end{gathered} \quad 5.53$$

$$\begin{gathered} I_{ic} = \Big(\psi(P_S) * G^{ic}_{PI_{v_{ac}}}(s) * V^{*}_{ac_{MG_2}} - \psi(P_S) * G^{ic}_{PI_{v_{ac}}}(s) * k_{ic} * G^{ic}_{PI_{V_{dc}}}(s) \\ * e_{V_{bus}} - \psi(P_S) * G^{ic}_{PI_{v_{ac}}}(s) * V_{ac_{MG_2}}\Big) * G^{ic}_{cl_{ICCL}}(s) \end{gathered} \quad 5.54$$

There are three transfer functions in the interconnecting converter control system. The transfer function between $I_{ic}(s)$ and $e_{V_{bus}}(s)$; between $I_{ic}(s)$ and $V^{*}_{ac_{MG_2}}(s)$; and between $I_{ic}(s)$ and $V_{ac_{MG_2}}(s)$ can be obtained as

$$\left.\frac{I_{ic}(s)}{e_{V_{bus}}(s)}\right|_{V^{*}_{ac_{MG_2}}(s),\ V_{ac_{MG_2}}(s)=0} = -\psi(P_S) * G^{ic}_{PI_{v_{ac}}}(s) * k_{ic} * G^{ic}_{PI_{V_{dc}}}(s) * G^{ic}_{cl_{ICCL}}(s) \quad 5.55$$

Now the transfer function between DC voltage error and DC bus voltage can be obtained as follows:

$$G^{ic}_{VL}(s) = \frac{V_{DC}(s)}{e_{V_{bus}}(s)} = \frac{I_{ic}(s)}{e_{V_{bus}}(s)} * \frac{1}{sC_{bus}} \quad 5.56$$

The closed loop transfer function,

$$G^{ic}_{cl_{VL}}(s) = \frac{V_{DC}(s)}{V^{*}_{DC}(s)} = \frac{G^{ic}_{cl}(s)}{1 + G^{ic}_{cl}(s)} \quad 5.57$$

The transfer function related to AC reference voltage is:

$$\left.\frac{I_{ic}(s)}{V^{*}_{ac_{MG_2}}(s)}\right|_{e_{V_{bus}}(s),\ V_{ac_{MG_2}}(s)=0} = \psi(P_S) * G^{ic}_{PI_{v_{ac}}}(s) * G^{ic}_{cl_{ICCL}}(s) \quad 5.58$$

The characteristic equation of the AC reference voltage-based transfer function is provided by:

$$s(s^3 10 L_{ic} T_s + s^2 L_{ic} + k^{ic}_{p_I} s + k^{ic}_{i_I}) = 0 \quad 5.59$$

The poles related to the characteristic equation 4.60 can be obtained as follows:

$$s_1 = 0$$
$$s^3 10 L_{ic} T_s + s^2 L_{ic} + k_{p_I}^{ic} s + k_{i_I}^{ic} = 0 \quad 5.60$$

The values of L_{ic}, T_s, $k_{p_I}^{ic}$, and $k_{i_I}^{ic}$ determine the all poles. L_{ic} and T_s cannot cause the system to become unstable because they are positive values. To preserve stability, it's crucial to tune the PI current control precisely.

The transfer function related to AC voltage is:

$$\left.\frac{I_{ic}(s)}{V_{ac_{MG_2}}(s)}\right|_{e_{V_{bus}}(s),\ V^*_{ac_{MG_2}}(s)=0} = -\psi(P_S) * G_{PI_{v_{ac}}}^{ic}(s) * G_{cl_{ICCL}}^{ic}(s) \quad 5.61$$

With the exception of a negative sign difference, the transfer function of the AC voltage and the AC reference voltage are the same.

5.4.2 Parameter Analysis

The impact that parameter selections for the three transfer functions of the clustering converter control method have on system performance and stability is examined in this subsection.

5.4.2.1 Closed-loop Transfer Function of DC Bus Voltage

The closed-loop transfer function of the DC bus voltage (refer to equation 4.57) represents the system response in the absence of the two inputs corresponding to the AC reference voltage and the AC measurement voltage of HMG-2. Parameters related to this transfer function are the inductor (L_{ic}), DC bus capacitor (C_{bus}), sampling time (T_s), both the current and voltage controller's PI values, and the power management function ($\psi(P_s)$). The stability of the system is unaffected by the constant and positive values of the inductor, capacitor, and sampling period. The power management function has no effect on system stability because it merely determines how the controller functions and what extent the parallel BDC framework performs. Finally, the proportional and

integral values of both the current and voltage PI controllers have a significant impact on system performance. Therefore, these values need to be tuned carefully to maintain system stability and performance.

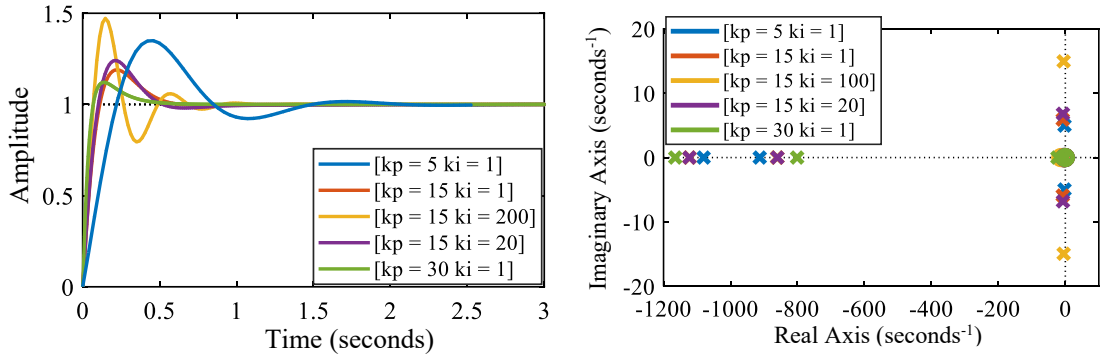

(a) (b)

Fig. 5.15: The closed-loop DC voltage transfer function due to changes in the DC voltage PI controller: a) Step response; b) Pole zero map.

Fig. 5.15a shows the impact of the voltage PI controller on system performance for a fixed value of gain, the current PI controller, and the AC voltage PI controller. The system's step response shows that for a fixed value of gain ($k_{ic} = 0.01$) and integral value ($k_{iv}^{ic} = 1$), a proportional value lower than 1 ($k_{pv}^{ic} < 1$) can lead to instability in the system. At $k_{pv}^{ic} = 5$, the system maintains the step response, but the response is full of transient oscillations. With the increase in proportional gain, the oscillation decreases. At $k_{pv}^{ic} > 10$, the oscillation greatly decreases. When the k_{pv}^{ic} is set to 30, the oscillation almost disappears. However, for a fixed value of gain ($k_{ic} = 0.01$) and proportional value ($k_{pv}^{ic} = 15$), a higher integral value causes a higher transient oscillation. That is, a higher value of integral gain causes overshoot in the system step response. Overshoot decreases when the value of integral gain decreases to a certain value. At $k_{pv}^{ic} = 30$ and $k_{iv}^{ic} = 1$, the system's step response becomes smooth. The pole-zero map with different proportional and integral values of the voltage PI controller is displayed in Fig. 5.15b. The map illustrates how system instability can result from a proportional value lower than 1 that moves the system pole to the right side of the plane. As the k_{pv}^{ic} increases, the roots move

further on the left side of the plane and restore system stability. The value of k_{iV}^{ic}, however, only has an impact on the system's transient performance; it has no effect on the poles shifting to the right.

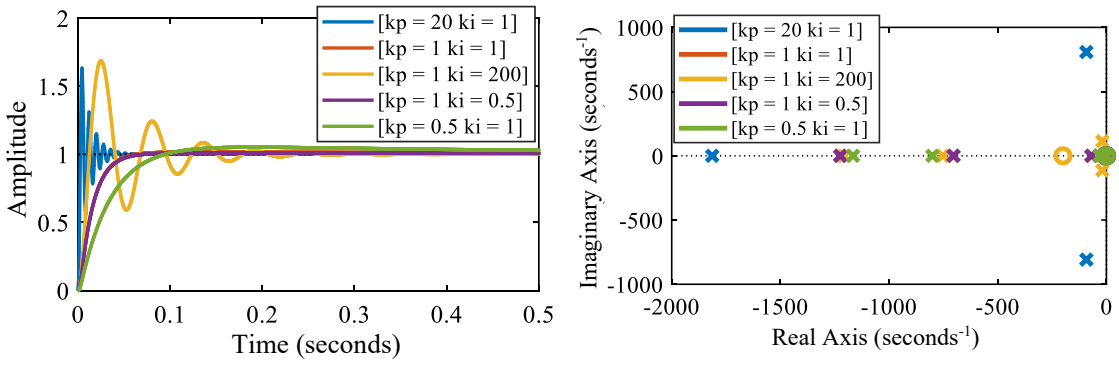

(a) (b)

Fig. 5.16: The closed-loop DC voltage transfer function due to changes in the AC voltage PI controller: a) Step response; b) Pole zero map.

Fig. 5.16a shows the impact of AC voltage PI controller on system performance. The system's step response shows that both proportional and integral values have a great impact on system performance and stability. The system's step response shows that for fixed values of DC voltage PI controller (), a fixed value of gain ($k_{ic} = 0.01$) and integral value ($k_{i_{vac}}^{ic} = 1$), a proportional value higher than 30 ($k_{p_{vac}}^{ic} > 30$) can lead to instability in the system. At $k_{p_{vac}}^{ic} = 30$, the system maintains the step response, but the response is full of transient oscillations. With the decrease in proportional gain, the oscillation decreases. At $k_{p_{vac}}^{ic} > 5$, the oscillation greatly decreases. When the $k_{p_{vac}}^{ic}$ is set to 1, the oscillation disappears totally. Moreover, the integral value has a great impact on stability. For example, for fixed values of DC voltage PI controller ($k_{pV}^{ic} = 30$ and $k_{iV}^{ic} = 1$), a fixed value of gain ($k_{ic} = 0.01$) and proportional value ($k_{p_{vac}}^{ic} = 1$), an integral value higher than 300 ($k_{i_{vac}}^{ic} > 300$) can lead to instability in the system. At $k_{i_{vac}}^{ic} = 300$, the system maintains the step response, but the response is full of transient oscillations. With the decrease in integral gain, the oscillation decreases. The pole-zero map with different proportional and integral values of the voltage

PI controller is displayed in Fig. 5.16b. The map illustrates how system instability can result from a proportional value higher than 30 that moves the system pole to the right side of the plane. As the $k_{p_{v_{ac}}}^{ic}$ decreases, the roots move further on the left side of the plane and restore system stability. The value of $k_{i_{v_{ac}}}^{ic}$ has an impact on the system's transient performance and stability; therefore, shifting to the right the poles due to an increase in values greater than 300.

Fig. 5.17a shows the impact of the current PI controller on system performance. The system's step response shows that both proportional and integral values have a great impact on system performance and stability. The system's step response shows that for fixed values of DC voltage PI controller ($k_{pV}^{ic} = 30$ and $k_{iV}^{ic} = 1$), fixed values of AC voltage PI controller ($k_{p_{v_{ac}}}^{ic} = 0.5$ and $k_{i_{v_{ac}}}^{ic} = 1$), a fixed value of gain ($k_{ic} = 0.01$) and integral value ($k_{i_{v_{ac}}}^{ic} = 1$), a proportional value lower than 0.05 ($k_{p_{v_{ac}}}^{ic} > 0.05$) can lead to instability in the system. With the increase in proportional gain, the system starts to maintain the step response and the oscillation decreases. Moreover, the integral value has a great impact on stability. For example, for fixed values of DC voltage PI controller (), a fixed value of gain ($k_{ic} = 0.01$) and proportional value ($k_{p_{v_{ac}}}^{ic} = 5$), a higher integral value can lead to instability in the system. With the decrease in integral gain, the oscillation decreases. The pole-zero map with various proportional and integral values of the voltage PI controller is displayed in Fig. 5.17b. The map illustrates how system instability can result from a lower proportional value that moves the system pole to the right side of the plane. As the $k_{p_i}^{ic}$ increases, the roots move further on the left side of the plane and restore system stability. The value of $k_{i_i}^{ic}$ has an impact on the system's transient performance and stability; therefore, shifting to the right the poles due to an increase in values. Therefore, a compromise between $k_{p_i}^{ic}$ and $k_{i_i}^{ic}$ must be explored to obtain the required behaviour of the system.

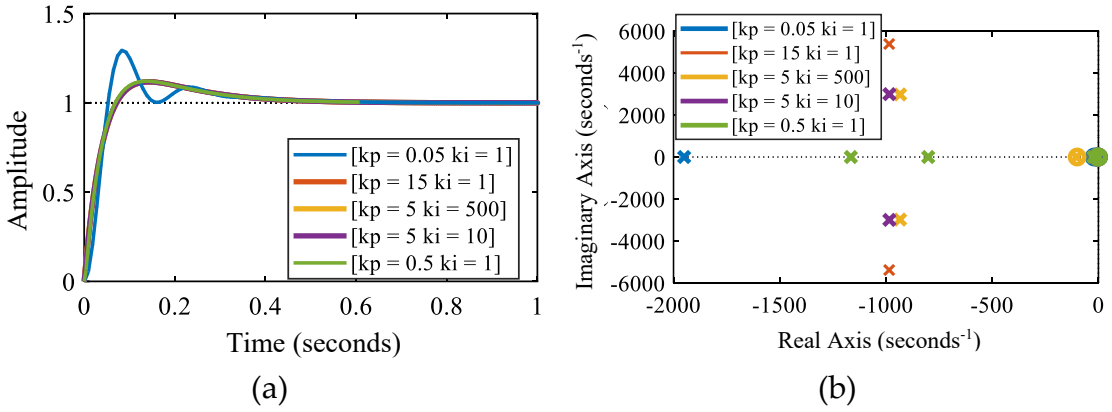

Fig. 5.17: The closed-loop DC voltage transfer function due to changes in the current PI controller: a) Step response; b) Pole zero map.

Fig. 5.18 displays the system response of the clustering converter controller for the DC bus voltage part. This response is obtained for certain and well-tuned values of both voltage and current in the PI controller ($k_{pV}^{ic} = 30$, $k_{pI}^{ic} = 0.5$, $k_{p_{vac}}^{ic} = 0.5$, $k_{iV}^{ic} = 1$, $k_{iI}^{ess} = 1$, and $k_{i_{vac}}^{ic} = 3$). For certain values of the PI controller, the gain margin is 34.8 dB and the phase margin is 85.2 degrees. Moreover, the system and controller parameters under consideration result in a bandwidth of 7.49 Hz.

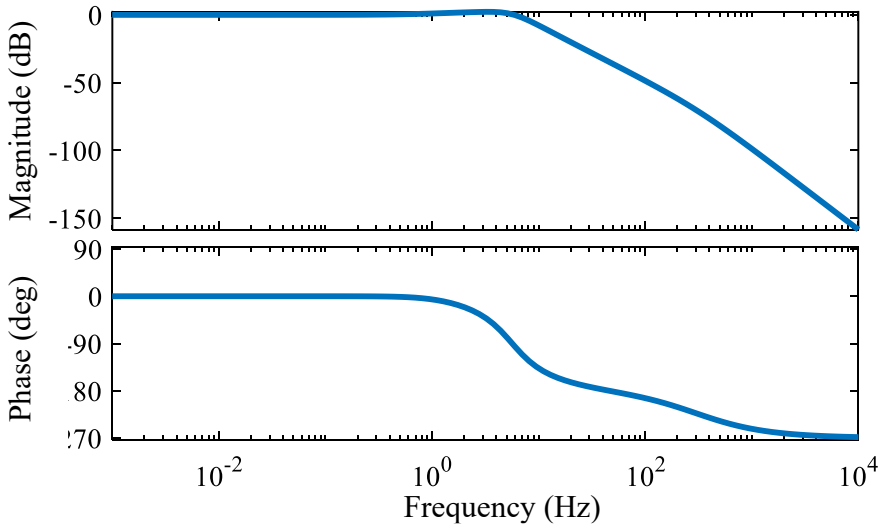

Fig. 5.18: Bode plot of the closed loop transfer function of DC bus voltage.

5.4.2.2 Transfer Function Related to AC Reference and Measured Voltages

The transfer function of the AC reference and AC measured voltage (in equation 4.59 and equation 4.62) represents the system response when the DC

bus voltage inputs is not present. Parameters related to this transfer function are the DC bus voltage (V_{DC}), inductor (L_{ic}), sampling time (T_s), the voltage and current controller's PI values, and the power management function ($\psi(P_s)$). The stability of the system is unaffected by the constant and positive values of the inductor, DC voltage, and sampling period. Since the power management function only defines the controller's operation, it has no impact on system stability. The proportional and integral values of the current PI controller have a significant impact on system performance and stability, which have already been analysed for DC bus voltage.

Fig. 5.19 shows the system response for the AC voltage part. This response is obtained for well-tuned values of current PI controller ($k_{p_I}^{ic} = 0.5$, $k_{p_{v_{ac}}}^{ic} = 0.5$, $k_{i_I}^{ess} = 1$, and $k_{i_{v_{ac}}}^{ic} = 3$), and gain ($k_{ic} = 0.01$). This open-loop transfer function provides stable operation with a phase margin of 118dB.

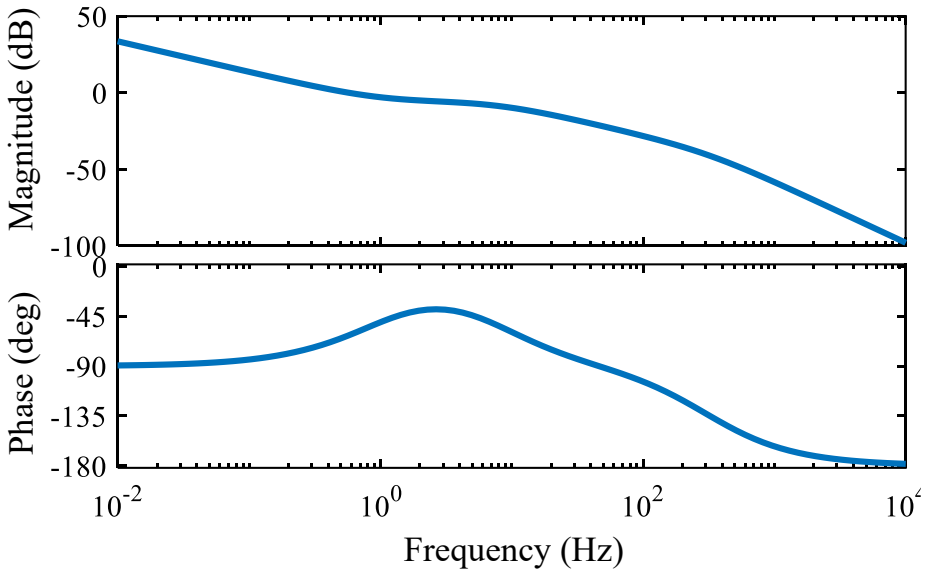

Fig. 5.19: Bode plot of the grid power-based transfer function.

The parameter analysis of the clustering converter control provides the following summary:

- A lower value of proportional gain in the DC voltage PI controller creates system instability. The oscillation diminishes and the system

stability margin grows as the DC voltage PI controller's proportional gain rises. On the other hand, the degree of integral gain does not affect the poles shifting to the right; rather, it simply affects the system's transient performance. In other words, overshoot in the system step response results from a higher integral gain value.

- The gain (k) has to be chosen precisely to maintain system stability. A lower value of k causes system instability.
- The stability and performance of the system are significantly impacted by the proportional and integral values of the AC voltage PI controller. The system becomes unstable when the proportional or integral value increases. The oscillation lessens and stability is restored when the proportional and integral gain decrease.
- A lower proportional value of the current PI controller can lead to instability in the system. With the increase in proportional gain, the system starts to maintain the step response, and the oscillation decreases. Moreover, the integral value has a great impact on stability. For example, a higher integral value can lead to instability in the system. With the decrease in integral gain, the roots move further on the left side of the plane and restore system stability.

The current PI controller values must be modified in line with the DC bus voltage transfer function response since exact parameter tuning of these values may be dependent on other transfer functions in the system.

5.5 SUMMARY

This chapter analyses the stability of the three proposed control strategies related to the interlinking converter of HMG, ESS control, and clustering converter.

A state-space model of each control block is developed in order to examine the small-signal stability of the enhanced droop-based dual voltage control of the

interlinking converter. The LCL filter dynamics, voltage control for current reference generation, current control with feedforward and active damping signals, and droop control for frequency regulation complete the controller.

In order to assess the stability of the proposed ESS management and control, the required transfer functions pertaining to the different variables in the controller are configured. The inner current controller, which generates switching signals, and the outer ESS management control, which generates the reference current, constitute a significant part of the entire control strategy.

A dual voltage-based outer controller and an inner current controller serve as the clustering converter's control technique. In order to evaluate the effectiveness of the suggested control of the connecting converter, all required transfer functions are established and analysed.

Chapter 6

COMPARATIVE ANALYSIS WITH PREVIOUS CONTROL STRATEGIES

6.1 INTRODUCTION

A crucial aspect in analysing the performance of converter control strategies is comparative analysis, which helps to highlight a controller's positive aspects by distinguishing it from other existing systems. This chapter presents the necessary comparison of the three converter systems with proposed control strategies with other existing control methods.

6.2 INTERKLINKING CONVERTER OF HYBRID MICROGRID

A particular kind of MG depending on both DC and AC busbars, known as HMG, is an effective framework with the utilization and facilities of both AC and DC electric powers from both the load and generating sides [162]. The HMG is developing at an impressive rate due to the benefits of AC and DC MGs, respectively. The bidirectional interlinking VSC serves as the interface between the DC and AC MGs found in the HMG. An HMG can operate in either on-grid or off-grid modes. To exchange power with the main grid under usual conditions and protect the MG and loads in the event of a grid failure, the HMG's interlinking converter must be controlled and operated in order to achieve a quick, reliable, and seamless transition between on- and off-grid modes. The independent control of interlinking converters in off-grid mode is crucial for the development of HMG since it is primarily responsible for facilitating the transfer

of power between AC and DC MGs by keeping frequency and voltage within allowable ranges [51].

6.2.1 Comparative Analysis with Conventional $P-f$ and $Q-V$ Droop Control and AC Voltage-based Voltage Controller

The droop control strategy is a well-known approach for load sharing with several advantages, such as a plug-and-play functionality, communication-free energy distribution, and improved flexibility. Reactive power-voltage ($Q-V$) and active power-frequency ($P-f$) droop control schemes are extensively employed in interlinking converters of HMGs.

6.2.1.1 Structural Difference with Conventional Droop

The $P-f/Q-V$ and $P_{DC}-V_{DC}$ droop control techniques are used for the AC and DC MGs, separately, in the HMG control approach described in [163], which is referred to as the traditional control strategy in this article. Regulating the power transfer through the interlinking converter enables both AC and DC DERs to adjust the variations in demand in each MG, thereby coordinating the operation of DC and AC MGs.

The control strategy of a conventional droop control consists of three controllers: a power controller, a voltage controller, and a current controller. The power controller includes the droop characteristics expressed in equations (1) and (2), which indicate that an abrupt power supply imbalance will result in variations to the AC MG's voltage and frequency and DC MG's voltage [164].

$$\omega_{ac} = \omega^{*}{}_{ac} - m_p P_{AC} \qquad v_{AC} = v_{AC}^{*} - n_q Q \qquad 6.1$$

$$V_{DC} = V_{DC}^{*} - m_{DC} P_{DC} \qquad 6.2$$

Where ω_{ac}, and $\omega^{*}{}_{ac}$ are the measured and reference angular frequency, v_{ac}, and $v^{*}{}_{ac}$ are the measured and reference AC bus voltage, P_{AC} and Q are the measured active and reactive power, V_{DC}, and V_{DC}^{*} are the measured and reference DC bus voltage, P_{DC} is the measured DC power. m_p, n_q and m_{DC} is the droop

gains. To ensure precise power-sharing in various circumstances, the droop gain is properly selected. Only the AC bus voltage-based control is included in the voltage control to provide the reference current necessary for power sharing. As such, using the same controller operation in grid-connected mode is not feasible.

This study presents an improved control technique for the interlinking converters of the two HMGs in the interconnected system, which facilitates proper operation in three operating modes along with a smooth transition between islanding and grid-connected modes. The suggested approach minimizes the delay related to power computation and averaging by directly using voltage and frequency instead of active and reactive power in the droop characteristics. The voltage-frequency ($V - f$)-based droop controller, along with the DC and AC voltage-based voltage controllers, adjusts the power transfer between the AC and DC MGs.

6.2.1.2 Comparative Analysis Based on Simulation Results

Simulation outcomes employing both conventional and proposed droop control strategies for a HMG with a 125kW capacity (designed in Chapter 3) are provided to demonstrate the efficacy of the interlinking converter's suggested control strategy. The wind generation and PV generation are maintained at a specific speed (14 m/s) and solar irradiances (1000 W/m^2). The simulation is performed only in islanded mode, as the conventional droop control with an AC voltage controller cannot operate in grid-connected mode.

Fig. 6.1 and Fig. 6.2 depict the control performance of the interlinking converter with both controllers, where the HMG is operated in off-grid mode along with transient events such as load variations on the AC side. On the AC side, a 30kW resistive-inductive (RL) load is added in order to examine the performance during variations in load. Results in Fig. 6.1 demonstrate that by providing a quick and damped dynamic response, the suggested technique minimizes the transient overshoots of DER's output powers caused by changes

in load. Additionally, the performance in steady-state conditions is quite smooth and causes less fluctuation. Instead, the traditional methods result in output power, frequency, and voltage overshoots during startup and load fluctuations.

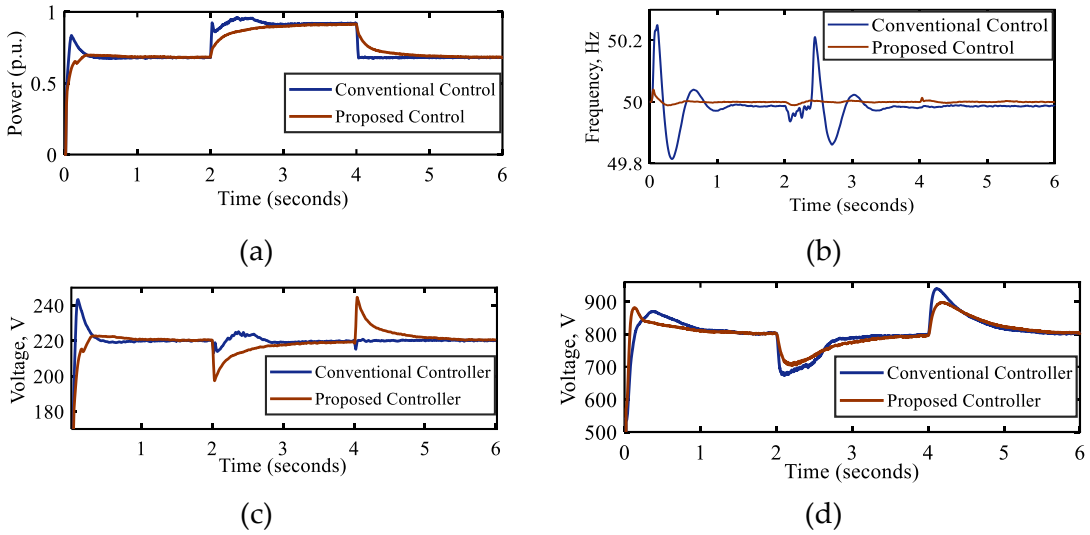

Fig. 6.1: Control performance of the interlinking converter of the HMG with both controllers: a) Load power in per unit, b) Frequency, c) AC rms voltage, and d) DC bus voltage.

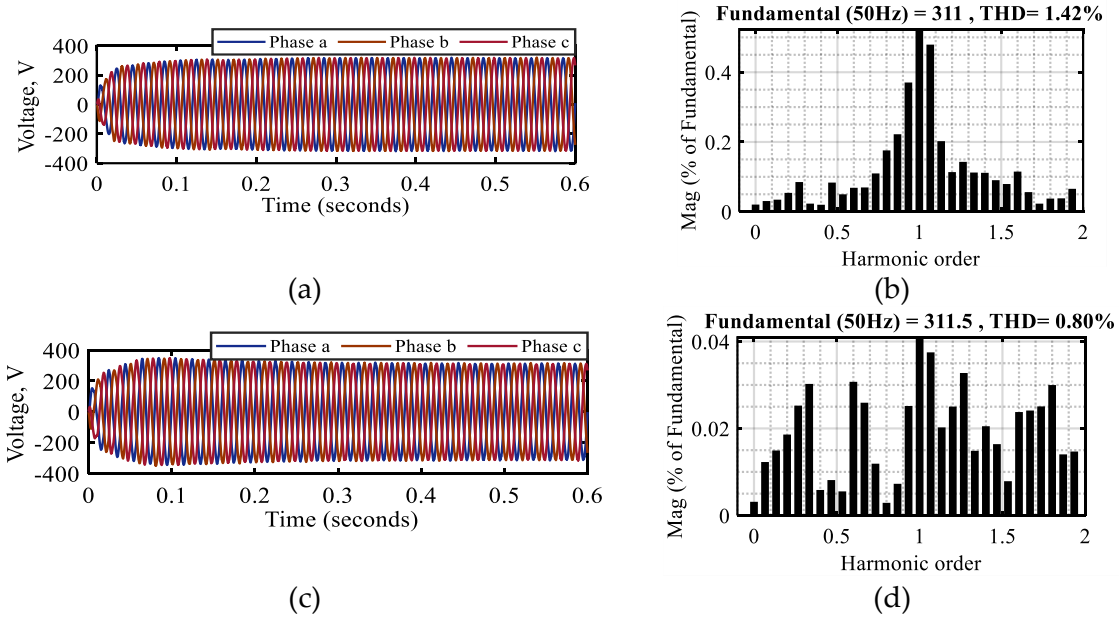

Fig. 6.2: Control performance of the interlinking converter of the HMG with both controllers: a) Waveform of AC bus voltage under the conventional controller, b) THD under the conventional controller, c) Waveform of AC bus voltage under the proposed controller, and d) THD under the proposed controller.

Fig. 6.2b shows the THD value of the three-phase AC bus voltages with a conventional controller, which is 1.41%. Fig. 6.2d shows that with the proposed

controller, the AC-bus voltages are sinusoidal and well-balanced, with a low THD value of 0.80%. These findings show that the suggested control system outperforms the conventional droop control approach (described in [165]).

6.2.2 Comparison with Relevant Control Strategies of Interlinking Converter

Numerous control strategies for interlinking converters are examined in the existing literature, considering many aspects including power flow regulation, stability, load types, operations, and power quality. An improved control technique for the HMG's interlinking converter is proposed in [166] to address the converter's nonlinear properties, facilitate a smooth transition between grid-connected and islanded modes, and enhance power quality. In [167], the distribution of power among all DGs is implemented without the requirement for extra PI controllers through the use of a distributed active power management approach for interlinking converters in an islanding HMG. Hardware-in-the-loop (HiL) implementation of an integrated control strategy with various control levels to regulate power management and DC and AC voltages in hierarchically controlled HMG is proposed in [168]. The hierarchical control of HMG consists of the decentralized and centralized layers, which permit the communication fault ride-through ability and mitigate the negative consequences of communication difficulties. For HMG, a novel interlinking converter architecture is suggested in [169], which consists of a converter connected in series with a static VAR compensator and an improved droop control. $P-\delta$ and $Q-P-V$ droop for active and reactive power regulation, as well as $P-Q-\alpha$ droop control for the static VAR compensator, comprise the droop control. In [102], a simplified droop structure of interlinking converters for control and power exchange in an autonomous HMG is proposed. An equivalent mathematical model that calculates how changes in load affect frequency and DC voltage is also provided. Without requiring any kind of communication, the suggested design permits independent power exchange in either direction.

Table 6.1: Comparison with the formerly developed hybrid microgrid's interlinking converter control strategies

Ref.	Operation			Number of Controllers	THD (%)	With dynamic load	Controller Delay	Flexibility in power variations
	GC	IS	IMG					
[166]	✓	✓	✗	Two (Different in IS and GC)	2.7	Not analysed	PLL, power calculation and two controllers	Not Analysed
				Remarks	A smooth transition between GC and IS modes; Reduced grid current distortion			
[167]	✗	✓	✗	Single	Not given	Not analysed	Power calculation	Not Analysed
				Remarks	Proper power sharing; Reduced number of PI controllers; Method for parameter estimation			
[168]	✓	✓	✗	Single	Not given	Not analysed	Power calculation	Ensured
				Remarks	Prevent unsmooth transitions; Mitigate communication faults; Improve resilience and reliability			
[169]	✗	✓	✗	Converter with SVC	3	Not analysed	Power calculation	Ensured
				Remarks	Quick harmonic compensation; Proper power regulation; Robust controller;			
P	✓	✓	✓	Single	0.80	Less power oscillation	No power calculation and PLL delays	Ensured
				Remarks	Robust and reliable controller; Less control delay; Flexible operation under various modes; Seamless transition; Better power quality			

GC	Grid-connected	**IS**	Islanded	**IMG**	Interconnected microgrid
THD	Total harmonic distortion	**P**	Proposed	**PI**	Proportional integral
PLL	Phase locked loop			**SVC**	Static VAR compensator
✓	Applicable	✗	Not Applicable		

The suggested controller performs well in steady-state situations, controlling the power from the main grid in the on-grid mode or sustaining the AC and DC-bus voltages in the isolated mode in response to a specific percentage of dynamic loads, fluctuations in load conditions, DG failures, and source power variations. Furthermore, despite operating modes, a smooth transition between on-grid and off-grid modes is realized without switching between two controllers. The suggested method, in comparison with prevailing control techniques, uses output voltage measurements directly in the control loops and does not require power calculations or load current control. As a result, the feedback signal delay, measurement delay, and sensor requirement are reduced, enabling precise load allocation during transients. The results of a simulation

conducted on an HMG show that the proposed control strategy is effective for power flow control in an HMG with a lower value of the AC bus voltage's THD, which is about 0.80%. Table 6.1 presents a comparison of the proposed control strategies [166-169] of the interlinking converter with some previously introduced control strategies based on various factors, such as the ability to operate in three modes, THD, dynamic load analysis, communication, system delay, and flexibility in operations. The comparative analysis in Table 6.1 shows that the designed control strategy of the interlinking converter produces superior outcomes in several aspects compared to some earlier studies in this field.

6.3 ENERGY STORAGE SYSTEM CONTROLLER

The dependable operation of the energy infrastructure is facing various issues as a result of the expanding MG systems' integration into the electrical network. Under various grids, loads, and RES circumstances, the power system must keep the frequency and voltage within the allowed ranges. Under these situations, an ESS is necessary for the critical and frequency-sensitive loads to operate effectively.

To manage the power flow in a DC MG working in grid-tied mode and to regulate the charging and discharging process of the battery bank-based ESS according to the power supply, a PMS utilizing a virtual inertia concept and a SoC-based management mechanism is provided in [42]. By minimizing the high-rate power peaks, the suggested technique enhances the ESS life cycle and creates an independent power transfer within the DC MG. Another PMS for ESS is suggested in [103], which enhances an HMG's power quality. To provide stable voltage in the DC bus, the ESS, equipped with a droop-based power flow control, is linked to the DC bus between the two converter levels. In [170], the ESS is scheduled to operate in a grid-supportive way, considering the safe SoC bounds. To offer smooth MG operation with prioritized load shedding and power quality enhancement during unusual circumstances, a suitable grid-adaptive PMS is

proposed to provide current references for MG-connected converters. In [171], an improved droop control approach is used to provide a decentralized SoC control technique where each ESS's SoC is balanced in the discharge process. When this control approach is applied, the storage device with a higher SoC supports the load with more power, whereas the one with the lowest SoC supports the load with less power. Each converter's output power will therefore be proportionate to each ESS's SoC level. To improve system reliability, hierarchical control of hybrid ESS, which combines centralized and distributed control, is suggested in [172]. To reduce bus voltage fluctuation and restrict slack terminal SoC instability, secondary voltage control and independent SoC recovery are used.

An independent and smooth power flow is accomplished inside each individual MG and MG cluster in on-grid mode with the proposed ESS management and control, whereas the AC main grid solely concentrates on maintaining the DC bus and handling the excess or deficit of power. During transient responses, the system's inertia is increased due to the virtual inertia approach used in ESS control. The SoC-based management enhances the battery bank lifespan by preventing the overcharging or discharging of the battery bank by restricting the ESS function to secure levels. Various activation processes for the mode changes are not required with this integrated control and management framework in response to the necessary condition adjustments. As a result, adverse effects like an uneven transition and system failure due to an imprecise switching can be prevented. Table 6.2 compares the formerly introduced controls and management [42, 170-172] with the designed virtual-inertia-based ESS control in each HMG based on various factors, including the number of controllers required, power reference requirements, the ability to operate in three modes, flexibility in operations, and computation delays. The comparative analysis in Table 6.2 shows that the proposed control and management system produces superior performance in several aspects compared to the prior research.

Table 6.2: Comparison with the previously developed controller of energy storage system

Ref.	Operation			Transfer of Data	MG Type	Control Stages	Control Mode	Controller Delay	Flexibility in power variations
	GC	IS	IMG						
[42]	✓	✓	×	ESS power; VSC Power; Mode switch	DC MG	Two (for GC and IS mode)	Constant current in GC Constant Voltage in IS	Power calculation and two control stages	Not Analysed
				Remarks	Independent power flow within MG; Improved ESS life cycle; Includes virtual inertia concept				
[170]	✓	✓	×	Power data	DC MG	Single	Constant current	Power calculation; Various mode detection	Ensured
				Remarks	Proper DC bus voltage regulation; Power quality improvement; Smooth MG operation in various modes				
[171]	×	✓	×	AC bus power	AC MG	Single	Constant voltage	Power calculation	Ensured
				Remarks	Regulate the power flow; Power management among ESSs with different SoC levels				
[172]	×	✓	×	Power data	DC MG	Two	Constant voltage	Power calculation	Ensured
				Remarks	Quick harmonic compensation; Proper power regulation; Robust controller;				
P	✓	✓	✓	Grid current	HMG	Single	Constant Voltage	No power calculation and mode switch	Ensured
				Remarks	Autonomous power flow in IS and GC modes; Provides smooth transition; Single controller				

GC	Grid-connected	**IS**	Islanded	**IMG**	Interconnected microgrid
ESS	Energy storage system	**P**	Proposed	**HMG**	Hybrid microgrid
VSC	Voltage source converter	**MG**	Microgrid	**SoC**	State of charge
✓	Applicable	×	Not Applicable		

6.4 INTERFACE TECHNIQUE FOR CLUSTERING

Clustering converters have become the standard process for connecting MGs, irrespective of their properties like voltage and frequency. These converter interfaces not only regulate power flow but also enhance the MG cluster network's power quality. With their ability to effectively connect and manage interactions across MGs, networked converters are therefore anticipated to become the energy routes of the future.

In [173], a two-level distributed control framework consisting of a networked MG control level and an individual MG control level is developed for

the MG cluster. To link two nearby DC MGs and regulate the bidirectional flow of power between them, a converter framework utilizing a DAB and a full-bridge bidirectional DC-DC converter (BDC) is suggested in [66]. To offer an environment where the MGs are capable of sustaining one another during unforeseen circumstances, a networked MG structure is presented in [20], which consists of two AC MGs connected by a back-to-back converter. In [22], a more effective power-sharing plan is implemented to maintain the bus voltage in MG operations by utilizing the DAB's modularity capability. To increase voltage stability, a strong bidirectional power exchange control system is constructed between DABs on various high-voltage and low-voltage buses. To facilitate mutually beneficial power supply among MGs and enhance the effective use of RESs, a cluster configuration for numerous AC and DC MGs connected by BADCs and BDCs to a common DC bus is proposed in [57], [174]. To enable the interconnected MGs to function collectively and provide mutual support during power fluctuations, a decentralized, multi-time-level power control technique is suggested in [174]. The suggested control technique is able to maintain power fluctuations on three different time scales: two are operated at the MG level and one at the system level. An improved flexible droop control technique is presented in [68] along with a unified PMS for intra- and inter-MG power distribution in an interconnected MG system.

Clustering methods using converter frameworks help achieve high levels of controllability in terms of frequency and voltage, effective power management, improved power quality, and flexibility. The clustering method using DC buses of HMGs leads to more sophisticated control since it simultaneously balances two control goals: coordinated operation between DC and AC MGs in a single HMG using an interlinking converter and power coordination among nearby HMGs using a converter. To prevent overstressing any one entity, power should

ideally be shared between the two MGs in proportion to the converter's power ratings, which is enabled by the parallel BDC framework.

Table 6.3: Comparison with the previously introduced clustering technique of networked microgrid.

Ref.	Operation			Converter stages/ Design	IMG Type	With dynamic load	Converter topology	Controller Delay	Flexibility in power variations
	GC	IS	IMG						
[68]	✓	✓	✓	Two/ Complex	AC MG	Not Analysed	Back-to-back	Power calculation and two controllers	Ensured
				Remarks	Bidirectional power sharing; Adaptive droop control; Maximum utilization of RESs				
[66]	×	✓	✓	Two/ Complex	DC MG	Not Analysed	DAB and full bridge	Power calculation and two controllers	Ensured
				Remarks	Proper DC bus voltage regulation; Power quality improvement; Smooth MG operation in various modes				
[20]	×	✓	✓	Two/ Complex	AC MG	Not Analysed	Back-to-back	Power calculation and two controllers	Not Analysed
				Remarks	Angle droop control; Overload detection; Power support during any contingencies				
[22]	×	✓	✓	Single/ Simple	DC MG	Not Analysed	DAB	Power calculation and two controllers	Not Analysed
				Remarks	DC voltage regulation; Proper power sharing; Reliable and uninterrupted operation; Improved power quality				
[174]	×	✓	✓	Single/ Simple	AC/ DC MGs	Not analysed	AC/DC converter	Power calculation	Ensured
				Remarks	Stabilized power fluctuation; Interconnecting MGs with different frequencies; Proper power coordination				
P	✓	✓	✓	Single/ Simple	HMG	Low power oscillation	BDC	No power calculation and mode switch	Ensured
				Remarks	Controlled power flow; Fewer conversion stages; Interconnection of hybrid microgrids				

GC	Grid-connected	**IS**	Islanded	**IMG**	Interconnected microgrid
DAB	Dual active bridge	**P**	Proposed	**HMG**	Hybrid microgrid
BDC	Bidirectional DC-DC converter			**MG**	Microgrid
✓	Applicable	×	Not Applicable		

Based on a number of characteristics, including operating modes, control operation, converter stages, design complexity, dynamic load analysis, interconnected MG types, and operational flexibility, Table 6.3 compares the suggested clustering method for HMGs with the existing clustering method presented in various studies [20, 22, 66, 68, 174]. When compared to the previously explored clustering approach, the study in Table 6.3 shows that the

suggested control and clustering strategy for networked HMGs produces greater performance in numerous areas.

6.5 SUMMARY

A comparative analysis is performed based on various relevant factors to highlight the merits of the three proposed control strategies for HMG's interlinking converter, ESS controllers, and clustering converters.

The suggested controller for the interlinking converter performs well in all three modes, such as grid-connected, islanded, and interconnected modes, by sustaining the AC and DC-bus voltages within prescribed limits. Despite the different operating modes, a seamless switch between the on- and off-grid modes is achieved without switching between controllers. Furthermore, when compared to existing control systems, the proposed method minimizes the sensor required, measurement delay, and feedback signal delay. With a THD performance of roughly 0.80%, this control approach performs better as well.

With the assistance of the suggested ESS management and control, an autonomous and seamless power flow is achieved inside each individual MG and MG cluster in grid-tied mode. Because ESS control uses a virtual inertia approach, the system's inertia increases during transients. By limiting the ESS function to safe levels, the SoC-based management prolongs the battery bank's life by preventing overcharging and extending the battery bank's extension.

High levels of controllability concerning frequency and voltage, efficient power management, enhanced power quality, and flexibility can be attained by clustering techniques that employ converter frameworks. Reducing conversion stages and creating a more straightforward control structure are the results of clustering HMGs using their DC buses.

Chapter 7

CONCLUSIONS

7.1 GENERAL

A novel interconnection scheme along with modified control strategies for the interlinking converter in HMG and ESS control is proposed for two nearby HMGs that operate in both grid-tied and islanded modes. With the proposed control structure, every HMG within the MG cluster can operate autonomously in both on- and off-grid modes, while the main grid or neighbouring MG only supplies the excess or deficit of power when demand exceeds generation.

ESS power management and control is proposed to operate reliably in three operating modes. Using a virtual inertia approach, the system's inertia is increased to manage the ESS response to transients. The battery-bank-based ESS life cycle is prolonged by an SoC-based regulation that restricts ESS operation to secure ranges and prevents it from being overcharged or drowned.

It demonstrates how a set of parallel DC converter frameworks can be used to connect an HMG operating in grid-tied mode to an HMG running in islanded mode. To support the HMG during emergencies, the clustering converter's operation is crucial. The normal operation of the networked MG is explained, along with its overloading and power surplus conditions.

7.2 KEY FINDINGS

A voltage-frequency (V-f) droop-based control strategy is proposed for the interlinking converter of HMG to ensure proper operation in all operating

modes, such as islanded, grid-tied, and interconnecting modes, and smooth transit between islanded and grid-tied modes. The interlinking converter control does not require any power calculation due to the use of V-f droop control instead of conventional P-f and Q-V droop control, thus decreasing the sensor requirement (current sensor) and delay associated with power calculation. Moreover, the proposed control strategy doesn't require any other controller to switch between on- and off-grid modes (with less than 1% frequency variations). As a result, the disturbance due to the mode switch among various controllers is significantly reduced.

A communication link is necessary for the proposed ESS management system, but this link can be simplified by only transmitting the AC grid active current component (I_{g_d}), which is the sole information that has to be conveyed to the ESS. With only one control stage and no need for a reference power calculation in outer control, the ESS control is capable of moving between modes quickly and accurately, preventing faulty transitions. The virtual inertia method, along with appropriate parameter selection ($J = 3$ and $D = 1$), can improve the charging and discharging performance of ESS in any transient condition by enhancing the system's inertia. SoC-based management reduces the burden on ESSs by limiting SoC between 20% and 90%, thus improving the ESS life cycle.

Since this clustering technique relies on DC connections, it reduces the number of conversion units (one converter stage with 4 IGBT switches), weight, size, and system expense. Moreover, DC interconnection ensures higher efficiency, lower losses, elimination of the skin effect and bulky transformers, no reactive power and synchronization requirements, more proficient current carrying capacity, and improved reliability.

The proposed control structure, with the three main control strategies of interlinking converters and ESS control, provides an additional degree of control freedom and flexibility over the power management in the HMG cluster. The

simulation findings demonstrate the suggested control structure's reliability in accomplishing the interconnected HMG system's two primary control objectives, which enable the system to operate self-sufficiently and provide stable energy distribution within the HMG cluster. The control structure efficiently manages the power surplus and shortage in any HMG during load variations and source power variations or outages. It can maintain system power quality (mainly THD) within IEEE limits (For HMG-1 load current THD is 1.53%, for HMG-2 THD is 1.59%). Moreover, the system frequency variations are also remains in below 1%. It is evident from stability analysis that choosing the control parameters accurately improves system performance and stability without degrading frequency or voltage. Therefore, the PI controller values, inertia coefficients, and all associated controller gains need to be accurately tuned using step response, pole-zero map, and bode plot to maintain the system stability and enhance system performance.

7.3 LIMITATIONS OF THE STUDY

The three control strategies use the PI controller to minimize the error and provide the desired signal for an accurate response. However, the value of all PI controllers in the system needs to be tuned accurately to ensure system stability. The droop coefficient of each droop control needs to be the same and well-measured to maintain system stability and performance.

Only a certain amount of dynamic induction motor load can be supported by the suggested system. When certain thresholds are exceeded, the system becomes unstable. Moreover, oscillations in system voltage and frequency result from dynamic load increases over a particular threshold.

7.4 RECOMMENDATIONS FOR FURTHER STUDY

In order to sustain dynamic loads above the system's maximum limits, an appropriate damping controller with ESS can be developed. Therefore, the

proposed networked system can be integrated with any power oscillation damping controller in the future to investigate the system's performance under various percentages of dynamic load penetration.

Based on theoretical analysis, the system is more reliable, and efficient, and has fewer conversion steps than AC technology; nevertheless, an experimental analysis can be conducted to verify those analyses in real-world scenarios. Software-based RT-SiL simulation is used to examine the system's performance; this is merely a first step toward experimental validation. Therefore, the system can be experimentally verified in the future using hardware-in-the-loop simulation.

Bibliography

[1] L. Mariam, M. Basu, and M. F. Conlon, "Microgrid: Architecture, policy and future trends," *Renewable and Sustainable Energy Reviews,* vol. 64, pp. 477-489, 2016.

[2] M. H. Saeed, W. Fangzong, B. A. Kalwar, and S. Iqbal, "A review on microgrids' challenges & perspectives," *IEEE Access,* vol. 9, pp. 166502-166517, 2021.

[3] A. Muhtadi, D. Pandit, N. Nguyen, and J. Mitra, "Distributed energy resources based microgrid: Review of architecture, control, and reliability," *IEEE Transactions on Industry Applications,* vol. 57, no. 3, pp. 2223-2235, 2021.

[4] E. Planas, J. Andreu, J. I. Gárate, I. M. De Alegría, and E. Ibarra, "AC and DC technology in microgrids: A review," *Renewable and Sustainable Energy Reviews,* vol. 43, pp. 726-749, 2015.

[5] I. Serban, S. Cespedes, C. Marinescu, C. A. Azurdia-Meza, J. S. Gomez, and D. S. Hueichapan, "Communication requirements in microgrids: A practical survey," *IEEE Access,* vol. 8, pp. 47694-47712, 2020.

[6] A. K. Marvasti, Y. Fu, S. DorMohammadi, and M. Rais-Rohani, "Optimal operation of active distribution grids: A system of systems framework," *IEEE Transactions on Smart Grid,* vol. 5, no. 3, pp. 1228-1237, 2014.

[7] S. Choudhury, "Review of energy storage system technologies integration to microgrid: Types, control strategies, issues, and future prospects," *Journal of Energy Storage,* vol. 48, p. 103966, 2022.

[8] M. Uddin, H. Mo, D. Dong, S. Elsawah, J. Zhu, and J. M. Guerrero, "Microgrids: A review, outstanding issues and future trends," *Energy Strategy Reviews,* vol. 49, p. 101127, 2023.

[9] Z. Wang and J. Wang, "Self-healing resilient distribution systems based on sectionalization into microgrids," *IEEE Transactions on Power Systems,* vol. 30, no. 6, pp. 3139-3149, 2015.

[10] Z. Wang, B. Chen, J. Wang, and C. Chen, "Networked microgrids for self-healing power systems," *IEEE Transactions on smart grid,* vol. 7, no. 1, pp. 310-319, 2015.

[11] Z. Shuai, Y. Sun, Z. J. Shen, W. Tian, C. Tu, Y. Li, and X. Yin, "Microgrid stability: Classification and a review," *Renewable and Sustainable Energy Reviews,* vol. 58, pp. 167-179, 2016.

[12] M. J. Hossain, M. A. Mahmud, F. Milano, S. Bacha, and A. Hably, "Design of robust distributed control for interconnected microgrids," *IEEE Transactions on Smart Grid,* vol. 7, no. 6, pp. 2724-2735, 2015.

[13] B. Chen, J. Wang, X. Lu, C. Chen, and S. Zhao, "Networked microgrids for grid resilience, robustness, and efficiency: A review," *IEEE Transactions on Smart Grid,* vol. 12, no. 1, pp. 18-32, 2020.

[14] P. Sharma, H. D. Mathur, P. Mishra, and R. C. Bansal, "A critical and comparative review of energy management strategies for microgrids," *Applied Energy,* vol. 327, p. 120028, 2022.

[15] E. Bullich-Massagué, F. Díaz-González, M. Aragüés-Peñalba, F. Girbau-Llistuella, P. Olivella-Rosell, and A. Sumper, "Microgrid clustering architectures," *Applied energy,* vol. 212, pp. 340-361, 2018.

[16] J. Lai, X. Lu, Z. Dong, and S. Cheng, "Resilient distributed multiagent control for AC microgrid networks subject to disturbances," *IEEE Transactions on Systems, Man, and Cybernetics: Systems,* vol. 52, no. 1, pp. 43-53, 2021.

[17] B. Fan, S. Guo, J. Peng, Q. Yang, W. Liu, and L. Liu, "A consensus-based algorithm for power sharing and voltage regulation in DC microgrids," *IEEE Transactions on Industrial Informatics,* vol. 16, no. 6, pp. 3987-3996, 2019.

[18] M. Zolfaghari, M. Abedi, and G. B. Gharehpetian, "Power flow control of interconnected AC–DC microgrids in grid-connected hybrid microgrids using modified UIPC," *IEEE Transactions on Smart Grid,* vol. 10, no. 6, pp. 6298-6307, 2019.

[19] J. Lai, X. Lu, X. Yu, and A. Monti, "Cluster-oriented distributed cooperative control for multiple AC microgrids," *IEEE Transactions on Industrial Informatics,* vol. 15, no. 11, pp. 5906-5918, 2019.

[20] M. Goyal and A. Ghosh, "Microgrids interconnection to support mutually during any contingency," *Sustainable Energy, Grids and Networks,* vol. 6, pp. 100-108, 2016.

[21] Y. Han, X. Ning, L. Li, P. Yang, and F. Blaabjerg, "Droop coefficient correction control for power sharing and voltage restoration in hierarchical controlled DC microgrids," *International Journal of Electrical Power & Energy Systems,* vol. 133, p. 107277, 2021.

[22] D. Das, M. J. Hossain, S. Mishra, and B. Singh, "Bidirectional power sharing of modular DABs to improve voltage stability in DC microgrids," *IEEE Transactions on Industry Applications,* vol. 58, no. 2, pp. 2369-2377, 2022.

[23] M. Z. Kreishan and A. F. Zobaa, "Optimal allocation and operation of droop-controlled islanded microgrids: A review," *energies,* vol. 14, no. 15, p. 4653, 2021.

[24] Q. Xu, Y. Xu, Z. Xu, L. Xie, and F. Blaabjerg, "A hierarchically coordinated operation and control scheme for DC microgrid clusters under uncertainty," *IEEE Transactions on Sustainable Energy,* vol. 12, no. 1, pp. 273-283, 2020.

[25] Y. Shan, J. Hu, and B. Shen, "Distributed Secondary Frequency Control for AC Microgrids Using Load Power Forecasting Based on Artificial Neural Network," *IEEE Transactions on Industrial Informatics,* 2023.

[26] M. M. A. Abdelaziz, M. F. Shaaban, H. E. Farag, and E. F. El-Saadany, "A multistage centralized control scheme for islanded microgrids with PEVs," *IEEE Transactions on Sustainable Energy,* vol. 5, no. 3, pp. 927-937, 2014.

[27] L. Meng, Q. Shafiee, G. F. Trecate, H. Karimi, D. Fulwani, X. Lu, and J. M. Guerrero, "Review on control of DC microgrids and multiple microgrid clusters," *IEEE journal of emerging and selected topics in power electronics,* vol. 5, no. 3, pp. 928-948, 2017.

[28] M. Batool, F. Shahnia, and S. M. Islam, "Multi-level supervisory emergency control for operation of remote area microgrid clusters," *Journal of Modern Power Systems and Clean Energy,* vol. 7, no. 5, pp. 1210-1228, 2019.

[29] Z. H. A. Al-Tameemi, T. T. Lie, G. Foo, and F. Blaabjerg, "Control strategies of DC microgrids cluster: A comprehensive review," *Energies,* vol. 14, no. 22, p. 7569, 2021.

[30] M. E. T. Souza and L. C. G. Freitas, "Grid-Connected and Seamless Transition Modes for Microgrids: An Overview of Control Methods, Operation Elements and General Requirements," *IEEE Access,* 2022.

[31] Z. Wang, B. Chen, J. Wang, M. M. Begovic, and C. Chen, "Coordinated energy management of networked microgrids in distribution systems," *IEEE Transactions on Smart Grid,* vol. 6, no. 1, pp. 45-53, 2014.

[32] M. Naderi, Y. Khayat, Q. Shafiee, T. Dragicevic, H. Bevrani, and F. Blaabjerg, "Interconnected autonomous AC microgrids via back-to-back converters—Part I: Small-signal modeling," *IEEE Transactions on Power Electronics,* vol. 35, no. 5, pp. 4728-4740, 2019.

[33] D. Chen and L. Xu, "Autonomous DC voltage control of a DC microgrid with multiple slack terminals," *IEEE Transactions on Power Systems,* vol. 27, no. 4, pp. 1897-1905, 2012.

[34] J. Zhou, H. Zhang, Q. Sun, D. Ma, and B. Huang, "Event-based distributed active power sharing control for interconnected AC and DC microgrids," *IEEE Transactions on Smart Grid,* vol. 9, no. 6, pp. 6815-6828, 2017.

[35] P. Sanjeev, N. P. Padhy, and P. Agarwal, "Autonomous power control and management between standalone DC microgrids," *IEEE Transactions on Industrial Informatics,* vol. 14, no. 7, pp. 2941-2950, 2017.

[36] S. Ferdous, F. Shahnia, and G. Shafiullah, "Power sharing and control strategy for provisionally coupled microgrid clusters through an isolated power exchange network," *Energies,* vol. 14, no. 22, p. 7514, 2021.

[37] M. Panda, D. V. Bhaskar, and T. Maity, "An efficient SoC-balancing based power management strategy for interconnected subgrids of DC microgrid," *Journal of Energy Storage,* vol. 50, p. 104287, 2022.

[38] H. Yu, S. Niu, Z. Shao, and L. Jian, "A scalable and reconfigurable hybrid AC/DC microgrid clustering architecture with decentralized control for coordinated operation," *International Journal of Electrical Power & Energy Systems,* vol. 135, p. 107476, 2022.

[39] F. Chen, R. Burgos, D. Boroyevich, and X. Zhang, "Low-frequency common-mode voltage control for systems interconnected with power converters," *IEEE Transactions on Industrial Electronics,* vol. 64, no. 1, pp. 873-882, 2016.

[40] S. Ullah, A. M. Haidar, P. Hoole, H. Zen, and T. Ahfock, "The current state of Distributed Renewable Generation, challenges of interconnection and opportunities for energy conversion based DC microgrids," *Journal of Cleaner Production,* vol. 273, p. 122777, 2020.

[41] A. Sesetti, H. K. Nunna, S. Doolla, and A. K. Rathore, "Multi-agent based energy trading platform for energy storage systems in distribution systems with inter-connected microgrids," in *2018 IEEE Industry Applications Society Annual Meeting (IAS)*, 2018, pp. 1-8: IEEE.

[42] P. J. dos Santos Neto, T. A. dos Santos Barros, J. P. C. Silveira, E. Ruppert Filho, J. C. Vasquez, and J. M. Guerrero, "Power management strategy based on virtual inertia for DC microgrids," *IEEE Transactions on Power Electronics,* vol. 35, no. 11, pp. 12472-12485, 2020.

[43] X. Li, L. Guo, Y. Li, Z. Guo, C. Hong, Y. Zhang, and C. Wang, "A unified control for the DC–AC interlinking converters in hybrid AC/DC microgrids," *IEEE Transactions on Smart Grid,* vol. 9, no. 6, pp. 6540-6553, 2017.

[44] S. Peyghami, H. Mokhtari, and F. Blaabjerg, "Autonomous operation of a hybrid AC/DC microgrid with multiple interlinking converters," *IEEE Transactions on Smart Grid,* vol. 9, no. 6, pp. 6480-6488, 2017.

[45] Y. Yang, S. Bremner, C. Menictas, and M. Kay, "Battery energy storage system size determination in renewable energy systems: A review," *Renewable and Sustainable Energy Reviews,* vol. 91, pp. 109-125, 2018.

[46] K. Rajesh, S. Dash, R. Rajagopal, and R. Sridhar, "A review on control of ac microgrid," *Renewable and sustainable energy reviews,* vol. 71, pp. 814-819, 2017.

[47] F. S. Al-Ismail, "DC microgrid planning, operation, and control: A comprehensive review," *IEEE Access,* vol. 9, pp. 36154-36172, 2021.

[48] M. S. Golsorkhi and M. Savaghebi, "A decentralized control strategy based on VI droop for enhancing dynamics of autonomous hybrid AC/DC microgrids," *IEEE Transactions on Power Electronics,* vol. 36, no. 8, pp. 9430-9440, 2021.

[49] M. N. Tasnim, T. Ahmed, M. A. Dorothi, S. Ahmad, G. Shafiullah, S. Ferdous, and S. Mekhilef, "Voltage-Oriented Control-Based Three-Phase, Three-Leg Bidirectional AC–DC Converter with Improved Power Quality for Microgrids," *Energies,* vol. 16, no. 17, p. 6188, 2023.

[50] N. Khosravi, R. Baghbanzadeh, A. Oubelaid, M. Tostado-Véliz, M. Bajaj, Z. Hekss, S. Echalih, Y. Belkhier, M. Abou Houran, and K. M. Aboras, "A novel control approach to improve the stability of hybrid AC/DC microgrids," *Applied Energy,* vol. 344, p. 121261, 2023.

[51] A. Ordono, E. Unamuno, J. A. Barrena, and J. Paniagua, "Interlinking converters and their contribution to primary regulation: a review," *International Journal of Electrical Power & Energy Systems,* vol. 111, pp. 44-57, 2019.

[52] P. Li, T. Guo, X. Han, H. Liu, J. Yang, J. Wang, Y. Yang, and Z. Wang, "The optimal decentralized coordinated control method based on the H∞ performance index for an AC/DC hybrid microgrid," *International Journal of Electrical Power & Energy Systems,* vol. 125, p. 106442, 2021.

[53] S. Moayedi and A. Davoudi, "Distributed tertiary control of DC microgrid clusters," *IEEE Transactions on Power Electronics,* vol. 31, no. 2, pp. 1717-1733, 2015.

[54] Y. Han, K. Zhang, H. Li, E. A. A. Coelho, and J. M. Guerrero, "MAS-based distributed coordinated control and optimization in microgrid and microgrid clusters: A comprehensive overview," *IEEE Transactions on Power Electronics,* vol. 33, no. 8, pp. 6488-6508, 2017.

[55] M. Faisal, M. A. Hannan, P. J. Ker, A. Hussain, M. B. Mansor, and F. Blaabjerg, "Review of energy storage system technologies in microgrid applications: Issues and challenges," *Ieee Access,* vol. 6, pp. 35143-35164, 2018.

[56] F. A. Inthamoussou, J. Pegueroles-Queralt, and F. D. Bianchi, "Control of a supercapacitor energy storage system for microgrid applications," *IEEE transactions on energy conversion,* vol. 28, no. 3, pp. 690-697, 2013.

[57] X. Zhou, L. Zhou, Y. Chen, J. M. Guerrero, A. Luo, W. Wu, and L. Yang, "A microgrid cluster structure and its autonomous coordination control strategy," *International Journal of Electrical Power & Energy Systems,* vol. 100, pp. 69-80, 2018.

[58] Z. Rostami, S. N. Ravadanegh, N. T. Kalantari, J. M. Guerrero, and J. C. Vasquez, "Dynamic modeling of multiple microgrid clusters using regional demand response programs," *Energies,* vol. 13, no. 16, p. 4050, 2020.

[59] D. Saha, N. Bazmohammadi, J. C. Vasquez, and J. M. Guerrero, "Multiple microgrids: A review of architectures and operation and control strategies," *Energies,* vol. 16, no. 2, p. 600, 2023.

[60] C. Li, T. Dragicevic, N. L. D. Aldana, A. C. L. Hernández, Y. Guan, T. B. Rasmussen, and S. Beheshtaein, "Grid architecture for future distribution system—A cyber-physical system perspective," in *IECON 2017-43rd Annual Conference of the IEEE Industrial Electronics Society*, 2017, pp. 5235-5239: IEEE.

[61] S. Ferdous, F. Shahnia, and G. Shafiullah, "Realising a system of coupled microgrid networks using single-phase interconnection lines," *IET Smart Grid,* vol. 4, no. 3, pp. 346-364, 2021.

[62] S. Adhikari, Q. Xu, Y. Tang, P. Wang, and X. Li, "Decentralized control of two DC microgrids interconnected with tie-line," *Journal of Modern Power Systems and Clean Energy,* vol. 5, no. 4, pp. 599-608, 2017.

[63] Q. Shafiee, T. Dragičević, J. C. Vasquez, and J. M. Guerrero, "Hierarchical control for multiple DC-microgrids clusters," *IEEE transactions on energy conversion,* vol. 29, no. 4, pp. 922-933, 2014.

[64] J. Ma, M. Zhu, X. Cai, and Y. W. Li, "Configuration and operation of DC microgrid cluster linked through DC-DC converter," in *2016 IEEE 11th Conference on Industrial Electronics and Applications (ICIEA)*, 2016, pp. 2565-2570: IEEE.

[65] M. Lee, W. Choi, H. Kim, and B.-H. Cho, "Operation schemes of interconnected DC microgrids through an isolated bi-directional DC-DC converter," in *2015 IEEE Applied Power Electronics Conference and Exposition (APEC)*, 2015, pp. 2940-2945: IEEE.

[66] U. Vuyyuru, S. Maiti, and C. Chakraborty, "Active power flow control between DC microgrids," *IEEE Transactions on Smart Grid,* vol. 10, no. 5, pp. 5712-5723, 2019.

[67] M. Kumar, S. C. Srivastava, S. N. Singh, and M. Ramamoorty, "Development of a control strategy for interconnection of islanded direct current microgrids," *IET Renewable Power Generation,* vol. 9, no. 3, pp. 284-296, 2015.

[68] S. Sinha, S. Ghosh, and P. Bajpai, "Power sharing through interlinking converters in adaptive droop controlled multiple microgrid system," *International Journal of Electrical Power & Energy Systems,* vol. 128, p. 106649, 2021.

[69] J. Khodabakhsh and G. Moschopoulos, "Simplified hybrid AC–DC microgrid with a novel interlinking converter," *IEEE Transactions on Industry Applications,* vol. 56, no. 5, pp. 5023-5034, 2020.

[70] X. Hou, K. Sun, N. Zhang, F. Teng, X. Zhang, and T. C. Green, "Priority-driven self-optimizing power control scheme for interlinking converters of hybrid AC/DC microgrid clusters in decentralized manner," *IEEE Transactions on Power Electronics,* vol. 37, no. 5, pp. 5970-5983, 2021.

[71] F. Bandeiras, E. Pinheiro, M. Gomes, P. Coelho, and J. Fernandes, "Review of the cooperation and operation of microgrid clusters," *Renewable and Sustainable Energy Reviews,* vol. 133, p. 110311, 2020.

[72] A. Ouammi, H. Dagdougui, L. Dessaint, and R. Sacile, "Coordinated model predictive-based power flows control in a cooperative network of smart microgrids," *IEEE Transactions on Smart grid,* vol. 6, no. 5, pp. 2233-2244, 2015.

[73] M. Islam, F. Yang, and M. Amin, "Control and optimisation of networked microgrids: A review," *IET Renewable Power Generation,* vol. 15, no. 6, pp. 1133-1148, 2021.

[74] A. Arabpour and H. Hojabri, "An improved centralized/decentralized accurate reactive power sharing method in AC microgrids," *International Journal of Electrical Power & Energy Systems,* vol. 148, p. 108908, 2023.

[75] K. Jithin, R. Harikumar, N. Mayadevi, and V. Mini, "A centralized control algorithm for power management in interconnected dc microgrids," in *Proceedings of Symposium on Power Electronic and Renewable Energy Systems Control: PERESC 2020*, 2021, pp. 451-461: Springer.

[76] Y. Wang, A. O. Rousis, D. Qiu, and G. Strbac, "A stochastic distributed control approach for load restoration of networked microgrids with mobile energy storage systems," *International Journal of Electrical Power & Energy Systems,* vol. 148, p. 108999, 2023.

[77] C. Samende, F. Gao, S. M. Bhagavathy, and M. McCulloch, "Decentralized voltage control for efficient power exchange in interconnected DC clusters," *IEEE Transactions on Sustainable Energy,* vol. 12, no. 1, pp. 103-115, 2020.

[78] X.-K. Liu, J. Cai, L. Xing, and Y.-W. Wang, "Distributed Event-Triggered Current Sharing Control for Islanded DC Microgrids With Quantized State," *IEEE Transactions on Sustainable Energy,* 2023.

[79] X. Hou, Y. Sun, J. Lu, X. Zhang, L. H. Koh, M. Su, and J. M. Guerrero, "Distributed hierarchical control of AC microgrid operating in grid-connected, islanded and their transition modes," *Ieee Access,* vol. 6, pp. 77388-77401, 2018.

[80] J. M. Guerrero, J. C. Vasquez, J. Matas, L. G. De Vicuña, and M. Castilla, "Hierarchical control of droop-controlled AC and DC microgrids—A general approach toward standardization," *IEEE Transactions on industrial electronics,* vol. 58, no. 1, pp. 158-172, 2010.

[81] F. Gao, R. Kang, J. Cao, and T. Yang, "Primary and secondary control in DC microgrids: a review," *Journal of Modern Power Systems and Clean Energy,* vol. 7, no. 2, pp. 227-242, 2019.

[82] M. A. Zamee and D. Won, "A novel plant propagation-based cascaded fractional order PI controller for optimal operation of grid-connected single-stage three-phase solar photovoltaic system," *Applied Sciences,* vol. 9, no. 20, p. 4269, 2019.

[83] M. N. Alam, S. Chakrabarti, and A. Ghosh, "Networked microgrids: State-of-the-art and future perspectives," *IEEE Transactions on Industrial Informatics,* vol. 15, no. 3, pp. 1238-1250, 2018.

[84] L. Che, M. Shahidehpour, A. Alabdulwahab, and Y. Al-Turki, "Hierarchical coordination of a community microgrid with AC and DC microgrids," *IEEE Transactions on smart grid,* vol. 6, no. 6, pp. 3042-3051, 2015.

[85] E. Planas, A. Gil-de-Muro, J. Andreu, I. Kortabarria, and I. M. de Alegría, "General aspects, hierarchical controls and droop methods in microgrids: A review," *Renewable and Sustainable Energy Reviews,* vol. 17, pp. 147-159, 2013.

[86] Z. Li, M. Shahidehpour, F. Aminifar, A. Alabdulwahab, and Y. Al-Turki, "Networked microgrids for enhancing the power system resilience," *Proceedings of the IEEE,* vol. 105, no. 7, pp. 1289-1310, 2017.

[87] B. Fan, Q. Li, W. Wang, G. Yao, H. Ma, X. Zeng, and J. M. Guerrero, "A novel droop control strategy of reactive power sharing based on adaptive virtual impedance in microgrids," *IEEE Transactions on Industrial Electronics,* vol. 69, no. 11, pp. 11335-11347, 2021.

[88] A. Tah and D. Das, "An enhanced droop control method for accurate load sharing and voltage improvement of isolated and interconnected DC microgrids," *IEEE Transactions on Sustainable Energy,* vol. 7, no. 3, pp. 1194-1204, 2016.

[89] A. Trivedi and M. Singh, "$ L_ {1} $ adaptive droop control for AC microgrid with small mesh network," *IEEE Transactions on Industrial Electronics,* vol. 65, no. 6, pp. 4781-4789, 2017.

[90] P. Kou, D. Liang, and L. Gao, "Distributed EMPC of multiple microgrids for coordinated stochastic energy management," *Applied energy,* vol. 185, pp. 939-952, 2017.

[91] K. Liu, T. Liu, Z. Tang, and D. J. Hill, "Distributed MPC-based frequency control in networked microgrids with voltage constraints," *IEEE Transactions on Smart Grid,* vol. 10, no. 6, pp. 6343-6354, 2019.

[92] P. Xie, Y. Jia, H. Chen, J. Wu, and Z. Cai, "Mixed-stage energy management for decentralized microgrid cluster based on enhanced tube model predictive control," *IEEE Transactions on Smart Grid,* vol. 12, no. 5, pp. 3780-3792, 2021.

[93] R. Huang, Y. Xiao, M. Liu, X. Shen, W. Huang, Y. Peng, and J. Shen, "Multilevel Dynamic Master-Slave Control Strategy for Resilience Enhancement of Networked Microgrids," *Energies,* vol. 15, no. 10, p. 3698, 2022.

[94] P. Karami, M. Baharizadeh, M. S. Golsorkhi, and M. H. Ershadi, "A coordinated control of hybrid AC/DC microgrids based on master–slave method," *Electrical Engineering,* vol. 104, no. 5, pp. 3619-3629, 2022.

[95] X. Lu, J. Lai, and G.-P. Liu, "Master–Slave Cooperation for Multi-DC-MGs via Variable Cyber Networks," *IEEE transactions on cybernetics,* vol. 52, no. 8, pp. 8425-8438, 2021.

[96] R. Trivedi and S. Khadem, "Implementation of artificial intelligence techniques in microgrid control environment: Current progress and future scopes," *Energy and AI,* vol. 8, p. 100147, 2022.

[97] D. O. Amoateng, M. Al Hosani, M. S. Elmoursi, K. Turitsyn, and J. L. Kirtley, "Adaptive voltage and frequency control of islanded multi-microgrids," *IEEE Transactions on Power Systems,* vol. 33, no. 4, pp. 4454-4465, 2017.

[98] Z. Zhao, P. Yang, Y. Wang, Z. Xu, and J. M. Guerrero, "Dynamic characteristics analysis and stabilization of PV-based multiple microgrid clusters," *IEEE Transactions on Smart grid,* vol. 10, no. 1, pp. 805-818, 2017.

[99] L. Yin, T. Yu, B. Yang, and X. Zhang, "Adaptive deep dynamic programming for integrated frequency control of multi-area multi-microgrid systems," *Neurocomputing,* vol. 344, pp. 49-60, 2019.

[100] H. Shayeghi, A. Rahnama, and H. Alhelou, "Frequency control of fully-renewable interconnected microgrid using fuzzy cascade controller with demand response program considering," *Energy Reports,* vol. 7, pp. 6077-6094, 2021.

[101] B. Liang, L. Kang, J. He, F. Zheng, Y. Xia, Z. Zhang, Z. Zhang, G. Liu, and Y. Zhao, "Coordination control of hybrid AC/DC microgrid," *The Journal of Engineering,* vol. 2019, no. 16, pp. 3264-3269, 2019.

[102] S. M. Malik, Y. Sun, W. Huang, X. Ai, and Z. Shuai, "A generalized droop strategy for interlinking converter in a standalone hybrid microgrid," *Applied energy,* vol. 226, pp. 1056-1063, 2018.

[103] J. P. C. Silveira, P. J. dos Santos Neto, T. A. dos Santos Barros, and E. Ruppert Filho, "Power management of energy storage system with modified interlinking converters topology in hybrid AC/DC microgrid," *International Journal of Electrical Power & Energy Systems,* vol. 130, p. 106880, 2021.

[104] X. Hou, Y. Sun, W. Yuan, H. Han, C. Zhong, and J. M. Guerrero, "Conventional P-ω/QV droop control in highly resistive line of low-voltage converter-based AC microgrid," *Energies,* vol. 9, no. 11, p. 943, 2016.

[105] M. Naderi, Y. Khayat, Q. Shafiee, F. Blaabjerg, and H. Bevrani, "Dynamic modeling, stability analysis and control of interconnected microgrids: A review," *Applied Energy,* vol. 334, p. 120647, 2023.

[106] M. Farrokhabadi, C. A. Canizares, J. W. Simpson-Porco, E. Nasr, L. Fan, P. A. Mendoza-Araya, R. Tonkoski, U. Tamrakar, N. Hatziargyriou, and D. Lagos, "Microgrid stability definitions, analysis, and examples," *IEEE Transactions on Power Systems,* vol. 35, no. 1, pp. 13-29, 2019.

[107] H. Ali, G. Magdy, and D. Xu, "A new optimal robust controller for frequency stability of interconnected hybrid microgrids considering non-inertia sources and uncertainties," *International Journal of Electrical Power & Energy Systems,* vol. 128, p. 106651, 2021.

[108] G. K. Suman, J. M. Guerrero, and O. P. Roy, "Robust Frequency Control in Interconnected Microgrids: An H $ _2 $/H $ _ {\infty} $ Control Approach," *IEEE Systems Journal,* vol. 16, no. 2, pp. 2044-2055, 2021.

[109] M. Khamies, G. Magdy, M. E. Hussein, F. A. Banakhr, and S. Kamel, "An efficient control strategy for enhancing frequency stability of multi-area power system considering high wind energy penetration," *IEEE Access,* vol. 8, pp. 140062-140078, 2020.

[110] E. Zhao, E. Liu, L. Li, Y. Han, P. Yang, and C. Wang, "Hierarchical Control Strategy Based on Droop Coefficient Calibration and Bus Voltage Compensation for DC Microgrid Cluster," in *2021 IEEE 2nd China International Youth Conference on Electrical Engineering (CIYCEE)*, 2021, pp. 1-7: IEEE.

[111] M.-A. Nasr, S. Nikkhah, G. B. Gharehpetian, E. Nasr-Azadani, and S. H. Hosseinian, "A multi-objective voltage stability constrained energy management system for isolated microgrids," *International Journal of Electrical Power & Energy Systems,* vol. 117, p. 105646, 2020.

[112] M. A. Hassan, "Dynamic stability of an autonomous microgrid considering active load impact with a new dedicated synchronization scheme," *IEEE Transactions on Power Systems,* vol. 33, no. 5, pp. 4994-5005, 2018.

[113] S. S. Khorramabadi and A. Bakhshai, "Critic-based self-tuning PI structure for active and reactive power control of VSCs in microgrid systems," *IEEE Transactions on smart grid,* vol. 6, no. 1, pp. 92-103, 2014.

[114] H. Moussa, A. Shahin, J.-P. Martin, B. Nahid-Mobarakeh, S. Pierfederici, and N. Moubayed, "Harmonic power sharing with voltage distortion compensation of droop controlled islanded microgrids," *IEEE Transactions on Smart Grid,* vol. 9, no. 5, pp. 5335-5347, 2017.

[115] M. Bajaj and A. K. Singh, "Grid integrated renewable DG systems: A review of power quality challenges and state-of-the-art mitigation techniques," *International Journal of Energy Research,* vol. 44, no. 1, pp. 26-69, 2020.

[116] Y. Naderi, S. H. Hosseini, S. G. Zadeh, B. Mohammadi-Ivatloo, J. C. Vasquez, and J. M. Guerrero, "An overview of power quality enhancement techniques applied to distributed generation in electrical distribution networks," *Renewable and Sustainable Energy Reviews,* vol. 93, pp. 201-214, 2018.

[117] S. B. Rao, Y. P. Kumar, M. Amir, and F. Ahmad, "An adaptive neuro-fuzzy control strategy for improved power quality in multi-microgrid clusters," *IEEE Access,* vol. 10, pp. 128007-128021, 2022.

[118] M. S. Munir, Y. W. Li, and H. Tian, "Improved residential distribution system harmonic compensation scheme using power electronics interfaced DGs," *IEEE Transactions on Smart Grid,* vol. 7, no. 3, pp. 1191-1203, 2016.

[119] A. Q. Al-Shetwi, M. Hannan, K. P. Jern, M. Mansur, and T. M. I. Mahlia, "Grid-connected renewable energy sources: Review of the recent integration requirements and control methods," *Journal of Cleaner Production,* vol. 253, p. 119831, 2020.

[120] R. N. Beres, X. Wang, M. Liserre, F. Blaabjerg, and C. L. Bak, "A review of passive power filters for three-phase grid-connected voltage-source converters," *IEEE journal of emerging and selected topics in power electronics,* vol. 4, no. 1, pp. 54-69, 2015.

[121] W. U. Tareen, S. Mekhilef, M. Seyedmahmoudian, and B. Horan, "Active power filter (APF) for mitigation of power quality issues in grid integration of wind and photovoltaic energy conversion system," *Renewable and Sustainable Energy Reviews,* vol. 70, pp. 635-655, 2017.

[122] M.-S. Karbasforooshan and M. Monfared, "An improved reference current generation and digital deadbeat controller for single-phase shunt active power filters," *IEEE Transactions on Power Delivery,* vol. 35, no. 6, pp. 2663-2671, 2020.

[123] B. Xie, K. Guo, M. Mao, L. Zhou, T. Liu, Q. Zhang, and G. Hao, "Analysis and improved design of phase compensated proportional resonant controllers for grid-connected inverters in weak grid," *IEEE Transactions on Energy Conversion,* vol. 35, no. 3, pp. 1453-1464, 2020.

[124] C. Xie, D. Liu, K. Li, J. Zou, K. Zhou, and J. M. Guerrero, "Passivity-based design of repetitive controller for $ LCL $-type grid-connected inverters suitable for microgrid applications," *IEEE Transactions on Power Electronics,* vol. 36, no. 2, pp. 2420-2431, 2020.

[125] F. Nejabatkhah, Y. W. Li, and H. Tian, "Power quality control of smart hybrid AC/DC microgrids: An overview," *Ieee access,* vol. 7, pp. 52295-52318, 2019.

[126] Q.-N. Trinh and H.-H. Lee, "An enhanced grid current compensator for grid-connected distributed generation under nonlinear loads and grid voltage distortions," *IEEE Transactions on Industrial Electronics,* vol. 61, no. 12, pp. 6528-6537, 2014.

[127] S. Y. Mousazadeh Mousavi, A. Jalilian, M. Savaghebi, and J. M. Guerrero, "Secondary-control-based harmonics compensation scheme for voltage-and current-controlled inverters in islanded microgrids," *IET Renewable Power Generation,* vol. 14, no. 12, pp. 2176-2182, 2020.

[128] Y. W. Li and J. He, "Distribution system harmonic compensation methods: An overview of DG-interfacing inverters," *IEEE industrial electronics magazine,* vol. 8, no. 4, pp. 18-31, 2014.

[129] B. Keyvani-Boroujeni, B. Fani, G. Shahgholian, and H. H. Alhelou, "Virtual impedance-based droop control scheme to avoid power quality and stability problems in VSI-dominated microgrids," *IEEE Access,* vol. 9, pp. 144999-145011, 2021.

[130] M. M. Shabestary and Y. A.-R. I. Mohamed, "Autonomous coordinated control scheme for cooperative asymmetric low-voltage ride-through and grid support in active distribution networks with multiple DG units," *IEEE Transactions on Smart Grid,* vol. 11, no. 3, pp. 2125-2139, 2019.

[131] A. A. Alkahtani, S. T. Alfalahi, A. A. Athamneh, A. Q. Al-Shetwi, M. B. Mansor, M. Hannan, and V. G. Agelidis, "Power quality in microgrids including supraharmonics: Issues, standards, and mitigations," *IEEE access,* vol. 8, pp. 127104-127122, 2020.

[132] W. Pinthurat, B. Hredzak, G. Konstantinou, and J. Fletcher, "Techniques for compensation of unbalanced conditions in LV distribution networks with integrated renewable generation: An overview," *Electric Power Systems Research,* vol. 214, p. 108932, 2023.

[133] F. H. M. Rafi, M. Hossain, M. S. Rahman, and S. Taghizadeh, "An overview of unbalance compensation techniques using power electronic converters for active distribution systems with renewable generation," *Renewable and Sustainable Energy Reviews,* vol. 125, p. 109812, 2020.

[134] A. Vijay, S. Doolla, and M. C. Chandorkar, "Unbalance mitigation strategies in microgrids," *IET Power Electronics,* vol. 13, no. 9, pp. 1687-1710, 2020.

[135] B. Liu, X. Zhao, Y. Liu, Y. Zhu, and J. Chen, "Control strategy of clustered micro-grids for grid voltage unbalance compensation without communications," *IET Generation, Transmission & Distribution,* vol. 14, no. 20, pp. 4410-4415, 2020.

[136] M. Castilla, M. Velasco, J. Miret, Á. Borrell, and R. Guzmán, "Control scheme for negative-sequence voltage compensation and current sharing in inverter-based grid-connected microgrids," *IEEE Transactions on Power Electronics,* vol. 37, no. 6, pp. 6556-6567, 2022.

[137] S. D'silva, M. Shadmand, S. Bayhan, and H. Abu-Rub, "Towards grid of microgrids: Seamless transition between grid-connected and islanded modes of operation," *IEEE Open Journal of the Industrial Electronics Society,* vol. 1, pp. 66-81, 2020.

[138] A. Nisar and M. S. Thomas, "Comprehensive control for microgrid autonomous operation with demand response," *IEEE Transactions on Smart Grid,* vol. 8, no. 5, pp. 2081-2089, 2016.

[139] M. H. Andishgar, E. Gholipour, and R.-a. Hooshmand, "An overview of control approaches of inverter-based microgrids in islanding mode of operation," *Renewable and Sustainable Energy Reviews,* vol. 80, pp. 1043-1060, 2017.

[140] J. Hmad, A. Houari, A. E. M. Bouzid, A. Saim, and H. Trabelsi, "A review on mode transition strategies between grid-connected and standalone operation of voltage source inverters-based microgrids," *Energies,* vol. 16, no. 13, p. 5062, 2023.
[141] T.-V. Tran, T.-W. Chun, H.-H. Lee, H.-G. Kim, and E.-C. Nho, "PLL-based seamless transfer control between grid-connected and islanding modes in grid-connected inverters," *IEEE Transactions on Power Electronics,* vol. 29, no. 10, pp. 5218-5228, 2013.
[142] M. Ganjian-Aboukheili, M. Shahabi, Q. Shafiee, and J. M. Guerrero, "Seamless transition of microgrids operation from grid-connected to islanded mode," *IEEE Transactions on Smart Grid,* vol. 11, no. 3, pp. 2106-2114, 2019.
[143] M. Sandelic, S. Peyghami, A. Sangwongwanich, and F. Blaabjerg, "Reliability aspects in microgrid design and planning: Status and power electronics-induced challenges," *Renewable and Sustainable Energy Reviews,* vol. 159, p. 112127, 2022.
[144] N. Karami, N. Moubayed, and R. Outbib, "General review and classification of different MPPT Techniques," *Renewable and Sustainable Energy Reviews,* vol. 68, pp. 1-18, 2017.
[145] H. Rezk and A. M. Eltamaly, "A comprehensive comparison of different MPPT techniques for photovoltaic systems," *Solar energy,* vol. 112, pp. 1-11, 2015.
[146] L. Xu, L. Yao, and C. Sasse, "Grid integration of large DFIG-based wind farms using VSC transmission," *IEEE Transactions on power systems,* vol. 22, no. 3, pp. 976-984, 2007.
[147] F. Nejabatkhah and Y. W. Li, "Overview of power management strategies of hybrid AC/DC microgrid," *IEEE Transactions on power electronics,* vol. 30, no. 12, pp. 7072-7089, 2014.
[148] B. Sahoo, S. K. Routray, P. K. Rout, and M. M. Alhaider, "Power quality and stability assessment of hybrid microgrid and electric vehicle through a novel transformation technique," *Sustainable Energy Technologies and Assessments,* vol. 51, p. 101927, 2022.
[149] A. Reznik, M. G. Simões, A. Al-Durra, and S. Muyeen, "$ LCL $ filter design and performance analysis for grid-interconnected systems," *IEEE transactions on industry applications,* vol. 50, no. 2, pp. 1225-1232, 2013.
[150] M. Ahmed, M. Abdelrahem, A. Farhan, I. Harbi, and R. Kennel, "DC-link sensorless control strategy for grid-connected PV systems," *Electrical Engineering,* pp. 1-11, 2021.
[151] D. Cittanti, F. Mandrile, M. Gregorio, and R. Bojoi, "Design space optimization of a three-phase LCL filter for electric vehicle ultra-fast battery charging," *Energies,* vol. 14, no. 5, p. 1303, 2021.
[152] C. Gurrola-Corral, J. Segundo, M. Esparza, and R. Cruz, "Optimal LCL-filter design method for grid-connected renewable energy sources," *International Journal of Electrical Power & Energy Systems,* vol. 120, p. 105998, 2020.
[153] V. Miskovic, V. Blasko, T. M. Jahns, A. H. Smith, and C. Romenesko, "Observer-based active damping of $ LCL $ resonance in grid-connected voltage source converters," *IEEE Transactions on Industry Applications,* vol. 50, no. 6, pp. 3977-3985, 2014.
[154] M. Büyük, A. Tan, M. Tümay, and K. Ç. Bayındır, "Topologies, generalized designs, passive and active damping methods of switching ripple filters for

voltage source inverter: A comprehensive review," *Renewable and Sustainable Energy Reviews,* vol. 62, pp. 46-69, 2016.

[155] Z. Yao, L. Xiao, and J. M. Guerrero, "Improved control strategy for the three-phase grid-connected inverter," *IET Renewable Power Generation,* vol. 9, no. 6, pp. 587-592, 2015.

[156] Z. Xin, P. C. Loh, X. Wang, F. Blaabjerg, and Y. Tang, "Highly accurate derivatives for LCL-filtered grid converter with capacitor voltage active damping," *IEEE Transactions on Power Electronics,* vol. 31, no. 5, pp. 3612-3625, 2015.

[157] J. Samanes, A. Urtasun, E. Gubia, and A. Petri, "Robust multisampled capacitor voltage active damping for grid-connected power converters," *International Journal of Electrical Power & Energy Systems,* vol. 105, pp. 741-752, 2019.

[158] D. Pan, X. Ruan, C. Bao, W. Li, and X. Wang, "Capacitor-current-feedback active damping with reduced computation delay for improving robustness of LCL-type grid-connected inverter," *IEEE Transactions on Power Electronics,* vol. 29, no. 7, pp. 3414-3427, 2013.

[159] W. Wu, Y. Chen, A. Luo, L. Zhou, X. Zhou, L. Yang, Y. Dong, and J. M. Guerrero, "A virtual inertia control strategy for DC microgrids analogized with virtual synchronous machines," *IEEE Transactions on Industrial Electronics,* vol. 64, no. 7, pp. 6005-6016, 2016.

[160] "IEEE Standard for Interconnection and Interoperability of Distributed Energy Resources with Associated Electric Power Systems Interfaces."

[161] J. C. Basilio and S. Matos, "Design of PI and PID controllers with transient performance specification," *IEEE Transactions on education,* vol. 45, no. 4, pp. 364-370, 2002.

[162] Y. Xia, W. Wei, M. Yu, X. Wang, and Y. Peng, "Power management for a hybrid AC/DC microgrid with multiple subgrids," *IEEE Transactions on power electronics,* vol. 33, no. 4, pp. 3520-3533, 2017.

[163] P. C. Loh, D. Li, Y. K. Chai, and F. Blaabjerg, "Autonomous operation of hybrid microgrid with AC and DC subgrids," *IEEE transactions on power electronics,* vol. 28, no. 5, pp. 2214-2223, 2012.

[164] N. Pogaku, M. Prodanovic, and T. C. Green, "Modeling, analysis and testing of autonomous operation of an inverter-based microgrid," *IEEE Transactions on power electronics,* vol. 22, no. 2, pp. 613-625, 2007.

[165] K. Yu, Q. Ai, S. Wang, J. Ni, and T. Lv, "Analysis and optimization of droop controller for microgrid system based on small-signal dynamic model," *IEEE Transactions on Smart Grid,* vol. 7, no. 2, pp. 695-705, 2015.

[166] T. H. Nguyen, T. L. Van, A. Nawaz, and A. Natsheh, "Feedback linearization-based control strategy for interlinking inverters of hybrid AC/DC microgrids with seamless operation mode transition," *Energies,* vol. 14, no. 18, p. 5613, 2021.

[167] J.-W. Chang, G.-S. Lee, S.-I. Moon, and P.-I. Hwang, "A novel distributed control method for interlinking converters in an islanded hybrid AC/DC microgrid," *IEEE Transactions on Smart Grid,* vol. 12, no. 5, pp. 3765-3779, 2021.

[168] J. Wang, C. Jin, and P. Wang, "A uniform control strategy for the interlinking converter in hierarchical controlled hybrid AC/DC microgrids," *IEEE Transactions on industrial electronics,* vol. 65, no. 8, pp. 6188-6197, 2017.

[169] L. Wang, X. Fu, and M.-C. Wong, "Operation and control of a hybrid coupled interlinking converter for hybrid AC/low voltage DC microgrids," *IEEE Transactions on Industrial Electronics,* vol. 68, no. 8, pp. 7104-7114, 2020.

[170] N. Korada and M. K. Mishra, "Grid adaptive power management strategy for an integrated microgrid with hybrid energy storage," *IEEE Transactions on Industrial Electronics,* vol. 64, no. 4, pp. 2884-2892, 2016.

[171] O. Palizban and K. Kauhaniemi, "Distributed cooperative control of battery energy storage system in AC microgrid applications," *Journal of Energy Storage,* vol. 3, pp. 43-51, 2015.

[172] J. Xiao, P. Wang, and L. Setyawan, "Hierarchical control of hybrid energy storage system in DC microgrids," *IEEE Transactions on Industrial Electronics,* vol. 62, no. 8, pp. 4915-4924, 2015.

[173] W. Yao, Y. Wang, Y. Xu, P. Lin, Y. Qi, and Q. Wu, "Distributed layered control and stability analysis of islanded networked-microgrids," *International Journal of Electrical Power & Energy Systems,* vol. 129, p. 106889, 2021.

[174] Y. Xia, W. Wei, M. Yu, Y. Peng, and J. Tang, "Decentralized multi-time scale power control for a hybrid AC/DC microgrid with multiple subgrids," *IEEE Transactions on Power Electronics,* vol. 33, no. 5, pp. 4061-4072, 2017.

Appendices

Appendix A: State-Space Matrix of Interlinking Converter Model

$$[A_{ILC}] = \begin{bmatrix} -m_p & 0 & 0 & 0 & 0 & 0 & 0 \\ 0 & 0 & 0 & 0 & 0 & 0 & 0 \\ 0 & 0 & 0 & 0 & 0 & 0 & 0 \\ 0 & k_{iv} & 0 & 0 & 0 & -1 & 0 \\ 0 & 0 & k_{iv} & 0 & 0 & 0 & -1 \\ 0 & \frac{k_{pi}k_{iv}}{L_f} & 0 & \frac{k_{ii}}{L_f} & 0 & \frac{-k_{pi}-R_f}{L_f} & \omega-\omega_n \\ 0 & 0 & \frac{k_{pi}k_{iv}}{L_f} & 0 & \frac{k_{ii}}{L_f} & \omega-\omega_n & \frac{-k_{pi}-R_f}{L_f} \\ 0 & 0 & 0 & 0 & 0 & \frac{1}{C_f} & 0 \\ 0 & 0 & 0 & 0 & 0 & 0 & \frac{1}{C_f} \\ -\frac{c}{L_c} & 0 & 0 & 0 & 0 & 0 & 0 \\ -\frac{d}{L_c} & 0 & 0 & 0 & 0 & 0 & 0 \end{bmatrix}$$

$$\begin{bmatrix} 0 & 0 & 0 & 0 \\ -1 & 0 & 0 & 0 \\ 0 & -1 & 0 & 0 \\ -k_{pv} & -\omega_n C_f & F & 0 \\ \omega_n C_f & -k_{pv} & 0 & 0 \\ \frac{-k_{pi}k_{pv}-1}{L_f} & \frac{-k_{pi}\omega_n C_f + I_{lq}}{L_f} & \frac{k_{pi}F}{L_f} & 0 \\ \frac{k_{pi}\omega_n C_f}{L_f} & \frac{-k_{pi}k_{pv}-1-I_{ld}}{L_f} & 0 & \frac{k_{pi}F}{L_f} \\ 0 & \omega_n + V_{oq} & -\frac{1}{C_f} & 0 \\ -\omega_n & -V_{od} & 0 & -\frac{1}{C_f} \\ \frac{1}{L_c} & I_{oq} & -\frac{R_c}{L_c} & \omega_n \\ 0 & \frac{-I_{od}}{L_c} & -\omega_n & -\frac{R_c}{L_c} \end{bmatrix}$$

$$[B_{ILC}] = \begin{bmatrix} 0 & 0 \\ 0 & 0 \\ 0 & 0 \\ 0 & 0 \\ 0 & 0 \\ 0 & 0 \\ 0 & 0 \\ 0 & 0 \\ 0 & 0 \\ 0 & 0 \\ 0 & 0 \\ \frac{cos\delta_o}{L_c} & -\frac{sin\delta_o}{L_c} \\ \frac{sin\delta_o}{L_c} & -\frac{cos\delta_o}{L_c} \end{bmatrix} \qquad [B_{com}] = \begin{bmatrix} -1 \\ 0 \\ 0 \\ 0 \\ 0 \\ 0 \\ 0 \\ 0 \\ 0 \\ 0 \\ 0 \\ 0 \\ 0 \end{bmatrix}$$

$$\left[C_{ILC_\omega}\right] = [0 \quad -m_p \quad 0 \quad 0 \quad 0 \quad 0 \quad 0 \quad 0 \quad 0 \quad 0 \quad 0 \quad 0 \quad 0]$$

$$\left[C_{ILC_i}\right] = \begin{bmatrix} a & 0 & 0 & 0 & 0 & 0 & 0 & 0 & 0 & 0 & 0 & cos\delta_o & -sin\delta_o \\ b & 0 & 0 & 0 & 0 & 0 & 0 & 0 & 0 & 0 & 0 & sin\delta_o & cos\delta_o \end{bmatrix}$$

Appendix B: Parameters of Interlinking Converter

The parameters related to the state-space matrix, A in the interlinking converter model:

Table 1: Parameters related to the state-space matrix.

Symbols	Values
I_{id}	11
I_{iq}	-5.5
I_{od}	11
I_{oq}	0.4
V_{od}	311
V_{oq}	0
V_D	311
V_Q	0
ω_o	314
δ_o	0

Appendix C: Detailed Configuration of the Lab Set up for RT-SIL

Fig. 1: LAB setup with required Equipment.

Fig. 2: Configuration of the OPAL-RT Simulator (OP5600).

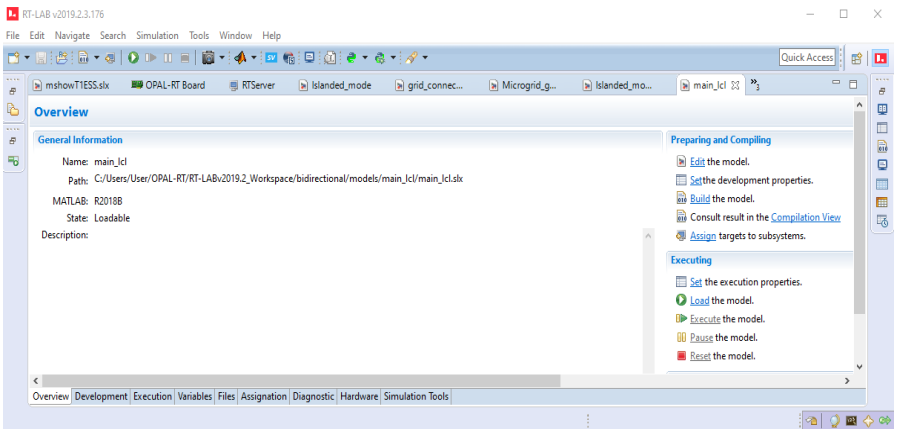

Fig. 3: Configuration of the RT LAB Window.

Fig. 4: RT SIL setup with Ethernet cable, host PC, and OP5600 target.

Appendix D: MATLAB/ Simulink Model of Control Strategies

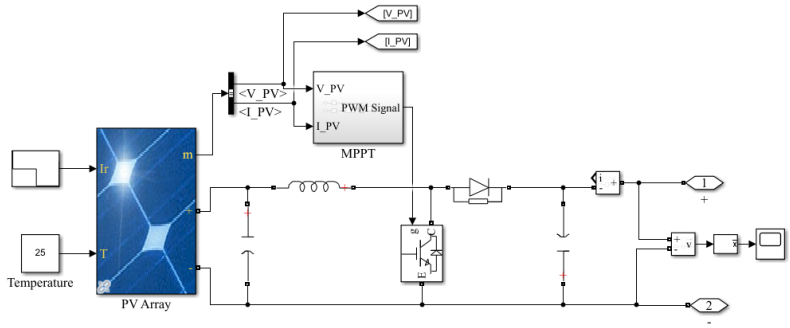

Fig. 5: Block Diagram of Photovoltaic System.

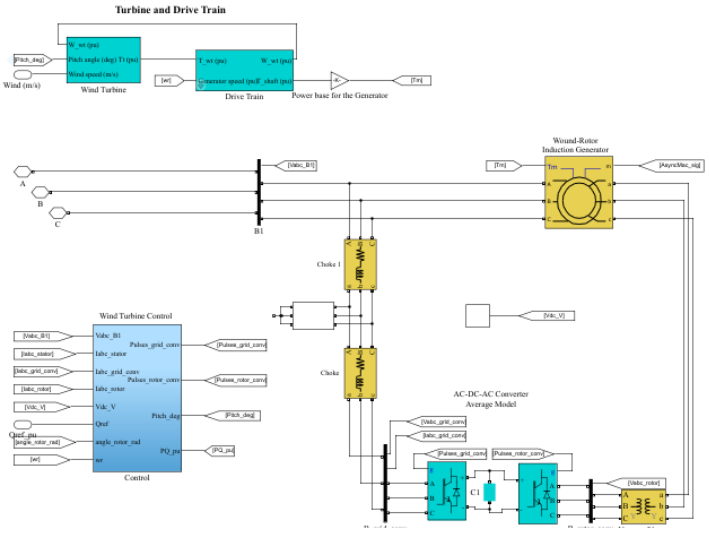

Fig. 6: Block Diagram of Wind Generator.

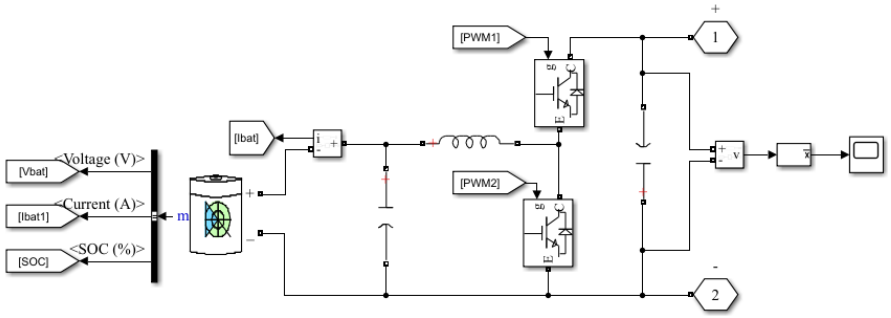

Fig. 7: Block Diagram of Energy Storage System.

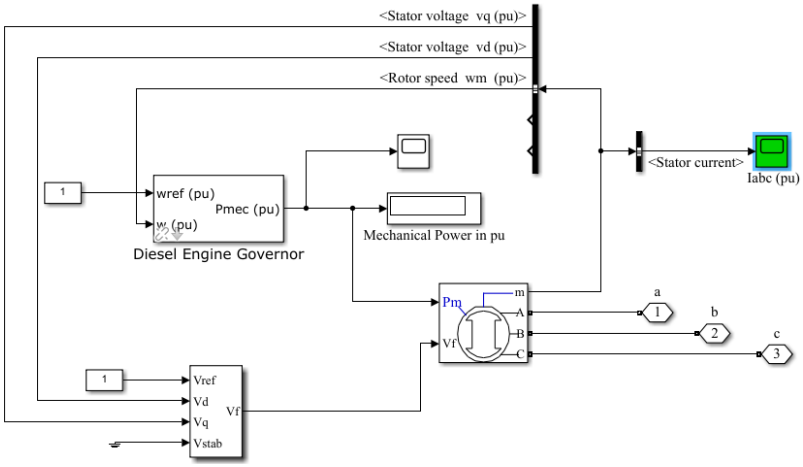

Fig. 8: Block Diagram of Diesel Generator.

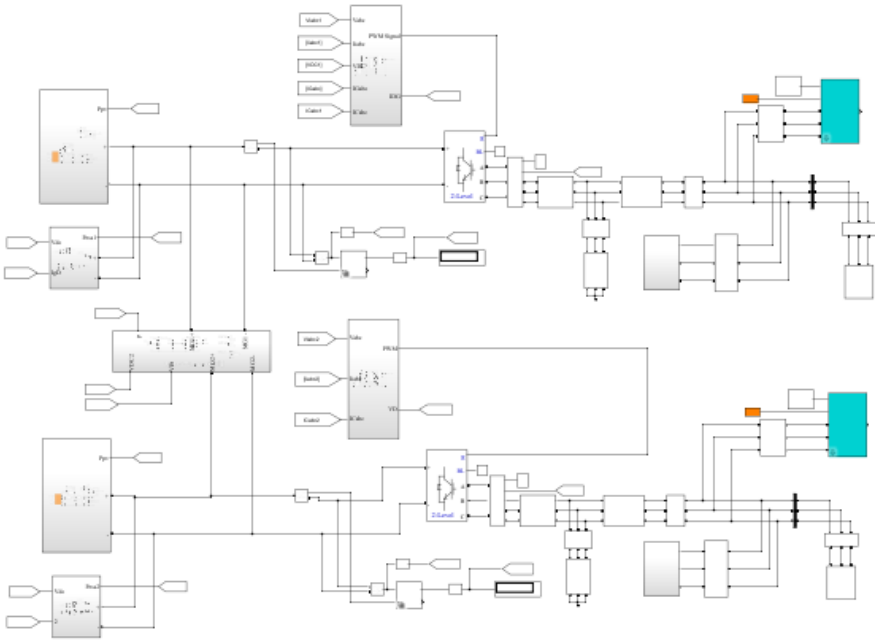

Fig. 9: Block Diagram of Networked Microgrid.